

RARE-EARTH FREE PERMANENT MAGNETS AND PERMANENT MAGNET  
SYNCHRONOUS MOTORS

by

JIHOON PARK

YANG-KI HONG, COMMITTEE CHAIR

TIMOTHY A. HASKEW

SHUHUI LI

GARY J. MANKEY

SUBHADRA GUPTA

A DISSERTATION

Submitted in partial fulfillment of the requirements  
for the degree of Doctor of Philosophy  
in the Department of Electrical and Computer Engineering  
in the Graduate School of  
The University of Alabama

TUSCALOOSA, ALABAMA

2016

Copyright Jihoon Park 2016  
ALL RIGHTS RESERVED

## ABSTRACT

In this dissertation, basic and applied research programs are engaged that range from the fundamental magnetism and magnetic properties of ferro- and ferrimagnetic materials to the design and fabrication of rare-earth (RE) free permanent and soft magnetic materials for an interior permanent magnet synchronous motor (IPMSM) (i.e., motor for electric vehicles and plug-in electric vehicles) and heat-assisted magnetic recording media (HAMR) with 4 Tb/in<sup>2</sup> information storage applications.

The applied research program emphasizes the design and synthesis of new RE-free permanent magnetic materials and magnetic exchange coupled core(hard)-shell(soft) particles to achieve a high maximum energy product  $[(BH)_{\max}]$ , and the design of an advanced IPMSM based on RE-free permanent magnets.

The electronic structures of hard magnetic materials such as Mn-Al, Mn-Bi, Mn-Bi-X, Fe-Pt, Fe-Pt-X, SrFe<sub>12</sub>O<sub>19</sub>, and SrFe<sub>12</sub>O<sub>19</sub>-X (X = transition elements) and soft magnetic materials such as nanocrystalline and Mn-B were calculated based on the density functional theory (DFT), and their exchange coupled magnetic properties with soft magnets were designed according to the size and shape of the particles. The calculated magnetic and electronic properties were used to obtain the temperature dependence of saturation magnetization  $M_s(T)$  and anisotropy constant  $K(T)$  within the mean field theory. Thereby, the temperature dependence of the maximum energy product  $[(BH)_{\max}(T)]$  is calculated using the calculated  $M_s(T)$  and  $K(T)$ .

The experimental approaches were based on chemical and ceramic processes to synthesize hard and soft magnetic materials. Prior to synthesis, material design parameters were optimized by first-principles calculations and micromagnetic simulations.

Lastly, performance of RE-free MnAl, MnBi, SrFe<sub>12</sub>O<sub>19</sub>, and Alnico IPMSMs, designed with the finite element method (FEM), at 23 and 200 °C were evaluated and compared to a RE Nd-Fe-B IPMSM. The performance parameters include torque, efficiency, and power. It was found that the performance of the MnBi and Alnico IPMSM is comparable with the Nd-Fe-B IPMSM.

## DEDICATION

This dissertation is dedicated to everyone who helped and guided me through the trials and tribulations of creating this manuscript. In particular, my advisor, Professor Dr. Yang-Ki Hong and MMDL (magnetic materials and device laboratory) members who stood by me throughout the time taken to complete this masterpiece.

## LIST OF ABBREVIATIONS AND SYMBOLS

AC	Alternating current
AF	Anti-ferromagnetic
ASW	Augmented spherical wave
$B$	Magnetic flux density
$(BH)_{\max}$	Maximum energy product
$(BH)_{\max}(T)$	Temperature dependence of maximum energy product
$B_J$	Brillouin function
$B_r$	Remanent magnetic flux density
$B_s$	Saturation magnetic flux density
DC	Direct current
$DCD$	dc demagnetization curve
DFT	Density functional theory
DI	Deionized
DOS	Density of states
DSAFPMM	Dual stator axial flux permanent magnet motor
$E$	Energy
EDX	Energy dispersive X-ray
$E_{ex}$	Exchange energy

$E_F$	Fermi energy
EMF	Back electromotive force
EV	Electric vehicles
FEM	Finite element method
FLAPW	Full potential linear-augmented plane wave
FLMTO	Full potential linear-muffin-tin-orbital
FM	Ferromagnetic
FPLAPW	Full-potential linearized augmented plane wave
$f_h$	Volume fraction of magnetically hard phase
$f_s$	Volume fraction of magnetically soft phase
f.u.	Formula unit
G	Gauss
GGA	Generalized gradient approximation
$H$	Applied magnetic field
HAMR	Heat-assisted magnetic recording
$H_c$	Coercivity
$H_{ci}$	Intrinsic coercivity
$H_{ci}(T)$	Temperature dependence of intrinsic coercivity
HEV	Hybrid electric vehicles
$I$	Current
IPMSM	Interior permanent magnet synchronous motor
$IRM$	Isothermal remanent magnetization
$J$	Angular quantum number

$J (= S + L)$	Total angular momentum
$J_0$	Molecular field parameter
$J_{ij}$	Exchange integrals
$K$	Anisotropy constant
$K_{eff}$	Effective anisotropy constant
$K_{eff}(0)$	Effective anisotropy constant at 0 K
$k_B$	Boltzmann constant
$L$	Orbital contribution
LAPW	Linearized augmented plane wave
LDA	Local density functional approximation
LMTO-ASA	Linear-muffin-tin-orbital method within the atomic-sphere-approximation
LSDA	Local-spin-density approximation
LTP	Low temperature phase
MAE	Magnetocrystalline anisotropy energy
MD	Molecular dynamics
MFA	Mean field approximation
MHF	Magnetic hyperfine fields
$M_r$	Remanent magnetization (emu/cm <sup>3</sup> )
$M_s$	Saturation magnetization (emu/cm <sup>3</sup> )
$M_s(0)$	Saturation magnetization at 0 K
$M_s(T)$	Temperature dependence of saturation magnetization
$m_i$	Magnetic moment at $i$ -th sublattice
$m_i(T)$	Temperature dependence of magnetic moment at $i$ -th sublattice

$n_i$	Number of $i$ -th atoms
Oe	Oersted
PMSM	Permanent magnet synchronous machine
PPMS	Physical property measurement system
RE	Rare earth
RE-free	Rare earth free
RMT	Muffin tin radii
$R_{SD}$	Critical radius of single domain limit
$r$	Average winding radius
$S$	Spin moment
SEM	Scanning electron microscope
SEM-EDS	Scanning electron microscopy-energy dispersive X-ray spectrometry
SFD	Switching field distribution
$S_i$	Spin of the $i$ -th Mn atom
SPMSM	Surface permanent magnet synchronous motor
STEM	Scanning transmission electron microscopy
$T$	Torque
$T_c$	Curie temperature
$T/T_c$	Normalized temperature
TEM	Transmission electron microscopy
$T_N$	Néel temperature
$U$	Coulomb interaction parameter
u.c.	Unit cell

VASP	Vienna Ab-initio Simulation Package
VCA	Virtual crystal approximation
VSM	Vibrating sample magnetometer
XRD	X-ray diffraction
$Z$	Number of conductors
$z_{ij}$	Number of neighboring $j$ -th atoms to $i$ -th atom
$\text{\AA}$	Angstrom
$\alpha$	Temperature coefficient of magnetization
$\beta$	Temperature coefficient of intrinsic coercivity
$\Delta\sigma_s$	Difference of saturation magnetization
$\Delta H_{ci}$	Difference of intrinsic coercivity
$\Delta_i$	Energy difference between the excited state at the $i$ sublattice and the ground state
$\Delta_j$	Energy difference between the excited state at the $j$ sublattice and the ground state
$\Delta_{ij}$	Energy difference of exchange energies between the excited state at both the $i$ and $j$ sublattices and the ground state
$\Delta M$	Delta $M$
$\delta_w$	Domain wall thickness
$\eta_i$	Conversion ratio parameters
$\mu_B$	Bohr magneton
$\rho$	Density
$\sigma$	Magnetization (emu/g)
$\sigma_s$	Saturation magnetization (emu/g)
$\sigma_r$	Remanent magnetization (emu/g)

$\sigma_{\text{ex}}$  Magnetization of exchange coupled magnet

$\chi$  Mass percentage of soft phase

## ACKNOWLEDGMENTS

It is my greatest pleasure to have this opportunity to express my sincere gratitude to everyone who helped me during my Ph.D. program at the University of Alabama. The most important person is my advisor Prof. Yang-Ki Hong, who guided me into the field of magnetism and magnetic materials. He provided me his excellent guidance, expertise, and moral support which were all essential for my success not only as a student, but also in my professional life.

I would like to thank all my committee members, Dr. Haskew, Dr. Mankey, Dr. Gupta, and Dr. Li for serving on my committee and for their great support and guidance on my dissertation and academic progress. I would also like to thank all my former and current lab colleagues: Dr. Seok Bae, Dr. Terimitsu Tanaka, Dr. Jeevan Jalli, Dr. Jaejin Lee, Dr. Xia Xu, Woncheol Lee, Minyeong Choi, Hoyun Won, Gavin Abo, Nichola Neveu, Gatlin LaRochelle, and Maxwell Fazeli for their constant help and support.

Finally, I would like to thank all of my family members for their tremendous love, encouragement, and support.

## CONTENTS

ABSTRACT .....	ii
DEDICATION .....	iv
LIST OF ABBREVIATIONS AND SYMBOLS .....	v
ACKNOWLEDGMENTS .....	xi
LIST OF TABLES .....	xvii
LIST OF FIGURES .....	xix
1. INTRODUCTION .....	1
1.1. Motivation.....	1
1.2. Objective.....	2
1.3. Permanent magnetic materials .....	2
1.3.1. Single-phase permanent magnetic materials.....	3
1.3.2. Magnetic exchange coupled permanent magnetic materials .....	10
1.4. References.....	13
2. ELECTRONIC STRUCTURE AND MAGNETIC PROPERTIES OF TAU-PHASE MnAl.....	14
2.1. Introduction.....	14
2.2. Calculations and experiments .....	15
2.3. Results and discussion .....	15
2.4. Conclusions.....	19
2.5. References.....	19
3. ELECTRONIC STRUCTURE AND MAXIMUM ENERGY PRODUCT AT ELEVATED TEMPERATURE OF LOW TEMPERATUER PHASE MnBi .....	21
3.1. Introduction.....	21
3.2. Method of Calculations.....	22

3.3. Results and Discussion .....	23
3.3.1. Density of States and Magnetic Moments .....	23
3.3.2. Magnetocrystalline Anisotropy Constant .....	24
3.3.3. Curie Temperature .....	25
3.3.4. Temperature Dependence of Saturation Magnetization and Maximum Energy Product.....	27
3.3.5. Electron Density Maps and $c/a$ Ratio Dependence of Magnetic Moment.....	30
3.4. Conclusions.....	33
3.5. References.....	33
4. ELECTRONIC STRUCTURE AND MAGNETIC PROPERTIES OF STRONTIUM FERRITE.....	35
4.1 Maximum energy product at elevated temperatures for strontium ferrite.....	35
4.1.1. Introduction.....	35
4.1.2. Magnetic structure of strontium ferrite .....	36
4.1.3. Method of calculations.....	37
4.1.4. Results.....	40
4.1.4.1. Exchange integrals (interactions between the five magnetic sublattices) .....	40
4.1.4.2. Temperature dependence of saturation magnetization $M_s(T)$ and maximum energy product $(BH)_{\max}(T)$ .....	42
4.1.5. Conclusion .....	49
4.1.6. References.....	50
4.2 Thermomagnetic stability of strontium ferrite particles with different shapes.....	53
4.2.1. Introduction.....	53
4.2.2. Experimental.....	54

4.2.3. Results and discussion .....	55
4.2.4. Conclusions.....	65
4.2.5. References.....	66
4.3 Coercivity of strontium ferrite platelets near single domain size ...	69
4.3.1. Introduction.....	69
4.3.2. Results and discussion .....	69
4.3.3. Conclusions.....	75
4.3.4. References.....	75
5. ELECTRONIC STRUCTURE OF La-Co SUBSTITUTED STRONTIUM FERRITE .....	77
5.1. Introduction.....	77
5.2. Method of calculations.....	78
5.3. Results and discussion .....	78
5.4. Conclusions.....	82
5.5. References.....	82
6. ELECTRONIC STRUCTURE AND MAGNETIC PROPERTIES OF Mn SUBSTITUTED FePt.....	84
6.1. Introduction.....	84
6.2. Method of calculations.....	85
6.3. Results and discussion .....	86
6.3.1. Density of states and magnetic moments of FePt and Fe <sub>0.5</sub> Mn <sub>0.5</sub> Pt.....	86
6.3.2. Curie temperature and anisotropy constant of L1 <sub>0</sub> -ordered FePt and Fe <sub>0.5</sub> Mn <sub>0.5</sub> Pt .....	90
6.3.3. Curie temperature, magnetization, and anisotropy constant of Fe <sub>1-x</sub> Mn <sub>x</sub> Pt.....	93
6.3.4. Temperature dependence of magnetization and anisotropy constant of Fe <sub>1-x</sub> Mn <sub>x</sub> Pt.....	96

6.4. Conclusions.....	100
6.5. References.....	101
7. ELECTRONIC STRUCTURE AND MAGNETIC PROPERTIES OF NANOCRYSTALLINE SOFT MAGNETS .....	103
7.1. Introduction.....	103
7.2. Method of calculations.....	104
7.3. Results and discussion .....	106
7.4. Conclusions.....	110
7.5. References.....	111
8. ELECTRONIC STRUCTURE AND MAGNETIC PROPERTIES OF MnB SOFT MAGNETS .....	113
8.1. Introduction.....	113
8.2. Method of calculations.....	113
8.3. Results and discussion .....	114
8.4. Conclusions.....	118
8.5. References.....	118
9. MAGNETIC PROPERTIES OF EXCHANGE COUPLED MnAl/FeCo .....	119
9.1. Introduction.....	119
9.2. Experiments .....	120
9.3. Results and discussion .....	121
9.4. Conclusions.....	126
9.5. References.....	127
10. ELECTRIC MACHINE: PERMANENT MAGNET SYNCHRONOUS MOTOR .....	128
10.1. Introduction.....	128
10.2. Background: principles of motor .....	129

10.3. Permanent Magnet Synchronous Motors (PMSM).....	133
10.4. Design of IPMSM.....	138
10.5. Finite Element Analysis – Maxwell 3D.....	140
10.6. Results and discussion .....	141
10.7. Conclusions.....	145
10.8. References.....	146
11. CONCLUSIONS.....	148
12. FUTURE WORK.....	150
APPENDIX.....	153

## LIST OF TABLES

3.1	The calculated spin and orbital magnetic moments per formula unit (f.u.) and Mn and Bi atoms for low temperature phase (LTP) MnBi in units of $\mu_B$ . Magnetic moments from both spin-polarized and spin-orbit coupling calculations are listed .....	24
3.2	The number of nearest neighbors ( $z_{0i}$ ) and corresponding distances ( $r_{0i}$ ) in the unit of Å in LTP MnBi .....	26
4.1.1.	The five magnetic sublattices ( $2a$ , $2b$ , $12k$ , $4f_1$ , and $4f_2$ ) in the unit cell of SrFe <sub>12</sub> O <sub>19</sub> . $n_i$ is the number of Fe <sup>3+</sup> ions at $i$ th sublattice in the unit cell, and $\sigma_i^{(0)} = +1$ or $-1$ represents the ground state spin configuration at $i$ th sublattice.....	38
4.1.2.	The number of nearest neighbors and corresponding distance for the five magnetic sublattices ( $2a$ , $2b$ , $12k$ , $4f_1$ , and $4f_2$ ) in the unit cell of SrFe <sub>12</sub> O <sub>19</sub> . $z_{ij}$ is the number of neighbors (Fe <sup>3+</sup> ions) at $j$ th sublattice to $i$ th sublattice, and $r_{ij}$ is the corresponding distances in nm. The second-nearest neighbors are also given if $r_{ij}$ is shorter than 0.4 nm .....	39
4.1.3.	The energy difference $\Delta(U_{eff})$ in eV between the ground state and excited states. The magnetic moment $m$ in $\mu_B$ are also listed for the excited spin configurations. The $s_1$ and $s_2$ denote the excited sublattices.....	41
4.2.1.	Thermomagnetic stability for peanut-like SrM particles and hexagonal SrM platelets .....	65
4.3.1.	The detailed values of Fe/Sr molar ratio dependence of average diameter ( $D$ ) of SrM platelets, and corresponding magnetization ( $\sigma$ ) at 21 kOe and intrinsic coercivity ( $H_{ci}$ ) .....	73
5.1.	Effect of La and Co substitution on magnetic moment and lattice constant of SrM ( $x = 0.0$ ) and La-Co SrM ( $x = 0.5$ ).....	79
6.1.	Calculated (Cal.) and experimental (Exp.) spin and orbital magnetic moments ( $\mu_B$ ) of L1 <sub>0</sub> -ordered FePt and Fe <sub>0.5</sub> Mn <sub>0.5</sub> Pt.....	90
6.2.	The number of nearest neighbors ( $z_{0i}$ ) and corresponding distances ( $r_{0i}$ ) in the unit of Å in FePt and Fe <sub>0.5</sub> Mn <sub>0.5</sub> Pt .....	92

6.3. Calculated (Cal.) and experimental (Exp.) magnetizations, magnetocrystalline anisotropy energies (MAE), anisotropy constants ( $K$ ), and Curie temperatures ( $T_c$ ) of $L1_0$ -ordered FePt and $Fe_{0.5}Mn_{0.5}Pt$ .....	92
7.1. Calculated and experimental total and element specific spin and orbital magnetic moments ( $\mu_B$ ) and corresponding magnetic flux density (T) for crystalline $Fe_3Si$ .....	107
7.2. Calculated magnetic moments ( $\mu_B$ ) and corresponding magnetic flux density (T) for the amorphous Fe-B in $Fe_{89}Cu_1Si_{10-y}B_y$ .....	107
7.3. Calculated magnetic moments ( $\mu_B$ ) and corresponding magnetic flux density (T) for the amorphous Fe-B in $Fe_{88}Cu_2Si_{10-y}B_y$ .....	109
7.4. Calculated magnetic flux density (T) and volumes ( $\text{\AA}^3$ ) for $(10 - y) \cdot Fe_3Si$ , Fe-B, and $1 \cdot Cu$ , and corresponding magnetic flux density (T) for $Fe_{89}Cu_1Si_{10-y}B_y$ .....	110
7.5. Calculated magnetic flux density (T) and volumes ( $\text{\AA}^3$ ) for $(10 - y) \cdot Fe_3Si$ , Fe-B, and $2 \cdot Cu$ , and corresponding magnetic flux density(T) for $Fe_{88}Cu_2Si_{10-y}B_y$ .....	110
8.1. Magnetization directions and corresponding relative energies ( $\Delta E$ ) in the unit of mRy.....	115
8.2. The calculated spin and orbital magnetic moments per formula unit (f.u.) and Mn and B atoms for MnB in the unit of $\mu_B$ .....	116
8.3. The calculated magnetic moments per formula unit ( $\mu_B/f.u.$ ) and corresponding magnetizations ( $emu/cm^3$ ) and magnetic flux densities (T) of MnB .....	116
10.1. Comparison of the electric motors for hybrid electric vehicle (HEV) application .....	135
10.2. Comparison of the interior permanent magnet synchronous motor (IPMSM) and surface permanent magnet synchronous motor (SPMSM).....	136

## LIST OF FIGURES

1.1. Schematic illustration of $r_a/r_{3d}$ ratio versus exchange integral .....	3
1.2. The $c/a$ ratio dependence of magnetic moment and relative total energy for MnBi .....	4
1.3. Density of states (DOS) for (a) distorted MnBi ( $c/a = 1.00$ ) and (b) LTP MnBi ( $c/a = 1.37$ ). The black line represents the total DOS, and blue and pink lines represent the partial DOS of Mn and Bi, respectively. The red vertical line corresponds to the Fermi energy ( $E_F$ ) .....	5
1.4. Spin-orbit-lattice interactions.....	5
1.5. The increasing stable $c/a$ ratio for MnBi-X, and its corresponding magnetic moment .....	7
1.6. Strategic approaches in saturation magnetization ( $M_s$ ), anisotropy constant ( $K$ ), and Curie temperature ( $T_c$ ) calculations .....	8
1.7. Strategic approaches in temperature dependence of magnetization [ $M(T)$ ] and anisotropy constant [ $K(T)$ ] calculations.....	9
1.8. Concept of core-shell nanomagnet with strong, positive magnetic exchange coupling.....	10
2.1. (a) Partial phase diagram of Mn-Al [6], and molecular structures of (b) $\epsilon'$ -phase and (c) $\tau$ -phase MnAl.....	16
2.2. (a) Density of states of $\epsilon'$ -phase MnAl and (b) density of states of $\tau$ -phase MnAl .....	16
2.3. The $c/a$ dependence of magnetic moment and relative total energy...17	17
2.4. XRD spectra for Mn <sub>54</sub> Al <sub>46</sub> alloy .....	18
2.5. (a) The saturation magnetization and (b) the $\tau$ -phase percentage according to the annealing time.....	19

3.1. Density of states (DOS) for LTP MnBi in the (a) $\langle 100 \rangle$ and (b) $\langle 001 \rangle$ magnetization directions. The black line represents the total DOS, and blue and pink lines represent the partial DOS of Mn and Bi, respectively. The red vertical line corresponds to the Fermi energy ( $E_F$ ) .....	25
3.2. The calculated and experimental temperature dependence of saturation magnetization $M_s(T)$ for LTP MnBi .....	28
3.3. Experimental intrinsic coercivity ( $H_{ci}$ ) as a function of temperature for LTP MnBi .....	28
3.4. The calculated temperature dependence of the maximum energy product $(BH)_{\max}(T)$ and experimental $(BH)_{\max}$ for LTP MnBi and experimental $(BH)_{\max}(T)$ for Nd-Fe-B .....	30
3.5. The $c/a$ dependence of magnetic moment and relative total energy for MnBi .....	31
3.6. The 3D and 2D electron density maps for LTP MnBi in (a) (110), (b) (100) and (c) (001) planes. The peaks, colors, and contour lines indicate the electron density .....	31
3.7. Yellow boxes indicate the low electron density areas of the hexagonal LTP MnBi structure .....	32
4.1.1. The unit cell (left), spin configurations of $Fe^{3+}$ at each layer (middle), and lattice constants and number of $Fe^{3+}$ at each sublattice (right) for hexagonal strontium ferrite ( $SrFe_{12}O_{19}$ ) [28]. The spins at the nearest neighbors are anti-ferromagnetically coupled as shown (middle) .....	37
4.1.2. The sublattice exchange integrals as a function of $U_{eff}$ (3.7, 7.0, and 10.3 eV) .....	42
4.1.3. The calculated sublattice magnetic moments as a function of temperature $m(T)$ . The exchange integrals used to calculate the sublattice magnetic moments are from the exchange energies with $U_{eff}$ of 7.0 eV .....	46
4.1.4. The calculated and experimental saturation magnetizations as a function of temperature $M_s(T)$ . The open circles are the $M_s(T)$ from the calculated sublattice $m(T)$ , and full circles are experimental $M_s(T)$ .....	47
4.1.5. The temperature dependence of half-remanent magnetization $B_r/2(T)$ and intrinsic coercivity $H_{ci}(T)$ . The open circles are the calculated $B_r/2(T)$ , and full squares are the semi-empirical $H_{ci}(T)$ ..	47

4.1.6. The calculated maximum energy product as a function of temperature $(BH)_{\max}(T)$ . The open circles are the calculated data from the calculated temperature dependences of saturation magnetization $M_s(T)$ . Red and blue squares indicate experimental room temperature $(BH)_{\max}$ .....	48
4.2.1. XRD patterns of as-synthesized submicron polyhedral and nanometer spherical $\text{Fe}_3\text{O}_4$ particles.....	56
4.2.2. (a) TEM and (b) SEM images of as-synthesized polyhedral $\text{Fe}_3\text{O}_4$ particles (370 nm in average diameter) and (c) TEM and (d) SEM images of spherical $\text{Fe}_3\text{O}_4$ particles (50 nm in average diameter). The insets in (b) and (d) show the shapes of polyhedral and spherical $\text{Fe}_3\text{O}_4$ particles, respectively .....	57
4.2.3. XRD patterns for (a) as-calcined and (b) acid-washed peanut-like SrM particles, and for (c) as-calcined and (d) acid-washed hexagonal SrM platelets .....	57
4.2.4. SEM images of (a) and (b) for peanut-like SrM particles (0.45 $\mu\text{m}$ ), and of (c) and (d) for hexagonal SrM platelets (1 $\mu\text{m}$ ) .....	58
4.2.5. Schematic illustrations for the formation of (a) peanut-like SrM particles (0.45 $\mu\text{m}$ in average diameter) and (b) hexagonal SrM platelets (1.0 $\mu\text{m}$ in average diameter) .....	59
4.2.6. Magnetic hysteresis loops and virgin curves of as-calcined and acid-washed peanut-like SrM particles and hexagonal SrM platelets at 300 K.....	60
4.2.7. Delta M curves derived for peanut-like SrM particles and hexagonal SrM platelets .....	62
4.2.8. Temperature dependence of saturation magnetization measured for peanut-like SrM particles and hexagonal SrM hexagonal platelets. The inset represents magnetic hysteresis loops at 400 K .....	63
4.2.9. Temperature dependence of intrinsic coercivity measured for peanut-like SrM particles and hexagonal SrM platelets.....	64
4.3.1. XRD patterns of the SrM particles for Fe/Sr = (a) 6, (b) 8, and (c) 10.....	70
4.3.2. SEM images and histograms of the SrM particles for Fe/Sr = (a) 6, (b) 8, and (c) 10 .....	71

4.3.3. The Fe/Sr molar ratio ( $x$ ) dependence of average diameter ( $D$ ) and thickness ( $t$ ) for the SrM platelets.....	72
4.3.4. Magnetic hysteresis loops for the SrM platelets with various sizes .....	72
4.3.5. The average diameter dependence of magnetization ( $\sigma$ ) at 21 kOe and intrinsic coercivity ( $H_{ci}$ ) of SrM platelets .....	73
4.3.6. The average diameter dependence of intrinsic coercivity ( $H_{ci}$ ) for hexagonal SrM platelets (this work) and hexagonal BaM platelets [1] .....	74
5.1. Sublattice magnetic moments in Bohr magneton ( $\mu_B$ )/atom as a function of the concentration of La/Co ( $x$ ) .....	79
5.2. Total magnetic moments in Bohr magneton ( $\mu_B$ )/u.c. as a function of the concentration of La/Co ( $x$ ) .....	80
5.3. Density of states (DOS) for (a) SrFe <sub>12</sub> O <sub>19</sub> ( $x = 0.0$ ) and (b) Sr <sub>0.5</sub> La <sub>0.5</sub> Fe <sub>11.5</sub> Co <sub>0.5</sub> O <sub>19</sub> ( $x = 0.5$ ). The DOS near the Fermi energy ( $E_F$ ) in the green boxes are enlarged on the right sides. The blue lines represent total DOS, and the red vertical lines correspond to the $E_F$ .....	81
6.1. Crystal structures of (a) L1 <sub>0</sub> -ordered FePt and (b) Fe <sub>0.5</sub> Mn <sub>0.5</sub> Pt with atoms colored as Fe-red, Pt-purple, and Mn-blue .....	86
6.2. Density of states (DOS) of (a) FePt and (b) Fe <sub>0.5</sub> Mn <sub>0.5</sub> Pt for majority and minority spin states. The black line represents the total DOS, and blue, green, and pink lines represent the partial DOS of Fe, Mn, and Pt, respectively. The red vertical line corresponds to the Fermi energy ( $E_F$ ).....	88
6.3. Predicted and experimental $x$ dependence of Curie temperature $T_c(x)$ for Fe <sub>1-x</sub> Mn <sub>x</sub> Pt. The $T_c$ of 650 - 600 K for HAMR application are marked by the yellow region. The required $x$ to meet the $T_c$ of 650 - 600 K is between 0.0294 and 0.0713, and marked by the blue region.....	94
6.4. Predicted and experimental $x$ dependence of magnetization $M_s(x)$ and anisotropy constant $K(x)$ for Fe <sub>1-x</sub> Mn <sub>x</sub> Pt. The $M_s$ and $K$ for $x$ of 0.0294 and 0.0713 (blue region) are 1041 - 919 emu/cm <sup>3</sup> and 9.96 - 8.36 × 10 <sup>6</sup> J/m <sup>3</sup> (yellow regions), respectively .....	95
6.5. The calculated temperature dependence of magnetizations $M_s(T)$ for Fe <sub>1-x</sub> Mn <sub>x</sub> Pt ( $x = 0.0000, 0.0294, \text{ and } 0.0713$ ) and experimental	

magnetizations for different compositions, morphologies, and temperature .....	97
6.6. The calculated temperature dependence of anisotropy constants $K(T)$ for $\text{Fe}_{1-x}\text{Mn}_x\text{Pt}$ ( $x = 0.0000, 0.0294, \text{ and } 0.0713$ ) and experimental $K$ for different compositions, morphologies, and temperatures .....	98
6.7. The normalized $x$ dependence of magnetization $M_s(x)$ and anisotropy constant $K(x)$ for experimental and calculated $\text{Fe}_{1-x}\text{Mn}_x\text{Pt}$ .....	99
7.1. Crystal structure of $\text{Fe}_3\text{Si}$ with atoms colored as Fe-red and Si-light blue.....	105
7.2. Density of states (DOS) for $\text{Fe}_3\text{Si}$ . The black line represents the total DOS, and blue, green, and pink lines represent the partial DOS of Fe ( $8c$ ), Fe ( $4b$ ), and Si, respectively. The red vertical line corresponds to the Fermi energy ( $E_F$ ).....	106
7.3. Density of states (DOS) for (a) $\text{Fe}_{62}\text{B}_1$ and (b) $\text{Fe}_{86}\text{B}_9$ . The blue and green lines represent the total DOS of $\text{Fe}_{62}\text{B}_1$ and $\text{Fe}_{86}\text{B}_9$ , respectively. The red vertical line corresponds to the Fermi energy ( $E_F$ ) .....	108
7.4. Density of states (DOS) for (a) $\text{Fe}_{61}\text{B}_1$ and (b) $\text{Fe}_{85}\text{B}_9$ . The blue and green lines represent the total DOS of $\text{Fe}_{61}\text{B}_1$ and $\text{Fe}_{85}\text{B}_9$ , respectively. The red vertical line corresponds to the Fermi energy ( $E_F$ ) .....	109
7.5. Magnetic flux density for the $\text{Fe}_{90-x}\text{Cu}_x\text{Si}_{10-y}\text{B}_y$ ( $1 \leq x \leq 2$ and $1 < y < 9$ ). The yellow region indicates the magnetic flux density higher than 1.8 T, and the green region corresponds to the B concentration of $4 < y < 9$ .....	111
8.1. Crystal structures of MnB with atoms colored as Mn-red and B-black .....	114
8.2. Density of states (DOS) for MnB. The black line represents the total DOS, and blue and green lines represent the partial DOS of Mn and B, respectively. The red vertical line corresponds to the Fermi energy ( $E_F$ ).....	115
8.3. The calculated temperature dependence of magnetization $M_s(T)$ for MnB. The $M_s(T)$ is compared with calculated and experimental magnetizations .....	117

9.1. Elemental mapping image of ferromagnetic $\tau$ -phase $Mn_{54}Al_{46}/\alpha$ - phase $Fe_{65}Co_{35}$ composite ( $f_h = 0.819$ ) .....	122
9.2. (a) the XRD patterns and (b) hysteresis loops for synthesized single phase $\tau$ -phase $Mn_{54}Al_{46}$ , $\alpha$ -phase $Fe_{65}Co_{35}$ , and composite ( $f_h = 0.819$ ).....	123
9.3. The calculated and experimental $f_h$ dependence of (a) magnetization $\sigma(f_h)$ and (b) intrinsic coercivity $H_{ci}(f_h)$ for $\tau$ -phase $Mn_{54}Al_{46}/\alpha$ -phase $Fe_{65}Co_{35}$ composites .....	125
10.1. (a) The right-hand rule between current $I$ in a uniform magnetic field $B$ and force $F$ in a rectangular loop, and (b) schematic drawing of magnetic fields in the loop.....	129
10.2. A simple direct current motor. (a) Brushes are aligned with commutator segments and (b) each brush is in contact with both commutator segments.....	130
10.3. (a) Two-pole and (b) three-pole DC motors .....	131
10.4. (a) Typical design [1] and (b) an actual example of a BLDC motor [2].....	132
10.5. Schematic drawing of a BLDC motor .....	133
10.6. The comparison between rectangular and sinusoidal currents in a BLDC motor and PMSM, respectively .....	134
10.7. Various rotor configurations of an IPMSM [8] .....	137
10.8. Design of 8-pole V-shape IPMSM motor in (a) 2-D and (b) 3-D view .....	138
10.9. Detailed design parameters of (a) the outer diameters of stator and rotor and (b) inside of rotor of the IPMSM .....	139
10.10. The energy and coenergy relations for (a) linear material and (b) nonlinear material under constant current conditions (steady state) [8].....	140
10.11. IPMSM operation views with magnetic flux density and current flux line. IPMSM with Nd-Fe-B magnet at (a) 23 °C and (b) 200 °C, and MnBi at (c) 23 °C and (d) 200 °C are shown .....	142
10.12. Rotor rotation angle dependence of torque at (a) 23 °C and (b) 200 °C.....	143

10.13. Temperature dependence of average torque from IPMSM with Nd-Fe-B, MnBi, and SrFe <sub>12</sub> O <sub>19</sub> .....	144
12.1. Design methodology of new permanent magnetic materials based on ferromagnetic Mn or Fe.....	150
12.2. Dual Stator Axial Flux Permanent Magnet Motor (DSAFPMM) and (b) Permanent Magnet assisted Synchronous Reluctance Motor (PMa-SynRM) design. The blue, yellow, and green colors indicate three-phases .....	151

## CHAPTER 1

### INTRODUCTION

#### 1.1. Motivation

Magnetic materials with large magnetization ( $M$ ), anisotropy constant ( $K$ ), and Curie temperature ( $T_c$ ) consistently attract attention due to their potentials for permanent magnet (PM) applications. Recently, these applications have been expanding towards sustainable energy devices, including electric vehicle (EV) motors and wind power generators. The most important characteristics of the PM is the maximum energy product  $[(BH)_{\max}]$ . The  $(BH)_{\max}$  can be estimated as  $(BH)_{\max} = (B_r)^2/4$  for  $H_{ci} > B_r/2$  or  $(BH)_{\max} = (B_r - H_{ci})H_{ci}$  for  $H_{ci} < B_r/2$ , where  $B_r$  is the residual flux density and  $H_{ci}$  is the intrinsic coercivity of magnetic materials. Therefore, high  $B_r$  and  $H_{ci}$  along with high  $T_c$  are necessary to achieve PMs with high  $(BH)_{\max}$  at an EV's operation temperature.

Although for the last two decades rare-earth (RE) magnetic materials, in particular Nd-Fe-B, have dominated PM applications, there are two important issues that must still be addressed for continued full utilization of PMs in high-efficiency sustainable energy applications. One is the technical, or scientific, issue caused by the low operation temperature range of the RE hard magnetic materials, and the other is that supply-limited RE minerals produce price and global energy security problems. Even though Nd<sub>2</sub>Fe<sub>14</sub>B possesses high  $4\pi M_s$  of 1.61 T and  $K$  of  $4.9 \times 10^6$  J/m<sup>3</sup> at room temperature [1], its operation temperature is limited to 150 °C because of its low  $T_c$  of 250 °C. The  $M_s$  and  $H_{ci}$  of Nd<sub>2</sub>Fe<sub>14</sub>B rapidly decrease with temperature, implying negative temperature coefficients ( $\alpha = \Delta\sigma_s/\sigma_s = -0.11$  %/K and  $\beta = \Delta H_{ci}/H_{ci} = -0.6$  %/K) of  $M_s$

and  $H_{ci}$  [2]. The  $K$  of  $Nd_2Fe_{14}B$  is almost negligible at 150 °C, which is the operation temperature of an EV's motor. The low  $K$  of  $Nd_2Fe_{14}B$  at the elevated temperatures is attributed to a low  $T_c$  of about 250 °C and large negative  $\beta$ .

## 1.2. Objective

In order to address the technical and supply issues of the RE magnetic materials, new RE-free magnetic materials must be developed. Therefore, this dissertation introduces magnetic properties of current and newly-developed RE-free magnetic materials. Theoretical and experimental researches are closely performed together to find upper limits of  $M$  and  $K$  and optimize chemical composition and synthetic processes of the designed RE-free magnetic materials. The theoretical research is performed based on the concept of combining (i) electronic structure calculations of pure or doped/substituted magnetic materials to obtain the  $M$  and  $K$  [3,4], (ii) mean field theory to calculate the  $T_c$  [5], and (iii) the Brillouin function [6] and Callen-Callen semi-empirical relation [7] to estimate temperature dependent magnetization  $M(T)$  and anisotropy constant  $K(T)$ . The theoretically calculated magnetic materials are then experimentally synthesized. The synthetic processes include DC/RF magnetron sputtering, wet-chemistry, solid-state reaction, arc-melting, ball milling, pressing [magnetic compaction/CIP (cold isostatic pressing)], and sintering.

## 1.3. Permanent magnetic materials

A permanent magnetic material is ferro- and ferrimagnetic material that is permanently magnetized after magnetizing with high magnetic field, therefore, the  $B_r$  is not zero, but strong enough to attract or repulse other magnetic materials. Optimizing the properties of a magnetic

material for a particular application involves tuning the three important criteria, i.e.,  $M$ ,  $K$ , and  $T_c$ . Magnetic flux density ( $B$ ) of the PM under the EV's motor operation condition plays a key role in the determination of torque, efficiency, and power of EVs. High  $B$  at the motor operation condition originates from high  $M$ ,  $K$ , and  $T_c$ , which can be achieved either by enhancing i) single-phase magnetic properties or ii) magnetic exchange coupling between high  $M$  and  $H_{ci}$  materials.

### 1.3.1. Single-phase permanent magnetic materials

Saturation magnetization ( $M_s$ ),  $K$ , and  $T_c$  are determined by three physical concepts: strong quantum-mechanical exchange forces between  $3d$  electrons from neighboring transition elements, strong spin-orbit coupling, and strong exchange energy between spins from neighboring transition elements, respectively.

In order to gain further insight into  $M$  enhancement, the ratio of an atomic radius ( $r_a$ ) to the radius ( $r_{3d}$ ) of  $3d$  electron shell of the atom is discussed below in terms of the exchange integral ( $J_{ex}$ ). The exchange force is a consequence of the *Pauli Exclusion Principle*. Fig. 1.1 shows the relation between interatomic distance and  $J_{ex}$ . As two atoms become closer, the ratio

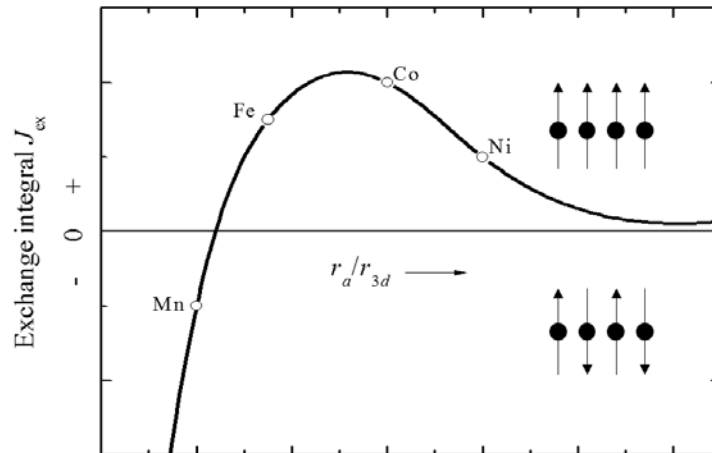


FIG. 1.1. Schematic illustration of  $r_a/r_{3d}$  ratio versus exchange integral.

$r_a/r_{3d}$  decreases. When this ratio becomes large,  $J_{\text{ex}}$  is small and positive. As the ratio decreases, therefore, the  $3d$  electrons approach more closely to each other, and the positive exchange interaction becomes stronger, resulting in ferromagnetic spin configurations. A further decrease in the interatomic distance changes the  $J_{\text{ex}}$  to negative values. This leads to antiparalleled spins, i.e., antiferromagnetism. It is noted that the exchange force depends mainly on interatomic distance and creates the unbalanced spins resulting in ferromagnetism. For example, Mn is antiferromagnetic due to the short interatomic distance between Mn atoms. However, when Mn is alloyed with Bi, the distance between Mn atoms increases, thereby, becoming ferromagnetic. The interatomic distance dependence of  $J_{\text{ex}}$  can be confirmed by  $c/a$  ratio dependence of  $M$  and relative total energy for MnBi, where  $c$  and  $a$  are the lattice constants as shown in Fig. 1.2 [8]. The  $c/a$  ratio of MnBi is directly related to the  $r_a/r_{3d}$  ratio since it represents the interatomic distance in the  $c$  direction. Magnetic moment gradually increases as the  $c/a$  increases, and the total energy of MnBi decreases and reaches a minimum at  $c/a = 1.37$ . This suggests that the low temperature phase (LTP) MnBi is thermodynamically stable at this ratio. Furthermore, the

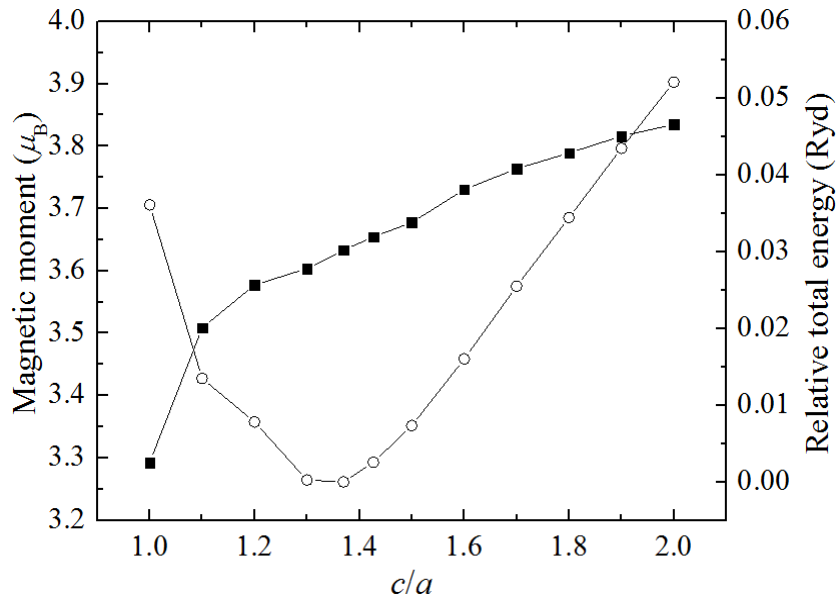


FIG. 1.2. The  $c/a$  ratio dependence of magnetic moment and relative total energy for MnBi.

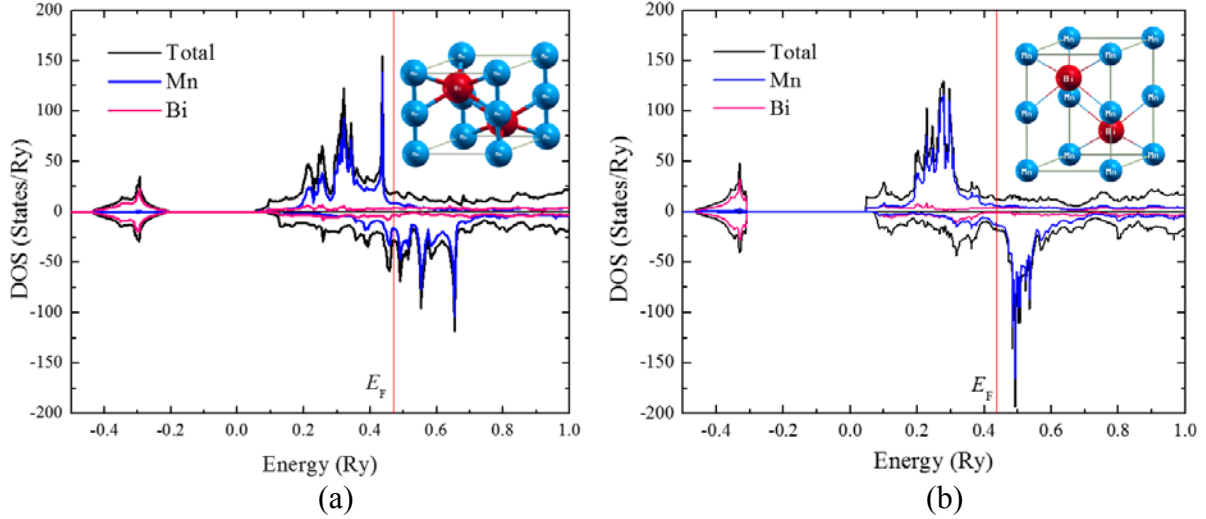


FIG. 1.3. Density of states (DOS) for (a) distorted MnBi ( $c/a = 1.00$ ) and (b) LTP MnBi ( $c/a = 1.37$ ). The black line represents the total DOS, and blue and pink lines represent the partial DOS of Mn and Bi, respectively. The red vertical line corresponds to the Fermi energy ( $E_F$ ).

density of states (DOS) in Fig. 1.3 explains the effect of atomic distance on  $M$  of MnBi. By comparing the shapes of the DOS between  $c/a = 1.00$  and  $c/a = 1.37$  in Fig. 1.3, it is clear that the unbalanced DOS around  $E_F$  becomes obvious as the  $c/a$  ratio increases. This results in high  $M$  at the higher  $c/a$  ratio.

Next, spin-orbit coupling is the origin of  $K$ . A spin is coupled with an orbit, and the orbit is strongly coupled with a lattice as shown in Fig. 1.4. This is because orbital magnetic moments

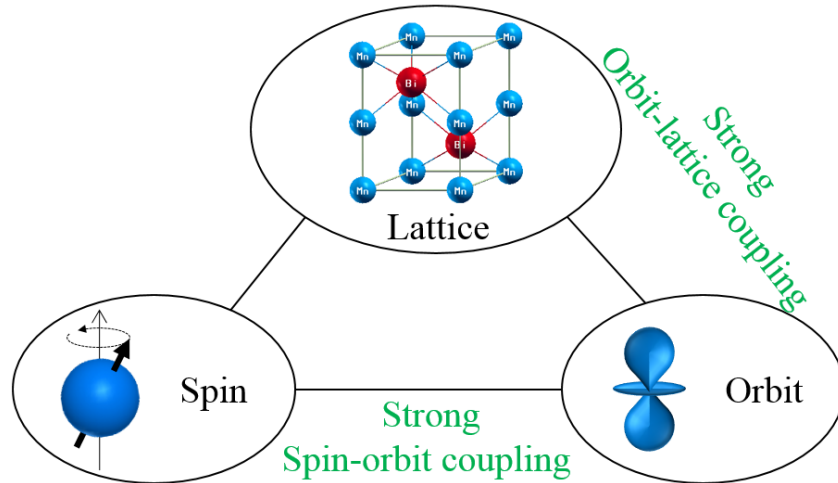


FIG. 1.4. Spin-orbit-lattice interactions.

are almost quenched. Therefore, the orientations of the orbits are strongly coupled with the lattice. In the case of low symmetry crystals, e.g., uniaxial structures like  $\tau$ -phase MnAl, LTP MnBi, or M-type hexaferrite (BaFe<sub>12</sub>O<sub>19</sub>: BaM or SrFe<sub>12</sub>O<sub>19</sub>: SrM), the spin-orbit coupling is strong, thereby a large magnetocrystalline anisotropy exists. It is noted that the spin-lattice coupling contribution to  $K$  is almost negligible. As a result, the energy required to rotate the spin from the easy direction is the energy required to overcome the spin-orbit coupling. In general,  $K$  decreases with increasing temperature, and vanishes at the  $T_c$ . However, the  $K$  for LTP MnBi and M-type hexaferrite increase with increasing temperature.

Regarding the magnetic transition from ferromagnetic to paramagnetic, i.e.,  $T_c$ , the  $T_c$  is related to exchange energy. The exchange energy is given by the *Heisenberg Exchange Hamiltonian*,

$$E_{ex} = -2J_{ex}S_iS_j = -2JS_iS_j \cos \phi, \quad (1.1)$$

where  $S_i$  is the spin of  $i$ -th atom,  $S_j$  is the spin of  $j$ -th atom, and  $\phi$  is the angle between the spins. If  $J_{ex}$  is positive,  $E_{ex}$  is minimum when the spins are parallel ( $\cos\phi = 1$ ) and maximum when they are antiparallel ( $\cos\phi = -1$ ). This suggests that a large positive  $J_{ex}$  is needed to retain a strong exchange energy, therefore, to be ferromagnetic, i.e., possess a high  $T_c$ . This relation can be well explained by the  $J_{ex}$  and  $T_c$  of Fe, Co, and Ni. As seen in Fig. 1.1, it is noted that  $J_{ex}(\text{Co}) > J_{ex}(\text{Fe}) > J_{ex}(\text{Ni})$ , thereby  $T_c(\text{Co}) = 1304 \text{ K} > T_c(\text{Fe}) = 1043 \text{ K} > T_c(\text{Ni}) = 631 \text{ K}$ . The detailed relation between  $J_{ex}$  and  $T_c$  is described by the mean field approximation (MFA) [5] as follows:

$$T_c = \frac{2}{3k_B} J_0 \gamma \quad J_0 = \sum_j J_{0j}, \quad (1.2)$$

where  $J_0$  is the molecular field parameter calculated by summing the exchange integrals  $J_{0j}$  and  $k_B$  is the Boltzmann constant. The factor  $\gamma$  is given by  $S(S+1)/S^2$  for quantum spins and 1 for

classical spins. The operating temperature of the PM of an EV's motor is about 200 °C (473 K). Therefore, the  $T_c$  of the PM needs to be much higher than 473 K. Nd-Fe-B shows a high  $M$  that originates from a high concentration of Fe in the structure and a high  $K$  due to strong orbit-lattice coupling between localized 4f electron shell from RE element (Nd) and crystal lattice. The element B causes the interatomic distance between Fe atoms of Nd-Fe-B to increase, thereby increasing  $M$ . However, the  $T_c$  of Nd-Fe-B is still too low for high-temperature applications and shows a negative temperature coefficient  $K$ . As aforementioned, the  $(BH)_{\max}$  decreases with increasing temperature and becomes very small at elevated temperatures.

In order to increase the  $T_c$  and  $M$ , a magnetic material must possess a large  $J_{\text{ex}}$ . One way to obtain an enhanced  $T_c$ , with high  $M$  and  $K$ , is to dope or substitute a single or paired element into magnetic material to increase the interatomic distance between Mn or Fe atoms, thereby enhancing  $E_{\text{ex}}$ , i.e., causing a high  $T_c$ . For example, Fig. 1.5 depicts the  $c/a$  ratio

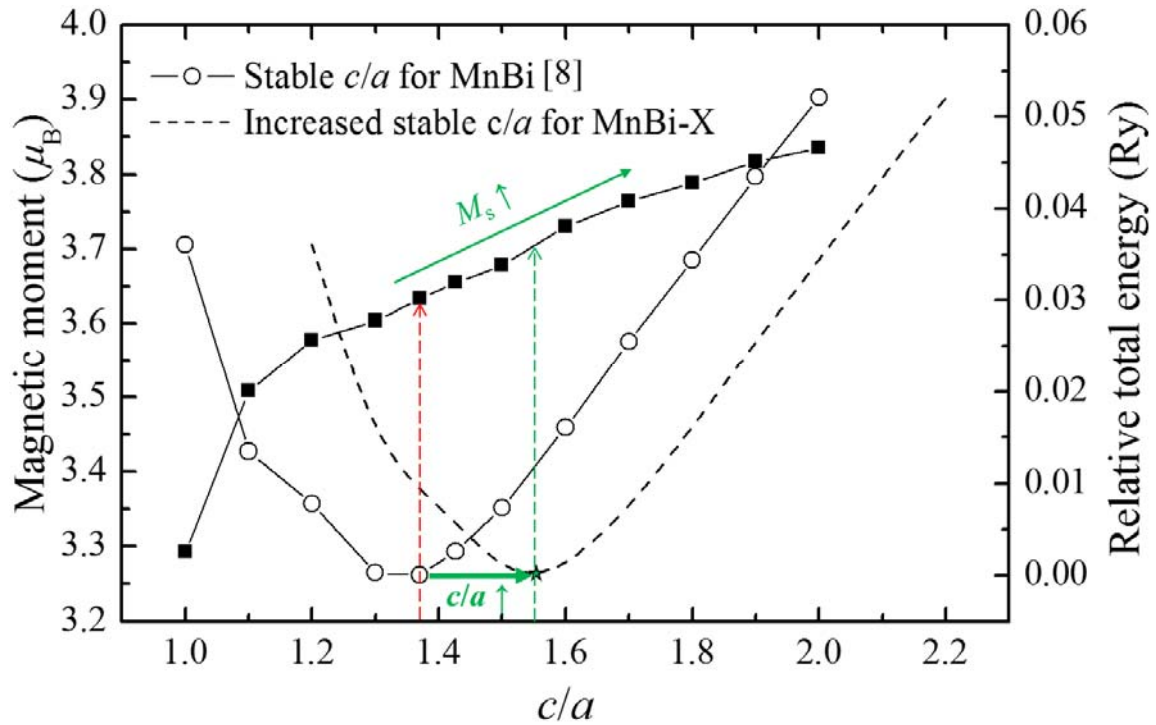


FIG. 1.5. The increasing stable  $c/a$  ratio for MnBi-X, and its corresponding magnetic moment.

dependence of  $M$  and relative total energies of MnBi and Mn-Bi-X alloy. The single or paired element should have a strong affinity with the other elements in the crystal structure of magnetic material.

The theoretical magnetic properties of RE-free magnetic materials can be investigated by (i) the first-principles calculations to obtain  $M_s$  and  $K$  [3,4], (ii) the MFA to calculate the  $T_c$  [5], and (iii) the Brillouin function [6] and Callen-Callen experimental relation [7] to estimate  $M_s(T)$  and  $K(T)$ . Strategic approaches in calculation of  $M_s$ ,  $K$ ,  $T_c$ ,  $M(T)$ , and  $K(T)$  are described in Fig. 1.6 and 1.7. The electronic structures of RE-free magnetic material will be calculated based on density functional theory (DFT) within the generalized gradient approximation (GGA) or local-spin-density approximation (LSDA). Spin and orbital magnetic moments are calculated for the magnetization directions of  $\langle 100 \rangle$  and  $\langle 001 \rangle$ . The total energies calculated for

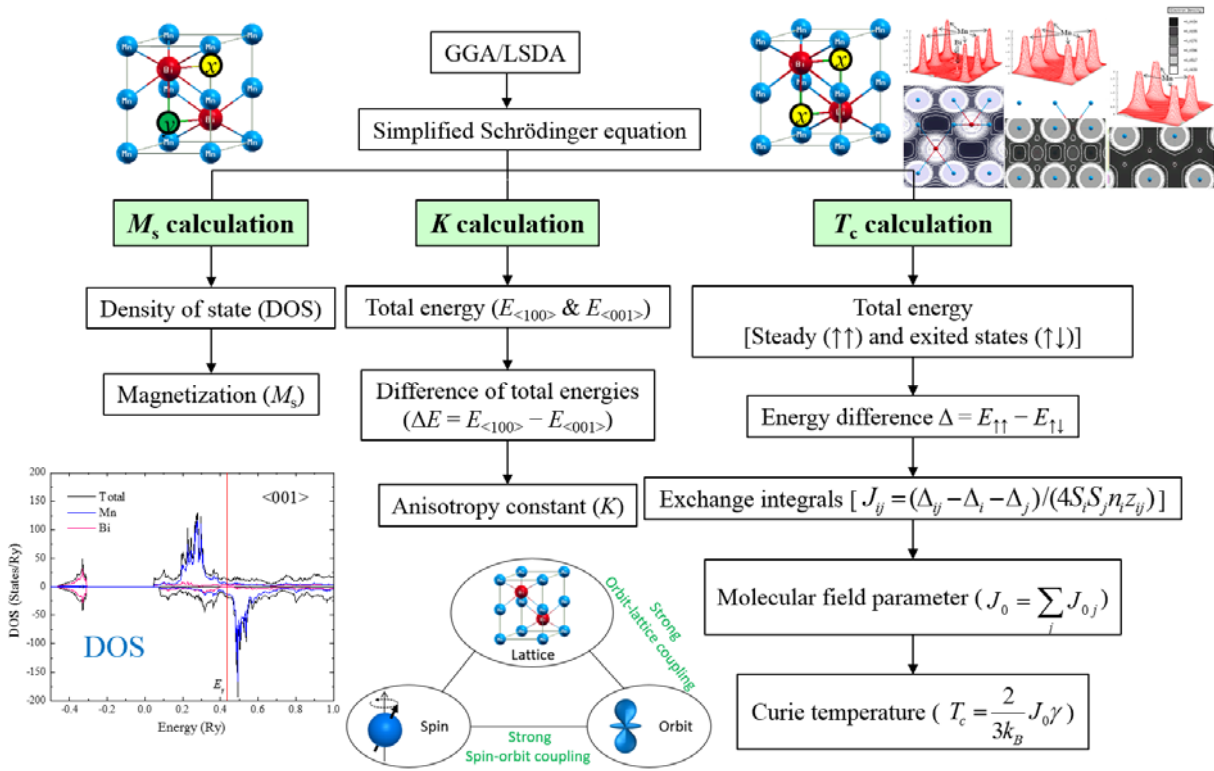


FIG. 1.6. Strategic approaches in saturation magnetization ( $M_s$ ), anisotropy constant ( $K$ ), and Curie temperature ( $T_c$ ) calculations.

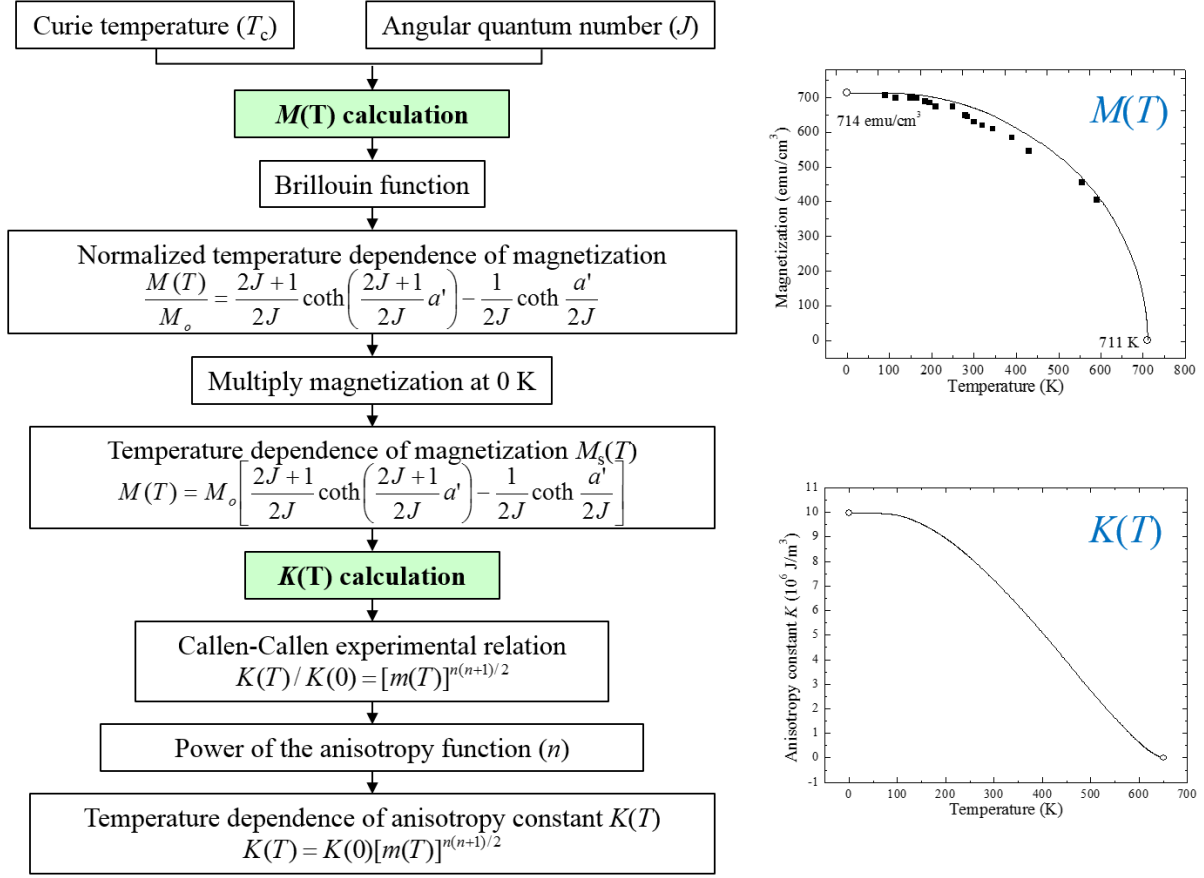


FIG. 1.7. Strategic approaches in temperature dependence of magnetization [ $M(T)$ ] and anisotropy constant [ $K(T)$ ] calculations.

these two different magnetization directions are used to obtain  $K$ . Fig. 1.6 shows our calculation procedure for  $M_s$ ,  $K$ , and  $T_c$  calculations.

Because EV motors operate at high temperature, it is necessary to obtain  $M_s(T)$  and  $K(T)$ .

The  $M_s(T)$  within the MFA [6] is given by

$$M_s(T) = M_s(0)B_J(\tau), \quad (1.3)$$

where  $B_J$  is the Brillouin function with angular quantum number  $J$  and normalized temperature  $\tau = T/T_c$ . Similarly, within the MFA, the  $K(T)$  is given by the Callen-Callen experimental relation [7] as

$$K(T) = K(0)[m(T)]^{n(n+1)/2}, \quad (1.4)$$

where  $n$  is the power of the anisotropy function and  $m(T)$  is the normalized saturation magnetization  $M_s(T)/M_s(0)$ . It is noted that  $n$  for uniaxial anisotropy is 2. Fig. 1.7 details our calculation procedure for the  $M_s(T)$  and  $K(T)$ .

### 1.3.2. Magnetic exchange coupled permanent magnetic materials

Even though some single-phase RE permanent magnetic materials possess both high  $M$  and  $H_{ci}$ , the  $T_c$  is still low, which results in a low  $(BH)_{max}$  at elevated temperatures. Therefore, magnetic exchange coupled two-phase magnetic materials were proposed in 1991 [9]. The soft magnetic phase can be exchange coupled with the hard magnetic phase within twice the domain wall thickness ( $2\delta_w$ ) of hard magnetic phase [9]. The exchange coupled two-phase magnets make

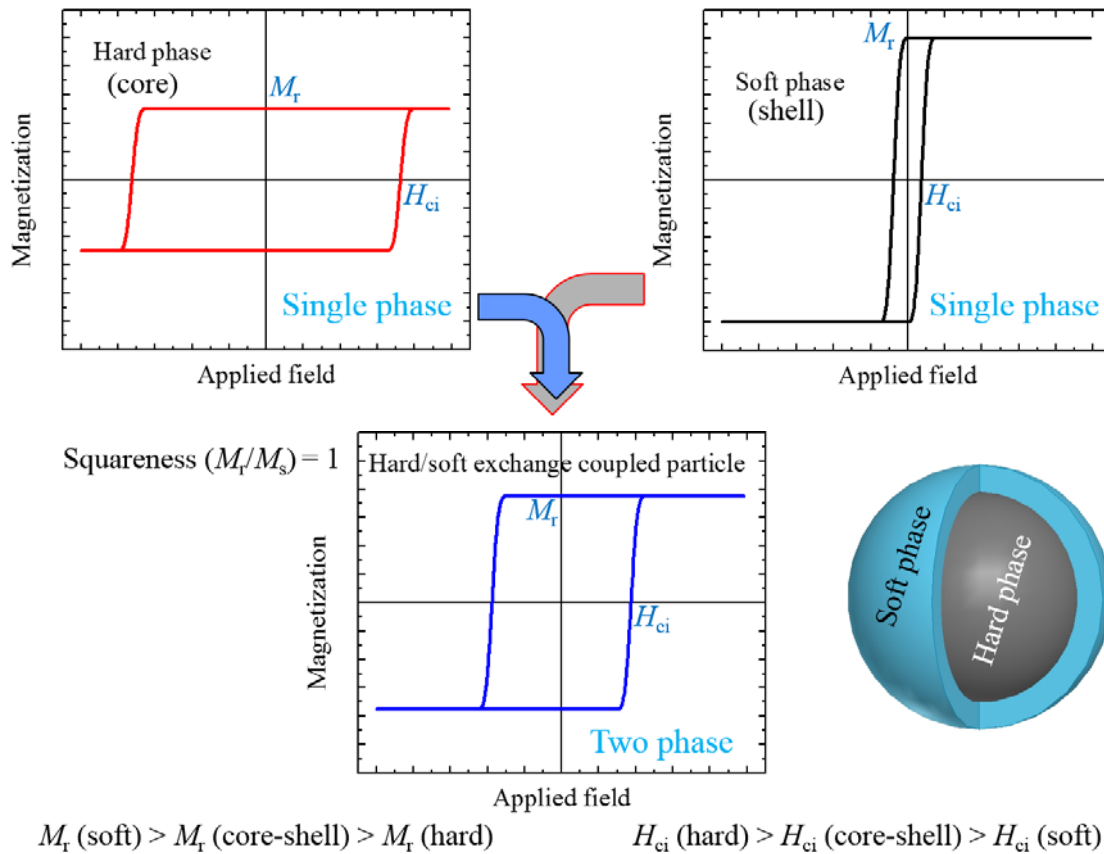


FIG. 1.8. Concept of core-shell particle with strong, positive magnetic exchange coupling.

full use of high  $H_{ci}$  from the hard magnetic phase and high  $M$  from soft magnetic phase along with high  $T_c$  from both hard and soft magnetic phases. The exchange coupling concept of enhancement of the  $(BH)_{\max}$  in core-shell nanostructures can be seen in Fig. 1.8.

According to theoretical studies on two-phase magnetic material, the saturation magnetization ( $M_{ex}$ ) [9] and anisotropy constant ( $K_{ex}$ ) [10] of the two phase magnetic material can be expressed as:

$$M_{ex} = f_s M_s + f_h M_h, \quad (1.5)$$

$$K_{ex} = f_s K_s + f_h K_h, \quad (1.6)$$

where  $\sigma$  is the saturation magnetization in emu/g,  $\rho$  is the density, and  $f$  is the volume fraction.  $h$  and  $s$  in the subscript denote hard and soft magnetic phases, respectively. Therefore, the  $(BH)_{\max}$  of the exchange coupled magnetic material can be estimated by either Eq. (1.7) or (1.8) [11].

$$(BH)_{\max} = \frac{4\pi[K_s + f_h(K_h - K_s)]}{10^5}, \quad (1.7)$$

$$(BH)_{\max} = \frac{[B_{r_s} - f_h(B_{r_s} - B_{r_h})]^2}{4}. \quad (1.8)$$

Eq. (1.7) is used for the case of  $H_N < B_r/2$ , and Eq. (1.8) is for  $H_N > B_r/2$ , where  $H_N$  is the nucleation field. Eq. (1.7) takes only intrinsic properties, i.e., the  $K$  and  $H_N$  rather than extrinsic  $H_{ci}$ . Since the  $(BH)_{\max}$  is determined by both intrinsic and extrinsic properties, Eq. (1.7) is not experimentally feasible.

A more practical  $(BH)_{\max}$  equation for the exchange coupled magnetic materials can be expressed by experimental  $M$  and  $H_{ci}$ .  $H_{ci}$  due to  $K$  [12] is

$$H_{ci} = \frac{\alpha K}{M}, \quad (1.9)$$

where  $\alpha$  is a constant depending on the crystal structure and degree of alignment. For aligned particles,  $\alpha$  is 2; for unaligned (random) particles,  $\alpha$  is 0.64 for cubic crystals and 0.96 for uniaxial crystals. Then, the  $H_{ci}$  of the two-phase magnetic material can be modified to Eq. (1.8) by combining Eq. (1.6) and (1.9) [13]:

$$H_{ci\_ex} = \alpha \frac{(1-f_h)K_s + f_h K_h}{(1-f_h)M_s + f_h M_h}. \quad (1.10)$$

By replacing  $K$  in Eq. (1.10) with  $H_{ci}$  in Eq. (1.9), Eq. (1.10) becomes Eq. (1.11).

$$H_{ci\_ex} = \frac{M_s H_s (1-f_h) + M_h H_h f_h}{M_s (1-f_h) + M_h f_h}. \quad (1.11)$$

Eq. (1.11) suggests that the coercivity of a composite can be estimated by the experimental  $H_{ci}$  of the hard and soft phase materials instead of the  $K$  of each phase. Now, the practical upper limits of the  $(BH)_{\max}$  for the exchange coupled magnetic materials can be calculated by either Eq. (1.12) or (1.13) [this work].

$$(BH)_{\max} = H_{ci\_ex} (4\pi M_{ex} - H_{ci\_ex}), \quad (1.12)$$

$$(BH)_{\max} = \frac{(4\pi M_{ex})^2}{4}. \quad (1.13)$$

Eq. (1.12) is used for the case of  $H_{ci\_ex} < 4\pi M_{ex}/2$ , and Eq. (1.13) is for  $H_{ci\_ex} > 4\pi M_{ex}/2$ .

Eqs. (1.12) and (1.13) can be rewritten as Eqs. (1.14) and (1.15) below:

$$(BH)_{\max} = \left[ \frac{M_s H_s (1-f_h) + M_h H_h f_h}{M_s (1-f_h) + M_h f_h} \right] \left\{ [(1-f_h)M_s + f_h M_h] - \frac{M_s H_s (1-f_h) + M_h H_h f_h}{M_s (1-f_h) + M_h f_h} \right\}, \quad (1.14)$$

$$(BH)_{\max} = \frac{[(1-f_h)M_s + f_h M_h]^2}{4}. \quad (1.15)$$

In this section, calculations of  $M$ ,  $K$ ,  $H_{ci}$ , and  $(BH)_{\max}$  for an exchange coupled magnetic material are introduced.

#### 1.4. References

1. J. M. D. Coey, *Magnetism and Magnetic Materials*, (Cambridge University Press, Cambridge, 2009), p. 377
2. T. Akiya, H. Kato, M. Sagawa, and K. Koyama, *IOP Conf. Ser.: Mater. Sci. Eng.* **1**, 012034 (2009).
3. P. Blaha, K. Schwarz, G. K. H. Madsen, D. Kvasnicka and J. Luitz, WIEN2k, Inst. f. Materials Chemistry TU Vienna (2001).
4. G. Kresse, M. Marsman, and J. Furthmüller, *Computational Physics*, Faculty of Physics, Universität Wien, Sensengasse 8, A-1130 Wien, Austria (2009).
5. Y. Fukuma, Z. Lu, H. Fujiwara, G. J. Mankey, W. H. Butler, *J. Appl. Phys.* **106**, 076101 (2009).
6. B. D. Cullity and C. D. Graham, *Introduction to Magnetic Materials*, Second Edition (Wiley, New Jersey, 2009), p. 121.
7. H. B. Callen and E. Callen, *J. Phys. Chem. Solids.* **27**, 1271 (1966).
8. J. H. Park, Y. K. Hong, J. J. Lee, W. C. Lee, S. G. Kim, and C. J. Choi (invited), *Metals* **4**, 455 (2014).
9. E. F. Kneller and R. Hawig, *IEEE Trans. Mag.* **27**, 3588 (1991).
10. R. Skomski and J. M. D. Coey, *Phys. Rev. B* **48**, 15812 (1993).
11. Y. K. Hong and S. Bae, U.S. Patent US2013/0342297, 26 December 2013.
12. C. Kittel, *Rev. Mod. Phys.* **21**, 541, (1949).
13. J. H. Park, Y. K. Hong, J. J. Lee, W. C. Lee, C. J. Choi, X. Xu, and A. M. Lane, *J. Magn.* **19**, 55e58 (2014).

## CHAPTER 2

### ELECTRONIC STRUCTURE AND MAGNETIC PROPERTIES OF TAU-PHASE MnAl<sup>1</sup>

#### 2.1. Introduction

Both hybrid cars and electric vehicles use rare earth magnets, such as Dy-substituted Nd<sub>2</sub>Fe<sub>14</sub>B, SmCo<sub>5</sub>, and Sm<sub>2</sub>Fe<sub>17</sub>N, due to their excellent magnetic properties. However, supply of rare earth elements, Nd, Sm, and Dy, is limited, therefore, expensive. Accordingly, developing strong permanent magnets without the rare earth elements is an emerging issue to address. Ferromagnetic  $\tau$ -phase MnAl alloy [1,2] has recently received much attention because of its high magnetic moment ( $2.4 \mu_B/\text{f.u.}$ ) [3] and magnetic crystalline anisotropy constant, low cost, and low density (5 g/cc). It has been reported that experimental saturation magnetization ( $\sigma_s$ ), coercivity ( $H_c$ ), and the Curie temperature ( $T_c$ ) for  $\tau$ -phase Mn<sub>54</sub>Al<sub>46</sub> are 89 emu/g, 4.8 kOe, and 382 °C, respectively [4]. It is noted that the  $\sigma_s$  and  $H_c$  are still low compared to the theoretical values.

To estimate achievable magnetic properties of  $\tau$ -phase Mn<sub>50</sub>Al<sub>50</sub> alloy, first principles calculations were used to calculate magnetic moment, relative total energy, and magnetocrystalline anisotropy energy (MAE). Consequently, the maximum energy product  $(BH)_{\text{max}}$  was calculated for  $\tau$ -phase Mn<sub>50</sub>Al<sub>50</sub> using the theoretical  $\sigma_s$ . Experimental magnetic moment of Mn<sub>54</sub>Al<sub>46</sub> is also reported and compared to the theoretical magnetic moment.

---

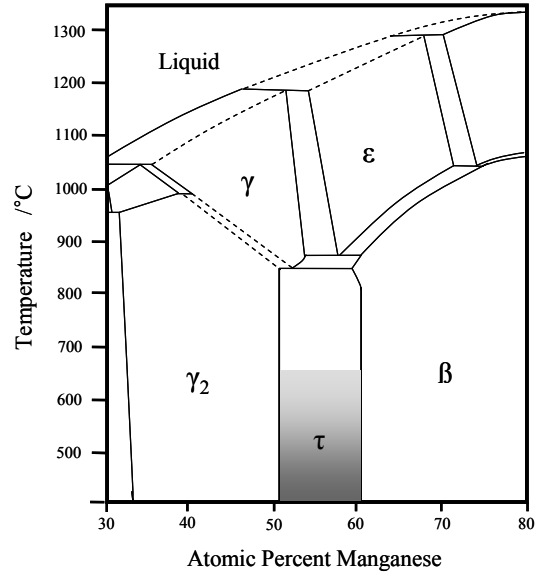
<sup>1</sup> This work was published as “Saturation magnetization and crystalline anisotropy calculations for MnAl permanent magnet,” in Journal of Applied Physics **107**, 09A731 (2010) by Jihoon Park, Yang-Ki Hong, et al.

## 2.2. Calculations and experiments

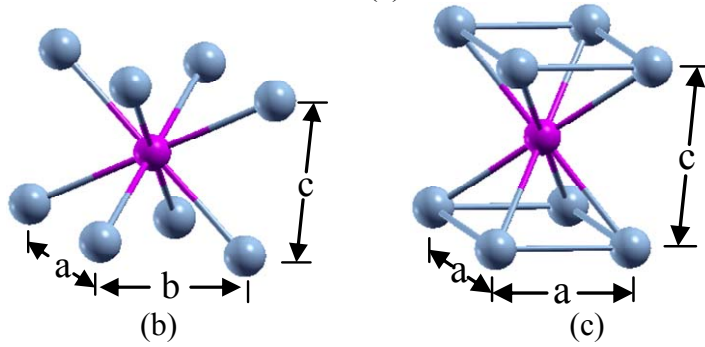
The linearized augmented plane wave (LAPW) method [5] was used to calculate magnetic moment and MAE of  $\tau$ -phase  $\text{Mn}_{50}\text{Al}_{50}$ , which were converted to  $(BH)_{\text{max}}$  and magnetocrystalline anisotropy field. In order to prepare MnAl alloy, 54 at. % of Mn and 46 at. % of Al powders were mixed and then melted in a tube furnace with argon environment. The melted  $\text{Mn}_{54}\text{Al}_{46}$  was held at 1150 °C to maintain  $\epsilon$ -phase (hexagonal closed-packed) and then quenched in deoxidized and deionized (DI) water. The quenched  $\text{Mn}_{54}\text{Al}_{46}$  ingot was annealed at 400 °C and 450 °C for 30 to 120 min in vacuum. Saturation magnetization and coercivity, and the percentages of  $\tau$ -phase were measured by vibrating sample magnetometer (VSM) and x-ray diffraction (XRD), respectively.

## 2.3. Results and discussion

Figure 2.1 (a) shows MnAl phase diagram [6], and molecular structures for  $\epsilon'$ - and  $\tau$ -phase MnAl are shown in Fig. 2.1 (b) and (c), respectively. Orthorhombic  $\epsilon'$ -phase is an intermediate ferromagnetic phase which is not shown in the phase diagram. Antiferromagnetic  $\epsilon$ -phase transforms to unstable ferromagnetic  $\epsilon'$ -phase at an elevated temperature, and then followed by the transformation of the unstable  $\epsilon'$ -phase to meta-stable ferromagnetic  $\tau$ -phase. Fig. 2.2 (a) and (b) show the density of states (DOS) diagrams for  $\epsilon'$ - and  $\tau$ -phase  $\text{Mn}_{50}\text{Al}_{50}$ , respectively. As shown in Fig. 2.2 (b), degeneracy of the states near  $E_F$  in  $\epsilon'$ -phase  $\text{Mn}_{50}\text{Al}_{50}$  is partly destroyed by tetragonal distortion occurred during the phase transformation. This results in an increase of magnetic moment from 1.88  $\mu_B$  for  $\epsilon'$ -phase to 2.37  $\mu_B$  for  $\tau$ -phase  $\text{Mn}_{50}\text{Al}_{50}$ . These moments were obtained by the difference between integrated up- and down-spins of DOS to the Fermi energy level. As the lattice parameter (c) between Mn atoms is increased from 3.006



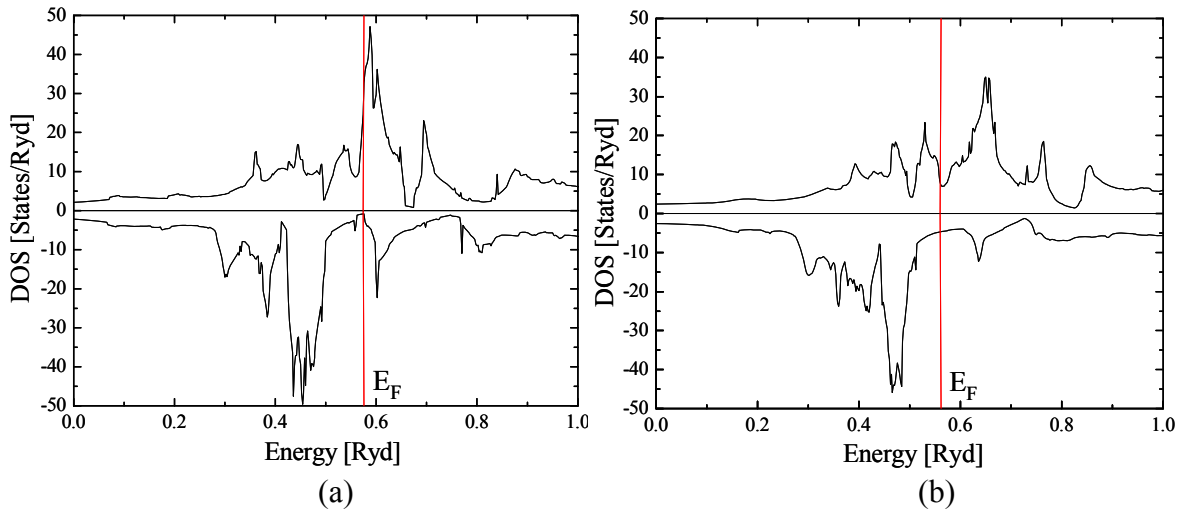
(a)



(b)

(c)

FIG. 2.1. (a) Partial phase diagram of Mn-Al [6], and molecular structures of (b)  $\epsilon'$ -phase and (c)  $\tau$ -phase MnAl.



(a)

(b)

FIG. 2.2. (a) Density of states of  $\epsilon'$ -phase MnAl and (b) density of states of  $\tau$ -phase MnAl.

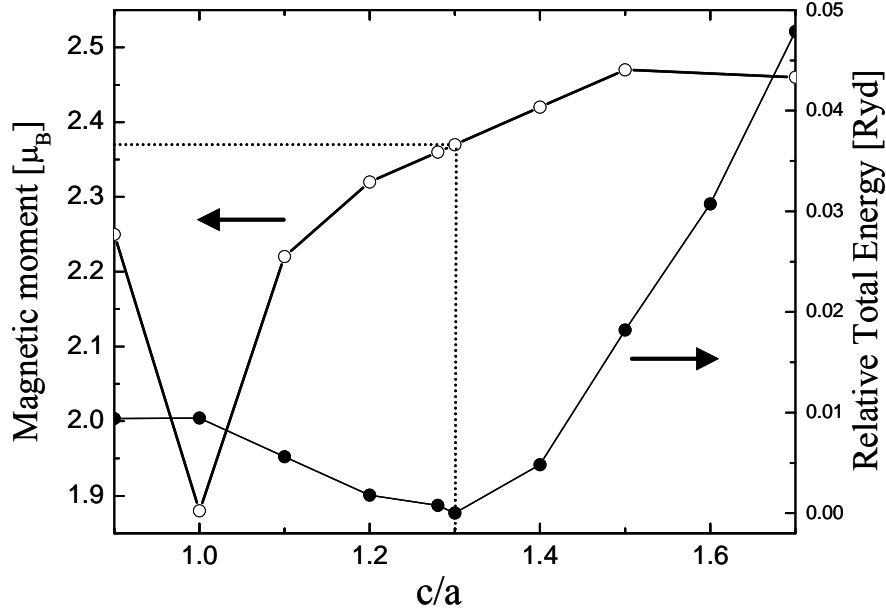


FIG. 2.3. The  $c/a$  dependence of magnetic moment and relative total energy.

Å for  $\epsilon'$ -phase  $Mn_{50}Al_{50}$  to 3.54 Å for  $\tau$ -phase  $Mn_{50}Al_{50}$ , magnetic spins in Mn atoms are aligned in the  $c$  direction of  $\tau$ -phase  $Mn_{50}Al_{50}$ , which causes the increase of magnetic moment of  $\tau$ -phase  $Mn_{50}Al_{50}$  [4].

Figure 2.3 shows the axial ratio  $c/a$  dependence of magnetic moment and total energy of ferromagnetic  $\tau$ -phase  $Mn_{50}Al_{50}$ . The lowest level of total energy occurs at 1.30 of  $c/a$  as shown in Fig. 2.3, therefore, providing the most stable structure of  $\tau$ -phase  $Mn_{50}Al_{50}$  with 2.37  $\mu_B$  (161 emu/g) of magnetic moment. The MAE of 0.259 meV ( $1.525 \times 10^6$  J/m<sup>3</sup>) was calculated by LAPW at 1.28 of  $c/a$  that gives 38 kOe of the magnetocrystalline anisotropy field with the saturation magnetization of 161 emu/g. The calculated MAE is close to the MAE estimated by Sakuma [3]. In addition, the maximum energy product,  $(BH)_{max}$ , was estimated to be 12.64 MGOe for  $\tau$ -phase  $Mn_{50}Al_{50}$  under the assumption of  $B_r = 0.7 B_s$ .

In the experiments, the composition of  $Mn_{54}Al_{46}$  was used to obtain stable  $\tau$ -phase MnAl alloy as shown in the phase diagram of Fig. 2.1 (a). During the melting, quenching, and

annealing processes for  $Mn_{54}Al_{46}$  alloy, 46 at. % Mn and 46 at. % Al atoms of  $\epsilon$ -phase was transformed to  $\tau$ -phase  $Mn_{50}Al_{50}$ , and 8 at. % Mn atoms remained. The excessive Mn atoms tend to occupy  $(0, 0, 0)$  and  $(\frac{1}{2}, \frac{1}{2}, \frac{1}{2})$  sites, causing anti-ferromagnetic couplings [2]. Therefore, the saturation magnetization of 144 emu/g was obtained for  $\tau$ -phase  $Mn_{54}Al_{46}$  that is lower than the theoretical saturation magnetization (161 emu/g) for  $Mn_{50}Al_{50}$ . This is because only 89.6 % (60.1 wt. % Mn and 29.5 wt. % Al transform to  $\tau$ -phase) of total weight contribute to the magnetization. In order to optimize  $\tau$ -phase and saturation magnetization of  $Mn_{54}Al_{46}$ , MnAl alloy was annealed at 400 or 450 °C for various annealing times ranging from 30 to 120 min. The XRD analysis confirms that the sample annealed at 450 °C for 60 min contains 73.1 %  $\tau$ -phase and 26.9 %  $\gamma_2$  and  $\beta$  phases, as shown in Fig. 2.4. Fig. 2.5 (a) and (b) show the effects of annealing temperature and time on magnetic moment and an amount of  $\tau$ -phase  $Mn_{54}Al_{46}$ . The highest experimental saturation magnetization, 98.3 emu/g, was obtained at the annealing temperature and time of 450 °C and 60 min, respectively, which magnetization results in 4.7

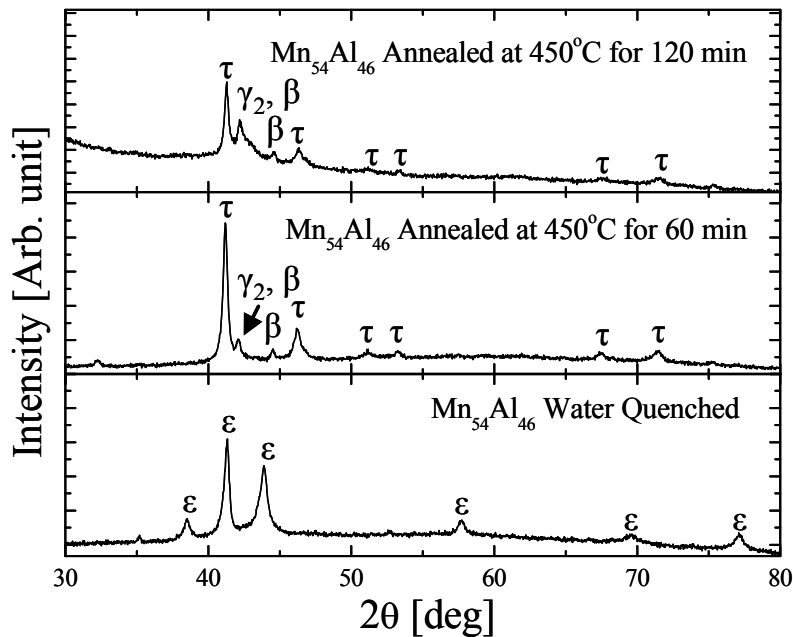


FIG. 2.4. XRD spectra for  $Mn_{54}Al_{46}$  alloy.

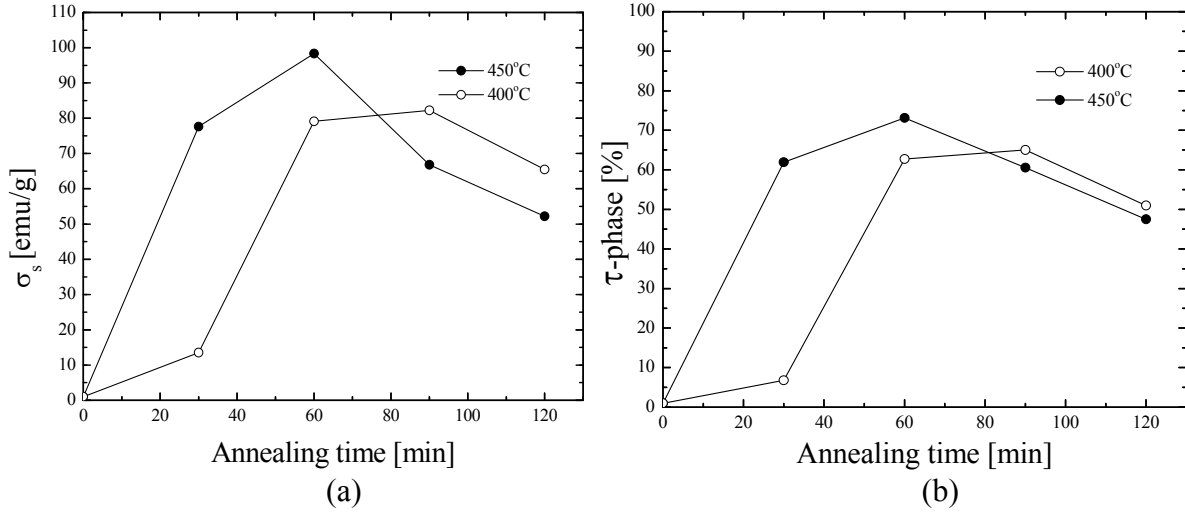


FIG. 2.5. (a) The saturation magnetization and (b) the  $\tau$ -phase percentage according to the annealing time.

MGOe of  $(BH)_{\max}$ . In addition,  $T_c$  was measured to be 388 °C that is close to the previously reported  $T_c$  of 382 °C by Q. Zeng [4].

## 2.4. Conclusions

The magnetic moment and MAE values of  $\tau$ -phase MnAl were obtained by first principles calculations, and the alloy was fabricated to compare the experimental values with the theoretical ones. The calculated magnetic moment and MAE for ferromagnetic  $\tau$ -phase  $Mn_{50}Al_{50}$  are 2.37  $\mu_B$  and 0.259 meV ( $1.525 \times 10^6$  J/m<sup>3</sup>), respectively, which results in the magnetocrystalline anisotropy field and  $(BH)_{\max}$  of 38 kOe and 12.64 MGOe without rare earth metals. The experimental saturation magnetization for  $\tau$ -phase  $Mn_{54}Al_{46}$  was 98.3 emu/g, which is about 70 percent of the theoretical value 144 emu/g. Experimental  $(BH)_{\max}$  of 4.7 MGOe was obtained, which is about 37 % of theoretical  $(BH)_{\max}$ .

## 2.5. References

1. H. Kono, *J. Phys. Soc. Japan* **13**, 1444 (1958).

2. A.J.J. Koch, P. Hokkeling, M.G.V.D. Steeg, and K.J.DeVos, *J. Appl. Phys.* **31**, 75S (1960).
3. A. Sakuma, *J. Phys. Soc. Japan* **63**, 1422 (1993).
4. Q. Zeng, I. Baker, J.B. Cui, and Z.C. Yan, *J. Magn. Magn. Mat.* **308**, 214 (2007).
5. P. Blaha, K. Schwarz, G. K. H. Madsen, D. Kvasnicka and J. Luitz, WIEN2k, Inst. f. Materials Chemistry TU Vienna (2001).
6. X.J. Liu, R. Kainuma, H. Ohtani, and K. Ishida, *J. All. Comp.* **235**, 256 (1996).

## CHAPTER 3

### ELECTRONIC STRUCTURE AND MAXIMUM ENERGY PRODUCT AT ELEVATED TEMPERATURE OF LOW TEMPERATURE PHASE MnBi<sup>2</sup>

#### 3.1. Introduction

The maximum energy product  $(BH)_{\max}$  of a permanent magnet at elevated temperatures has become increasingly important because a motor for electric vehicles (EV) should be operational at 473 K. Rare-earth Nd-Fe-B magnets show the highest  $(BH)_{\max}$  of 59 MGOe at room temperature [1], which is much larger than 5.4 MGOe for the most widely used low energy ferrite magnets [2]. Although the Nd-Fe-B magnets exhibit desirable magnetic flux density ( $B$ ) and intrinsic coercivity ( $H_{ci}$ ), therefore, large  $(BH)_{\max}$ , a large negative temperature coefficient of  $H_{ci}$ , a low Curie temperature ( $T_c$ ) of 523 K [3] and limited supply are the critical drawbacks that need to be addressed. Motors for electric vehicles (EV) must reliably operate at temperatures up to 473 K. Therefore, the usage of Nd-Fe-B magnets is limited to a lower temperature than 473 K, due to their negative temperature coefficient of  $H_{ci}$  and low  $T_c$ . On the other hand, low temperature phase (LTP) MnBi shows a positive magnetic anisotropy coefficient [4–6], resulting in  $H_{ci}$  of about 1.5 T at 300 K and 2 T at 400 K [5]. The high  $H_{ci}$  of LTP MnBi helps to make it usable at the operating temperature of the motor. The directionally-solidified LTP MnBi shows a remanent magnetic flux density ( $B_r$ ) of 0.8 T and  $(BH)_{\max}$  of 17 MGOe at 290 K [7]. However, arc-melted and mechanically-milled LTP MnBi powder shows a low  $B_r$  of 0.7 T and  $(BH)_{\max}$  of 11.00 MGOe [8] and  $B_r$  of 0.7 T and  $(BH)_{\max}$  of 11.95 MGOe [9] at 300 K. Therefore, it is

---

<sup>2</sup> This work was published as “Electronic Structure and Maximum Energy Product of MnBi (invited),” in *Metals* **4**, 455 (2014) by Jihoon Park, Yang-Ki Hong, et al.

imperative to predict the theoretical limit of  $(BH)_{\max}$  at elevated temperatures for the LTP MnBi magnet.

Coehoorn *et al.* performed first self-consistent spin-polarized band-structure calculations and obtained a magnetic moment of  $3.6 \mu_B$ , the density of states (DOS) and the band structures at 0 K [10]. Köhler *et al.* used first-principles calculation based on local density functional approximation (LDA) and the augmented spherical wave (ASW) band structure method to calculate the magneto-optical properties, a magnetic moment of  $3.61 \mu_B$ , a magnetocrystalline anisotropy constant ( $K$ ) of  $1.5 \times 10^6 \text{ J/m}^3$ , DOS and the band structures at 0 K [11]. Furthermore, Huberman *et al.* have predicted the normalized temperature dependence of magnetic moment within the mean-field theory [12]. However, the theoretical limit of saturation magnetization ( $M_s$ ), and thereby  $(BH)_{\max}$ , at elevated temperatures and the possibility of an increase in the  $M_s$  has not been reported.

In this paper, we calculated DOS, the magnetic moment, and  $K$  using first-principles calculations, and  $T_c$  by the mean field theory. Then, we used these magnetic properties to determine the temperature dependence of saturation magnetization  $M_s(T)$  and the maximum energy product  $(BH)_{\max}(T)$ . In addition, an electron density map was performed to find if any interstitial site is available for third alloying elements. Also, the lattice constant  $c/a$  ratio dependence of magnetic moment was investigated to explore a possible increase in  $M_s$ .

### 3.2. Method of calculations

The WIEN2k package [13] was used to perform first-principles calculations as presented in Fig. 1.6 and 1.7. The package is based on density functional theory (DFT) and uses the full-potential linearized augmented plane wave (FP-LAPW) method with the dual basis set. For the

LTP MnBi, the  $3s$ ,  $3p$ ,  $3d$  and  $4s$  states of Mn and the  $5p$ ,  $5d$ ,  $6s$  and  $6p$  states of Bi were taken as valence states. All calculations used a  $25 \times 25 \times 15$  k-point mesh generating 1,352 k-points in the irreducible part of the Brillouin zone. The muffin tin radii (RMT) of 2.50 a.u. for Mn and 2.23 a.u. for Bi and the experimental lattice constants  $a = 4.256 \text{ \AA}$  and  $c = 6.042 \text{ \AA}$  at 4.2 K [6] were used.

The density functional theory within the local-spin-density approximation (LSDA) was used for all spin-polarized and spin-orbit coupling calculations. Spin and orbital magnetic moments were calculated for the magnetization directions of  $\langle 100 \rangle$  and  $\langle 001 \rangle$ . The total energies calculated for these two different magnetization directions were used to obtain  $K$ .

### 3.3. Results and discussion

#### 3.3.1. Density of states and magnetic moments

Figure 3.1 (a) and (b) show the density of states (DOS) in  $\langle 100 \rangle$  and  $\langle 001 \rangle$  magnetization directions of the LTP MnBi, respectively, which were calculated based on spin-polarized and spin-orbit coupling. The DOS is divided into lower and higher energy regions. The lower energy region near  $-0.4 \text{ Ry}$  is mostly contributed by the  $s$  band of Bi, and the higher energy region near the Fermi energy ( $E_F$ ) is mostly contributed by the  $d$  band of Mn, as seen in Fig. 3.1 (a) and (b). The DOS near the  $E_F$  is a highly-degenerated energy state; slightly below the  $E_F$  in the majority spin state and slightly above the  $E_F$  in the minority spin state. These highly-degenerate energy states near  $E_F$  are the origin of the magnetic moment of LTP MnBi. This is because the degenerate energy states contribute to the difference between the number of electrons in the majority and minority spin states below  $E_F$ . The spin and orbital magnetic moments, which were calculated from the spin polarized and spin-orbit couplings, are given in

Table 3.1. The calculated spin and orbital magnetic moments per formula unit (f.u.) and Mn and Bi atoms for low temperature phase (LTP) MnBi in units of  $\mu_B$ . Magnetic moments from both spin-polarized and spin-orbit coupling calculations are listed.

Direction of magnetization	Spin moment		Orbital moment		Total moment	
	f.u.	Mn/Bi	f.u.	Mn/Bi	f.u.	Mn/Bi
Spin-polarized	3.50	3.57/-0.07			3.50	3.57/-0.07
<100>	3.52	3.57/-0.06	0.105	0.10595/-0.00009	3.63	3.68/-0.06
<001>	3.52	3.58/-0.06	0.084	0.08415/-0.00012	3.60	3.66/-0.06

Table 3.1. It is noted that the orbital magnetic moment from spin-orbit coupling calculations in the <100> magnetization direction is higher than that of the <001> magnetization direction. This difference results in the highest total magnetic moment of  $3.63 \mu_B/\text{f.u.}$  (formula unit) ( $79 \text{ emu/g}$  or  $714 \text{ emu/cm}^3$ ) for LTP MnBi. This magnetic moment value is in good agreement with the results of first-principles calculations based on local density functional approximation (LDA) and the augmented spherical wave (ASW) band structure method ( $3.61 \mu_B$ ) [11] and first self-consistent spin-polarized band-structure calculations ( $3.6 \mu_B$ ) [10]. However, this calculated value is smaller than the experimental neutron diffraction measurement value of  $3.8 \mu_B$  at 300 K [6] and the extrapolated value of  $3.9 \mu_B$  at 0 K [14].

### 3.3.2. Magnetocrystalline anisotropy constant

Magnetocrystalline anisotropy energy (MAE) is the total energy difference between <100> and <001> magnetization directions, *i.e.*,  $\Delta E = E_{\langle 100 \rangle} - E_{\langle 001 \rangle}$ . The calculated total energy difference is  $-0.163 \text{ meV/u.c.}$ , which corresponds to an in-plane  $K$  of  $-0.275 \times 10^6 \text{ J/m}^3$  at 0 K. The DOS in Fig. 3.1 (a) and (b), and the calculated  $K$  imply that forcing the magnetization direction from the easy plane to the  $c$ -axis results in destruction of the degeneracy near the  $E_F$ ,

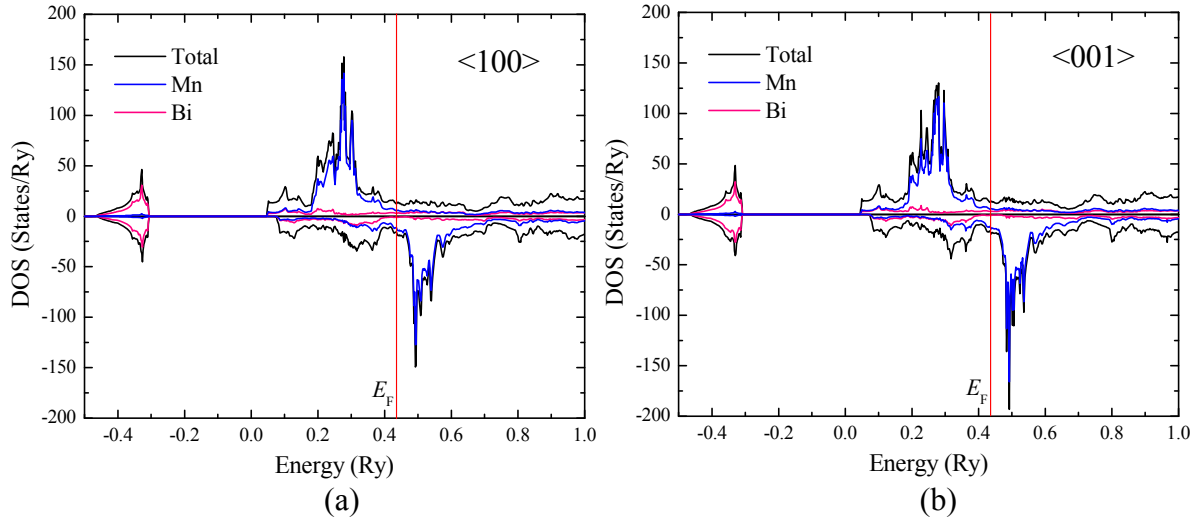


FIG. 3.1. Density of states (DOS) for LTP MnBi in the (a)  $\langle 100 \rangle$  and (b)  $\langle 001 \rangle$  magnetization directions. The black line represents the total DOS, and blue and pink lines represent the partial DOS of Mn and Bi, respectively. The red vertical line corresponds to the Fermi energy ( $E_F$ ).

thereby increasing the total energy. The destruction of degeneracy (lower and broader DOS peaks) can be observed by comparing the DOS of  $\langle 100 \rangle$  and  $\langle 001 \rangle$  magnetization directions below the  $E_F$ . Our calculated  $K$  is close to the experimental  $K$  of  $-0.155 \times 10^6 \text{ J/m}^3$  at 4.2 K [6], but smaller than the reported  $K$  value of  $1.5 \times 10^6 \text{ J/m}^3$  [11]. This indicates a strong anisotropy along with  $c$ -axis. It was experimentally observed that the spin rotated from the basal plane to the  $c$ -axis at about 90 K [15]. The  $K$  was measured in the range of 4.2 to 628 K [4] using a vibrating sample magnetometer (VSM) and by singular point detection (SPD) from 147 to 586 K [5]. The measured  $K$  is  $1.3 \times 10^6 \text{ J/m}^3$  [4] and  $1.8 \times 10^6 \text{ J/m}^3$  [5] at 300 K and  $2.3 \times 10^6 \text{ J/m}^3$  at 430 K [5], suggesting out-of-plane magnetization at the elevated temperatures.

### 3.3.3. Curie temperature

In this section, the  $T_c$  for LTP MnBi was calculated using the following mean field approximation (MFA) expression [16]:

$$T_c = \frac{2}{3k_B} J_0 \gamma, \quad J_0 = \sum_j J_{0j}, \quad (3.1)$$

where  $J_0$  is the molecular field parameter calculated by summing the exchange integrals ( $J_{0j}$ ) and  $k_B$  is the Boltzmann constant. The factor  $\gamma$  is given by  $S(S+1)/S^2$  for quantum spins and one for classical spins. In this work, we choose  $\gamma = 1$ , which gives a  $T_c$  close to the experimental one. This is because the temperature dependences of  $J_{0j}$  and  $S$  are mutually cancelled [17,18]. The  $J_{0j}$  are obtained by the exchange energy difference between the ground and excited states of sublattices. The exchange integral [15] is written as:

$$J_{ij} = (\Delta_{ij} - \Delta_i - \Delta_j) / (4S_i S_j n_i z_{ij}) \quad (3.2)$$

where  $\Delta_{ij}$  is the difference of exchange energies between the excited state at both the  $i$  and  $j$  sublattices and the ground state,  $\Delta_i$  is the difference between the excited state at the  $i$  sublattice and the ground state,  $\Delta_j$  is the difference between the excited state at the  $j$  sublattice and the ground state,  $S_i$  is the spin of the  $i$ -th Mn atom,  $n_i$  is the number of  $i$ -th Mn atoms and  $z_{ij}$  is the number of neighboring  $j$ -th Mn atoms to  $i$ -th Mn atom. The exchange interaction between spins is inversely and exponentially proportional to the corresponding distance. The distance and number of corresponding neighbors for LTP MnBi are given in Table 3.2. The distance of the third and fourth nearest neighbors is greater than 0.5 nm. Therefore, the exchange interactions between these spins are negligible. Accordingly, the energy difference  $\Delta$  between the ground and

Table 3.2. The number of nearest neighbors ( $z_{0i}$ ) and corresponding distances ( $r_{0i}$ ) in the unit of Å in LTP MnBi.

Material	# of nearest neighbors				Distance			
	$z_{01}$	$z_{02}$	$z_{03}$	$z_{04}$	$r_{01}$	$r_{02}$	$r_{03}$	$r_{04}$
LTP MnBi	2	6	12	2	3.02	4.26	5.22	6.04

excited states was calculated only for the first and second nearest neighbors. To include the significant exchange interaction with the nearest neighbors, the supercell structures (two LTP MnBi unit cells) were built. The input parameter  $S$  and  $n_i$  for LTP MnBi are two and one, respectively. The  $z_{ij}$  values for the first and second nearest neighbors were taken from Table 3.2.

As a result, the calculated first and second exchange integrals ( $J_{01}$  and  $J_{02}$ ) are 32.31 and 4.59 meV, respectively, which corresponds to the mean-field estimated  $T_c = 711$  K. Experimentally, the LTP MnBi structure transforms to the high temperature phase (HTP) MnBi at 628 K [4]; thereby, a dramatic drop of magnetization occurs at 628 K.

### 3.3.4. Temperature dependence of saturation magnetization and maximum energy product

We use the mean field theory to calculate  $M_s(T)$ . The  $M_s(T)$  within the MFA [19] is given by:

$$M_s(T) = M_s(0)B_J(\tau) \quad (3.3)$$

where  $M_s(0)$  is the saturation magnetization at 0 K,  $B_J$  is the Brillouin function with angular quantum number ( $J$ ) and normalized temperature ( $\tau = T/T_c$ ).  $J$  is the summation of spin moment ( $S$ ) and orbital contribution ( $L$ ). The calculated magnetic moment of  $3.63 \mu_B/\text{f.u.}$ ,  $T_c$  of 711 K and  $J$  of 2 were used to calculate the  $M_s(T)$ . Fig. 3.2 shows the calculated and experimental [5]  $M_s(T)$ . The calculated values are in good agreement with the experimental data.

Therefore, we used the calculated  $M_s(T)$  to estimate the temperature dependence of the maximum energy product  $(BH)_{\max}(T)$  for the LTP MnBi. In order to calculate the  $(BH)_{\max}(T)$ , the temperature dependence of intrinsic coercivity  $H_{ci}(T)$  is also needed. We used the experimental  $H_{ci}(T)$  [15] in Fig. 3.3 and assume coherent magnetization reversal and a rectangular hysteresis loop of LTP MnBi to estimate  $(BH)_{\max}(T)$ . The  $(BH)_{\max}$  is the maximum

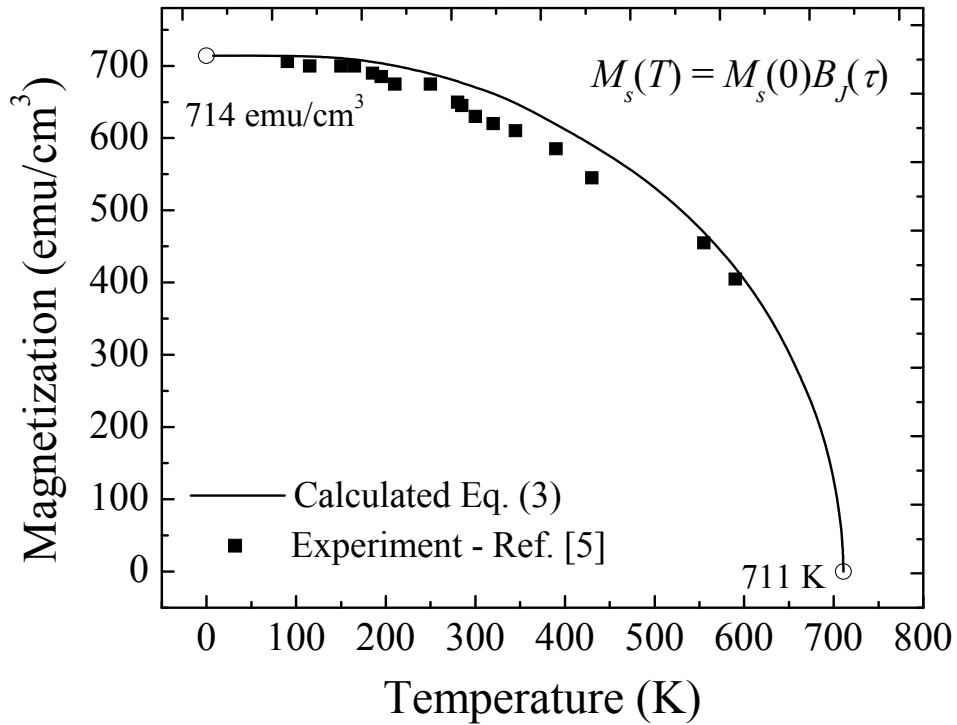


FIG. 3.2. The calculated and experimental temperature dependence of saturation magnetization  $M_s(T)$  for LTP MnBi.

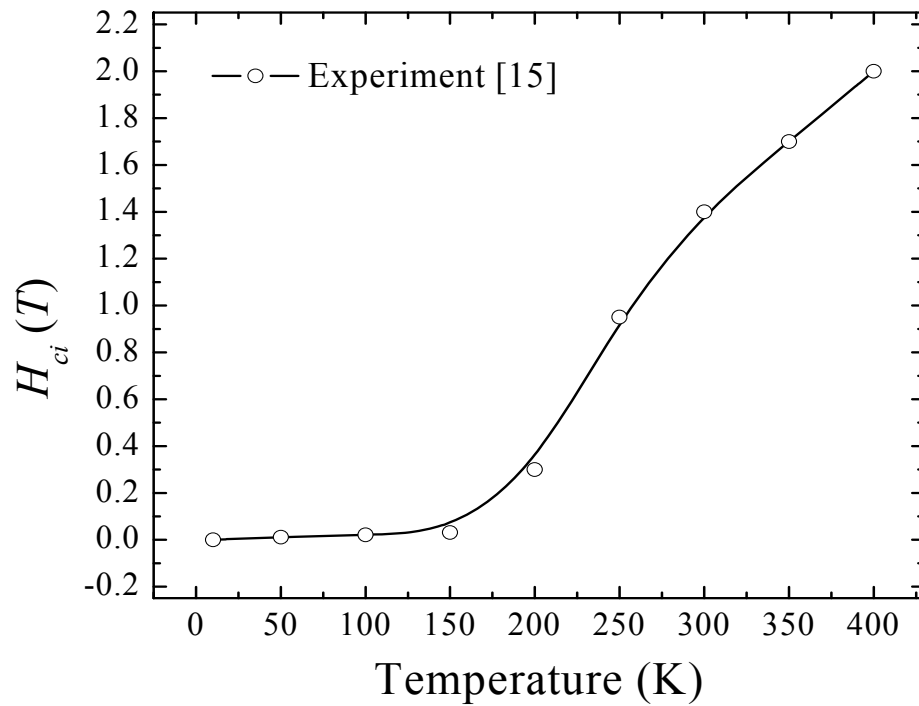


FIG. 3.3. Experimental intrinsic coercivity ( $H_{ci}$ ) as a function of temperature for LTP MnBi.

amount of magnetic energy stored in a magnet, which is the maximum rectangular area in the  $B$ - $H$  loop. Therefore, the  $(BH)_{\max}(T)$  can be calculated by either Eq. (3.4) or (3.5).

$$(BH)_{\max}(T) = [B_r(T) - H_{ci}(T)]H_{ci}(T) \quad (3.4)$$

$$(BH)_{\max}(T) = \frac{B_r^2(T)}{4}, \quad (3.5)$$

where  $B_r$  is the remnant magnetic flux density. Eq. (3.4) is used for the case of  $H_{ci} < B_r/2$ , and Eq. (3.5) is for  $H_{ci} > B_r/2$ . From a comparison between Fig. 3.2 and 3.3, the  $H_{ci}$  is smaller than  $B_r/2$  below 250 K, while it is greater than  $B_r/2$  above 250 K for LTP MnBi.

Therefore, Eq. (3.4) was used below 250 K, and Eq. (3.5) was used above 250 K to estimate  $(BH)_{\max}(T)$ . Fig. 3.4 shows the semi-theoretical  $(BH)_{\max}(T)$  and experimental  $(BH)_{\max}$  [8,9,13,20] for LTP MnBi, including experimental  $(BH)_{\max}(T)$  for Nd-Fe-B [3]. It is noted that the  $(BH)_{\max}$  of LTP MnBi dramatically increased from 1.7 MGOe at 100 K to 18.7 MGOe at 250 K and then gradually decreased to 6.2 MGOe at 600 K. The calculated  $(BH)_{\max}$  at 300 K is 17.7 MGOe, and it is in good agreement with the  $(BH)_{\max}$  of directionally-solidified LTP MnBi (17 MGOe at 290 K [7]). However, it is larger than those of arc-melted and mechanically-milled MnBi, which are 11 MGOe [8] for powder and 11.9 MGOe for a powder-wax mixture [9] at 300 K. Resin-bonded MnBi magnets show  $(BH)_{\max}$  values of 7.7 and 4.6 MGOe at 300 and 400 K, respectively [15], and a sintered MnBi magnet shows  $(BH)_{\max}$  values of 7.8 MGOe [9] and 5.8 MGOe [20] at 300 K. All of these  $(BH)_{\max}$  are smaller than the calculated values due to the imperfect rectangular demagnetization curve. As shown in Fig. 3.4, the semi-theoretical  $(BH)_{\max}$  of LTP MnBi (10.9 MGOe) was found to be higher than that of Nd-Fe-B (2 MGOe) at 500 K [3]. This result suggests that LTP MnBi is a good permanent magnet for high temperature applications.

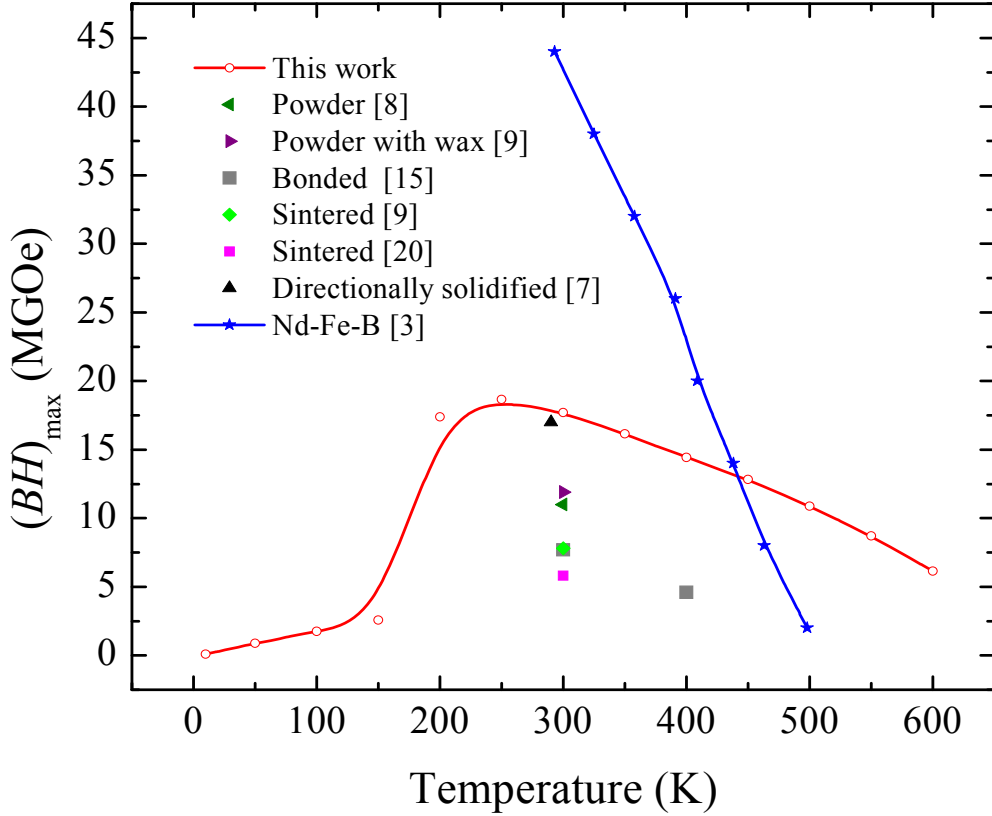


FIG. 3.4. The calculated temperature dependence of the maximum energy product  $(BH)_{\max}(T)$  and experimental  $(BH)_{\max}$  for LTP MnBi and experimental  $(BH)_{\max}(T)$  for Nd-Fe-B.

### 3.3.5. Electron density maps and $c/a$ ratio dependence of magnetic moment

In this section, we discuss the effect of doping element on the possibility of an increase in the  $M_s$  of LTP MnBi, and thereby  $(BH)_{\max}$ . Fig. 3.5 shows the  $c/a$  ratio dependence of the total magnetic moment and relative total energy with a constant volume. As the distance between Mn atoms in the  $c$ -axis increases, the magnetic moment increases and the total energy decreases up to a  $c/a$  ratio of about 1.37 and then increases. The magnetic moment at this ratio is  $3.63 \mu_B/\text{f.u.}$ , which is in good agreement with the above calculated moment.

In order to explore any possibility of increasing magnetic moment, we calculated the electron density and, thereby, findind interstitial sites available for the doping element. Fig. 3.6

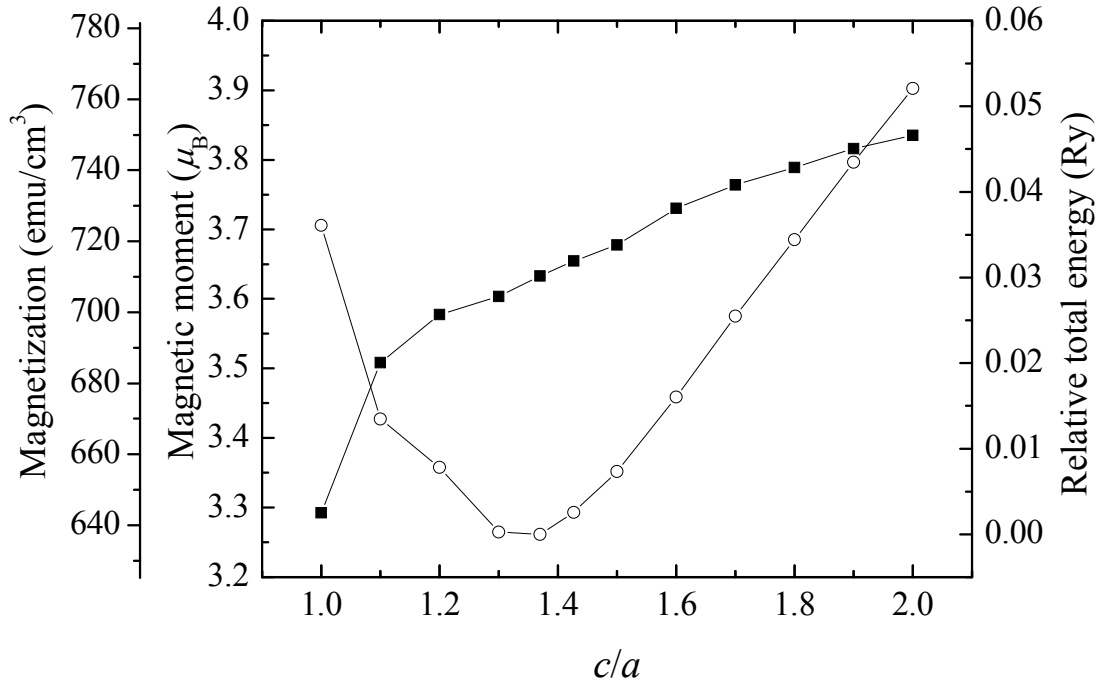


FIG. 3.5. The  $c/a$  dependence of magnetic moment and relative total energy for MnBi.

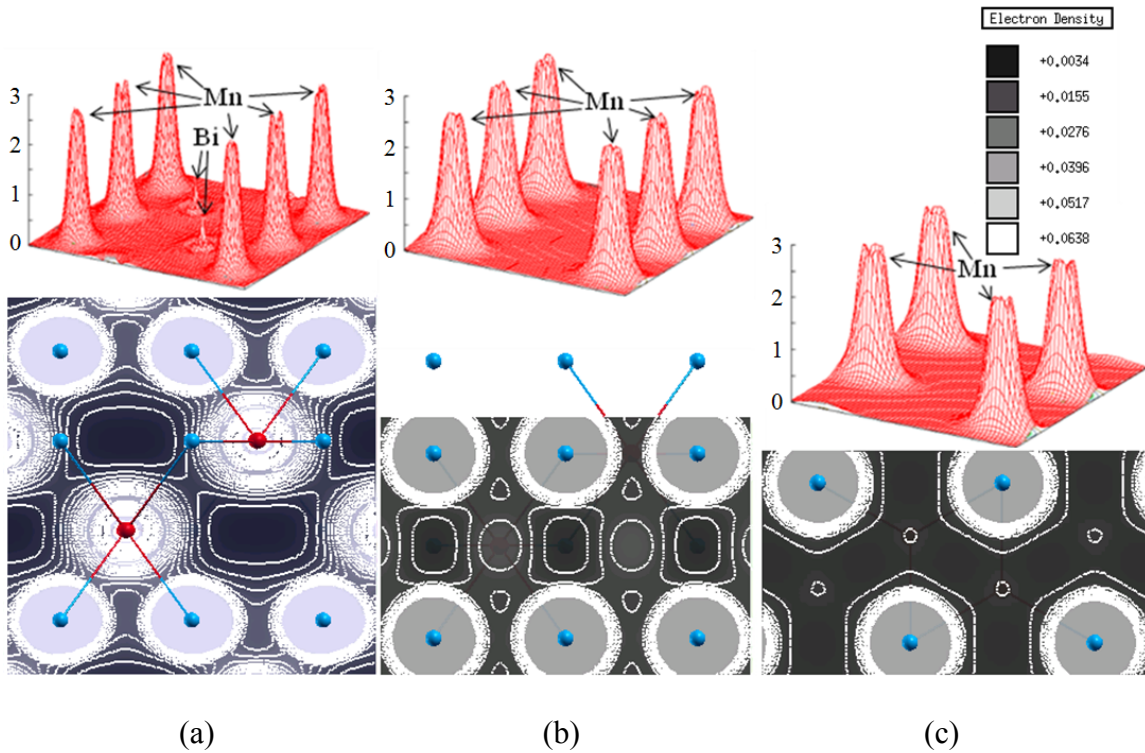


FIG. 3.6. The 3D and 2D electron density maps for LTP MnBi in (a) (110), (b) (100) and (c) (001) planes. The peaks, colors, and contour lines indicate the electron density.

shows the three- (3D) and two-dimensional (2D) electron density maps for (110), (100) and (001) planes. The 2-D electron density maps show that the positions of (0.667, 0.333, 0.250) and (0.333, 0.667, 0.750) have low electron density areas. Therefore, these sites can be interstitial sites for alloying elements.

The identified interstitial sites in the LTP MnBi structure are shown in Fig. 3.7. From these results, we can conclude that doping with a third element into the interstitial sites of LTP MnBi is feasible. In this way, it could be possible to increase the  $c/a$  ratio, thereby increasing  $M_s$ . We previously reported that the ternary and quaternary systems of MnBi-Co and MnBi-Co-Fe show increased  $M_s$  values of  $730 \text{ emu/cm}^3$  and  $810 \text{ emu/cm}^3$ , respectively, as compared to  $714 \text{ emu/cm}^3$  for LTP MnBi [21]. Moreover, it was found that the  $K$  increased from  $-0.275 \times 10^6 \text{ J/m}^3$  for LTP MnBi to  $1.9 \times 10^6 \text{ J/m}^3$  for MnBi-Co and  $1.62 \times 10^6 \text{ J/m}^3$  for MnBi-Co-Fe. These results imply that doping of the elements into the interstitial sites changes the weak easy plane anisotropy of LTP MnBi to the strong easy axis anisotropy at 0 K [21].

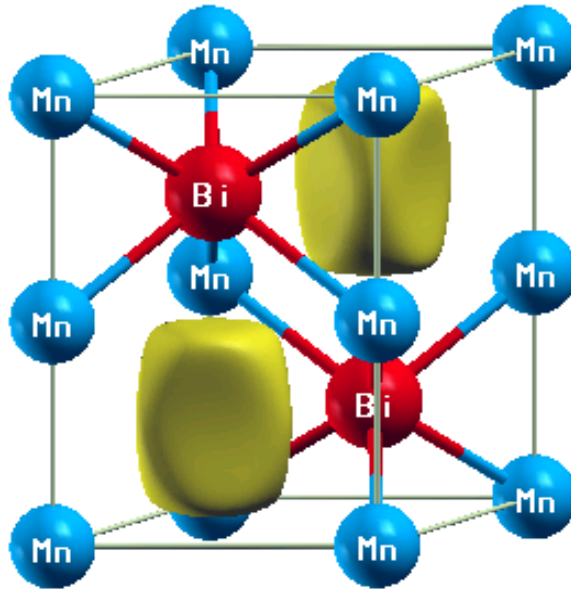


FIG. 3.7. Yellow boxes indicate the low electron density areas of the hexagonal LTP MnBi structure.

Although the  $M_s$  and  $K$  are enhanced by the doping, the  $T_c$  decreases to 325 K for MnBi-Co and 275 K for MnBi-Co-Fe [21] from 711 K for binary MnBi. These low  $T_c$  are the drawbacks of the Co and Co-Fe-doped MnBi-based permanent magnets, which precludes high temperature applications. It is noted that a structural transition by migration of Mn atoms to the interstitial sites occurs at elevated temperature, which cause anti-ferromagnetic coupling between Mn atoms [22]. The doping of a third element into the interstitial sites possibly prevents LTP MnBi from the structural transition, thereby maintaining the high  $T_c$ .

### 3.4. Conclusions

The calculated magnetic moment, MAE, and  $T_c$  are  $3.63 \mu_B/\text{f.u.}$  ( $79 \text{ emu/g}$  or  $714 \text{ emu/cm}^3$ ),  $-0.163 \text{ meV/u.c.}$  (or  $K = -0.275 \times 10^6 \text{ J/m}^3$ ) and 711 K, respectively. It was found that the  $(BH)_{\text{max}}$  at 300 K is 17.7 MGOe, which is in good agreement with the experimental result reported for directionally-solidified LTP MnBi (17 MGOe). The study of electron density maps and  $c/a$  ratio dependence of magnetic moment suggested that doping of a third element into interstitial sites of LTP MnBi can increase the  $M_s$ . The LTP MnBi outperforms Nd-Fe-B above 450 K.

### 3.5. References

1. S. Sugimoto, *J. Phys. D: Appl. Phys.* **44**, 064001 (2011).
2. Hitachi Ferrite Catalog 2007.
3. T. Akiya, H. Kato, M. Sagawa, and K. Koyama, *Mater. Sci. Eng.* **1**, 012034 (2009).
4. T. Chen and W. E. Stutius, *IEEE Trans. Magn.* **10**, 581 (1974).
5. X. Guo, X. Chen, Z. Altounian, and J. O. Ström-Olsen, *Phys. Rev. B* **46**, 14578 (1992).
6. B. W. Roberts, *Phys. Rev.* **104**, 607 (1956).

7. R. G. Pirich and D. J. Larson, U.S. Patent US4,784,703, 15 November 1988.
8. C. Chinnasamy, M. M. Jasinski, A. Ulmer, W. Li, G. Hadjipanayis, and J. Liu, *IEEE Trans. Magn.* **48**, 3641 (2012).
9. J. Cui, J. P. Choi, G. Li, E. Polikarpov, J. Darsell, N. Overman, M. Olszta, D. Schreiber, M. Bowden, T. Droubay, M. J. Kramer, N. A. Zarkevich, L. L. Wang, D. D. Johnson, M. Marinescu, I. Takeuchi, Q. Z. Huang, H. Wu, H. Reeve, N. V. Vuong, and J. P. Liu, *J. Phys.: Condens. Matter* **26**, 064212 (2014).
10. R. Coehoorn and R. A. de Groot, *J. Phys. F: Met. Phys.* **15**, 2135 (1985).
11. J. Köhler and J. Kübler, *J. Phys.: Condens. Matter* **8**, 8681 (1996).
12. B. A. Huberman and W. Streifer, *Phys. Rev. B* **12**, 2741 (1975).
13. P. Blaha, K. Schwarz, G. Madsen, D. Kvasnicka, and J. Luitz, *WIEN2k: An Augmented Plane Wave + Local Orbitals Program for Calculating Crystal Properties*; Karlheinz Schwarz Techn. Universität Wien: Vienna, Austria, 2001.
14. R. R. Heikes, *Phys. Rev.* **99**, 446 (1955).
15. J. B. Yang, W. B. Yelon, W. J. James, Q. Cai, M. Kornecki, S. Roy, N. Ali, and Ph. l'Heritier, *J. Phys.: Condens. Matter* **14**, 6509 (2002).
16. J. M. MacLaren, T. C. Schulthess, W. H. Butler, R. Sutton, and M. McHenry, *J. Appl. Phys.* **85**, 4833 (1999).
17. B. L. Gyorffy, A. J. Pindor, J. Staunton, G. M. Stocks, and H. Winter, *J. Phys. F* **15**, 1337 (1985).
18. A. I. Liechtenstein, M. I. Katsnelson, V. P. Antropov, and V. A. Gubanov, *J. Magn. Magn. Mater.* **67**, 65 (1987).
19. B. D. Cullity, C. D. Graham, *Introduction to Magnetic Materials*, 2nd ed.; Wiley: Hoboken, NJ, USA, 2009; p. 121.
20. N. V. R. Rao, A. M. Gabay, and G. C. Hadjipanayis, *J. Phys. D: Appl. Phys.* **46**, 062001 (2013).
21. Y. K. Hong, J. H. Park, O. N. Mryasov, S. G. Kim, S. H. Kim, J. J. Lee, G. S. Abo, C. J. Choi, and J. G. Lee, *AIP Advances* **3**, 052137 (2013).
22. P. R. Bandaru, T. D. Sands, Y. Kubota, and E. Marinero, *Appl. Phys. Lett.* **72**, 2337 (1998).

## CHAPTER 4

### ELECTRONIC STRUCTURE AND MAGNETIC PROPERTIES OF STRONTIUM FERRITE

#### 4.1 Maximum energy product at elevated temperatures of strontium ferrite<sup>3</sup>

##### 4.1.1. Introduction

Magnetization of 74 emu/g (377 emu/cm<sup>3</sup>) and effective anisotropy constant ( $K_{eff}$ ) of  $3.57 \times 10^6$  erg/cm<sup>3</sup> at 300 K, and Néel temperature ( $T_N$ ) of 750 K were reported for single crystal hexagonal strontium ferrite (SrFe<sub>12</sub>O<sub>19</sub>: SrM) [1]. There have been many attempts to improve the magnetic properties of SrM by substituting foreign cation(s) for its Fe or Sr sites. The substituted cations include: La-Co [2-12], Al [13], Cu-La [14], La-Zn [15,16], Mn-Co-Sn [17], Mn-Co-Ti [18], Mn-Co-Zr [19], Nd-Sm [20], Pb [21], Sn-Zn [22], Zn-Nd [23], Sn-Mg [24], and Er-Ni [25]. The hexagonal strontium ferrite has 24 magnetic Fe<sup>3+</sup> ions distributed among five crystallographically distinct magnetic sublattices, namely  $2a$ ,  $2b$ ,  $12k$ ,  $4f_1$ , and  $4f_2$ . Magnetic moment and magnetocrystalline anisotropy of SrM originate from electronic structure of Fe<sup>3+</sup> ions at the five distinct magnetic sublattices. Therefore, there are 15 possible exchange integrals. Since each magnetic site magnetically behaves differently at a given temperature, temperature dependent magnetic hyperfine field and magnetic moment of each magnetic site have been studied [26,27] to investigate the magnetization of SrM at elevated temperatures.

There are two different approaches to determine temperature dependence of magnetization for each sublattice of hexaferrite Sr(or Ba)Fe<sub>12</sub>O<sub>19</sub>. One approach is to calculate five sublattice magnetizations from five sublattice magnetic hyperfine fields (MHF), which are

---

<sup>3</sup> This work was published as “Maximum energy product at elevated temperatures for hexagonal strontium ferrite (SrFe<sub>12</sub>O<sub>19</sub>) magnet,” in *Journal of Magnetism and Magnetic Materials* **355**, 1 (2014) by Jihoon Park, Yang-Ki Hong, et al.

determined by Mössbauer spectra [26]. It is shown that  $4f_1$  and  $4f_2$  sublattices have almost the same temperature dependent magnetization behavior. Therefore, the other approach assumes only two sublattices, namely spin-up parallel ( $2a$ ,  $2b$ , and  $12k$  sites) and spin-down anti-parallel ( $4f_1$  and  $4f_2$ ) lattices, instead of five distinct sublattices [27]. Also, all exchange integral ( $J_{ij}$ ) were assumed to be identical except for  $J_{4f_2-12k}$  to calculate sublattice magnetizations using molecular field theory.

In this paper, we present calculation of fifteen exchange integrals for  $\text{SrFe}_{12}\text{O}_{19}$ , based on the density functional theory (DFT), to obtain the temperature dependence of magnetic moment  $m_i(T)$  of the five distinct sublattices. Then, the five  $m_i(T)$  were used to estimate temperature dependent maximum energy product,  $(BH)_{\max}(T)$ , at elevated temperatures. Electron exchange and correlation were treated with the generalized gradient approximation (GGA), and GGA+U method was used to improve the description of localized Fe  $3d$  electrons.

#### 4.1.2. Magnetic structure of strontium ferrite

SrM is a hexagonal ferrimagnetic material with five magnetic sublattices ( $2a$ ,  $2b$ ,  $12k$ ,  $4f_1$ , and  $4f_2$ ). There are two formula units of  $\text{SrFe}_{12}\text{O}_{19}$  in one unit cell. The magnetic moment of SrM originates from  $\text{Fe}^{3+}$  ions at each magnetic sublattice. As shown in Fig. 4.1.1, the  $\text{Fe}^{3+}$  ions at the five sublattices are anti-ferromagnetically coupled with each other. It appears that the magnetism of the ground state  $\text{Fe}^{3+}$  ion is mainly due to spin moment  $S$  ( $= 5/2$ ), with no orbital contribution  $L$  ( $= 0$ ). Therefore, the total angular momentum  $J$  ( $= S + L$ ) is  $5/2$  for the  $\text{Fe}^{3+}$  ion. The magnetic moment of the  $\text{Fe}^{3+}$  ion, therefore, is  $5 \mu_B$  in the ideal case. Since the spins in the  $2a$ ,  $2b$ , and  $12k$  sublattices are parallel to each other, but anti-parallel to those of the  $4f_1$  and  $4f_2$  sublattices, the net magnetic moment of one  $\text{SrFe}_{12}\text{O}_{19}$  unit cell (two formula units) is  $40 \mu_B$ .

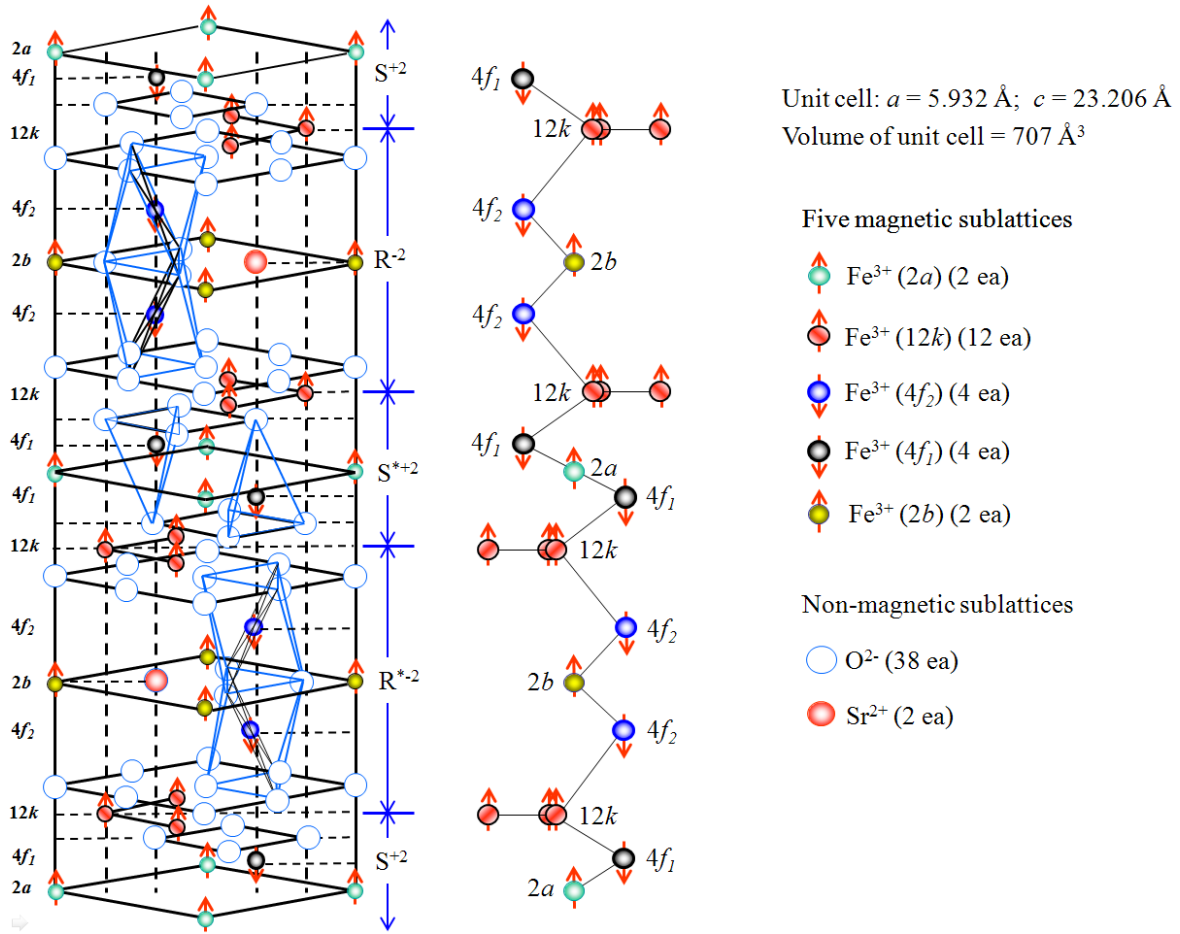


FIG. 4.1.1. The unit cell (left), spin configurations of  $\text{Fe}^{3+}$  at each layer (middle), and lattice constants and number of  $\text{Fe}^{3+}$  at each sublattice (right) for hexagonal strontium ferrite ( $\text{SrFe}_{12}\text{O}_{19}$ ) [28]. The spins at the nearest neighbors are anti-ferromagnetically coupled as shown (middle).

These inter-related magnetic sublattices to the nearest neighbors lead to strong mutual interdependence of the five sublattices.

#### 4.1.3. Method of calculations

In order to derive temperature dependence of saturation magnetization  $M_s(T)$ , it is needed to calculate the exchange integrals. The exchange integrals are obtained by the difference

between exchange energies of ground state and all excited states of sublattices. The exchange energy per unit cell in a system with  $N$  magnetic sublattices can be defined as

$$E_{ex} = \frac{1}{2} \sum_{i=1}^N \sum_{j \neq i=1}^N n_i z_{ij} J_{ij} (\vec{S}_i \vec{S}_j), \quad (4.1.1)$$

where  $n_i$  is the number of  $\text{Fe}^{3+}$  ions at  $i$ th sublattice,  $z_{ij}$  is the number of neighboring  $\text{Fe}^{3+}$  ions at  $j$ th sublattice to  $i$ th sublattice,  $J_{ij}$  is the exchange integrals, and  $\vec{S}_i$  is the spin of the  $\text{Fe}^{3+}$  ions at  $i$ th sublattice. When the ferrimagnetic spin configurations, i.e. only up and down, are considered, the  $\vec{S}_i$  and  $\vec{S}_j$  can be written as

$$\vec{S}_i \vec{S}_j = S_i S_j \sigma_i^{(\alpha)} \sigma_j^{(\alpha)}, \quad (4.1.2)$$

where  $\sigma_i^{(\alpha)} = \pm 1$ , and index  $\alpha$  is the sublattice spin arrangement. Therefore, the exchange energy can be rewritten as

$$E_{ex} = \frac{1}{2} \sum_{i=1}^N \sum_{j \neq i=1}^N n_i z_{ij} J_{ij} S_i S_j \sigma_i^{(\alpha)} \sigma_j^{(\alpha)}. \quad (4.1.3)$$

Now, the exchange integral [29] is written as

$$J_{ij} = (\Delta_{ij} - \Delta_i - \Delta_j) / (4S_i S_j n_i z_{ij} \sigma_i^{(0)} \sigma_j^{(0)}), \quad (4.1.4)$$

Table 4.1.1. The five magnetic sublattices ( $2a$ ,  $2b$ ,  $12k$ ,  $4f_1$ , and  $4f_2$ ) in the unit cell of  $\text{SrFe}_{12}\text{O}_{19}$ .  $n_i$  is the number of  $\text{Fe}^{3+}$  ions at  $i$ th sublattice in the unit cell, and  $\sigma_i^{(0)} = +1$  or  $-1$  represents the ground state spin configuration at  $i$ th sublattice.

Fe sublattice	$n_i$ (# of Fe)	$\sigma_i^{(0)}$ ( $\uparrow$ or $\downarrow$ )
$2a$	2	+1
$2b$	2	+1
$12k$	12	+1
$4f_1$	4	-1
$4f_2$	4	-1

Table 4.1.2. The number of nearest neighbors and corresponding distance for the five magnetic sublattices ( $2a$ ,  $2b$ ,  $12k$ ,  $4f_1$ , and  $4f_2$ ) in the unit cell of  $\text{SrFe}_{12}\text{O}_{19}$ .  $z_{ij}$  is the number of neighbors ( $\text{Fe}^{3+}$  ions) at  $j$ th sublattice to  $i$ th sublattice, and  $r_{ij}$  is the corresponding distances in nm. The second-nearest neighbors are also given if  $r_{ij}$  is shorter than 0.4 nm.

	$2a$		$2b$		$4f_1$		$4f_2$		$12k$	
	$z_{ij}$	$r_{ij}$								
$2a$	6	0.593	2	0.580	6	0.348	6	0.560	6	0.307
$2b$	2	0.580	6	0.593	6	0.621	6	0.369	6	0.370
$4f_1$	3	0.348	3	0.621	3	0.365	1	0.380	6	0.353
									3	0.358
$4f_2$	3	0.560	3	0.369	1	0.380	1	0.275	6	0.352
$12k$	1	0.307	1	0.370	2	0.353	2	0.352	2	0.293
					1	0.358			2	0.300

where  $\Delta_j$  is the difference of exchange energies between the excited state at both  $i$  and  $j$  sublattices and the ground state,  $\Delta_i$  is between the excited state at  $i$  sublattice and the ground state, and  $\Delta_j$  is between the excited state at  $j$  sublattice and the ground state. The  $n_i$  and  $\sigma_i^{(0)}$  for the five sublattices are given in Table 4.1.1, and the number of the nearest neighboring  $\text{Fe}^{3+}$  ions at  $j$ th sublattice to  $i$ th sublattice and corresponding distance  $r_{ij}$  are listed in Table 4.1.2.

In order to calculate the energy difference ( $\Delta_i$ ,  $\Delta_j$ , and  $\Delta_j$ ), the first principles calculations were performed using VASP [30] with the relaxed structure of  $\text{SrFe}_{12}\text{O}_{19}$ . The VASP is a package for performing ab initio quantum mechanical molecular dynamics (MD), mainly based on density functional theory (DFT) [31,32].

For improved description of  $3d$  electrons in  $\text{Fe}^{3+}$  ion, generalized gradient approximation with Coulomb and exchange interaction effects (GGA+ $U$ ) were employed, in which an on-site

potential is added to introduce intra-atomic interactions between the strongly correlated electrons. The total energy [33] is defined as

$$E = \frac{(U-J)}{2} \sum_{\sigma} (n_{m,\sigma} - n_{m,\sigma}^2), \quad (4.1.5)$$

where  $U$  is the Coulomb interaction parameter (energy necessary to add an electron to an already occupied localized orbital in an atom),  $J$  is the exchange interaction parameter (exchange between doubly occupied sites), and  $n$  is the occupation number of a  $d$ -orbital number  $m$  with spin  $\sigma$ . As can be seen from Eq. (4.1.5), the total energy depends on the difference between  $U$  and  $J$ , which is defined as the effective  $U$ ,  $U_{eff}$ . The  $U_{eff}$  affects the total energy difference between excited and ground states, thereby  $J_{ij}$ . The  $J_{ij}$  were applied to the Brillouin function to derive  $m(T)$  for the five sublattices ( $2a$ ,  $2b$ ,  $12k$ ,  $4f_1$ , and  $4f_2$ ), consequently  $(BH)_{max}$ .

#### 4.1.4. Results

##### 4.1.4.1. Exchange integrals (interactions between the five magnetic sublattices)

The relaxation for a SrM system gives the lattice constants of  $a$  and  $c$  of 5.932 and 23.206 Å, respectively. These constants are in good agreement with experimental ones of 5.88 and 23.04 Å [34]. The energy difference  $\Delta$  between the ground state and excited states was calculated with three different values of  $U_{eff}$  (= 3.7, 7.0, and 10.3 eV). All possible excited spin configurations, 21 sets at the five different magnetic sublattices, were considered. The calculated energy difference  $\Delta$  and magnetic moments per unit cell for each excited state are given in Table 4.1.3. It can be seen that the energy difference  $\Delta$  is smaller for larger  $U_{eff}$ , while the magnetic moment remains almost constant. However,  $U_{eff}$  values larger than 10.3 eV cause unreliable energy and magnetic moment for SrM.

The calculated energy difference  $\Delta$  was then used to obtain exchange integrals using Eq. (4.1.4). The input parameters  $n_i$ ,  $z_{ij}$ , and  $\sigma_i^{(0)}$  for each excited state were taken from Table 4.1.1 and 4.1.2. Fig. 4.1.2 shows exchange integrals for all the possible excited states as a function of  $U_{eff}$ . The exchange integrals become smaller as larger  $U_{eff}$  is used.

Table 4.1.3. The energy difference  $\Delta(U_{eff})$  in eV between the ground state and excited states. The magnetic moment  $m$  in  $\mu_B$  are also listed for the excited spin configurations. The  $s_1$  and  $s_2$  denote the excited sublattices.

$s_1$	$s_2$	$\Delta(3.7)$	$\Delta(7.0)$	$\Delta(10.3)$	$m(3.7)$	$m(7.0)$	$m(10.3)$
2a	-	0.914	0.519	0.163	20.00	19.99	20.00
2b	-	0.815	0.456	0.153	20.00	19.99	20.00
4f <sub>1</sub>	-	3.130	1.663	0.516	79.99	80.00	80.00
4f <sub>2</sub>	-	3.164	1.691	0.552	80.00	79.99	79.99
12k	-	3.818	2.091	0.660	-80.00	-79.99	-79.99
2a	2b	1.727	0.975	0.316	0.00	0.00	0.00
2a	4f <sub>1</sub>	2.012	1.112	0.346	60.01	59.99	59.99
2a	4f <sub>2</sub>	4.080	2.215	0.716	60.00	60.00	59.99
2a	12k	4.926	2.630	0.829	-100.00	-99.84	-99.99
2b	4f <sub>1</sub>	3.874	2.089	0.660	59.99	60.00	60.00
2b	4f <sub>2</sub>	1.692	0.931	0.306	60.01	59.99	59.99
2b	12k	5.362	2.885	0.916	-99.99	-100.00	-100.00
4f <sub>1</sub>	4f <sub>2</sub>	6.477	3.432	1.091	120.00	120.00	120.32
4f <sub>1</sub>	12k	2.609	1.455	0.470	-39.99	-40.00	-39.99
4f <sub>2</sub>	12k	2.766	1.539	0.490	-40.00	-40.00	-40.00
2f <sub>1-1</sub>	-	1.523	0.816	0.255	60.00	60.00	59.99
2f <sub>1-2</sub>	-	1.523	0.816	0.255	60.00	59.99	59.99
2f <sub>2-1</sub>	-	1.569	0.843	0.271	59.99	60.00	59.99
2f <sub>2-2</sub>	-	1.569	0.843	0.271	60.00	60.00	59.99
8k	-	0.782	0.496	0.144	0.00	0.00	0.00
4k	-	2.060	1.196	0.365	-39.99	-40.00	-39.99

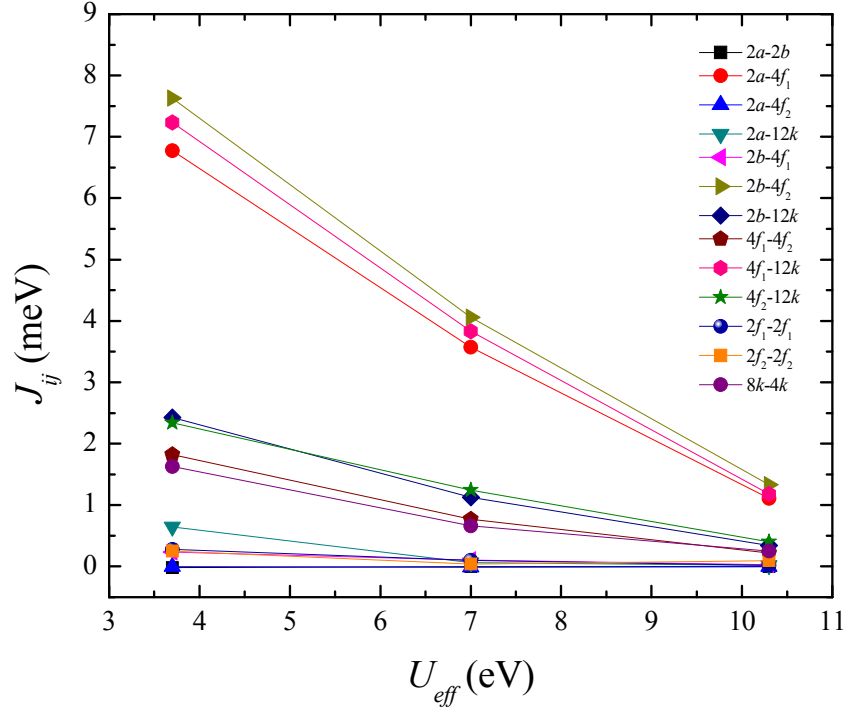


FIG. 4.1.2. The sublattice exchange integrals as a function of  $U_{eff}$  (3.7, 7.0, and 10.3 eV).

#### 4.1.4.2. Temperature dependence of saturation magnetization $M_s(T)$ and maximum energy product $(BH)_{max}(T)$

The exchange integrals and magnetic moments calculated with  $U_{eff} = 7.0$  eV were used to obtain the  $m(T)$  for the five sublattices ( $2a$ ,  $2b$ ,  $12k$ ,  $4f_1$ , and  $4f_2$ ). The magnetic moments at 0 K ( $m_{0,i}$ ) for  $2a$ ,  $2b$ ,  $12k$ ,  $4f_1$ , and  $4f_2$  sublattices are 4.427, 4.365, 4.432, -4.362, -4.400  $\mu_B$ , respectively. These moments were calculated by first principles calculations. In the case of a multiple sublattice system, the number of Brillouin functions is the same as the number of sublattices. Therefore, there are five different Brillouin functions for the SrM. The calculated exchange integrals for  $2a-4f_1$ ,  $2b-4f_2$ ,  $2b-12k$ ,  $12k-4f_1$ , and  $12k-4f_2$  in Fig. 4.1.2 were considered for the derivation of the five Brillouin functions, since those exchange integrals are dominant. It is noted that the spins at each sublattice are mostly anti-ferromagnetically coupled with the spins

at the nearest sublattices. By considering the five exchange integrals, the  $m(T)$  for the five sublattices in SrM can be written as

$$m_a / m_{0,a} = B[(s^2 / k_B T) | 2N_{a \cdot f_1} J_{a \cdot f_1} (m_{f_1} / m_{0,f_1}) |] \quad (4.1.6a)$$

$$m_b / m_{0,b} = B[(s^2 / k_B T) | 2N_{b \cdot f_2} J_{b \cdot f_2} (m_{f_2} / m_{0,f_2}) + 2N_{b \cdot k} J_{b \cdot k} (m_k / m_{0,k}) |] \quad (4.1.6b)$$

$$m_k / m_{0,k} = B[(s^2 / k_B T) | 2N_{k \cdot f_1} J_{k \cdot f_1} (m_{f_1} / m_{0,f_1}) + 2N_{k \cdot f_2} J_{k \cdot f_2} (m_{f_2} / m_{0,f_2}) + 2N_{k \cdot b} J_{k \cdot b} (m_b / m_{0,b}) |] \quad (4.1.6c)$$

$$m_{f_1} / m_{0,f_1} = B[(s^2 / k_B T) | 2N_{f_1 \cdot a} J_{f_1 \cdot a} (m_a / m_{0,a}) + 2N_{f_1 \cdot k} J_{f_1 \cdot k} (m_k / m_{0,k}) |] \quad (4.1.6d)$$

$$m_{f_2} / m_{0,f_2} = B[(s^2 / k_B T) | 2N_{f_2 \cdot b} J_{f_2 \cdot b} (m_b / m_{0,b}) + 2N_{f_2 \cdot k} J_{f_2 \cdot k} (m_k / m_{0,k}) |] \quad (4.1.6e)$$

The numbers of nearest neighbors  $N_{ij}$  in Eq. (4.1.6) were taken from Table 4.1.2 as

$$\begin{aligned} N_{a \cdot f_1} &= 6 \\ N_{b \cdot f_2} &= 6 \text{ and } N_{b \cdot k} = 6 \\ N_{k \cdot f_1} &= 3, N_{k \cdot f_2} = 2, \text{ and } N_{k \cdot b} = 1 \\ N_{f_1 \cdot a} &= 3 \text{ and } N_{f_1 \cdot k} = 9 \\ N_{f_2 \cdot b} &= 3 \text{ and } N_{f_2 \cdot k} = 6 \end{aligned}$$

Therefore, after substituting the above numbers for  $N_{ij}$ , Eq. (4.1.6) becomes Eq. (4.1.7).

$$m_a / m_{0,a} = B[(s^2 / k_B T) | 12 J_{a \cdot f_1} (m_{f_1} / m_{0,f_1}) |] \quad (4.1.7a)$$

$$m_b / m_{0,b} = B[(s^2 / k_B T) | 12 J_{b \cdot f_2} (m_{f_2} / m_{0,f_2}) + 12 J_{b \cdot k} (m_k / m_{0,k}) |] \quad (4.1.7b)$$

$$m_k / m_{0,k} = B[(s^2 / k_B T) | 6 J_{k \cdot f_1} (m_{f_1} / m_{0,f_1}) + 4 J_{k \cdot f_2} (m_{f_2} / m_{0,f_2}) + 2 J_{k \cdot b} (m_b / m_{0,b}) |] \quad (4.1.7c)$$

$$m_{f_1} / m_{0,f_1} = B[(s^2 / k_B T) | 6 J_{f_1 \cdot a} (m_a / m_{0,a}) + 18 J_{f_1 \cdot k} (m_k / m_{0,k}) |] \quad (4.1.7d)$$

$$m_{f_2} / m_{0,f_2} = B[(s^2 / k_B T) | 6 J_{f_2 \cdot b} (m_b / m_{0,b}) + 12 J_{f_2 \cdot k} (m_k / m_{0,k}) |] \quad (4.1.7e)$$

In order to calculate  $J_{ij}$  as a function of the  $T_N$ , limits were taken for the case that  $T$  approaches to

$T_N$ . For example, Eq. (4.1.7a) can be written as  $m_a / m_{0,a} = \frac{12 J_{a \cdot f_1} s^2}{k_B T} B(m_{f_1} / m_{0,f_1})$ . After

simple re-arrangement of the above equation,  $T$  becomes  $T = \frac{12J_{a,f_1}s^2}{k_B} \frac{B(m_{f_1}/m_{0,f_1})}{m_a/m_{0,a}}$ .

Therefore,  $T_N = \frac{12J_{a,f_1}s^2}{k_B} \frac{B(m_{f_1}/m_{0,f_1})}{m_a/m_{0,a}}$  when  $T$  approaches  $T_N$ . Now, a conversion ratio

parameter  $\eta_a$  is introduced to obtain  $B(m_{f_1}/m_{0,f_1}) = \eta_a B(m_a/m_{0,a})$ . Then,  $T_N$  can be

rewritten as  $T_N = \frac{12J_{a,f_1}s^2}{k_B} \eta_a \frac{B(m_a/m_{0,a})}{m_a/m_{0,a}}$ . Since  $\frac{B(m_a/m_{0,a})}{m_a/m_{0,a}} = \frac{s+1}{3s}$  for the case of  $T \approx T_N$ ,

five  $T_N$  equations for the five sublattices are obtained as

$$T_N = \frac{4s(s+1)J_{a,f_1}}{k_B} \eta_a \quad (4.1.8a)$$

$$T_N = \frac{4s \cdot J_{b,f_2}}{k_B} (1+b)\eta_b \cdot (s+1) \quad (4.1.8b)$$

$$T_N = \frac{2s \cdot J_{k,f_1}}{k_B} (3+2c_1+c_2)\eta_k \cdot \frac{(s+1)}{3} \quad (4.1.8c)$$

$$T_N = \frac{2s \cdot J_{f_1,k}}{k_B} (d+3)\eta_{f_1} \cdot (s+1) \quad (4.1.8d)$$

$$T_N = \frac{2s \cdot J_{f_2,k}}{k_B} (e+2)\eta_{f_2} \cdot (s+1), \quad (4.1.8e)$$

where  $b, c_1, c_2, d,$  and  $e$  are

$$\begin{aligned} b &= J_{b,k} / J_{b,f_2} \\ c_1 &= J_{k,f_2} / J_{k,f_1} \\ c_2 &= J_{k,b} / J_{k,f_1} \\ d &= J_{f_1,a} / J_{f_1,k} \\ e &= J_{f_2,b} / J_{f_2,k} \end{aligned}$$

The conversion ratio parameters  $\eta_i$  in Eq. (4.1.8) is calculated using the experimental  $T_N$  of 750 K [1] and the exchange integrals at  $U_{eff} = 7$  eV in Fig. 4.1.2. The following conversion ratio parameters were obtained.

$$\begin{aligned}\eta_a &= 0.5175 \\ \eta_b &= 0.3565 \\ \eta_k &= 0.7332 \\ \eta_{f_1} &= 0.2451 \\ \eta_{f_2} &= 0.5640\end{aligned}$$

Also, the exchange integrals in Eq. (4.1.8) can be rewritten as

$$\frac{J_{a:f_1}}{k_B} = \frac{T_N}{4s(s+1) \cdot \eta_a} \quad (4.1.9a)$$

$$\frac{J_{b:f_2}}{k_B} = \frac{T_N}{4s(s+1)(1+b) \cdot \eta_b} \quad (4.1.9b)$$

$$\frac{J_{k:f_1}}{k_B} = \frac{3T_N}{2s(s+1)(3+2c_1+c_2) \cdot \eta_k} \quad (4.1.9c)$$

$$\frac{J_{f_1:k}}{k_B} = \frac{T_N}{2s(s+1)(d+3) \cdot \eta_{f_1}} \quad (4.1.9d)$$

$$\frac{J_{f_2:k}}{k_B} = \frac{T_N}{2s(s+1)(e+2) \cdot \eta_{f_2}} \quad (4.1.9e)$$

After inserting the above exchange integral expressions of Eq. (4.1.9) and the calculated values of  $M_{0,i}$  into Eq. (4.1.7),  $m(T)$  for five sublattices become

$$\frac{m_a}{m_{0,a}} = 1.2 \coth \left( 1.2 \times 2.025 \frac{m_{f_1}/m_{0,f_1}}{T/T_N} \right) - 0.2 \coth \left( 0.2 \times 2.025 \frac{m_{f_1}/m_{0,f_1}}{T/T_N} \right) \quad (4.1.10a)$$

$$\frac{m_b}{m_{0,b}} = 1.2 \coth \left[ 1.2 \left( 2.3 \frac{m_{f_2}/m_{0,f_2}}{T/T_N} + 0.6383 \frac{m_k/m_{0,k}}{T/T_N} \right) \right] - 0.2 \coth \left[ 0.2 \left( 2.3 \frac{m_{f_2}/m_{0,f_2}}{T/T_N} + 0.6383 \frac{m_k/m_{0,k}}{T/T_N} \right) \right] \quad (4.1.10b)$$

$$\frac{m_k}{m_{0,k}} = 1.2 \coth \left[ 1.2 \left( 1.0869 \frac{m_{f_1}}{m_{0,f_1}} + 0.2356 \frac{m_{f_2}}{m_{0,f_2}} + 0.1064 \frac{m_b}{m_{0,b}} \right) / T/T_N \right] - 0.2 \coth \left[ 0.2 \left( 1.0869 \frac{m_{f_1}}{m_{0,f_1}} + 0.2356 \frac{m_{f_2}}{m_{0,f_2}} + 0.1064 \frac{m_b}{m_{0,b}} \right) / T/T_N \right] \quad (4.1.10c)$$

$$\frac{m_{f_1}}{m_{0,f_1}} = 1.2 \coth \left[ 1.2 \left( 1.0127 \frac{m_a}{m_{0,a}} + 1.8665 \frac{m_k}{m_{0,k}} \right) / T/T_N \right] - 0.2 \coth \left[ 0.2 \left( 1.0127 \frac{m_a}{m_{0,a}} + 1.8665 \frac{m_k}{m_{0,k}} \right) / T/T_N \right] \quad (4.1.10d)$$

$$\frac{m_{f_2}}{m_{0,f_2}} = 1.2 \coth \left[ 1.2 \left( 1.1505 \frac{m_b}{m_{0,b}} + 1.9571 \frac{m_k}{m_{0,k}} \right) / T/T_N \right] - 0.2 \coth \left[ 0.2 \left( 1.1505 \frac{m_b}{m_{0,b}} + 1.9571 \frac{m_k}{m_{0,k}} \right) / T/T_N \right] \quad (4.1.10e)$$

Since there is strong mutual interdependence among the above five equations, numerical analysis was performed, and the temperature dependence of magnetic moment  $m(T)$  for the five sublattices is shown in Fig. 4.1.3. The temperature behavior of magnetic moment is the same

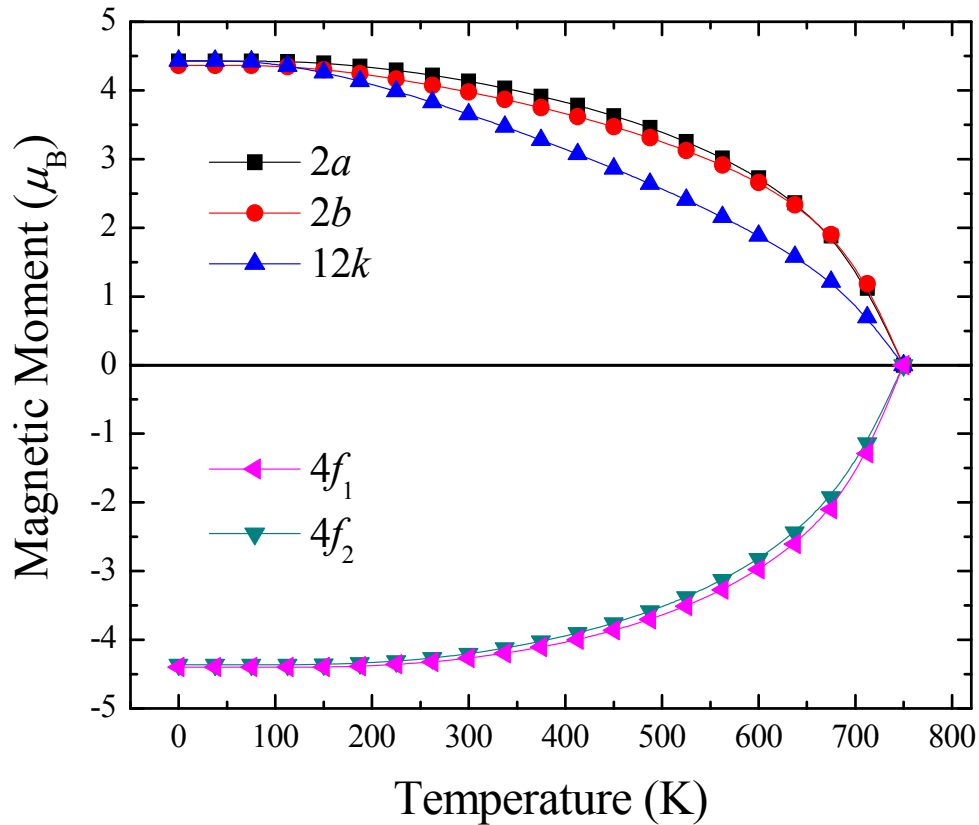


FIG. 4.1.3. The calculated sublattice magnetic moments as a function of temperature  $m(T)$ . The exchange integrals used to calculate the sublattice magnetic moments are from the exchange energies with  $U_{eff}$  of 7.0 eV.

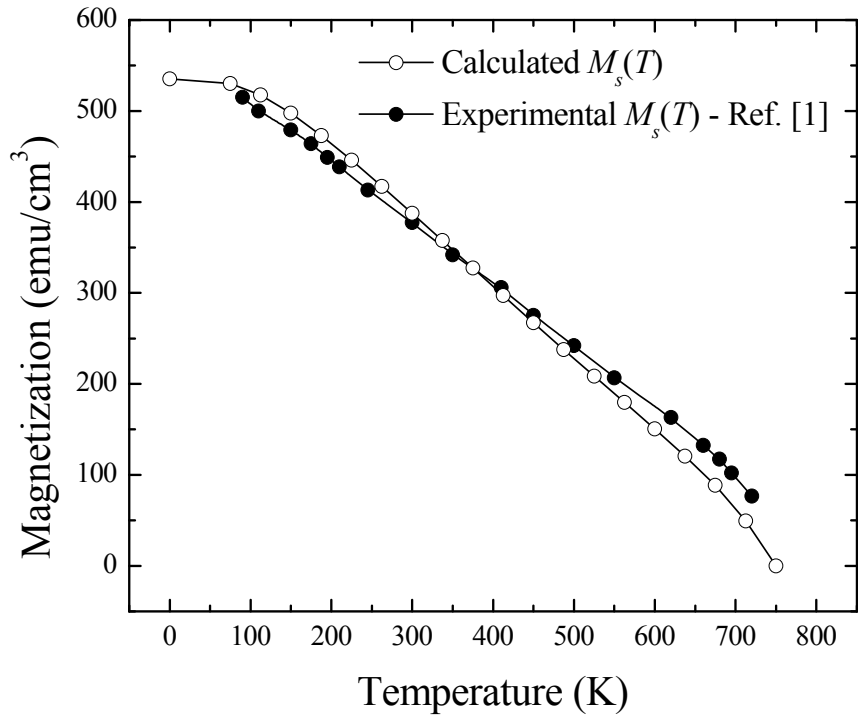


FIG. 4.1.4. The calculated and experimental saturation magnetizations as a function of temperature  $M_s(T)$ . The open circles are the  $M_s(T)$  from the calculated sublattice  $m(T)$ , and full circles are experimental  $M_s(T)$ .

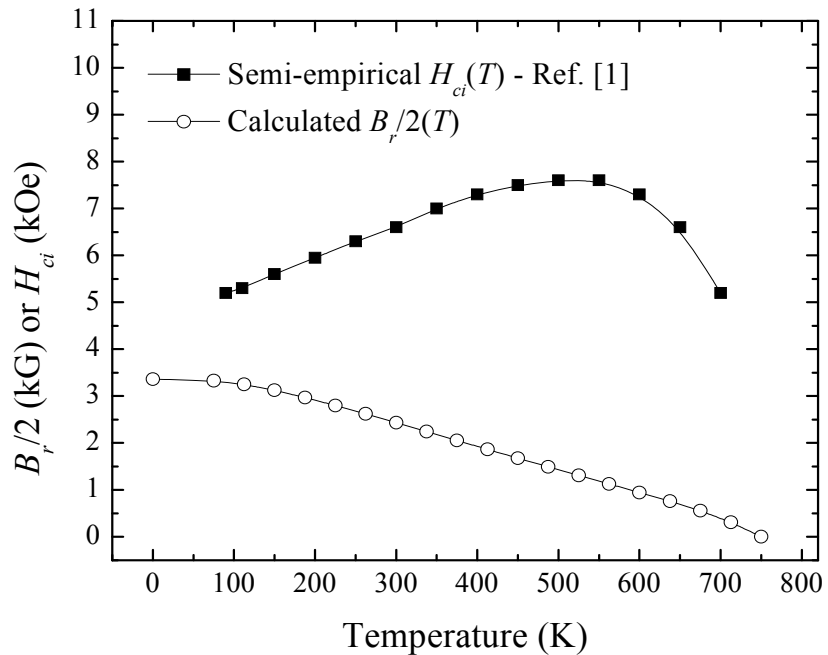


FIG. 4.1.5. The temperature dependence of half-remanent magnetization  $B_r/2(T)$  and intrinsic coercivity  $H_{ci}(T)$ . The open circles are the calculated  $B_r/2(T)$ , and full squares are the semi-empirical  $H_{ci}(T)$ .

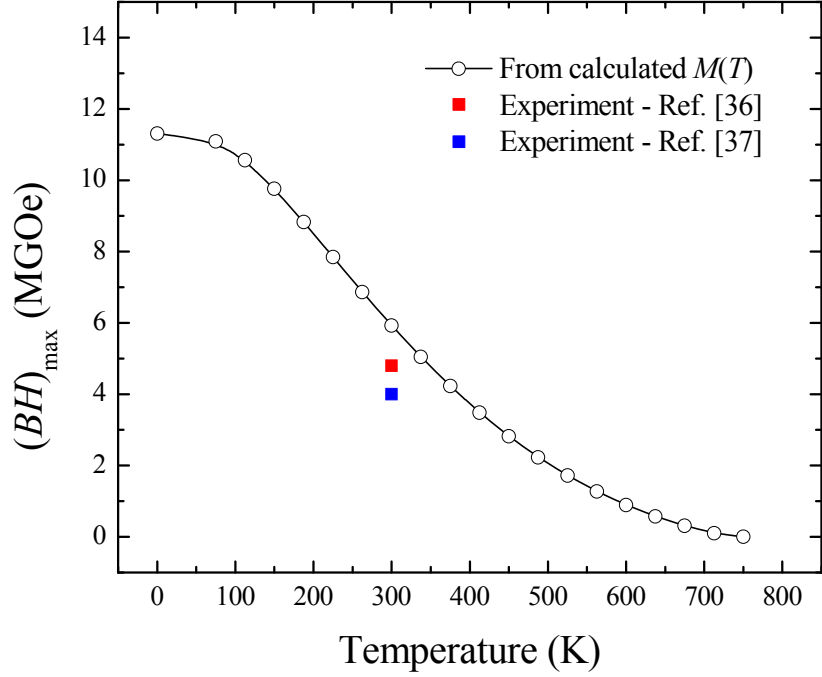


FIG. 4.1.6. The calculated maximum energy product as a function of temperature  $(BH)_{\max}(T)$ . The open circles are the calculated data from the calculated temperature dependences of saturation magnetization  $M_s(T)$ . Red and blue squares indicate experimental room temperature  $(BH)_{\max}$ .

behavior as well-known, typical ferromagnetic behavior of ferrite. The magnetic moment at  $12k$  sublattice decreases more rapidly than the other sublattices as the temperature increases, even though the  $T_N$  for all the sublattices is the same. After having converted magnetic moment to magnetization, the calculated and experimental [1]  $M_s(T)$  are compared in Fig. 4.1.4. The number of  $\text{Fe}^{3+}$  ions at  $12k$  sublattice per unit cell is 12, which is the same number as all the other  $\text{Fe}^{3+}$  ions summed, and the spin directions for the  $4f_1$  and  $4f_2$  sublattices are opposite to the  $2a$ ,  $2b$  and  $12k$  sublattices. Therefore, the total  $M_s(T)$  for SrM is very likely to follow  $m(T)$  for the  $12k$  sublattice.

The figure of merit for a permanent magnet is the maximum energy product  $(BH)_{\max}$ . Accordingly,  $(BH)_{\max}(T)$  is calculated based on the calculated  $M_s(T)$  and semi-empirical intrinsic coercivity  $(H_{ci}(T))$  [1]. The intrinsic coercivity  $(H_{ci})$  over the temperature range of 100 to 700 K

is larger than half of the remnant magnetization  $B_r/2$  for SrM as shown in Fig. 4.1.5. By neglecting pinning of the nucleation and assuming only coherent rotation with a rectangular magnetic hysteresis loop,  $B_r(T)$  can be taken the same as the temperature dependence of the saturation magnetization  $M_s(T)$ , and nucleation field ( $H_N$ ) is also the same as  $H_{ci}$ . Therefore,  $(BH)_{\max}(T)$  can be calculated by the following equation [35].

$$(BH)_{\max}(T) = \frac{B_r^2(T)}{4} \quad (4.1.11)$$

Fig. 4.1.6 shows the calculated  $(BH)_{\max}(T)$ . It reproduces the experimental  $(BH)_{\max}$  values at room temperature (4.8 [36] and 4.0 [37] MGOe) reasonably well. The difference may be attributed to imperfect magnetic orientation and existence of secondary phases, including hematite.

#### 4.1.5. Conclusion

The exchange integrals of hexagonal strontium ferrite ( $\text{SrFe}_{12}\text{O}_{19}$ ) were calculated in order to obtain the temperature dependences of magnetic moments  $m(T)$  for the five magnetic sublattices ( $2a$ ,  $2b$ ,  $12k$ ,  $4f_1$ , and  $4f_2$ ). The density functional theory (DFT) and generalized gradient approximation with Coulomb and exchange interaction effects (GGA+ $U$ ) were used for all calculations. The exchange integrals with  $U_{\text{eff}}$  of 7.0 eV were then employed to the five inter-related Brillouin functions for the sublattice  $m(T)$  calculations. The saturation magnetization  $M_s(T)$  for  $\text{SrFe}_{12}\text{O}_{19}$  was obtained by summation of the sublattice  $m(T)$  and compared with an experimental  $M_s(T)$ . It was found that the calculated  $M_s(T)$  was in good agreement with the experimental values. The temperature dependence of maximum energy product  $(BH)_{\max}(T)$  was also calculated from the  $M_s(T)$ . The calculated  $(BH)_{\max}(T)$  shows that the value at 300 K is 5.9

MGOe, which is close to the experimental values of Hitachi (4.8 MGOe) [36] and Cochardt (4.0 MGOe) [37].

#### 4.1.6. References

1. B. T. Shirk, W. R. Buessem, *Journal of Applied Physics* **40**, 1294 (1969).
2. A. Morel, J. M. Le Breton, J. Kreisel, G. Wiesinger, F. Kools, P. Tenaud, *Journal of Magnetism and Magnetic Materials* **242-245**, 1405 (2002).
3. J. M. Le Breton, J. Teillet, G. Wiesinger, A. Morel, F. Kools, P. Tenaud, *IEEE Transactions on Magnetics* **38**, 2952 (2002).
4. F. Kools, A. Morel, R. Grössinger, J. M. Le Breton, P. Tenaud, *Journal of Magnetism and Magnetic Materials* **242-245**, 1270 (2002).
5. Y. Ogata, Y. Kubota, T. Takami, M. Tokunaga, T. Shinohara, *IEEE Transactions on Magnetics* **35**, 3334 (1999).
6. P. Tenaud, A. Morel, F. Kools, J. M. Le Breton, L. Lechevallier, *Journal of Alloys and Compounds* **370**, 331 (2004).
7. D. H. Choi, S. W. Lee, I. B. Shim, C. S. Kim, *Journal of Magnetism and Magnetic Materials* **304**, e243 (2006).
8. G. Asti, F. Bolzoni, J. M. Le Breton, M. Ghidini, A. Morel, M. Solzi, F. Kools, P. Tenaud, *Journal of Magnetism and Magnetic Materials* **272-276**, e1845 (2004).
9. X. Liu, P. Hernández-Gómez, K. Huang, S. Zhou, Y. Wang, X. Cai, H. Sun, B. Ma, *Journal of Magnetism and Magnetic Materials* **305**, 524 (2006).
10. J. M. Le Breton, L. Lechevallier, J. F. Wang, R. Harris, *Journal of Magnetism and Magnetic Materials* **272-276**, 2214 (2004).
11. H. Nishio, Y. Minachi, H. Yamamoto, *IEEE Transactions on Magnetics* **45**, 5281 (2009).
12. H. Nishio, H. Yamamoto, *IEEE Transactions on Magnetics* **47**, 3641 (2011).
13. N. J. Shirtcliffe, S. Thompson, E. S. O'Keefe, S. Appleton, C. C. Perry, *Materials Research Bulletin* **42**, 281 (2007).
14. G. Coffey, J. Hardy, O. Marina, L. Pederson, P. Rieke, E. Thomsen, *Solid State Ionics* **175**, 73 (2004).
15. S. W. Lee, S. Y. An, I. B. Shim, C. S. Kim, *Journal of Magnetism and Magnetic Materials* **290-291**, 231 (2005).

16. X. Liu, J. Bai, F. Wei, Z. Yang, S. Takei, A. Morisako, M. Matsumoto, *Journal of Applied Physics* **87**, 6875 (2000).
17. A. Ghasemi, V. Šepelák, X. Liu, A. Morisako, *IEEE Transactions on Magnetics* **45**, 2456 (2009).
18. A. Ghasemi, A. Saatchi, M. Salehi, A. Hossienpour, A. Morisako, X. Liu, *Physica Status Solidi (a)* **203**, 2513 (2006).
19. A. Ghasemi, A. Morisako, *Journal of Alloys and Compounds* **456**, 485 (2008).
20. P. Sharma, A. Verma, R. K. Sidhu, O. P. Pandey, *Journal of Alloys and Compounds* **361**, 257 (2003).
21. S. Hussain, A. Maqsood, *Journal of Alloys and Compounds* **466**, 293 (2008).
22. A. Ghasemi, V. Šepelák, X. Liu, A. Morisako, *Journal of Applied Physics* **107**, 09A734 (2010).
23. Q. Fang, H. Bao, D. Fang, J. Wang, *Journal of Applied Physics* **95**, 6360 (2004).
24. A. Davoodi, B. Hashemi, *Journal of Alloys and Compounds* **509**, 5893 (2011).
25. M. N. Ashiq, M. J. Iqbal, M. Najam-ul-Haq, P. H. Gomez, A. M. Qureshi, *Journal of Magnetism and Magnetic Materials* **324**, 15 (2012).
26. J. J. van Loef, A. Broese van Groenou, Proceedings of the International Conference on Magnetism, Nottingham 1964 (The Institute of Physics and the Physical Society), London, 646 (1965).
27. S. P. Marshall, J. B. Sokoloff, *Journal of Applied Physics* **67**, 2017 (1990).
28. J. Jalli, Y. K. Hong, S. H. Gee, S. Bae, J.J. Lee, J. C. Sur, G. S. Abo, A. Lyle, S. I. Lee, H. C. Lee, T. Mewes, *IEEE Transactions on Magnetics* **44**, 2978 (2008).
29. P. Novák, J. Ruzs, *Physical Review B* **71**, 184433 (2005).
30. G. Kresse, M. Marsman, and J. Furthmüller, Computational Physics, Faculty of Physics, Universität Wien, Sensengasse 8, A-1130 Wien, Austria (2009).
31. G. Kresse, J. Hafner, *Physical Review B* **47**, 558 (1993).
32. G. Kresse, J. Furthmüller, *Physical Review B* **54**, 11169 (1996).
33. S. L. Dudarev, G. A. Botton, S. Y. Savrasov, C. J. Humphreys, A. P. Sutton, *Physical Review B* **57**, 1505 (1998).
34. K. Kimura, M. Ohgaki, K. Tanaka, H. Morikawa, F. Marumo, *Journal of Solid State Chemistry* **87**, 186 (1990).

35. R. Skomski, J. M. D. Coey, *Physical Review B* **48**, 15812 (1993).
36. Hitachi Ferrite Catalog 2007.
37. A. Cochardt, *Journal of Applied Physics* **34**, 1273 (1963).

## 4.2 Thermomagnetic stability of strontium ferrite particles with different shapes<sup>4</sup>

### 4.2.1. Introduction

M-type hexaferrite (BaFe<sub>12</sub>O<sub>19</sub>: BaM or SrFe<sub>12</sub>O<sub>19</sub>: SrM) magnet is the most widely used permanent magnet for electric machines owing to its high magnetization, magnetocrystalline anisotropy, Curie temperature, and chemical stability. There have been many synthetic methods to produce BaM or SrM particles. The conventional ceramic method requires firing a mixture of hematite ( $\alpha$ -Fe<sub>2</sub>O<sub>3</sub>) and barium or strontium carbonate (BaCO<sub>3</sub>/SrCO<sub>3</sub>) particles at 1200 °C [1]. The fired mixture is milled to reduce the particle size to the single magnetic domain size. This resulted in lattice strains in the particles [2]. The coercivity of ferrite prepared by this method is much lower than the theoretically estimated coercivity of single-domain particles [3]. Therefore, many unconventional processes, including sol-gel [4-9], hydrothermal [10-16], co-precipitation [17-24] reverse microemulsion processes [25-27], and spray pyrolysis [28] have been developed to address the above issue. Furthermore, precursor-directed synthetic method was also developed to achieve desired size and morphology with superior dispersibility [29-33]. Both saturation magnetization ( $\sigma_s$ ) and intrinsic coercivity ( $H_{ci}$ ) are much lower than those of single crystal SrM and BaM ( $\sigma_s = 74.3$  emu/g and  $H_{ci} = 6700$  Oe for SrM;  $\sigma_s = 72$  emu/g and  $H_{ci} = 6000$  Oe for BaM) [34]. Furthermore, *Park et al.*, calculated 76 emu/g of the saturation magnetization at 300 K for SrM [35].

Recently, *Zhao, et al.* have synthesized well-dispersed quasi-spherical BaM particles using a precursor-directed method. The  $\sigma_s$  and  $H_{ci}$  of the BaM particles are 68.3 emu/g and 5342 Oe at 300 K [36], respectively. In this process, spherical Fe<sub>3</sub>O<sub>4</sub> particles

---

<sup>4</sup> This work was published as “Thermomagnetic Stability of M-type Strontium Ferrite (SrFe<sub>12</sub>O<sub>19</sub>) Particles with Different Shapes,” in *Electronic Materials Letters* **12**, 100 (2016) by Jihoon Park, Yang-Ki Hong, et al.

were synthesized by dissolving  $\text{FeCl}_3 \cdot 6\text{H}_2\text{O}$  in ethylene glycol (organic solvent) and autoclaving at 200 °C for 10 hours. Then, a mixture of  $\text{Fe}_3\text{O}_4$  and  $\text{BaCO}_3$  was pre-calcined at 400 °C for 4 hours and calcined again at 950 °C for 6 hours to convert the  $\text{Fe}_3\text{O}_4/\text{BaCO}_3$  to 0.33  $\mu\text{m}$  BaM particles. Spherical shaped BaM has been reported for magnetic properties and interaction of the particles for recording media applications [29,30]. However, thermomagnetic stability of peanut-like SrM particles and M-type hexamers are not yet reported.

In this paper, we used a benign water-based and low temperature precursor-directed method to synthesize peanut-like SrM particles and hexagonal SrM platelets. The shape of SrM particles was controlled by both size and shape of precursory  $\text{Fe}_3\text{O}_4$  particles. Static magnetic properties, interactions, and thermomagnetic stability are reported for both peanut-like SrM particles and hexagonal SrM platelets.

#### 4.2.2. Experimental

Two types of  $\text{Fe}_3\text{O}_4$  particles with different size and shape were prepared. One is submicron polyhedral particles, and the other is nanometer spherical particles.  $\text{SrCO}_3$  nanoparticles were prepared as the Sr source for the transformation of a mixture of  $\text{Fe}_3\text{O}_4$  and  $\text{SrCO}_3$  to SrM. First, we synthesized spherical  $\text{Fe}_3\text{O}_4$  nanoparticles by the following process.  $\text{FeCl}_2$  was dissolved in deionized (DI) water, namely solution *A*, and both KOH and  $\text{KNO}_3$  were dissolved in DI water, i.e. solution *B*. Solution *A* was dropped into solution *B* at a rate of 0.8 mL/min under  $\text{N}_2$  atmosphere, and the mixed solution was heated to 90 °C under  $\text{O}_2$  atmosphere. Consequently, iron oxide precipitates formed. The precipitates containing solution was cooled down to room temperature and washed with

DI water to remove residual cations and anions. This process is called *forced hydrolysis*. For the synthesis of submicron polyhedral Fe<sub>3</sub>O<sub>4</sub> particles, we used the same process as the one used for the nanometer spherical Fe<sub>3</sub>O<sub>4</sub> particles, but reversing the mixing order of *A* and *B*.

Next, SrCO<sub>3</sub> nanoparticles were synthesized by adding citric acid to Sr(NO<sub>3</sub>)<sub>2</sub> dissolved DI water at 70 °C. NH<sub>3</sub>·H<sub>2</sub>O was subsequently dropped into the Sr(NO<sub>3</sub>)<sub>2</sub> solution until the pH of the solution reached 7. The solution was maintained at 100 °C until the solution turned to black solid bulk. The black bulk was manually ground, and then annealed at 600 °C for 2 hours to obtain 50 nm white SrCO<sub>3</sub> particles. The synthesized SrCO<sub>3</sub> nanoparticles were rice-like shaped.

Lastly, a mixture of polyhedral or spherical Fe<sub>3</sub>O<sub>4</sub> particles and SrCO<sub>3</sub> particles was calcined at 900 °C for 4 hours in air, therefore, transforming to SrM particles. The calcined particles were subject to acid-washing to remove secondary oxide phase such as paramagnetic SrFe<sub>2</sub>O<sub>4</sub>.

Crystalline phases of Fe<sub>3</sub>O<sub>4</sub> and SrM particles were identified with x-ray diffraction (XRD). The particles were characterized by vibrating sample magnetometer (VSM) and physical property measurement system (PPMS) for magnetic properties. The particle size and size distribution were determined from transmission electron microscopy (TEM) and scanning electron microscope (SEM) images.

#### 4.2.3. Results and discussion

The results from the three studied subjects are discussed in this section. The first subject is about crystalline identification and morphology of the synthesized Fe<sub>3</sub>O<sub>4</sub> and

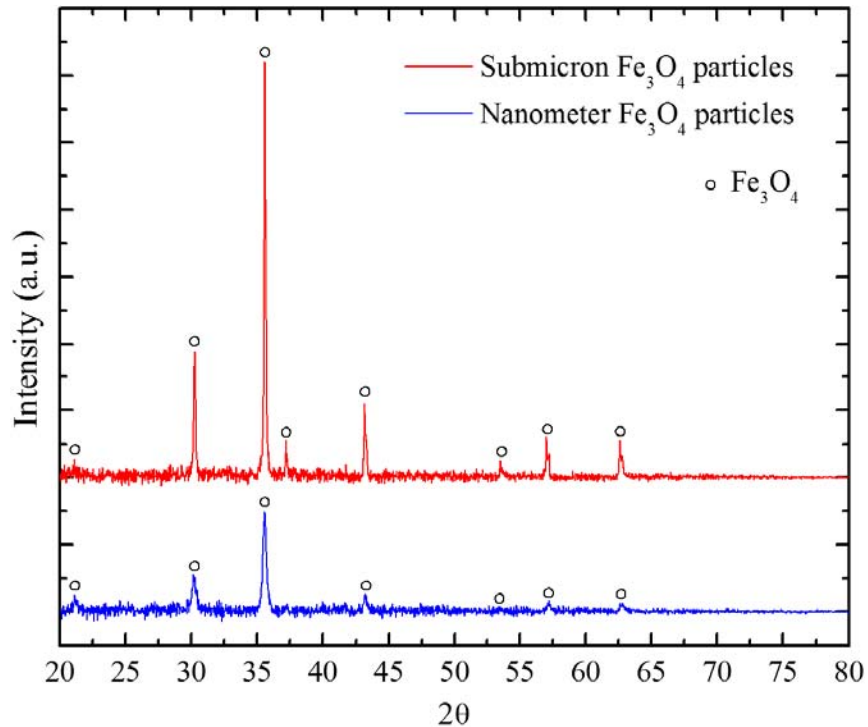


FIG. 4.2.1. XRD patterns of as-synthesized submicron polyhedral and nanometer spherical  $\text{Fe}_3\text{O}_4$  particles.

SrM particles. The second includes static magnetic properties and interactions for the two differently shaped SrM particles, i.e. peanut-like and hexagonal platelet. Lastly, thermomagnetic stability of the SrM particles is discussed.

Figure 4.2.1 shows XRD patterns for the two synthesized  $\text{Fe}_3\text{O}_4$  particles. All indexed XRD peaks correspond to  $\text{Fe}_3\text{O}_4$ . TEM and SEM images of submicron  $\text{Fe}_3\text{O}_4$  particles are shown in Fig. 4.2.2 (a) and (b), respectively, while those of nanometer  $\text{Fe}_3\text{O}_4$  particles are shown in Fig. 4.2.2 (c) and (d). The shape of  $\text{Fe}_3\text{O}_4$  particles in Fig. 4.2.2 (a) and (b) is polyhedral (370 nm in average diameter), and the particle shape in Fig. 4.2.2 (c) and (d) is spherical (50 nm in average diameter). As mentioned earlier, the order of solution preparation has a key role in determining the particle size and shape of  $\text{Fe}_2\text{O}_3$  particles. Fig. 4.2.3 shows XRD patterns for as-calcined and acid-washed SrM particles.

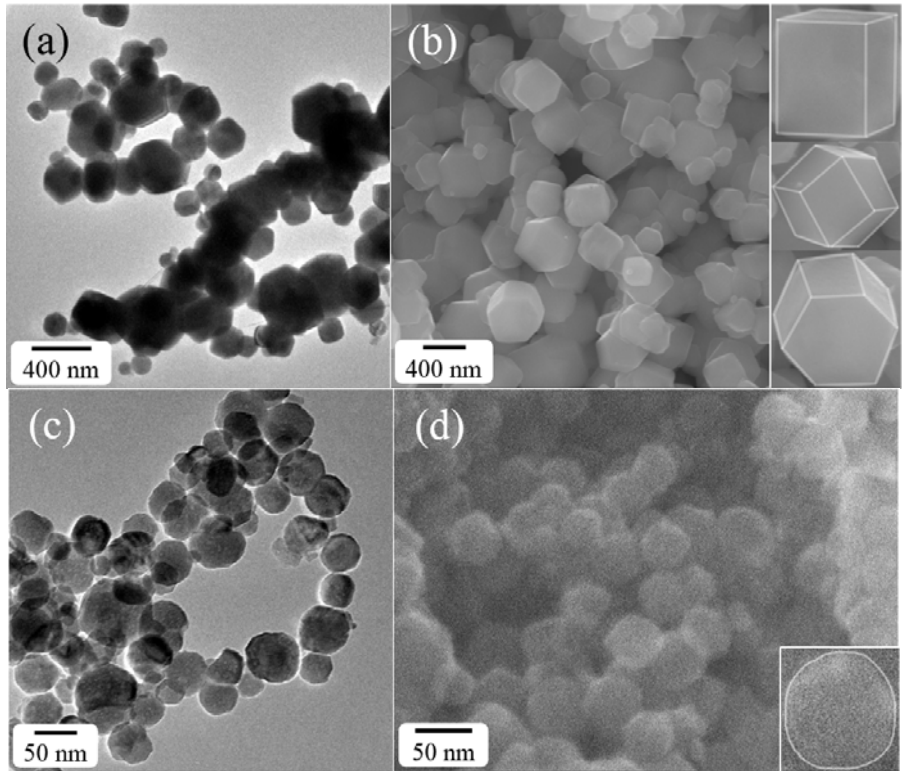


FIG. 4.2.2. (a) TEM and (b) SEM images of as-synthesized polyhedral  $\text{Fe}_3\text{O}_4$  particles (370 nm in average diameter) and (c) TEM and (d) SEM images of spherical  $\text{Fe}_3\text{O}_4$  particles (50 nm in average diameter). The insets in (b) and (d) show the shapes of polyhedral and spherical  $\text{Fe}_3\text{O}_4$  particles, respectively.

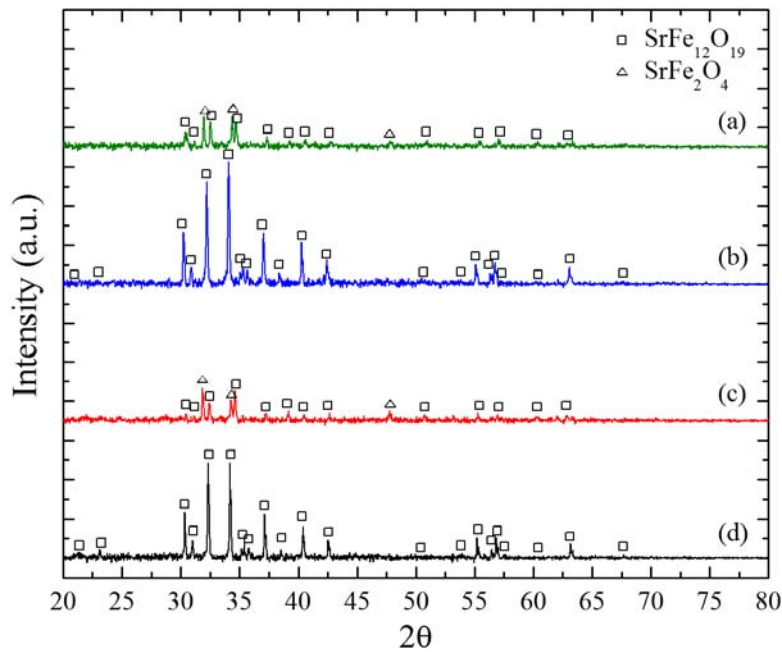


FIG. 4.2.3. XRD patterns for (a) as-calcined and (b) acid-washed peanut-like SrM particles, and for (c) as-calcined and (d) acid-washed hexagonal SrM platelets.

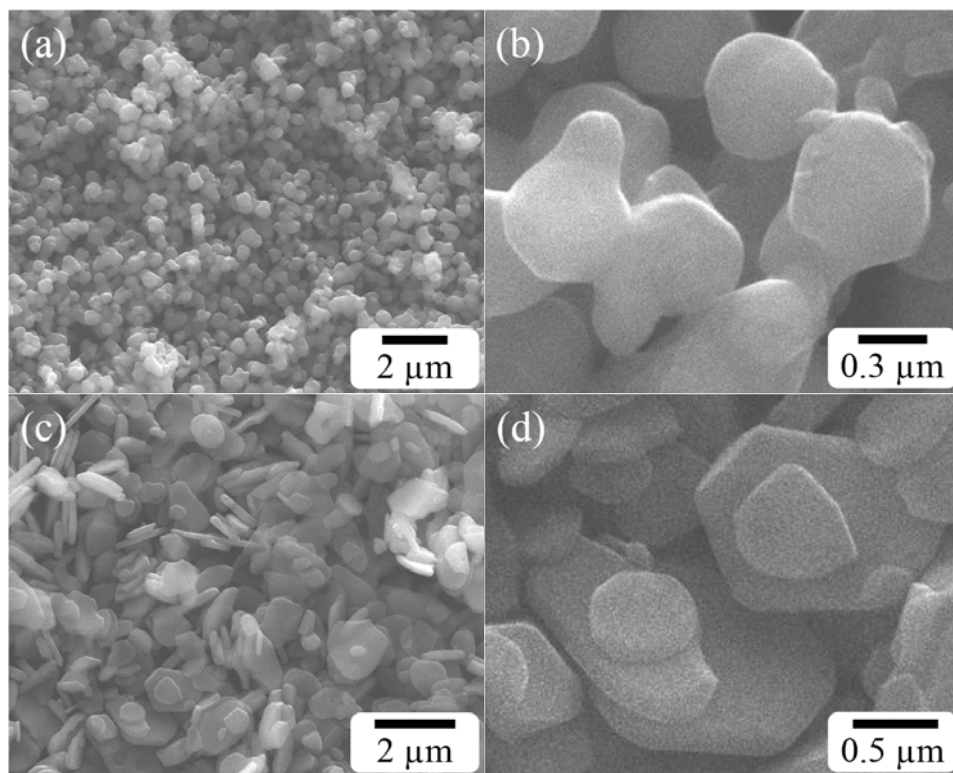


FIG. 4.2.4. SEM images of (a) and (b) for peanut-like SrM particles ( $0.45 \mu\text{m}$ ), and of (c) and (d) for hexagonal SrM platelets ( $1 \mu\text{m}$ ).

All XRD peaks correspond to SrM, including secondary phase of  $\text{SrFe}_2\text{O}_4$ . After acid-washing,  $\text{SrFe}_2\text{O}_4$  peaks disappear as shown in Fig. 4.2.3 (b) and (d). This indicates that acid-washed SrM is much purer than as-calcined one. Fig. 4.2.4 shows the particle size and morphology of the acid-washed peanut-like SrM particles and hexagonal SrM platelets. The average diameter of peanut-like SrM particles is  $0.45 \mu\text{m}$  and  $1.0 \mu\text{m}$  for hexagonal SrM platelets.

After calcining a mixture of polyhedral  $\text{Fe}_3\text{O}_4$  and  $\text{SrCO}_3$  particles, the original shape of  $\text{Fe}_3\text{O}_4$  seems to retain as shown in Fig. 4.2.4 (a) and (b). Even though the larger size  $\text{Fe}_3\text{O}_4$  ( $370 \text{ nm}$ ) was used in synthesis of peanut-like SrM particles, the resulted particle size ( $0.45 \mu\text{m}$ ) is smaller than hexagonal SrM platelets ( $1 \mu\text{m}$ ). Fig. 4.2.5 (a) and (b) show schematic illustrations for formation of peanut-like SrM particles and hexagonal

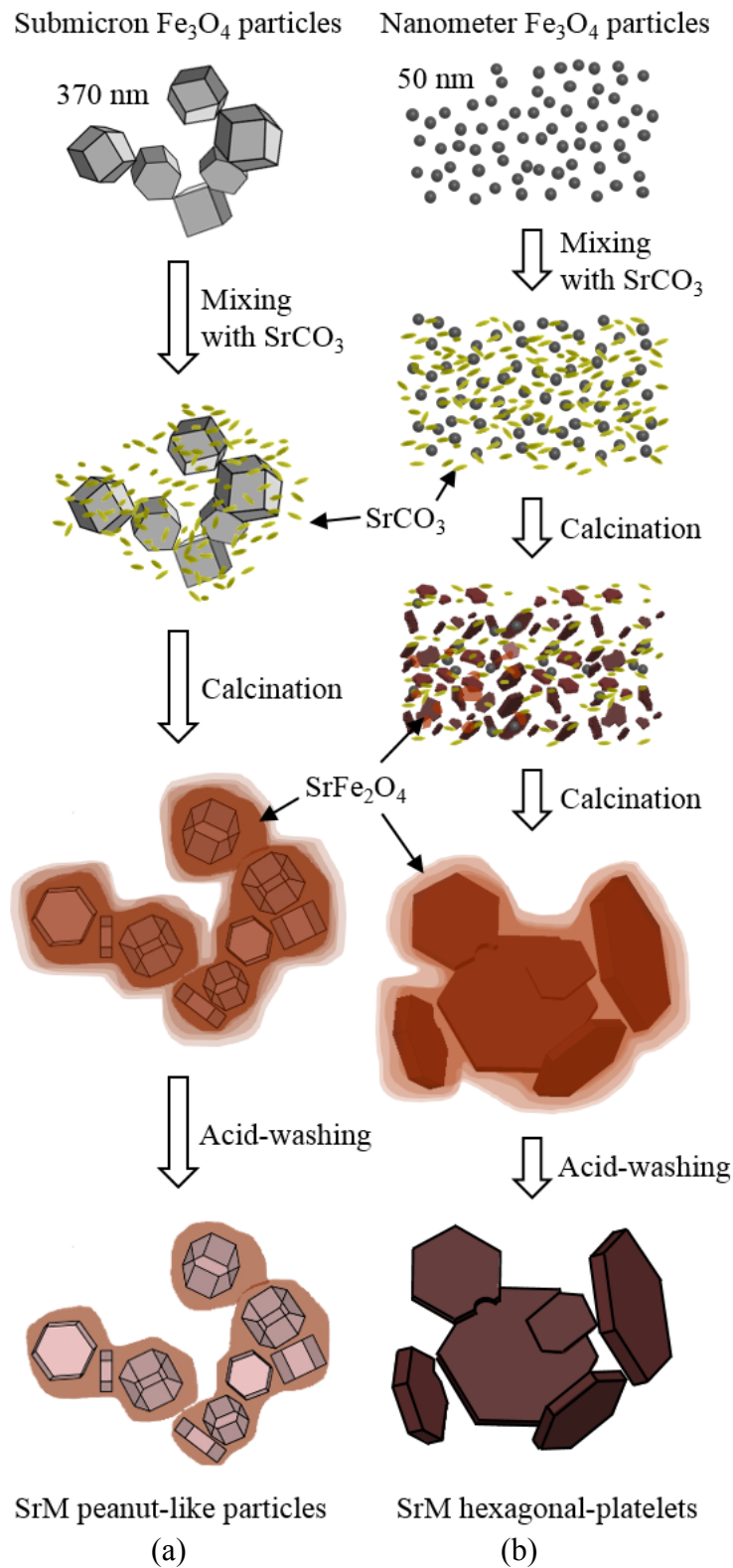


FIG. 4.2.5. Schematic illustrations for the formation of (a) peanut-like SrM particles ( $0.45 \mu\text{m}$  in average diameter) and (b) hexagonal SrM platelets ( $1.0 \mu\text{m}$  in average diameter).

SrM platelets. It is speculated that SrM nano-crystallites nucleate inside submicron  $\text{Fe}_3\text{O}_4$  particles and become sintered particles, namely peanut-like shape as shown in Fig. 4.2.5 (a). On the other hand, when 50 nm  $\text{Fe}_3\text{O}_4$  particles are used, Fe and Sr cations inter-diffuse and redistribute due to solid-state reaction between neighboring particles during the calcination, thereby crystallizing to SrM hexagonal platelets. It is noted that a low calcination temperature limits the inter-particle diffusions between SrM particles. Therefore, the secondary phase ( $\text{SrFe}_2\text{O}_4$ ) between SrM particles appears as a matrix to maintain the size and shape of both peanut-like SrM particles and hexagonal SrM platelets as shown in Fig. 4.2.5 (a) and (b).

Regarding static magnetic properties, Fig. 4.2.6 shows hysteresis loops before and

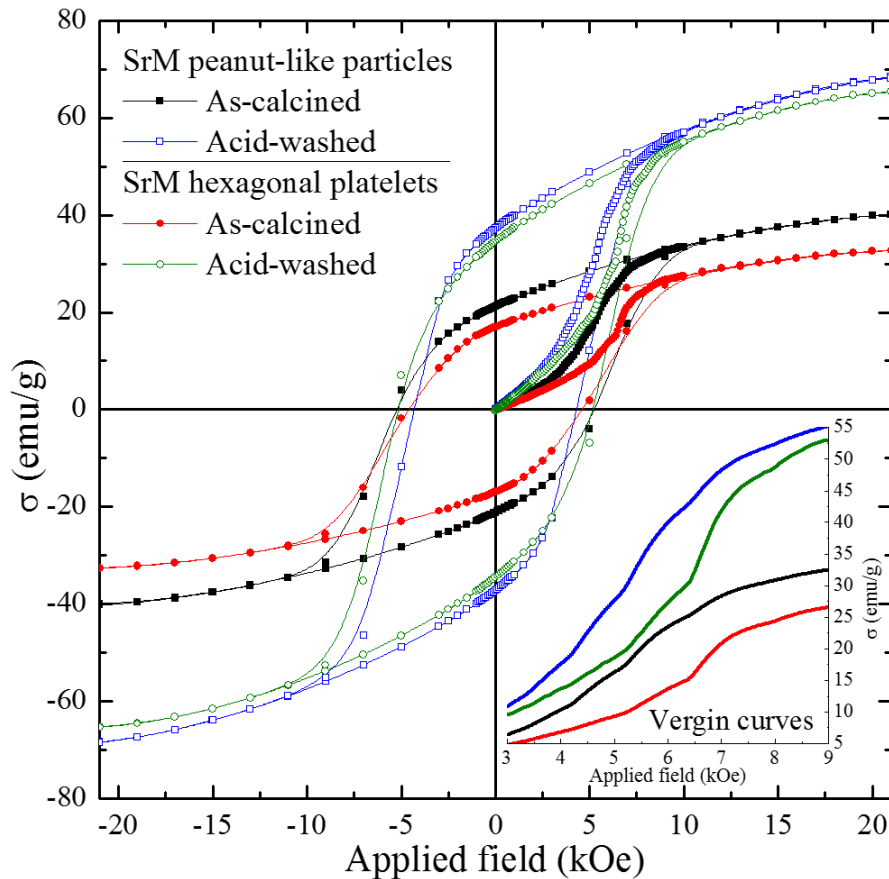


FIG. 4.2.6. Magnetic hysteresis loops and virgin curves of as-calcined and acid-washed peanut-like SrM particles and hexagonal SrM platelets at 300 K.

after acid-washing for both peanut-like SrM particles and hexagonal SrM platelets. As shown in Fig. 4.2.3, the secondary phase, paramagnetic SrFe<sub>2</sub>O<sub>4</sub>, disappeared after acid-washing. Therefore, the magnetization ( $\sigma$ ) at 21 kOe largely increased to 69 emu/g from 33 emu/g for peanut-like SrM particles, and to 65 emu/g from 40 emu/g for hexagonal SrM platelets. On the other hand, the  $H_{ci}$  slightly decreased to 4.3 kOe from 4.7 kOe for peanut-like SrM particles, and to 5.3 kOe from 5.4 kOe for hexagonal SrM platelets. This is attributed to an absence of the paramagnetic phase SrFe<sub>2</sub>O<sub>4</sub> in SrM powder. The shape of hysteresis loops indicates that the SrM particles follow the Stoner-Wolfarth magnetization reversal process [3]. This means that the SrM particles have single magnetic domain and uniaxial anisotropy, and are randomly oriented. However, it is noted that virgin curves of the hysteresis loops in Fig. 4.2.6 shows kinks. This implies that magnetic switching field distribution (SFD) is broad, therefore, implying a wide  $H_{ci}$  distribution for SrM powder. This is confirmed by the Henkel plot, which is presented below.

In general, magnetic particles are strongly agglomerated. Therefore, we have measured delta  $M$  ( $\Delta M$ ) curves (Henkel plot) for both peanut-like SrM particles and hexagonal SrM platelets to understand coercivity distribution and magnetic interaction. The  $\Delta M$  curve is defined as the difference of two zero-field remanence curves [37]:  $\Delta M(H) = 2IRM(H)/IRM(\infty) + DCD(H)/DCD(\infty) - 1$ , where  $IRM$  is the isothermal remanent magnetization,  $DCD$  is the dc demagnetization curve, and  $H$  is the applied magnetic field. A positive value of  $\Delta M$  implies exchange interactions, while the negative value is due to dipolar interactions. Fig. 4.2.7 shows measured  $\Delta M$  curves. A peak position in  $\Delta M$  curve corresponds to remanent coercivity. Multiple negative peaks are

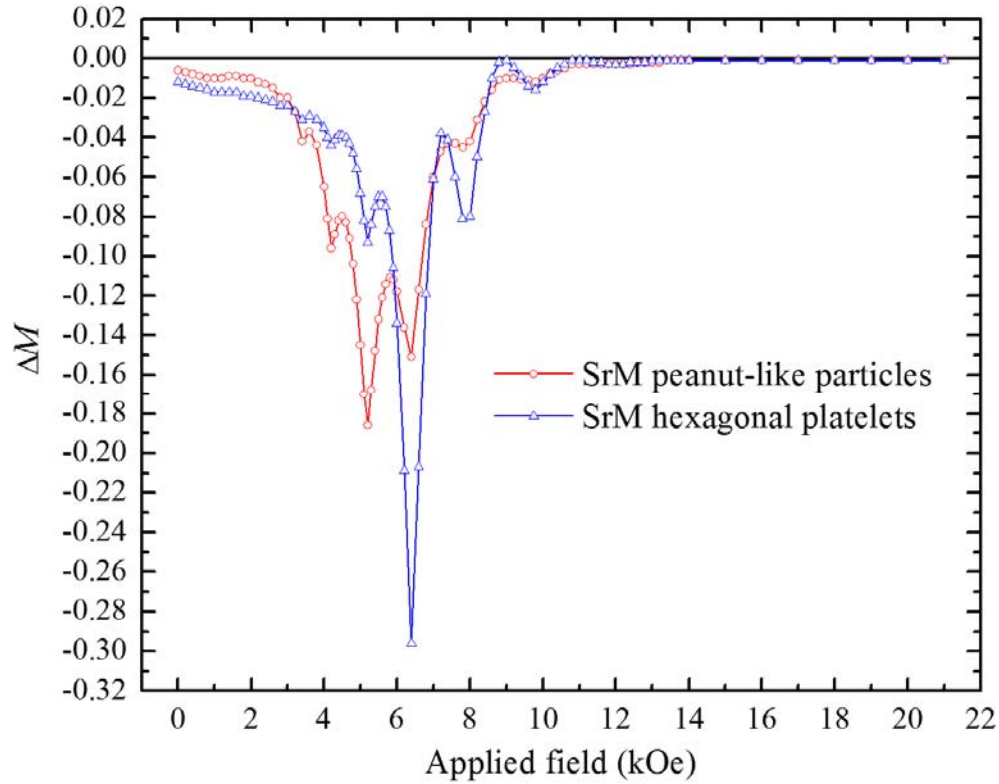


FIG. 4.2.7. Delta M curves derived for peanut-like SrM particles and hexagonal SrM platelets.

observed in the  $\Delta M$  curves, indicating that there are dipolar interactions between the particles, and multiple coercivities exist in both SrM powders. It is noted that peanut-like SrM particles show a broader coercivity distribution than hexagonal SrM platelets. A major remanent coercivity of the peanut-like SrM particles appears at a lower magnetic field, i.e. 5.2 kOe, and its distribution is wider than hexagonal SrM platelets (6.4 kOe), therefore, wider SFD for peanut-like SrM particles than hexagonal SrM platelets. This is because a peanut-like SrM particle contains several randomly oriented SrM nanocrystallites, as illustrated in Fig. 4.2.5 (a). The SrM nanocrystallites seem not to have the same coercivity, leading to a large SFD. This is in good agreement with the hysteresis loops in Fig. 4.2.6.

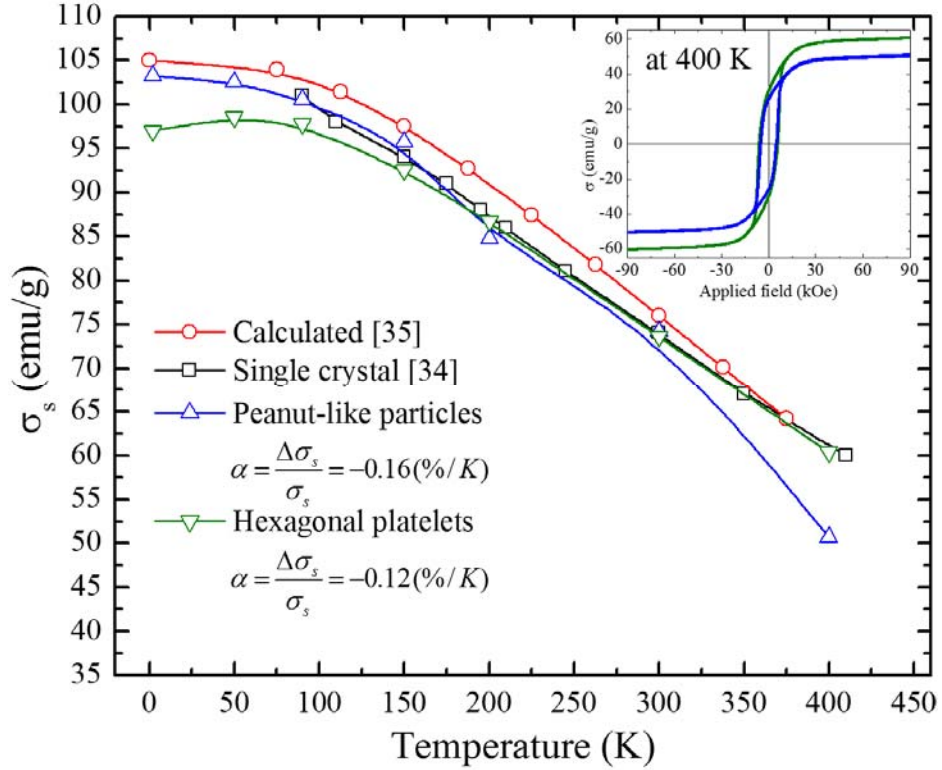


FIG. 4.2.8. Temperature dependence of saturation magnetization measured for peanut-like SrM particles and hexagonal SrM hexagonal platelets. The inset represents magnetic hysteresis loops at 400 K.

Lastly, thermomagnetic stability of the two differently shaped SrM particles will be discussed. Magnetic hysteresis loops at various temperatures were obtained with the maximum applied field of 9 T. Fig. 4.2.8 shows temperature dependence of saturation magnetization, i.e.  $\sigma_s(T)$ , for peanut-like SrM particles, hexagonal SrM platelets and SrM single crystal [34], including calculated result [35]. The  $\sigma_s$  of peanut-like SrM particles and hexagonal SrM platelets at 300 K are 74.2 and 73.6 emu/g, respectively. These values are close to the theoretical  $\sigma_s$  of 76 emu/g at 300 K [35]. Therefore, both peanut-like SrM particles and hexagonal SrM platelets seem to be close to pure SrM. However, it is noted that the  $\sigma_s$  at 2 K is 97.0 emu/g for hexagonal SrM platelet, which is smaller than  $\sigma_s$  (98.6 emu/g) at 50 K. This is an experimental error because the magnetization must decrease

with increasing temperature due to thermal agitation of ordered spins. The  $\sigma_s(T)$  of peanut-like SrM particles and hexagonal SrM platelets are in good agreement with the calculated and experimental  $\sigma_s(T)$  of SrM single crystal. This indicates that after acid-washing of as-calcined SrM particles, its purity increased as confirmed by x-ray patterns in Fig. 4.2.3. It is worth noting that  $\sigma_s$  still remains high even at 400 K; 60 emu/g for hexagonal SrM platelets and 50 emu/g for peanut-like SrM particles.

Thermomagnetic stability can be explained by the temperature coefficient of magnetization and intrinsic coercivity, i.e.  $\alpha = \Delta\sigma_s/\sigma_s$  and  $\beta = \Delta H_{ci}/H_{ci}$ . We took a slope of  $\sigma_s(T)$  or  $H_{ci}(T)$  curve to calculate  $\alpha$  or  $\beta$ . The  $\alpha$  is -0.16 %/K for peanut-like SrM particles, and is -0.12 %/K for hexagonal SrM platelets. Therefore, the hexagonal SrM platelets are more thermally stable than peanut-like SrM particles. Also, this is in good agreement with

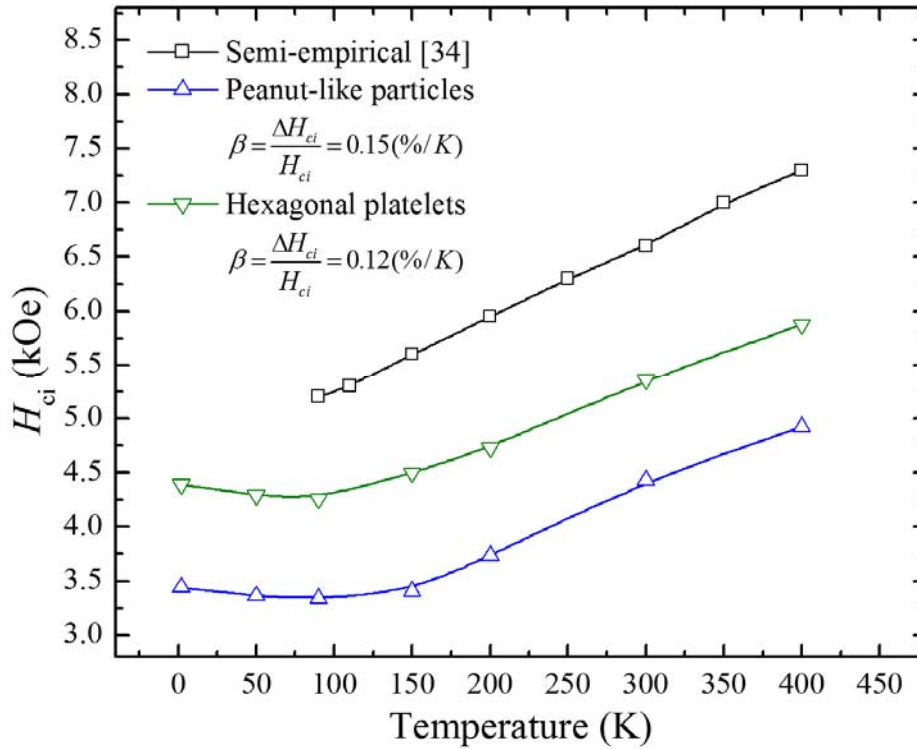


FIG. 4.2.9. Temperature dependence of intrinsic coercivity measured for peanut-like SrM particles and hexagonal SrM platelets.

that the hexagonal SrM platelets retain 60 emu/g at 400 K, but 50 emu/g for peanut-like SrM particles.

The other thermomagnetic stability of magnetic particles can be explained by the temperature dependence of intrinsic coercivity, i.e.  $H_{ci}(T)$ . Fig. 4.2.9 shows the temperature dependence of coercivity for peanut-like SrM particles, hexagonal SrM platelets, and SrM single crystal [34]. The  $H_{ci}(T)$  of SrM single crystal was semi-empirically calculated. All coercivities increase with temperature from 75 K to 400 K, showing positive temperature coefficients of coercivity. The  $H_{ci}$  of hexagonal SrM platelets is higher than that of peanut-like SrM particles at all measured temperatures. The  $\beta$  is 0.15 %/K for peanut-like SrM particles and 0.12 %/K for hexagonal SrM platelets. Therefore, the hexagonal SrM platelets are more stable than peanut-like SrM particles. Thermomagnetic stability for both SrM is summarized in Table 4.2.1.

Table 4.2.1. Thermomagnetic stability for peanut-like SrM particles and hexagonal SrM platelets.

Thermomagnetic stability	Peanut-like SrM particles	Hexagonal SrM platelets
$\alpha = \Delta\sigma_s/\sigma_s$ (%/K)	-0.16	-0.12
$\beta = \Delta H_{ci}/H_{ci}$ (%/K)	0.15	0.12

#### 4.2.4. Conclusions

Magnetizations at 21 kOe for both peanut-like SrM particles and hexagonal SrM platelets are close to the theoretical value at 300 K. The saturation magnetizations at 300 K are 74.2 emu/g for the peanut-like SrM particles and 73.6 emu/g for the hexagonal

SrM platelets, while intrinsic coercivities of the hexagonal SrM platelets (5.36 kOe) are higher than that of the peanut-like SrM particles (4.43 kOe).

The temperature coefficient of intrinsic coercivity ( $\beta = \Delta H_{ci}/H_{ci}$ ) is positive for both types of SrM. The  $\beta$  of the peanut-like SrM particles is 0.15 %/K and that of the hexagonal SrM platelets is 0.12 %/K. Both SrM particles exhibit good thermomagnetic stability up to 400 K.

#### 4.2.5. References

1. W. Zhong, W. Ding, N. Zhang, J. M. Hong, Q. J. Yan, and Y. W. Du, *J. Magn. Magn. Mater.* **168**, 196 (1997).
2. K. Haneda and H. Kojima, *J. Amer. Ceram. Soc.* **57**, 68 (1974).
3. E. C. Stoner and E. P. Wohlfarth, *Phil. Trans. Roy. Soc. London A* **240**, 599 (1948).
4. T. T. V. Nga, T. D. Hien, N. P. Duong, and T. D. Hoang, *J. Kor. Phys. Soc.* **52**, 1474 (2008).
5. W. Zhong, W. Ding, Y. Jiang, N. Zhang, J. Zhang, Y. Du, and Q. Yan, *J. Am. Ceram. Soc.* **80**, 3258 (1997).
6. C. Surig, K. A. Hempel, and C. Sauer, *J. Magn. Magn. Mater.* **157**, 268 (1996).
7. E. Paimozd, A. Ghasemi, A. Jafari, and H. Sheikh, *J. Magn. Magn. Mater.* **320**, L137 (2008).
8. R. C. Pullar, M. H. Stacey, M. D. Taylor, and A. K. Bhattacharya, *Acta. Mater.* **49**, 4241 (2001).
9. A. Mali and A. Ataie, *J. Alloys Compd.* **399**, 245 (2005).
10. C. H. Lin, Z. W. Shih, T. S. Chin, M. L. Wang, and Y. C. Yu, *IEEE Trans. Magn.* **26**, 15 (1990).
11. X. Liu, J. Wang, L. M. Gan, and S. C. Ng, *J. Magn. Magn. Mater.* **195**, 452 (1999).
12. A. Ataie, I. R. Harris, and C. B. Ponton., *J. Mater. Sci.* **30**, 1429 (1995).
13. M. L. Wang, Z. W. Shih, and C. H. Lin, *J. Cryst. Growth.* **114**, 435 (1991).

14. D. Barb, L. Diamandescu, A. Rusi, D. Tarabasanu-Mihaila, M. Morariu, and V. Teodorescu. *J. Mater. Sci.* **21**, 1118 (1986).
15. M. Jean, V. Nachbaur, J. Bran, and J. M. Breton, *J. All. Comp.* **496**, 306 (2010).
16. M. Drofenik, M. Kristl, A. Znidarsic, D. Hanzel and D. Lisjak, *J. Am. Ceram. Soc.* **90**, 2057 (2007).
17. W. Roos, *J. Am. Ceram. Soc.* **63**, 601 (1980).
18. M. M. Hessien, M. M. Rashad, M. S. Hassan, and K. El-Barawy, *J. Alloys Compd.* **476**, 373 (2009).
19. M. M. Rashad and I. A. Ibrahim, *J. Magn. Magn. Mater.* **323**, 2158 (2011).
20. E. V. Pashkova, E. D. Solovyova, I. E. Kotenko, T. V. Kolodiazhnyl, A. G. Belous. *J. Magn. Magn. Mater.* **323**, 2497 (2011).
21. D. Lisjak and M. Drofenik, *J. Euro. Ceram. Soc.* **26**, 3681 (2006).
22. D. Lisjak and M. Drofenik, *J. Mater. Sci.* **42**, 8606 (2007).
23. M. M. Rashad, M. Radwan and M. M. Hessien, *J. Alloys Compd.*, 453 (2008) 304.
24. H. F. Lu, R. Y. Hong, H. Z. Li, *J. Alloys Compd.* **509**, 10127 (2011).
25. J. Fang, J. Wang, L. M. Gan, S. C. Ng, J. Ding, and X. Liu, *J. Am. Ceram. Soc.* **83**, 1049 (2000).
26. D. A. Rawlinson and P. A. Sermon. *J. Phys. IV* **7**, C1–755 (1997).
27. X. Liu, J. Wang, L. M. Gan, S. C. Ng and J. Ding, *J. Magn. Magn. Mater.* **184**, 344 (1998).
28. G. H. An, T. Y. Hwang, Y. H. Choa, and K. Shin, *J. Elec. Mater.* **43**, 3574 (2014).
29. Y. K. Hong and H. S. Jung, *J. Appl. Phys.* **85**, 5549 (1999).
30. Y. K. Hong and M. H. Park, *IEEE Trans. Magn.* **36**, 3863 (2000).
31. S. H. Gee, Y. K. Hong, F. J. Jeffers, M. H. Park, S. C. Sur, C. Weatherspoon, and I. T. Nam, *IEEE Trans. Magn.* **41**, 4353 (2005).
32. J. Jalli, Y. K. Hong, S. Bae, G. Abo, J. J. Lee, J. C. Sur, S. H. Gee, S. G. Kim, S. Erwin, and A. Moitra, *IEEE Trans. Magn.* **45**, 3590 (2009).
33. J. Jalli, Y. K. Hong, J. J. Lee, G. Abo, J. H. Park, A. Lane, S. G. Kim, and S. Erwin, *IEEE Magn. Lett.* **1**, 4500204 (2010).

34. B. T. Shirk and W. R. Buessem, *J. Appl. Phys.* **40**, 1294 (1969).
35. J. H. Park, Y. K. Hong, S. G. Kim, S. H. Kim, L. Liyanage, J. J. Lee, W. C. Lee, G. Abo, K. H. Hur, and S. Y. An, *J. Magn. Magn. Mater.* **355**, 1 (2014).
36. H. Zhao, Y. Du, L. Kang, P. Xu, L. Du, Z. Sun, and X. Han, *Cryst. Eng. Comm.* **15**, 808 (2013).
37. P. E. Kelly, K. O'Grady, P. I. Mayo, and R. W. Chantrell, *IEEE Trans. Magn.* **25**, 3881 (1989).

### 4.3 Coercivity of strontium ferrite platelets near single domain size<sup>5</sup>

#### 4.3.1. Introduction

The systematic study of intrinsic coercivity ( $H_{ci}$ ) behavior of M-type hexaferrite ( $\text{BaFe}_{12}\text{O}_{19}$ : BaM or  $\text{SrFe}_{12}\text{O}_{19}$ : SrM) platelets near the single domain size ( $D_{SD}$ ) is still lacking [1], but over the range between 1.0 and 10  $\mu\text{m}$ . This size range is far from the  $D_{SD}$ . In order to complete the size dependence of coercivity behavior near the  $D_{SD}$ , we have synthesized M-type hexaferrite platelets with various diameters from 0.64 to 0.99  $\mu\text{m}$  by firing a mixture of acicular goethite ( $\alpha\text{-FeOOH}$ ) and  $\text{SrCO}_3$  particles at 900 °C in air. The platelet size was controlled by the molar ratio of  $\alpha\text{-FeOOH}$  to  $\text{SrCO}_3$ , and secondary phases were removed by acid (HCl) washing. The synthetic process will be published elsewhere.

#### 4.3.2. Results and discussion

Fig. 4.3.1 shows x-ray diffraction (XRD) patterns for  $\text{SrFe}_{12}\text{O}_{19}$  (SrM) platelets with various molar ratios. All XRD peaks correspond to SrM. The corresponding scanning electron microscope (SEM) images and histograms of SrM platelets are presented in Fig. 4.3.2. It is found that the average diameter ( $D$ ) increases from 0.65 to 0.92  $\mu\text{m}$  as the iron (Fe) to strontium (Sr) molar ratio (Fe/Sr) increases from 6 to 10.

Fig. 4.3.3 shows the molar ratio dependence of diameter ( $D$ ) and thickness ( $t$ ). It is noted that both the  $D$  and  $t$  linearly increase with the molar ratio by following Eq. (1):

$$D = 0.06465x + 0.28204 \text{ and } t = 0.03586x - 0.05078, \quad (4.3.1)$$

where  $x$  is the Fe/Sr molar ratio.

---

<sup>5</sup> This work was published as “Coercivity of  $\text{SrFe}_{12}\text{O}_{19}$  Hexaferrite Platelets Near Single Domain Size,” in *IEEE Magnetics Letters* **6**, 5500203 (2016) by Jihoon Park, Yang-Ki Hong, et al.

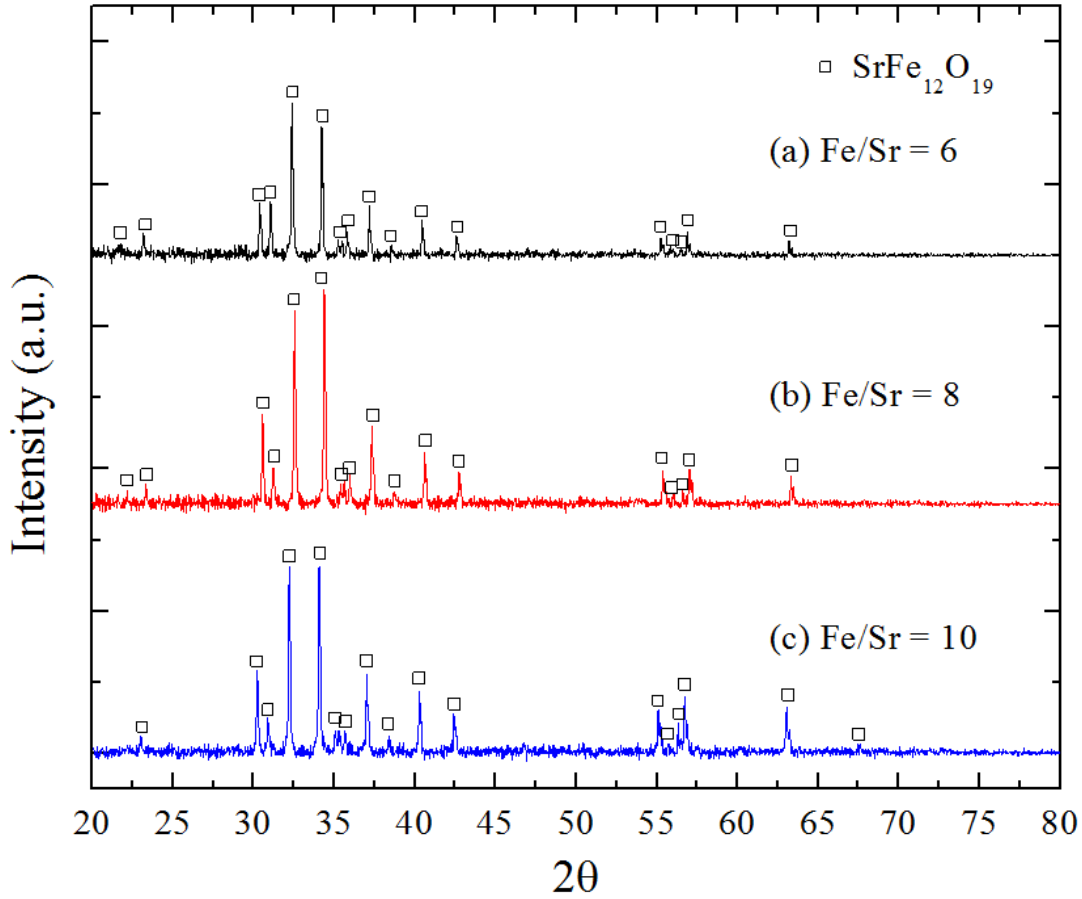


FIG. 4.3.1. XRD patterns of the SrM particles for Fe/Sr = (a) 6, (b) 8, and (c) 10.

We have measured the  $H_{ci}$  and  $\sigma$  of randomly oriented SrM platelets at 300 K. Fig. 4.3.4 shows magnetic hysteresis loops for SrM platelets with various  $D$ , and the inset shows the corresponding second quadrant of the loop to distinguish  $H_{ci}$ . The  $H_{ci}$  and  $\sigma$  are plotted as a function of  $D$  in Fig. 4.3.5 using the experimental data summarized in Table 4.3.1. The magnetization,  $\sigma$ , slightly decreases with increasing the  $D$ , while the intrinsic coercivity,  $H_{ci}$ , shows its maximum at  $\sim 0.83 \mu\text{m}$ . This diameter is a little larger than the theoretical  $0.74 \mu\text{m}$  ( $2R_{SD}$ ) of spherical SrM particles ( $R_{SD}$  = radius of single domain particle), which was calculated by Eq. (2) [2].

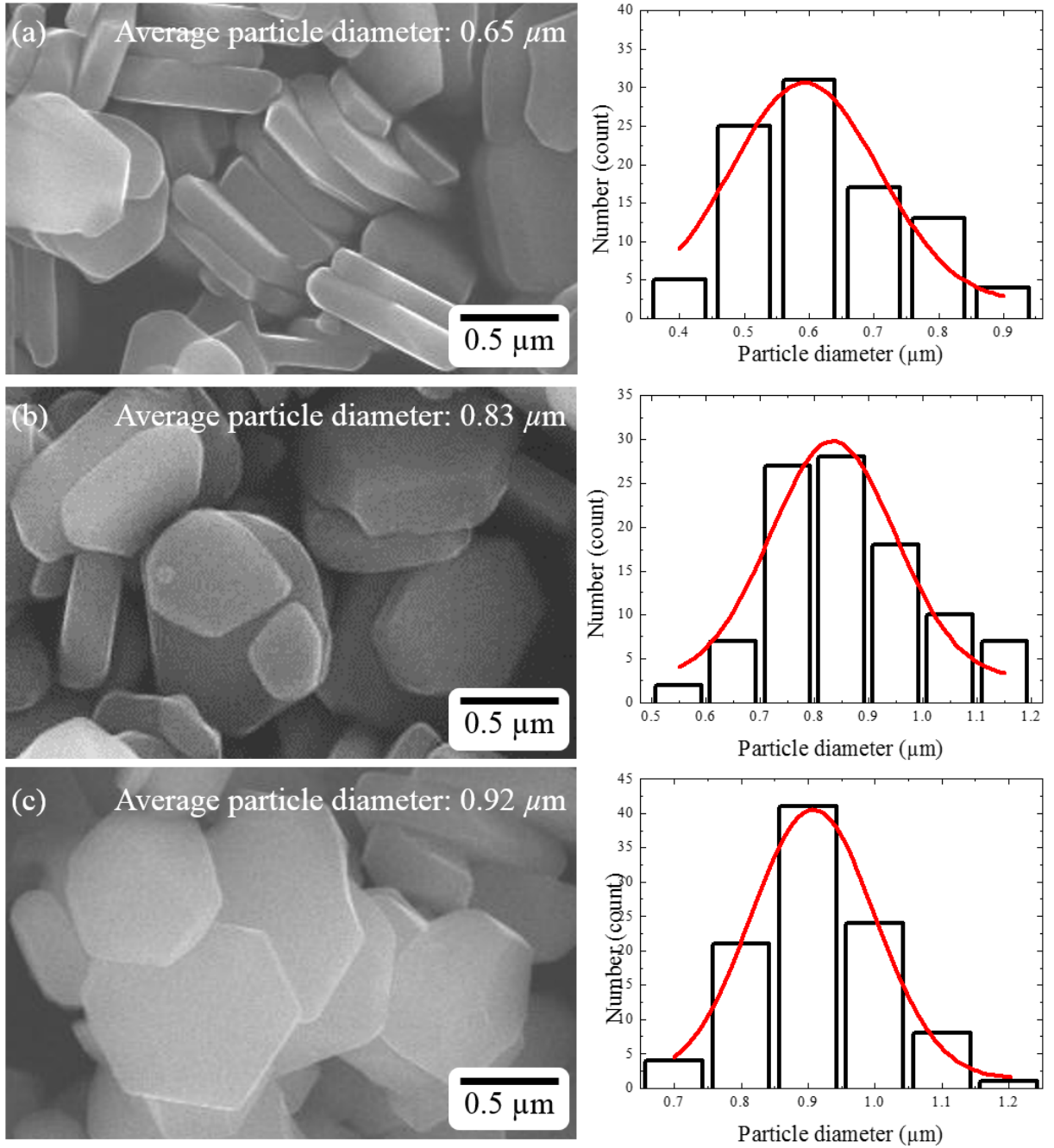


FIG. 4.3.2. SEM images and histograms of the SrM particles for Fe/Sr = (a) 6, (b) 8, and (c) 10.

$$R_{SD} = \frac{36\sqrt{AK}}{\mu_0 M_s^2}, \quad (4.3.2)$$

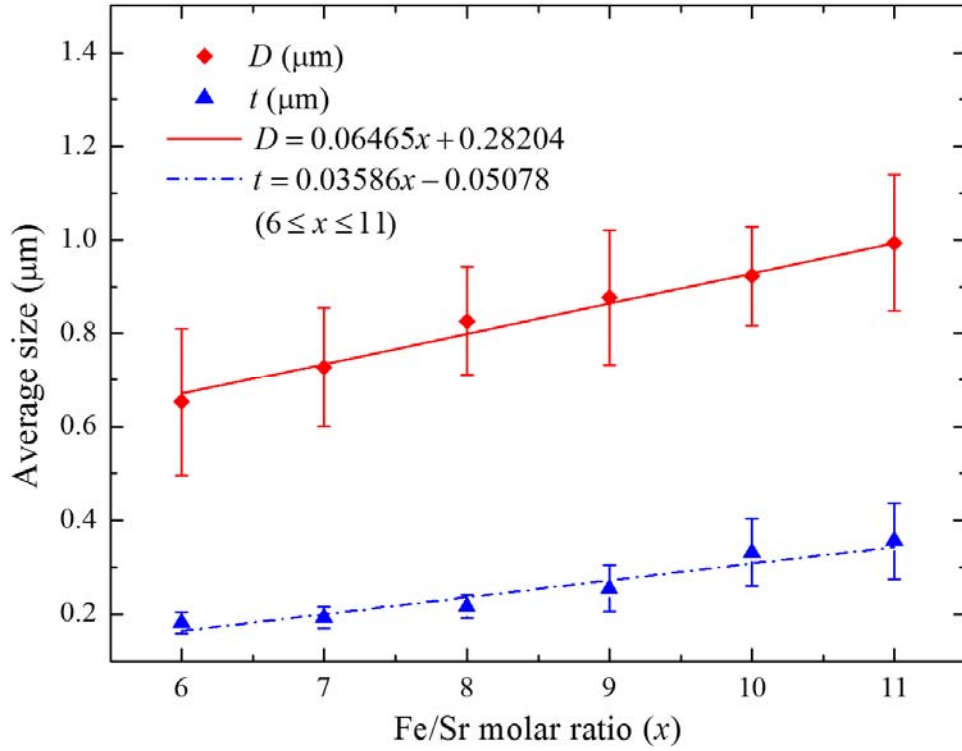


FIG. 4.3.3. The Fe/Sr molar ratio ( $x$ ) dependence of average diameter ( $D$ ) and thickness ( $t$ ) for the SrM platelets.

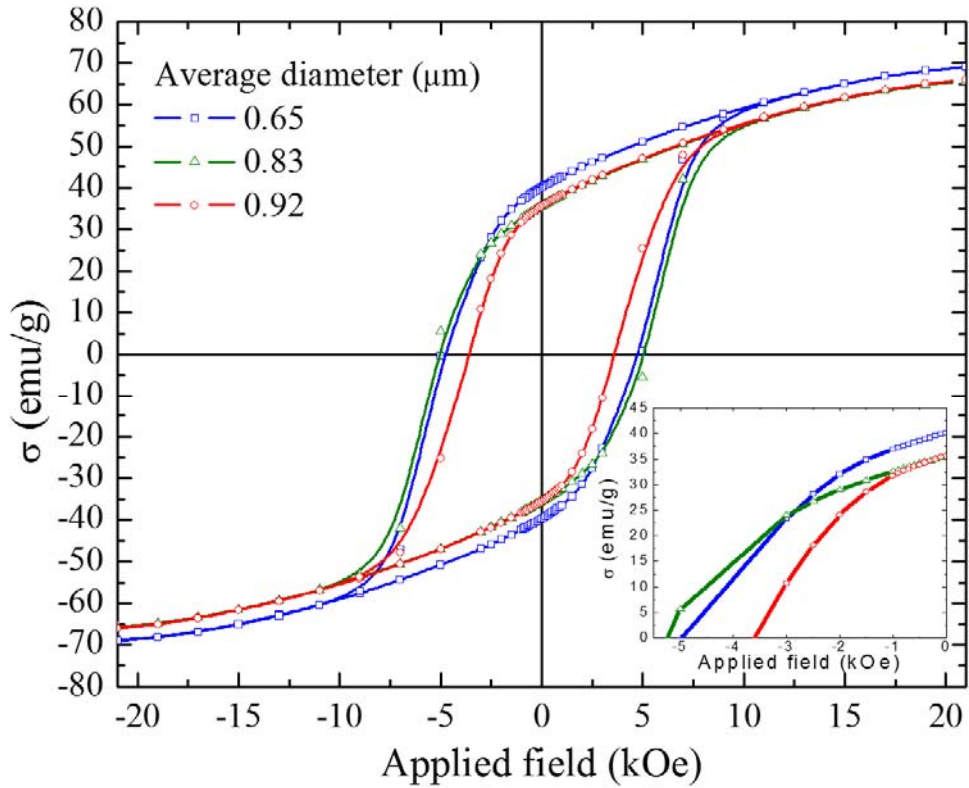


FIG. 4.3.4. Magnetic hysteresis loops for the SrM platelets with various sizes.

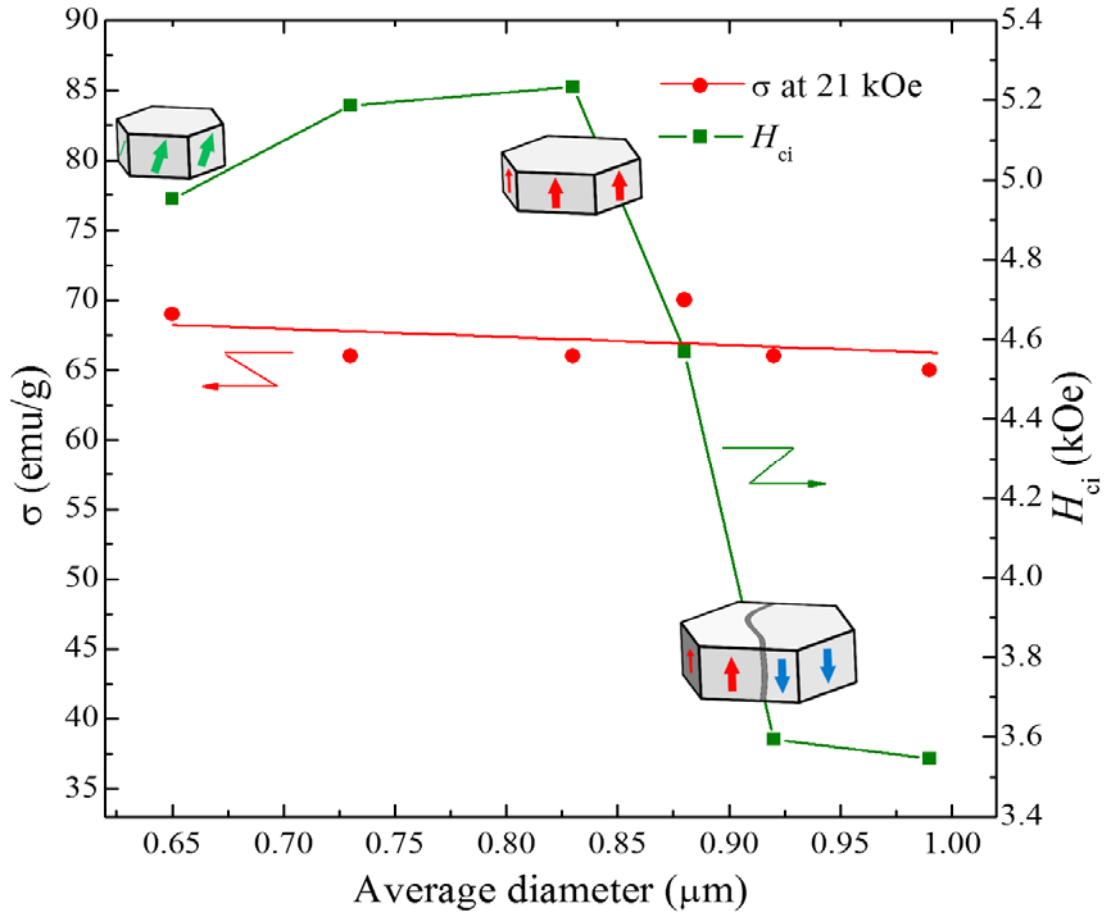


FIG. 4.3.5. The average diameter dependence of magnetization ( $\sigma$ ) at 21 kOe and intrinsic coercivity ( $H_{ci}$ ) of SrM platelets.

Table 4.3.1. The detailed values of Fe/Sr molar ratio dependence of average diameter ( $D$ ) of SrM platelets, and corresponding magnetization ( $\sigma$ ) at 21 kOe and intrinsic coercivity ( $H_{ci}$ ).

Fe/Sr	$D$ ( $\mu\text{m}$ )	$\sigma$ at 21 kOe (emu/g)	$H_{ci}$ (Oe)
6	$0.65 \pm 0.15$	69	4953
7	$0.73 \pm 0.12$	66	5186
8	$0.83 \pm 0.11$	66	5234
9	$0.88 \pm 0.14$	70	4570
10	$0.92 \pm 0.10$	66	3594
11	$0.99 \pm 0.14$	65	3546

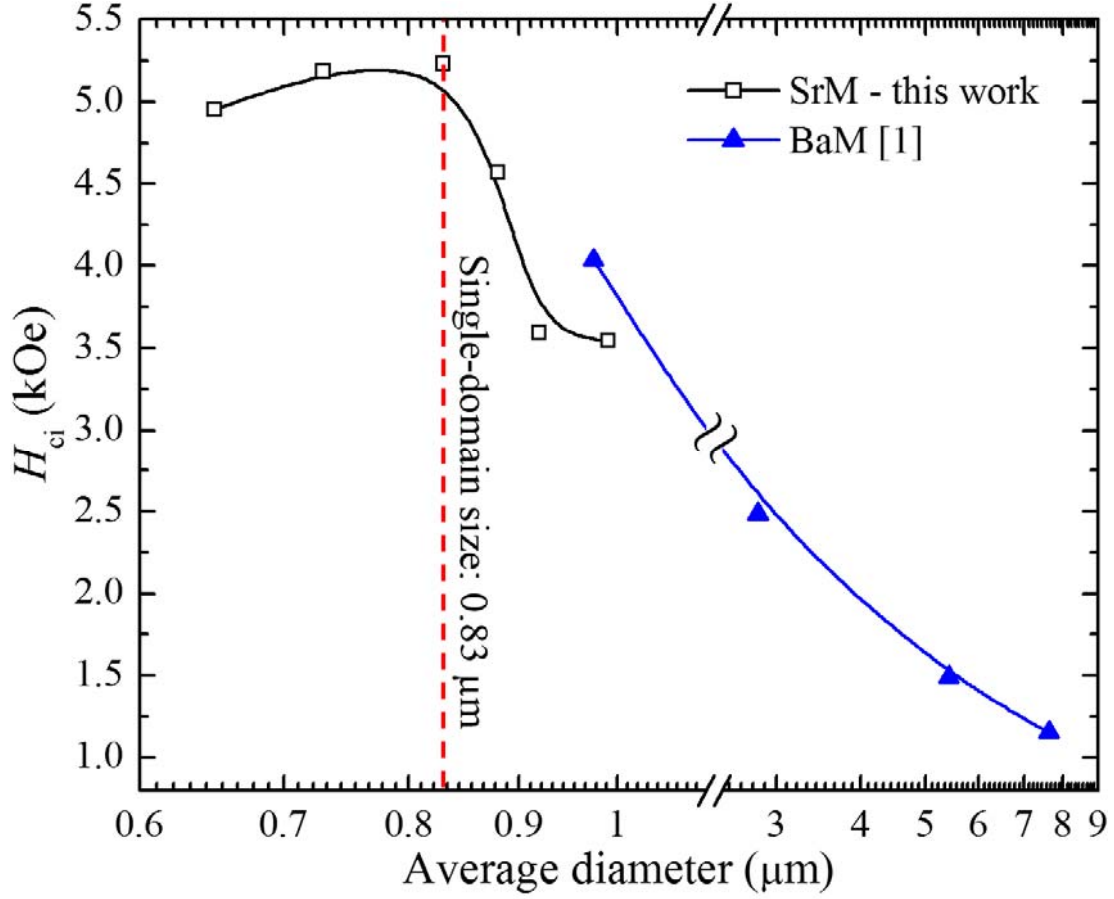


FIG. 4.3.6. The average diameter dependence of intrinsic coercivity ( $H_{ci}$ ) for hexagonal SrM platelets (this work) and hexagonal BaM platelets [1].

where  $A$  is the exchange constant,  $K$  is the effective anisotropy constant,  $\mu_0$  is the permeability of free space, and  $M_s$  is the saturation magnetization in  $\text{emu}/\text{cm}^3$  unit. We used  $0.61 \times 10^{-6}$  erg/cm of  $A$  [3],  $3.57 \times 10^6$  erg/cm<sup>3</sup> of  $K$  [4], and  $337$   $\text{emu}/\text{cm}^3$  ( $= 66$   $\text{emu}/\text{g}$ ) of  $M_s$  to calculate  $R_{SD}$  of  $0.37$   $\mu\text{m}$  ( $D_{SD} = 0.74$   $\mu\text{m}$ ). This  $H_{ci}$  difference between the platelet and spherical particles is consistent with the micromagnetic simulation results for hexagonally and spherically shaped hexaferrite single domain particles [5]. The single domain size ( $D_{SD}$ ) has been observed over the range of  $0.5$  to  $1.0$   $\mu\text{m}$  [6-11]. Therefore, our measured  $0.83$   $\mu\text{m}$  of the  $D_{SD}$  is in close agreement with the previously observed size.

We have extended the previous coercivity-to-size plot [1] to the single domain size and below by using the  $H_{ci}$  values in Table 4.3.1, and show the plot over the range of 0.65 to 8  $\mu\text{m}$  in Fig. 4.3.6. The  $H_{ci}$  above 0.83  $\mu\text{m}$  of the  $D_{SD}$  decreases as the particle size increases. This is attributed to domain wall motion of multi-domain particle.

#### 4.3.3 Conclusions

We have extended the size dependence of intrinsic coercivity,  $H_{ci}$ , of M-type hexaferrite platelets of Fig. 11.1 [1] to the single domain size and below. The single domain size of strontium hexaferrite ( $\text{SrFe}_{12}\text{O}_{19}$ ) platelet was experimentally determined and is in close agreement with the theoretical one.

#### 4.3.4. References

1. B. D. Cullity and C. D. Graham, Introduction to Magnetic Materials, Second Edition (Wiley, New Jersey, 2009), p. 361
2. D. Sellmyer and R. Skomski, Advanced Magnetic Nanostructures (Springer; 2006 edition).
3. Y. Liu, D. J. Sellmyer, and D. Shindo, Handbook of Advanced Magnetic Materials: Vol 1. Nanostructural Effects (Springer; 2006 edition).
4. B. T. Shirk and W. R. Buessem, *J. Appl. Phys.* **40**, 1294 (1969).
5. G. S. Abo, Y. K. Hong, J. Jalli, J. J. Lee, J. H. Park, S. Bae, S. G. Kim, B. C. Choi, and T. Tanaka, *J. Magn.* **17**, 1 (2012).
6. O. Kitakami, K. Goto, and T. Sakurai, *Jpn. J. Appl. Phys.* **27**, 2274 (1988).
7. R. Nawathery-Dikshit, S. R. Shinde, S. B. Ogale, S. D. Kulkarni, S. R. Sainkar, and S. K. Date, *Appl. Phys. Lett.* **68**, 3491 (1996).
8. L. K. Lagorce and M. G. Allen, *J. Microelectromech. Syst.* **6**, 307 (1997).
9. C. Thomas and J. G. Zhu, *J. Appl. Phys.* **75**, 5553 (1994).
10. P. Kersch, R. Grössinger, C. Kussbach, R. Sato-Turtelli, K. H. Müller, and L. Schultz, *J. Magn. Mater.* **242**, 1468 (2002).

11. R. K. Tenzer, *J. Appl. Phys.* **34**, 1267 (1963).

## CHAPTER 5

### ELECTRONIC STRUCTURE OF La-Co SUBSTITUTED STRONTIUM FERRITE<sup>6</sup>

#### 5.1. Introduction

The maximum energy product,  $(BH)_{\max}$ , of commercial La-Co substituted M-type hexaferrite ( $\text{Sr}_{1-x}\text{La}_x\text{Fe}_{12-x}\text{Co}_x\text{O}_{19}$ : La-Co-SrM) permanent magnets has already reached 5.2 MGOe [1]. This  $(BH)_{\max}$  increased from 4.8 MGOe [1] and 4.0 MGOe [2] for non-substituted M-type hexaferrite ( $\text{SrFe}_{12}\text{O}_{19}$ : SrM) permanent magnet. This is because partial substitution of  $\text{Sr}^{2+}$ - $\text{Fe}^{3+}$  by  $\text{La}^{3+}$ - $\text{Co}^{2+}$  in SrM increased intrinsic coercivity ( $H_{\text{ci}}$ ), while saturation magnetization ( $\sigma_s$ ) remained unchanged up to  $x = 0.3$  [3,4]. On the contrary, Kikuchi *et al.* [5] experimentally found that  $H_{\text{ci}}$  reached its maximum at  $x = 0.4$ , and the  $\sigma_s$  gradually decreased with increasing concentrations of  $\text{La}^{3+}$ - $\text{Co}^{2+}$ .

Hui *et al.* [6] have performed first principles calculations on  $\text{La}^{3+}$ - $\text{Co}^{2+}$  substituted SrM and reported that  $\text{Co}^{2+}$  substitution in the  $2a$  sites exhibits the lowest total energy. Both lattice constants,  $a$  and  $c$ , decreased with the substitution of  $\text{La}^{3+}$ - $\text{Co}^{2+}$  in the  $2d$  and  $2a$  sites, and the magnetic moment increased to  $46 \mu_{\text{B}}/\text{u.c.}$  from  $40 \mu_{\text{B}}/\text{u.c.}$  of SrM. This magnetic moment is surprisingly high for M-type hexaferrite. The electrical properties of  $\text{La}^{3+}$ - $\text{Co}^{2+}$  substituted SrM has not yet been studied. The  $\text{Fe}^{3+}$  cation at the  $2a$  site anti-ferromagnetically interacts with  $\text{Fe}^{3+}$  at the  $4f_1$  sites.

---

<sup>6</sup> This work was published as “Electronic Structure of La-Co Substituted Strontium Hexaferrite ( $\text{Sr}_{1-x}\text{La}_x\text{Fe}_{12-x}\text{Co}_x\text{O}_{19}$ ) Permanent Magnet,” in *IEEE Magnetics Letters* **7**, 5500403 (2016) by Jihoon Park, Yang-Ki Hong, et al.

Therefore, we have performed first principles calculations on  $\text{La}^{3+}$ - $\text{Co}^{2+}$  substituted SrM ( $\text{Sr}_{1-x}\text{La}_x\text{Fe}_{12-x}\text{Co}_x\text{O}_{19}$ ) hexaferrites with  $x = 0.0$  and  $0.5$  to calculate electronic structure and gain insight into the band gap ( $E_g$ ).

## 5.2. Methods of calculations

The WIEN2k program [7] was used to perform first principles calculations. This program package is based on the density functional theory (DFT) and uses the full-potential linearized augmented plane wave (FPLAPW) method with the dual basis set. Electron exchange and correlation were treated with the generalized gradient approximation (GGA) with Coulomb and exchange interaction effects (GGA+ $U$ ) to improve the description of localized Fe  $3d$  electrons. In our calculations, we have used a  $U_{\text{eff}}$  of 7.0 eV, determined by Néel temperature ( $T_N$ ) calculation of  $\text{SrFe}_{12}\text{O}_{19}$  [8]. The relaxed lattice constants,  $a$  and  $c$ , were used for the total energy and magnetic moment calculations. It has been reported that  $\text{Co}^{2+}$  cations preferentially occupy  $2a$  and  $4f_2$  sites [9,10,11], and the calculated total energy is the lowest when  $\text{Co}^{2+}$  substitutes  $\text{Fe}^{3+}$  at the  $2a$  site [6]. Therefore, in our calculations, we consider only that  $\text{Co}^{2+}$  cations occupy the  $2a$  sites.

## 5.3. Results and discussion

The lattice constants,  $a$  and  $c$ , of  $\text{Sr}_{0.5}\text{La}_{0.5}\text{Fe}_{11.5}\text{Co}_{0.5}\text{O}_{19}$  decreased to 5.86 and 22.98 Å, respectively, from 5.93 and 23.21 Å of  $\text{SrFe}_{12}\text{O}_{19}$ . This is in good agreement with experimental results [12]. Fig. 5.1 shows that the substitution of  $\text{Co}^{2+}$  in the  $2a$  site decreases the magnetic moment of the  $2a$  site, while all the other sites remain unchanged. The calculated total magnetic moments ( $m_{\text{tot}}$ ) and relaxed lattice constants are summarized in Table 5.1 for

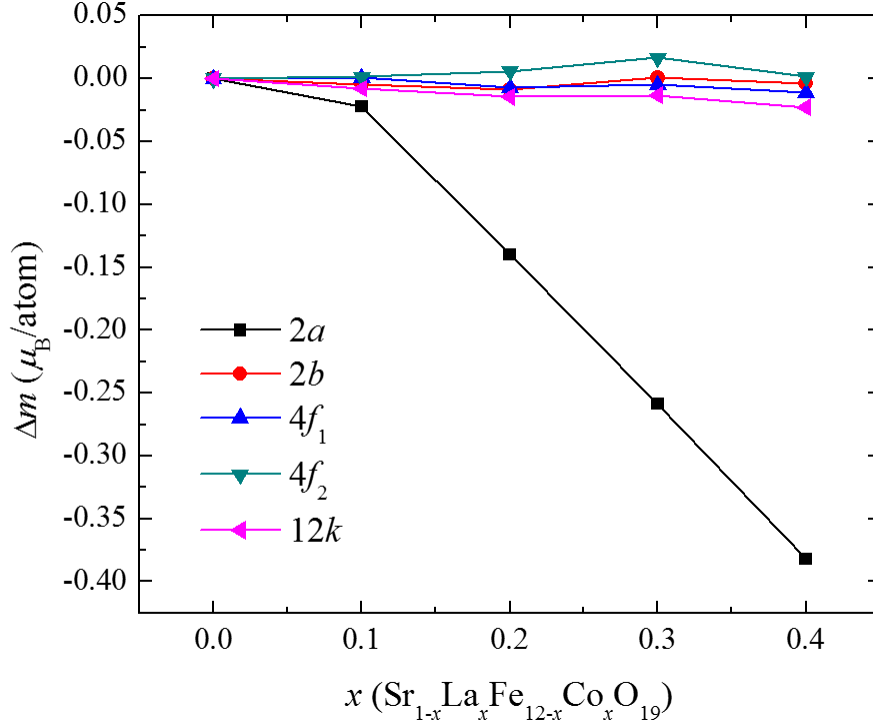


FIG. 5.1. Sublattice magnetic moments in Bohr magneton ( $\mu_B$ )/atom as a function of the concentration of La/Co ( $x$ ).

Table 5.1. Effect of La and Co substitution on magnetic moment and lattice constant of SrM ( $x = 0.0$ ) and La-Co SrM ( $x = 0.5$ ).

	SrFe <sub>12</sub> O <sub>19</sub>	Sr <sub>0.5</sub> La <sub>0.5</sub> Fe <sub>11.5</sub> Co <sub>0.5</sub> O <sub>19</sub>
Substituted site (La, Co)		2d, 2a
Magnetic Moment ( $\mu_B$ /u.c.)	40.00	37.04
$a$ (Å)	5.93	5.86
$c$ (Å)	23.21	22.98

$\text{Sr}_{1-x}\text{La}_x\text{Fe}_{12-x}\text{Co}_x\text{O}_{19}$  ( $x = 0.0$  and  $0.5$ ). The  $m_{\text{tot}}$  is the sum of magnetic moments from Fe ( $m_{2a}$ ,  $m_{2b}$ ,  $m_{12k}$ ,  $m_{4f1}$ , and  $m_{4f2}$ ) and O ( $m_o$ ) sublattices, and interstitial site ( $m_i$ ). Therefore, the  $m_{\text{tot}}$  was calculated by Eq. (5.1).

$$m_{\text{tot}} = 2m_{2a} + 2m_{2b} - 4m_{4f1} - 4m_{4f2} + 12m_{12k} + 38m_o + m_i \quad (5.1)$$

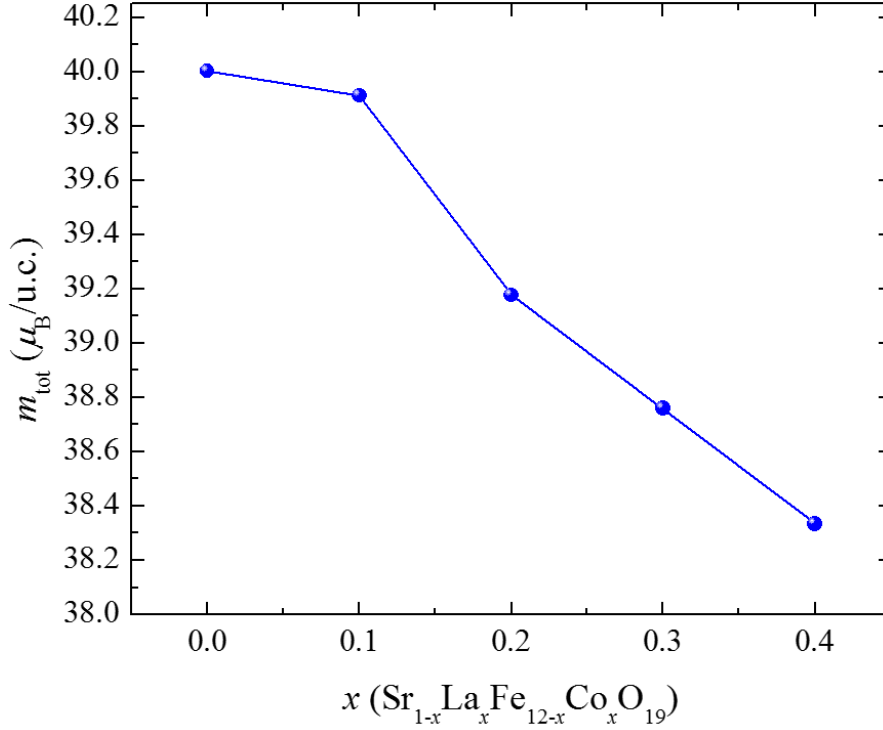
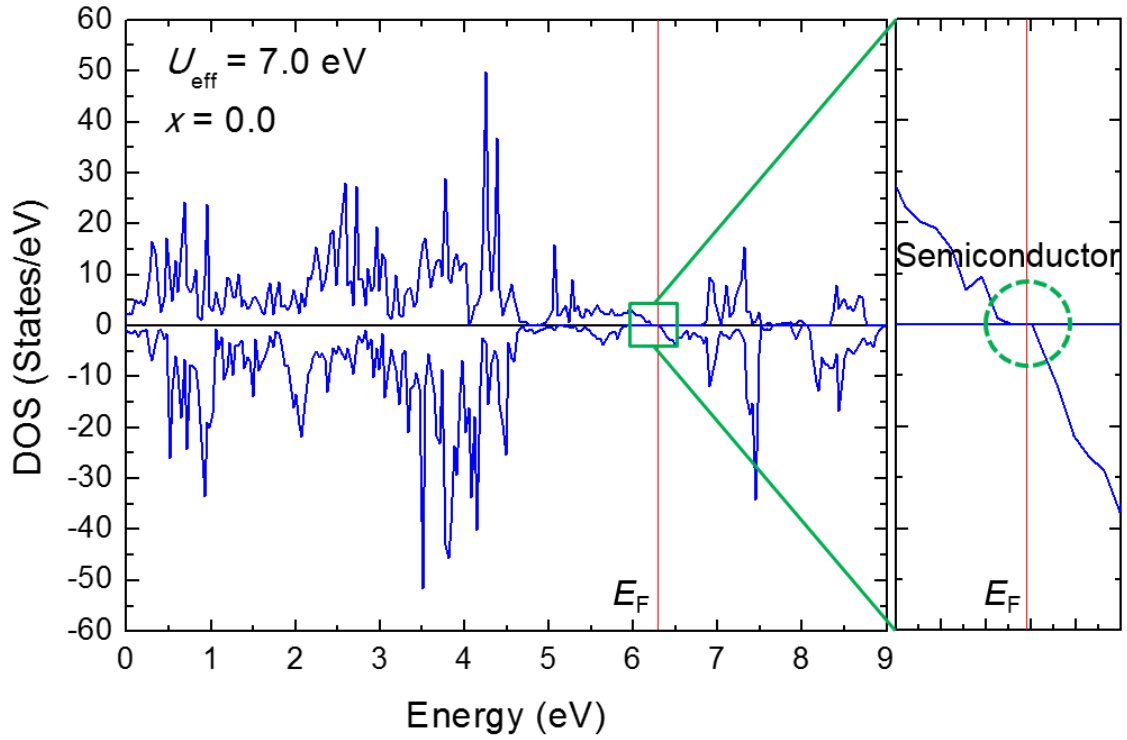


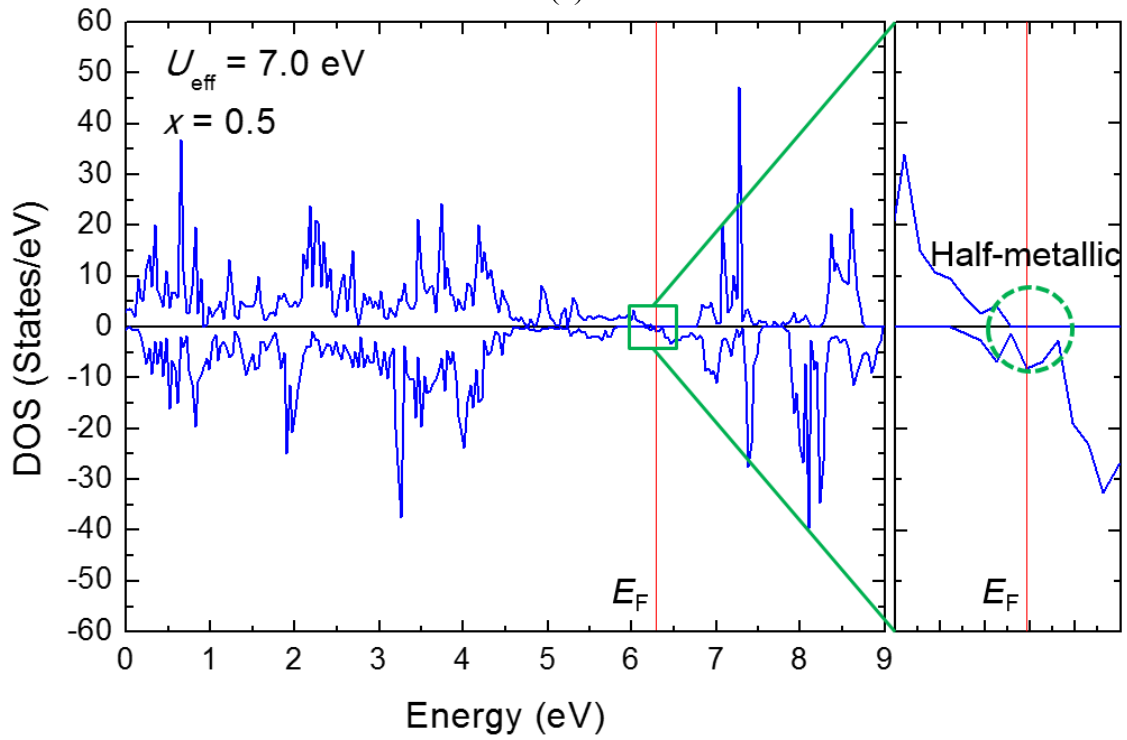
FIG. 5.2. Total magnetic moments in Bohr magneton ( $\mu_B$ )/u.c. as a function of the concentration of La/Co ( $x$ ).

Fig. 5.2 shows that the  $m_{\text{tot}}$  decreases as the concentration of  $\text{Co}^{2+}$  increases, which is in good agreement with experimental results [5]. It is noted that the substitution of  $\text{Co}^{2+}$  in the  $2a$  site has negligible influence on the magnetic moments at the other Fe sites. The  $m_{\text{tot}}$  decreased from  $40 \mu_B/\text{u.c.}$  at  $x = 0.0$  to  $37.04 \mu_B/\text{u.c.}$  at  $x = 0.5$ , which is much smaller than  $46 \mu_B/\text{u.c.}$  at  $x = 0.5$  [6].

Fig. 5.3 shows the density of states (DOS) for  $\text{Sr}_{1-x}\text{La}_x\text{Fe}_{12-x}\text{Co}_x\text{O}_{19}$  ( $x = 0.0$  and  $0.5$ ). We have interpreted calculated density of states (DOS) to gain insight into the band gap ( $E_g$ ) of M-type hexaferrites. Fig. 5.3 (a) shows that SrM is a semiconductor with an  $E_g$  of  $0.06 \text{ eV}$ , which is smaller than the reported  $0.63 \text{ eV}$  [13]. It is noted that the  $E_g$  of  $0.06 \text{ eV}$  is calculated by the energy difference between the highest energy of the majority spin valence band ( $6.24 \text{ eV}$ ) and the lowest energy of the minority spin conduction band ( $6.30 \text{ eV}$ ). On the other hand, the DOS in Fig. 5.3 (b) implies that the  $\text{La}^{3+}$ - $\text{Co}^{2+}$  substitution leads to the transfer of electrons to higher energy levels, thereby producing highly degenerated states within the energy levels higher than



(a)



(b)

FIG. 5.3. Density of states (DOS) for (a)  $\text{SrFe}_{12}\text{O}_{19}$  ( $x = 0.0$ ) and (b)  $\text{Sr}_{0.5}\text{La}_{0.5}\text{Fe}_{11.5}\text{Co}_{0.5}\text{O}_{19}$  ( $x = 0.5$ ). The DOS near the Fermi energy ( $E_F$ ) in the green boxes are enlarged on the right sides. The blue lines represent total DOS, and the red vertical lines correspond to the  $E_F$ .

the Fermi energy ( $E_F$ ). Therefore,  $\text{Sr}_{0.5}\text{La}_{0.5}\text{Fe}_{11.5}\text{Co}_{0.5}\text{O}_{19}$  becomes half-metallic because the  $E_g$  at the  $E_F$  exists only in the majority spin state.

#### 5.4. Conclusions

In summary, we have calculated electronic structures of M-type  $\text{Sr}_{1-x}\text{La}_x\text{Fe}_{12-x}\text{Co}_x\text{O}_{19}$  ( $x = 0.0$  and  $0.5$ ) ferrites. It was found that when  $\text{Co}^{2+}$  cations occupy only the  $2a$  sites, the magnetic moment of the  $2a$  site rapidly decreases with increasing concentrations of  $\text{La}^{3+}\text{-Co}^{2+}$ , but the magnetic moments of the other sites show negligible changes.  $\text{La}^{3+}\text{-Co}^{2+}$  substituted SrM becomes half-metallic because the  $E_g$  exists only in the majority spin state.

#### 5.5. References

1. Hitachi Metals Ltd. product catalog (2013).
2. A. Cochardt, *J. App. Phys.* **34**, 1273 (1963).
3. K. Iida, Y. Minachi, K. Masuzawa, M. Kawakammi, H. Nishio, and H. Taguchi, *J. Magn. Soc. Jpn.* **23**, 1093 (1999).
4. F. Kool, A. Morel, R. Grössinger, J. M. Le Breton, and P. Tenaud, *J. Magn. Magn. Mater.* **242**, 1270 (2002).
5. T. Kikuchi, T. Nakamura, T. Yamasaki, M. Nakanishi, T. Fujii, J. Takada, and Y. Ikeda, *J. Magn. Magn. Mater.* **322**, 2381 (2010).
6. Y. Hui, W. Cheng, Lin Gengqi, and X. Miao, *IEEE Trans. Magn.* **50**, 2800904 (2014).
7. P. Blaha, K. Schwarz, G. K. H. Madsen, D. Kvasnicka, and J. Luitz, WIEN2k (Institute for Materials Chemistry, TU Vienna) (2001).
8. J. H. Park, Y. K. Hong, S. G. Kim, S. H. Kim, L. S. I. Liyanage, J. J. Lee, W. C. Lee, G. S. Abo, K. H. Hur, S. Y. An, *J. Magn. Magn. Mater.* **355**, 1 (2014).
9. A. Morel, J. M. Le Breton, J. Kreisel, G. Wiesinger, F. Kool, and P. Tenaud, *J. Magn. Magn. Mater.* **242**, 1405 (2002).
10. G. Wiesinger, M. Müller, R. Grössinger, M. Pieper, A. Morel, F. Kool, P. Tenaud, J. M. Le Breton, and J. Kreisel, *Phys. Stat. Sol. (a)* **189**, 499 (2002).

11. J. M. Le Breton, J. Teillet, G. Wiesinger, A. Morel, F. Kools, and P. Tenaud, *IEEE Trans. Magn.* **38**, 2952 (2002).
12. L. Peng, L. Li, R. Wang, Y. Hu, X. Tu, and X. Zhong *J. Magn. Magn. Mater.* **393**, 399 (2015).
13. C. M. Fang, F. Kools, R. Metselaar, G. de With, and R. A. de Groot, *J. Phys.: Condens. Matter.* **15**, 6229 (2003).

## CHAPTER 6

### ELECTRONIC STRUCTURE AND MAGNETIC PROPERTIES OF Mn SUBSTITUTED FePt<sup>7</sup>

#### 6.1. Introduction

Ferromagnetic L1<sub>0</sub>-ordered FePt is a potentially promising material for heat-assisted magnetic recording (HAMR) application due to its high magnetocrystalline anisotropy that suppresses superparamagnetism in nanoscale grains. However, the corresponding high coercivity exceeds the magnetic field from a recording head. HAMR addresses this issue by temporarily lowering the coercivity by heating the local area of the recording media above the Curie temperature ( $T_c$ ). Recently, *Weller et al.* have suggested the following magnetic properties and Curie temperature of recording media to achieve the areal density of 4 Tb/in<sup>2</sup> [1]: saturation magnetization ( $M_s$ ) of 900 emu/cm<sup>3</sup>, magnetocrystalline anisotropy ( $K$ ) of  $5 \times 10^7$  ergs/cm<sup>3</sup>, and a Curie temperature ( $T_c$ ) of 650 - 600 K. The  $T_c$  of L1<sub>0</sub> Fe<sub>50</sub>Pt<sub>50</sub> is 753 K [2], and a lower  $T_c$  is desired to reduce the heat power requirement for HAMR. Experimental  $T_c$  and magnetic properties have been reported for Ni-, Cu-, and Mn-doped FePt [3-10], but those reported results do not meet the above desired properties.

For theoretical studies of Mn-doped FePt, *Burkert, et al.* performed first principles calculations on Fe<sub>1-x</sub>Mn<sub>x</sub>Pt using virtual crystal approximation (VCA) [12]. They assumed a ferromagnetic order up to 25 % Mn with the magnetic moments aligned parallel to each other. The calculated results show that the magnetic moment and magnetocrystalline anisotropy energy (MAE) increase with the Mn concentration ( $x$ ); magnetic moment increases by 2 %; and MAE

---

<sup>7</sup> This work was published as “Magnetic properties of Fe-Mn-Pt for heat assisted magnetic recording applications,” in *Journal of Applied Physics* **117**, 053911 (2015) by Jihoon Park, Yang-Ki Hong, et al.

increases by 33 % for  $x = 0.25$  as compared to pure FePt. However, these calculated results are in disagreement with experimental results that saturation magnetization ( $M_s$ ) and anisotropy constant ( $K$ ) decrease as  $x$  increases [11].

On the other hand, *Gruner, et al.* used large scale first principles calculations to investigate the structural and magnetic properties of  $\text{Fe}_{1-x}\text{Mn}_x\text{Pt}$  nanoparticles in the size range of up to 2.5 nm (561 atoms) [13]. They reported that substitution of Mn for Fe effectively increases the stability of single crystalline  $L1_0$  particles, however, compromises the stability of the ferromagnetic phase due to increased antiferromagnetic interaction. The authors concluded that only small additions of Mn can be tolerated for data recording applications. However, their work is limited to calculations of magnetic moment, crystalline stability, and stability of the ferromagnetic phase.

In this paper, we study the density of states (DOS) of  $L1_0$ -ordered FePt and Mn-substituted FePt ( $\text{Fe}_{0.5}\text{Mn}_{0.5}\text{Pt}$ ) system to understand the origins of  $M_s$ ,  $K$ , and phase stability, and then optimize the chemical composition of  $\text{Fe}_{1-x}\text{Mn}_x\text{Pt}$  for the desired magnetic properties and  $T_c$ . Spin and orbital magnetic moments and  $K$  were obtained by first principles calculations, and the mean field approximation (MFA) was used to calculate the  $T_c$ . Then, we predicted the Mn concentration ( $x$ ) dependence of  $T_c$  in the  $\text{Fe}_{1-x}\text{Mn}_x\text{Pt}$  system to find the range of  $x$  to meet the desired  $T_c$  of 650 - 600 K. The Brillouin function and Callen-Callen experimental relation were used to obtain temperature dependence of  $M_s$  and  $K$ , respectively, at the desired  $x$ .

## 6.2. Method of calculations

The WIEN2k package [14] was used to perform first-principles calculations. The package is based on density functional theory (DFT) and uses the full-potential linearized

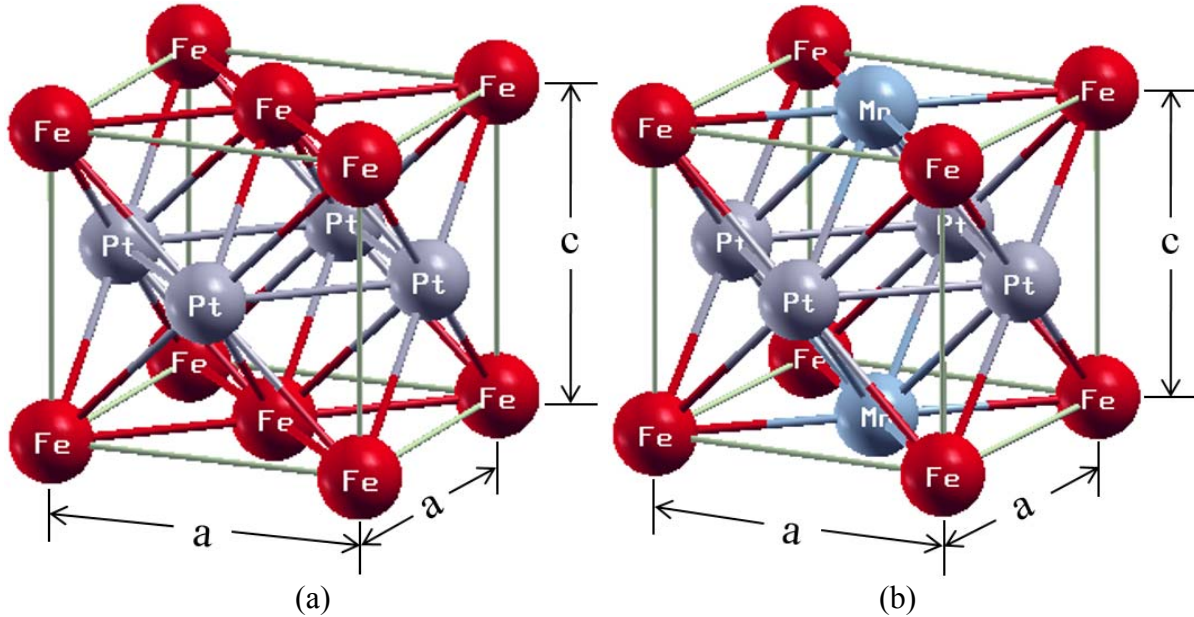


FIG. 6.1. Crystal structures of (a)  $L1_0$ -ordered FePt and (b)  $Fe_{0.5}Mn_{0.5}Pt$  with atoms colored as Fe-red, Pt-purple, and Mn-blue.

augmented plane wave (FP-LAPW) method with the dual basis set. For  $L1_0$ -ordered FePt and  $Fe_{0.5}Mn_{0.5}Pt$ , the  $3p$ ,  $3d$ , and  $4s$  states of Fe;  $4d$ ,  $4f$ ,  $5p$ ,  $5d$ , and  $6s$  states of Pt; and  $3p$ ,  $3d$ , and  $4s$  states of Mn are treated as valence states. All calculations use  $21 \times 21 \times 22$  reciprocal space meshes, generating 2,431 k-points in the irreducible part of the Brillouin zone. The muffin tin radii ( $R_{MT}$ ) for Fe, Pt, and Mn are set to 2.44 a.u. Experimental lattice constants of  $a = 3.86 \text{ \AA}$  and  $c = 3.71 \text{ \AA}$  [15] are used for the FePt calculation, while relaxed lattice constants of  $a = 3.77 \text{ \AA}$  and  $c = 3.69 \text{ \AA}$  are used for the  $Fe_{0.5}Mn_{0.5}Pt$  calculation. Fig. 6.1 shows the crystal structures of the  $L1_0$ -ordered FePt and  $Fe_{0.5}Mn_{0.5}Pt$  used in the present calculations. All spin-polarized and spin-orbit coupling calculations are based on density functional theory within the local-spin-density approximation (LSDA).

### 6.3. Results and discussion

#### 6.3.1. Density of states and magnetic moments of FePt and $Fe_{0.5}Mn_{0.5}Pt$

We used two different spin configurations for  $\text{Fe}_{0.5}\text{Mn}_{0.5}\text{Pt}$  to calculate magnetic properties ( $T_c$ ,  $M_s$ , and  $K$ ). They are ferromagnetic and ferrimagnetic spin configurations between Fe and Mn ions. The total energy difference between ferromagnetic and ferrimagnetic spin configurations reveals that the ferrimagnetic spin configuration is more stable than the ferromagnetic spin configuration. Therefore, we use the ferrimagnetic spin configuration for  $\text{Fe}_{0.5}\text{Mn}_{0.5}\text{Pt}$  in our calculations. Fig. 6.2 shows the density of states (DOS) for FePt and  $\text{Fe}_{0.5}\text{Mn}_{0.5}\text{Pt}$ . The DOS at energies higher than 0.1 Ry is mostly attributed to  $d$  bands of Fe, Mn, and Pt.

In FePt, the  $d$  bands of Pt form a bonding state, while the  $d$  bands of Fe form an anti-bonding state at the Fermi energy ( $E_F$ ) in the minority spin state. The  $d$  bands of both Fe and Pt significantly overlap below the  $E_F$  in the majority spin state; therefore, strong  $d$ - $d$  hybridization exists between Fe and Pt. Above the  $E_F$ , the  $d$  bands of Fe and Pt are almost completely overlapped in the majority spin state; while the shapes of both  $d$  bands are very similar in the minority spin state, the magnitudes are different. This indicates that the ferromagnetic spin configuration of FePt originates from the  $d$ - $d$  hybridization between Fe and Pt.

Substituting Mn for one of the two Fe atoms in a FePt unit cell ( $\text{Fe}_{0.5}\text{Mn}_{0.5}\text{Pt}$ ) resulted in a significant change in the DOS as shown in Fig. 6.2 (b), even though only one electron difference exists between FePt and  $\text{Fe}_{0.5}\text{Mn}_{0.5}\text{Pt}$ .  $\text{Fe}_{0.5}\text{Mn}_{0.5}\text{Pt}$  has similar characteristic of the  $d$ - $d$  hybridization between the  $d$  bands of Pt and Fe or Mn to FePt, but in different spin states. The  $d$  bands of Fe and Pt significantly overlap in the majority spin state below the  $E_F$ , and the  $d$  bands of Mn and Pt also overlap in the minority spin state. Above the  $E_F$ , the strong  $d$ - $d$  hybridization between the  $d$  bands of Pt and Fe (Mn) in both majority and minority states plays a key role in the DOS. The  $d$  bands of Fe and Pt are almost completely overlapped in the majority spin state,

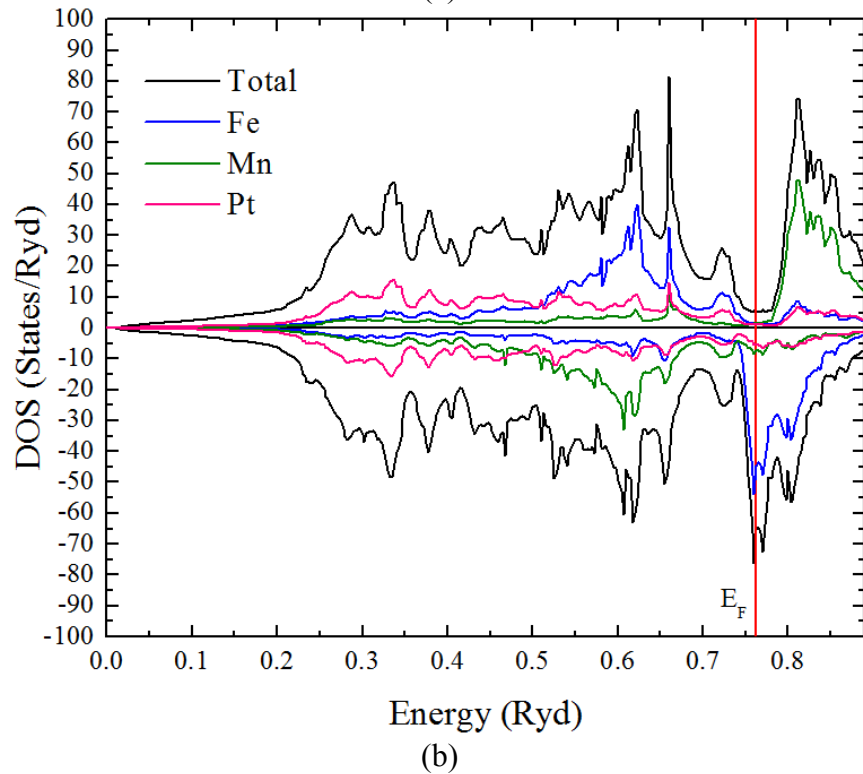
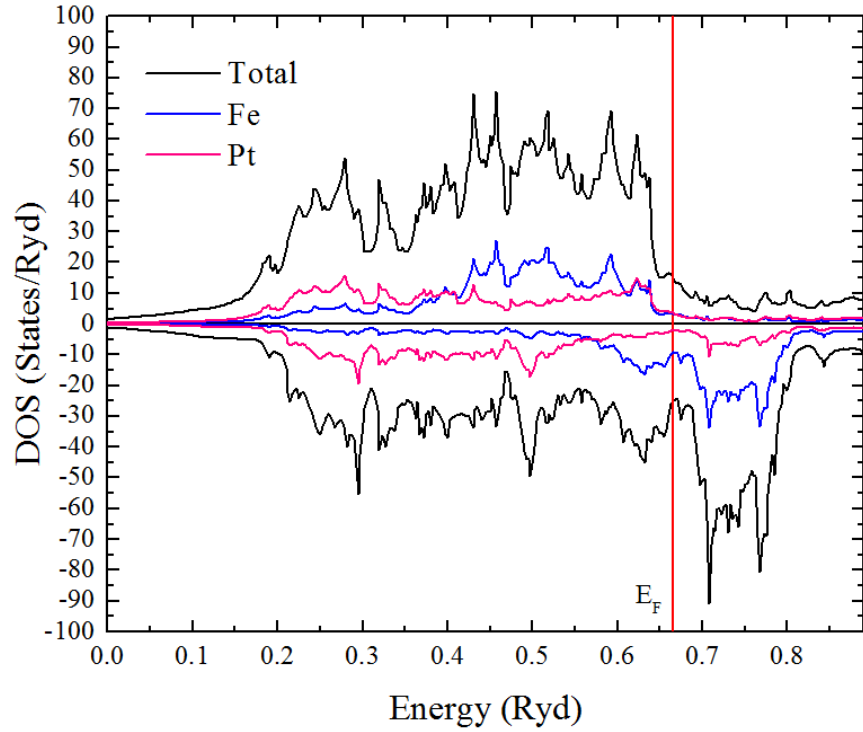


FIG. 6.2. Density of states (DOS) of (a) FePt and (b) Fe<sub>0.5</sub>Mn<sub>0.5</sub>Pt for majority and minority spin states. The black line represents the total DOS, and blue, green, and pink lines represent the partial DOS of Fe, Mn, and Pt, respectively. The red vertical line corresponds to the Fermi energy ( $E_F$ ).

while the  $d$  bands of Mn and Pt are overlapped in the minority spin state. The shapes of the  $d$  bands of Fe and Pt in the minority spin state and those of Mn and Pt in the majority spin state are similar, but only the magnitude is different. This strong  $d$ - $d$  hybridization results in the transfer of electrons to a lower energy level, thereby producing a pseudogap near the  $E_F$ .

Figure 6.2 (b) shows that the pseudogap in the majority spin state of  $\text{Fe}_{0.5}\text{Mn}_{0.5}\text{Pt}$  is exactly at the  $E_F$ , referring to an ordered intermetallic compound of high bonding strength and melting point; in fact, the DOS study of  $L1_0$ -ordered MnPt showed that the pseudogap exists in both majority and minority spin states [16]. However, the pseudogap in the minority spin state is located at lower energy than the  $E_F$ , inside a sharp peak of the DOS in Fig. 6.2 (b). This indicates that a disordered and unstable state, i.e., anti-bonding occurs. The DOS for  $\text{Fe}_{0.5}\text{Mn}_{0.5}\text{Pt}$  with ferromagnetic spin configuration (not shown in this paper) was also obtained. It was found that stronger  $d$ - $d$  hybridization occurs in the majority spin state than in the minority spin state, and the  $E_F$  lies neither in a pseudogap nor peak position in both majority and minority spin states. Therefore, non-bonding occurs. By comparing the total energies and DOS of ferromagnetic and ferrimagnetic spin configurations, we can conclude that the  $\text{Fe}_{0.5}\text{Mn}_{0.5}\text{Pt}$  system with ferrimagnetic spin configuration could be considered as a stable and ordered intermetallic compound.

This DOS analysis for the stability of  $\text{Fe}_{0.5}\text{Mn}_{0.5}\text{Pt}$  can be compared with an  $L1_0$ -ordered CoPt system. In CoPt, the  $E_F$  in the minority spin state lies in a sharp peak, and a pseudogap does not exist in both majority and minority spin states [17], which implies that  $\text{Fe}_{0.5}\text{Mn}_{0.5}\text{Pt}$  with the pseudogap could be a relatively stable structure. These Mn substitution effects on the DOS of FePt can be used to tune the position of the  $E_F$ , and make the crystal structure of  $\text{Fe}_{1-x}\text{Mn}_x\text{Pt}$  more stable by controlling the concentration of Mn ( $x$ ).

Table 6.1. Calculated (Cal.) and experimental (Exp.) spin and orbital magnetic moments ( $\mu_B$ ) of L1<sub>0</sub>-ordered FePt and Fe<sub>0.5</sub>Mn<sub>0.5</sub>Pt.

		Spin Moment			Orbital Moment			Total moment
		Fe	Pt	Mn	Fe	Pt	Mn	
FePt	Cal. <sup>a</sup>	2.87	0.38	–	0.064	0.045	–	3.359
	Cal. <sup>b</sup>	2.92	0.36	–	0.069	0.045	–	3.242
	Cal. <sup>c</sup>	2.92	0.33	–	–	–	–	3.23
	Cal. <sup>d</sup>	2.93	0.33	–	0.08	0.05	–	3.40
	Exp. <sup>e</sup> at 0 K	2.90	0.34	–	–	–	–	3.24
	Exp. <sup>f</sup> at 300 K	2.38	0.41	–	0.204	0.042	–	3.036
Fe <sub>0.5</sub> Mn <sub>0.5</sub> Pt Cal. <sup>g</sup>		2.28	0.007	-3.34	0.155	0.026	-0.05548	-0.928

<sup>a</sup>this work, WIEN2K calculations within the DFT-LSDA

<sup>b</sup>Reference 12. FP-LMTO-LDA

<sup>c</sup>Reference 16. VASP calculations within the DFT-GGA

<sup>d</sup>Reference 18. LMTO-ASA

<sup>e</sup>Reference 15. Fe<sub>50</sub>Pt<sub>50</sub> ~100  $\mu\text{m}$  particles - extrapolated to 0 K

<sup>f</sup>Reference 19. Fe<sub>50</sub>Pt<sub>50</sub> 6.3 nm particles at 300 K

<sup>g</sup>this work, WIEN2K calculations within the DFT-LSDA

We obtained magnetic moments of Fe, Pt, and Mn in FePt and Fe<sub>0.5</sub>Mn<sub>0.5</sub>Pt using spin-polarized and spin-orbit coupling calculations, and summarize them in Table 6.1. The total magnetic moment of FePt is in good agreement with theoretically [12,16,18] and experimentally obtained magnetic moments for both bulk [15] and nanoparticles [19] FePt. It was found that the orbital contribution to the total magnetic moment is much smaller than the spin contribution. The high magnetic moments of Fe in FePt, and Fe and Mn in Fe<sub>0.5</sub>Mn<sub>0.5</sub>Pt are attributed to the increased intensities of the *d* bands of both Fe and Mn near the  $E_F$  by the *d-d* hybridization with the *d* band of Pt. On the other hand, the *d* band of Pt in both FePt and Fe<sub>0.5</sub>Mn<sub>0.5</sub>Pt are distributed over a large energy range in both majority and minority spin states. Therefore, Pt gives a minor contribution to the total magnetic moment.

### 6.3.2. Curie temperature and anisotropy constant of L1<sub>0</sub>-ordered FePt and Fe<sub>0.5</sub>Mn<sub>0.5</sub>Pt

We calculated the Curie temperature ( $T_c$ ) for both FePt and Fe<sub>0.5</sub>Mn<sub>0.5</sub>Pt using the following MFA expression [20]:

$$T_c = \frac{2}{3k_B} J_0 \gamma \quad J_0 = \sum_j J_{0j}, \quad (6.1)$$

where  $J_0$  is the molecular field parameter calculated by summing the exchange integrals  $J_{0j}$ , and  $k_B$  is the Boltzmann constant. The factor  $\gamma$  is given by  $S(S+1)/S^2$  for quantum spins and 1 for classical spins [20]. We chose  $\gamma = 1.33$  based on our spin moment calculation in Table 6.1. The exchange integrals ( $J_{0j}$ ) are obtained from the difference of exchange energies between the ground and excited states of the spin configuration of sublattices. The ground state is the most stable spin configuration, while the excited state  $i$  refers to the configuration in which the spin at sublattice  $i$  is inverted relative to the ground state. The exchange integral [21] is written as

$$J_{ij} = (\Delta_{ij} - \Delta_i - \Delta_j) / (4S_i S_j n_i z_{ij}), \quad (6.2)$$

where  $S_i$  is the spin of  $i$ -th atom,  $\Delta_i$  is the difference of exchange energies between the ground state and the excited state where spin  $S_i$  at sublattice  $i$  is inverted relative to the ground state,  $\Delta_{ij}$  is the difference of exchange energies between the ground state and the excited state where both spins  $S_i$  and  $S_j$  at sublattices  $i$  and  $j$  are inverted relative to the ground state,  $n_i$  is the number of  $i$ -th atoms, and  $z_{ij}$  is the number of neighboring  $j$ -th atoms to  $i$ -th atom. Here, the exchange integrals  $J_{0j}$  of only significant interactions over all neighboring spins  $j$  were taken into account in our calculations by building the supercell structures (two L1<sub>0</sub>-ordered FePt or Fe<sub>0.5</sub>Mn<sub>0.5</sub>Pt unit cells). Note that the exchange integrals  $J_{0j}$  is derived using only Fe and/or Mn sublattice(s), since Pt has a small induced spin moment. The number of the nearest neighboring atoms ( $z_{ij}$ ) from the  $j$ -th sublattice to the  $i$ -th sublattice and corresponding distance ( $r_{ij}$ ) are listed in Table 6.2.

Table 6.2. The number of nearest neighbors ( $z_{0i}$ ) and corresponding distances ( $r_{0i}$ ) in the unit of Å in FePt and Fe<sub>0.5</sub>Mn<sub>0.5</sub>Pt.

	# of nearest neighbors				Distance			
	$z_{01}$	$z_{02}$	$z_{03}$	$z_{04}$	$r_{01}$	$r_{02}$	$r_{03}$	$r_{04}$
FePt	4	2	4	8	2.73	3.71	3.86	4.61
Fe <sub>0.5</sub> Mn <sub>0.5</sub> Pt	4	2	2	4	2.67	3.69	3.69	3.77

Table 6.3. Calculated (Cal.) and experimental (Exp.) magnetizations, magnetocrystalline anisotropy energies (MAE), anisotropy constants ( $K$ ), and Curie temperatures ( $T_c$ ) of L1<sub>0</sub>-ordered FePt and Fe<sub>0.5</sub>Mn<sub>0.5</sub>Pt.

	Magnetization (emu/cm <sup>3</sup> )	MAE (meV/u.c.)	$K$ ( $\times 10^6$ J/m <sup>3</sup> )	$T_c$ (K)	
FePt	Cal. <sup>a</sup>	1127	3.83	11.09	685
	Cal. <sup>b</sup>	–	5.6	16.3	–
	Cal. <sup>c</sup>	–	5.8	–	–
	Cal. <sup>d</sup>	–	–	7.7	–
	Cal. <sup>e</sup>	–	–	–	1105 <sup>e</sup>
		939 <sup>f</sup> at 0 K	–	7 <sup>i</sup> at 300 K	753 <sup>l</sup>
	Exp.	1019 <sup>g</sup> at 300 K	–	5.9 <sup>j</sup> at 300 K	623 <sup>m</sup>
	1130 <sup>h</sup> at 300 K	–	4.4 <sup>k</sup> at 300 K	–	
Fe <sub>0.5</sub> Mn <sub>0.5</sub> Pt	Cal. <sup>n</sup>	-329	-2.63	-8.06	90

<sup>a</sup>this work, WIEN2K calculations within the DFT-LSDA

<sup>b</sup>Reference 18. LMTO-ASA calculations

<sup>c</sup>Reference 16. VASP calculations within the DFT-GGA

<sup>d</sup>Reference 25. CLSDA calculations

<sup>e</sup>Reference 26. KKR-CPA calculations

<sup>f</sup>Reference 15. Fe<sub>50</sub>Pt<sub>50</sub> ~100 μm particles - extrapolated to 0 K

<sup>g</sup>Reference 19. Fe<sub>50</sub>Pt<sub>50</sub> 6.3 nm particles

<sup>h</sup>Reference 11. Fe<sub>53</sub>Pt<sub>47</sub> 75 nm film

<sup>i</sup>Reference 23. Fe-Pt bulk

<sup>j</sup>Reference 24. Fe<sub>48</sub>Pt<sub>52</sub> 4 nm particles

<sup>k</sup>Reference 11. Fe<sub>53</sub>Pt<sub>47</sub> 75 nm film

<sup>l</sup>Reference 2. Fe<sub>50</sub>Pt<sub>50</sub> bulk

<sup>m</sup>Reference 22. Fe-Pt 6 nm particles

<sup>n</sup>this work, WIEN2K calculations within the DFT-LSDA

As a result, the calculated  $J_0 = 4.89$  mRy for FePt corresponds to the mean-field estimated  $T_c = 685$  K, while the  $J_0 = 0.65$  mRy for Fe<sub>0.5</sub>Mn<sub>0.5</sub>Pt yields the  $T_c = 90$  K. The calculated  $T_c$  for FePt is in good agreement with the experimental  $T_c$  for bulk [2] and nanoparticles [22] FePt as given in Table 6.3. Since MFA overestimates  $T_c$  in general, this close agreement may suggest that our electronic structure calculation compensates by underestimating exchange energies.

Next, we calculated  $K$  for both FePt and Fe<sub>0.5</sub>Mn<sub>0.5</sub>Pt. MAE was obtained as the energy difference between  $\langle 100 \rangle$  and  $\langle 001 \rangle$  spin configurations, i.e.,  $\Delta E = E_{\langle 100 \rangle} - E_{\langle 001 \rangle}$ . The calculated  $K$  at  $T = 0$ ,  $K(0)$ , of FePt is  $11.09 \times 10^6$  J/m<sup>3</sup>, and is larger than experimental  $K$  for bulk [23], nanoparticles [24], and film [11] FePt at 300 K as given in Table 6.3. It is noted that the large  $K$  of FePt is attributed to the strong  $d$ - $d$  hybridization.

On the other hand, the substitution of Mn in FePt leads to a dramatic change of  $K(0)$  from a large positive value of  $11.09 \times 10^6$  J/m<sup>3</sup> to a large negative value of  $-8.06 \times 10^6$  J/m<sup>3</sup>. This indicates that Mn-substitution in FePt changes the direction of magnetization from out-of-plane to in-plane. Our calculated  $M_s(0)$ , MAE,  $K(0)$ , and  $T_c$  for FePt and Fe<sub>0.5</sub>Mn<sub>0.5</sub>Pt are given and compared with experimental [2,11,15,19,22,23,24] and calculated [16,18,25,26] values in Table 6.3.

### 6.3.3. Curie temperature, magnetization, and anisotropy constant of Fe<sub>1-x</sub>Mn<sub>x</sub>Pt

In this section, we use the calculated  $T_c$  for FePt and Fe<sub>0.5</sub>Mn<sub>0.5</sub>Pt to identify a composition range of Fe<sub>1-x</sub>Mn<sub>x</sub>Pt, which meets 600 - 650 K of  $T_c$  for 4 Tb/in<sup>2</sup> HAMR media requirements [1]. It has been reported that the  $T_c$  for Fe<sub>1-x</sub>Mn<sub>x</sub>Pt particles more or less linearly decreases with the  $x$  [6,7]. Our calculated  $T_c$  of FePt and Fe<sub>0.5</sub>Mn<sub>0.5</sub>Pt are 685 and 90 K,

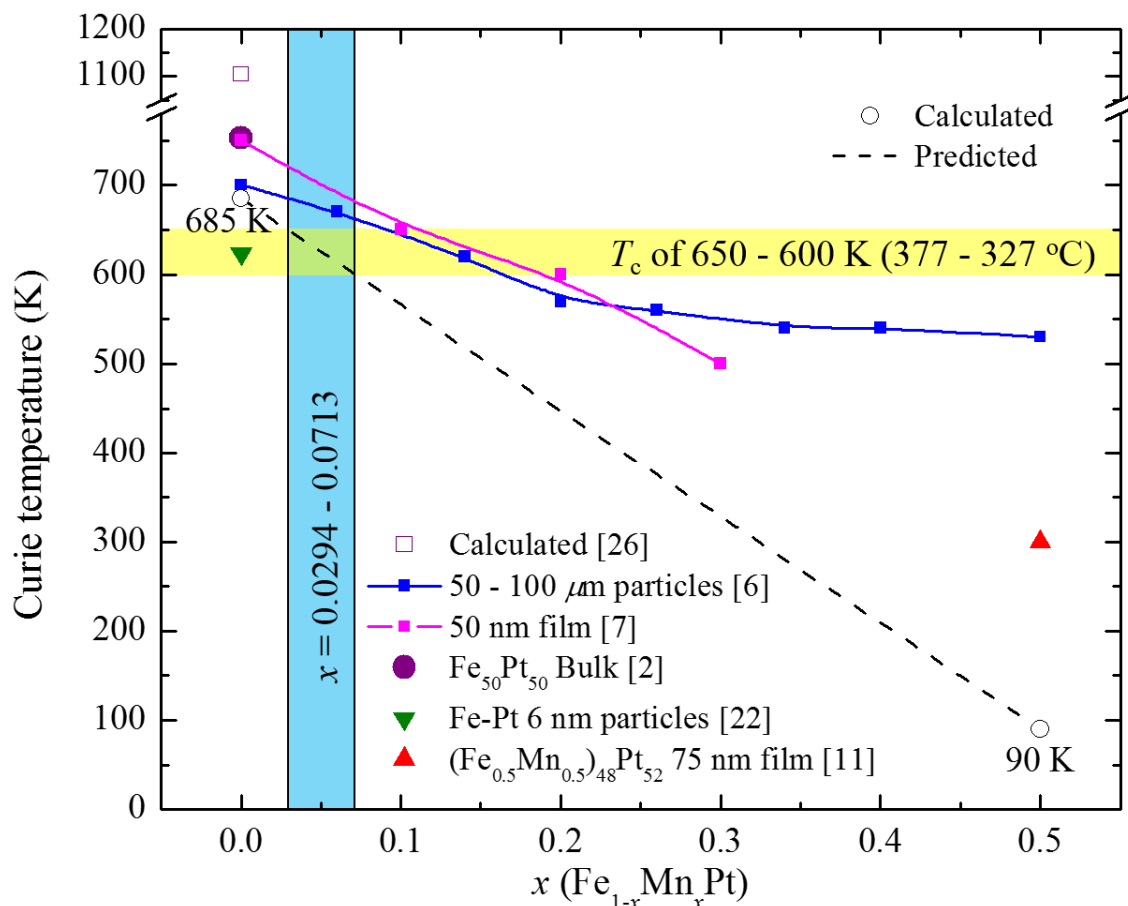


FIG. 6.3. Predicted and experimental  $x$  dependence of Curie temperature  $T_c(x)$  for  $\text{Fe}_{1-x}\text{Mn}_x\text{Pt}$ . The  $T_c$  of 650 - 600 K for HAMR application are marked by the yellow region. The required  $x$  to meet the  $T_c$  of 650 - 600 K is between 0.0294 and 0.0713, and marked by the blue region.

respectively. The  $T_c$  (685 K) at  $x = 0$  is in good agreement with the experimental  $T_c$  for FePt particles [6], but the  $T_c$  of 90 K at  $x = 0.5$  is much lower than the experimental one. The neutron diffraction measurement for  $\text{Fe}_{0.5}\text{Mn}_{0.5}\text{Pt}$  micron particles showed the  $T_c$  of 530 K [6], while the  $T_c$  of about 300 K was measured by the vibrating sample magnetometer (VSM) for  $\text{Fe}_{0.5}\text{Mn}_{0.5}\text{Pt}$  film [11], which is closer to our calculated value. These higher values of measured  $T_c$  could be attributed to the surface segregation of Mn or Fe [11] and phase transformation due to increasing instability of the L1<sub>0</sub>-ordered structure with increasing Mn concentration [6].

Therefore, we assume a linear relation between the  $T_c$  and  $x$  (broken line between 685 and 90 K in Fig. 6.3) to predict the composition dependence of  $T_c$ . It can be seen that the slope

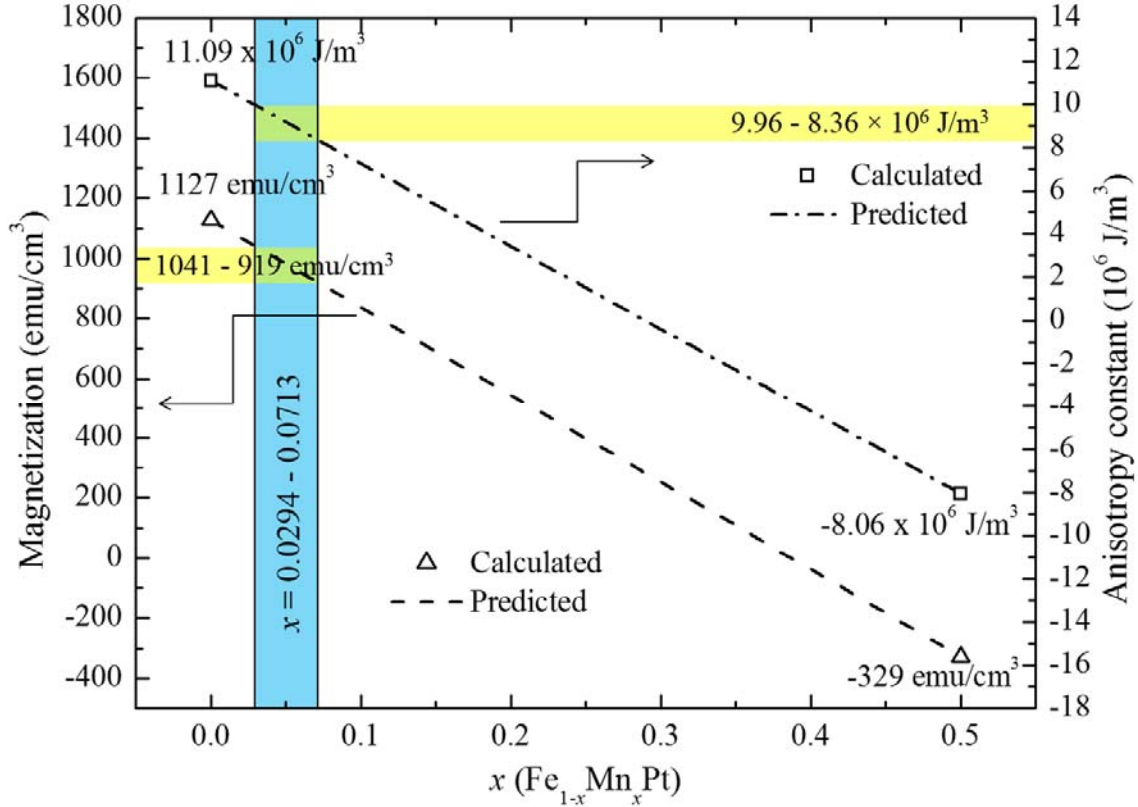


FIG. 6.4. Predicted and experimental  $x$  dependence of magnetization  $M_s(x)$  and anisotropy constant  $K(x)$  for  $\text{Fe}_{1-x}\text{Mn}_x\text{Pt}$ . The  $M_s$  and  $K$  for  $x$  of 0.0294 and 0.0713 (blue region) are 1041 - 919  $\text{emu}/\text{cm}^3$  and  $9.96 - 8.36 \times 10^6 \text{ J}/\text{m}^3$  (yellow regions), respectively.

of our calculated  $T_c(x)$  is close to experimental  $T_c(x)$  of the 50 nm film [7]. Because our calculations aim at the  $T_c$  in the range of 600 to 650 K for 4 Tb/in<sup>2</sup> HAMR media, we choose  $x = 0.0294 - 0.0713$  as highlighted in Fig. 6.3. The  $T_c$  between 600 and 650 K is marked by the yellow region, and the corresponding  $x$  is marked by the blue region.

Now, we focus on the  $M_s$  and  $K$  of  $\text{Fe}_{1-x}\text{Mn}_x\text{Pt}$ . It has been reported that transition metal substitution in FePt results in a steady reduction of  $M_s$  and  $K$  [3,11]. Therefore, we consider that the  $M_s$  and  $K$  of  $\text{Fe}_{1-x}\text{Mn}_x\text{Pt}$  would linearly decrease as a function of  $x$  at 0 K. Fig. 6.4 shows our calculated  $M_s$  and  $K$  at 0 K for  $x = 0$  and 0.5. The calculated  $M_s$  are 1127 and  $-329 \text{ emu}/\text{cm}^3$ , and  $K$  are  $11.09$  and  $-8.06 \times 10^6 \text{ J}/\text{m}^3$  for FePt and  $\text{Fe}_{0.5}\text{Mn}_{0.5}\text{Pt}$ , respectively. The negative sign for  $M_s$  of  $\text{Fe}_{0.5}\text{Mn}_{0.5}\text{Pt}$  indicates that the Mn spin is opposite to the direction of the Fe spin. The  $x$

dependence of magnetization  $M_s(x)$  and anisotropy constant  $K(x)$  for  $\text{Fe}_{1-x}\text{Mn}_x\text{Pt}$  is taken as a linear relation (broken lines) as shown in Fig. 6.4. As seen in Fig. 6.3, we choose  $x = 0.0294 - 0.0713$  because these compositions meet the desired Curie temperature range (600 - 650 K). Accordingly, the  $M_s = 1041 - 919 \text{ emu/cm}^3$  and  $K = 9.96 - 8.36 \times 10^6 \text{ J/m}^3$  were obtained at  $x = 0.0294 - 0.0713$  ( $\text{Fe}_{1-x}\text{Mn}_x\text{Pt}$ ) as shown in Fig. 6.4. The  $x = 0.0294 - 0.0713$  are marked by the blue region, and the corresponding  $M_s$  and  $K$  are identified by the yellow regions in Fig. 6.4. The experimental  $M_s$  and  $K$  at 300 K for  $\text{Fe}_{1-x}\text{Mn}_x\text{Pt}$  film more or less linearly decrease with the  $x$  [11]. This supports a linear relation between the  $M_s$  or  $K$  and  $x$  at 0 K. It is noted that the  $\text{Fe}_{1-x}\text{Mn}_x\text{Pt}$  films [11] are based on  $(\text{Fe}_{1-x}\text{Mn}_x)_{53\sim 47}\text{Pt}_{47\sim 53}$  composition, and  $M_s$  and  $K$  were measured at 300 K. Therefore, these measured  $M_s$  and  $K$  can be different from our calculated data, which are based on  $(\text{Fe}_{1-x}\text{Mn}_x)_{50}\text{Pt}_{50}$  at 0 K.

#### 6.3.4. Temperature dependence of magnetization and anisotropy constant of $\text{Fe}_{1-x}\text{Mn}_x\text{Pt}$

Information data is stored at room temperature. Therefore, it is needed to obtain  $M_s$  and  $K$  at room temperature for  $\text{Fe}_{1-x}\text{Mn}_x\text{Pt}$ . The temperature dependence of magnetization  $M_s(T)$  within MFA [27] is given by

$$M_s(T) = M_s(0)B_J(\tau), \quad (6.3)$$

where  $B_J$  is the Brillouin function with angular quantum number  $J$  and normalized temperature  $\tau = T/T_c$ . Similarly, within the MFA, the temperature dependence of anisotropy constant  $K(T)$  is given by the Callen-Callen experimental relation [28] as

$$K(T) = K(0)[m(T)]^{n(n+1)/2}, \quad (6.4)$$

where  $n$  is the power of the anisotropy function and  $m(T)$  is the normalized magnetization  $M_s(T)/M_s(0)$ .  $n$  for uniaxial anisotropy is 2. As seen in Fig. 6.4, the  $M_s$  of  $\text{Fe}_{1-x}\text{Mn}_x\text{Pt}$  ( $x = 0.0000$ ,

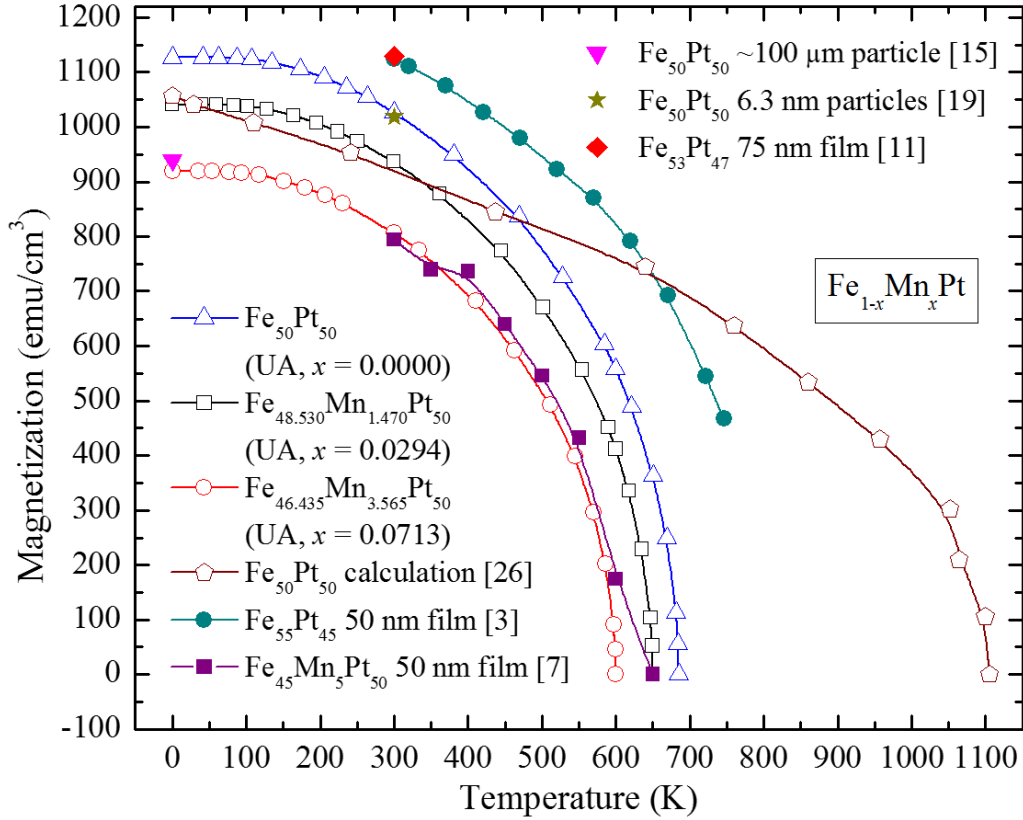


FIG. 6.5. The calculated temperature dependence of magnetizations  $M_s(T)$  for  $\text{Fe}_{1-x}\text{Mn}_x\text{Pt}$  ( $x = 0.0000, 0.0294, \text{ and } 0.0713$ ) and experimental magnetizations for different compositions, morphologies, and temperature.

0.0294, and 0.0713) at 0 K are 1127, 1041, and 919  $\text{emu}/\text{cm}^3$ , and  $K$  are 11.09, 9.96, and  $8.36 \times 10^6 \text{ J}/\text{m}^3$ , respectively.

We use these  $M_s(0)$  and  $K(0)$  to calculate the  $M_s(T)$  and  $K(T)$  of  $\text{Fe}_{1-x}\text{Mn}_x\text{Pt}$  ( $x = 0.0000, 0.0294, \text{ and } 0.0713$ ) with Eq. (6.3) and (6.4). The calculated  $M_s(T)$  and  $K(T)$  are compared with experimental  $M_s$  [3,7,11,15,19] and  $K$  [3,7,11,23,24] in Fig. 6.5 and 6.6, respectively. The experimental  $M_s$  for  $\text{Fe}_{50}\text{Pt}_{50}$  nanoparticles [20] at 300 K is in good agreement with our calculated  $M_s$ , while the  $M_s$  for  $\text{Fe}_{53}\text{Pt}_{47}$  film [11] and  $\text{Fe}_{55}\text{Pt}_{45}$  film [3] are higher than our calculated values. It is also noted that the  $M_s$  for  $\text{Fe}_{55}\text{Pt}_{45}$  film [3] is higher than our calculated  $M_s$  for  $\text{Fe}_{50}\text{Pt}_{50}$  in Fig. 6.5. This is due to higher Fe content in the former case.  $M_s(T)$  for  $\text{Fe}_{45}\text{Mn}_5\text{Pt}_{50}$  films [7] almost overlaps with our calculated  $M_s(T)$  of  $\text{Fe}_{46.435}\text{Mn}_{3.565}\text{Pt}_{50}$ . This

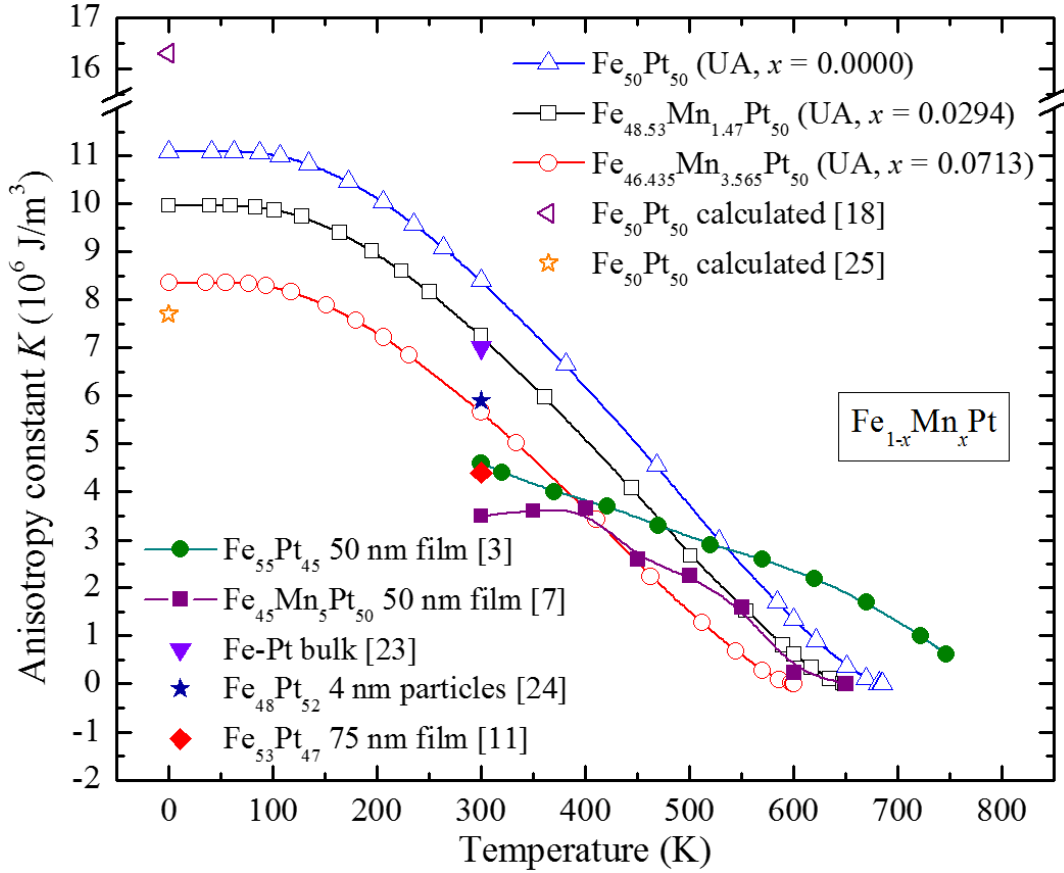


FIG. 6.6. The calculated temperature dependence of anisotropy constants  $K(T)$  for  $\text{Fe}_{1-x}\text{Mn}_x\text{Pt}$  ( $x = 0.0000, 0.0294, \text{ and } 0.0713$ ) and experimental  $K$  for different compositions, morphologies, and temperatures.

shows that our calculation method is reliable for FePt system. The calculated  $M_s(T)$  [26] is in disagreement with the experimental data. This is because the calculated  $T_c$  of 1105 K [26] is much higher than the experimental  $T_c$  of 753 K for  $\text{Fe}_{50}\text{Pt}_{50}$  bulk [2], 623 K for 6 nm Fe-Pt particles [22].

With regards to  $K(T)$ , our calculated value is higher than the experimental value below 550 K, but lower than the experimental value for  $\text{Fe}_{55}\text{Pt}_{45}$  film [3] above 550 K. It is also seen that the experimental  $K$  for Fe-Pt bulk [23] and  $\text{Fe}_{48}\text{Pt}_{52}$  nanoparticles [24] are higher than for  $\text{Fe}_{53}\text{Pt}_{47}$  [11] and  $\text{Fe}_{55}\text{Pt}_{45}$  films [3]. This can be explained by the variation of FePt composition.

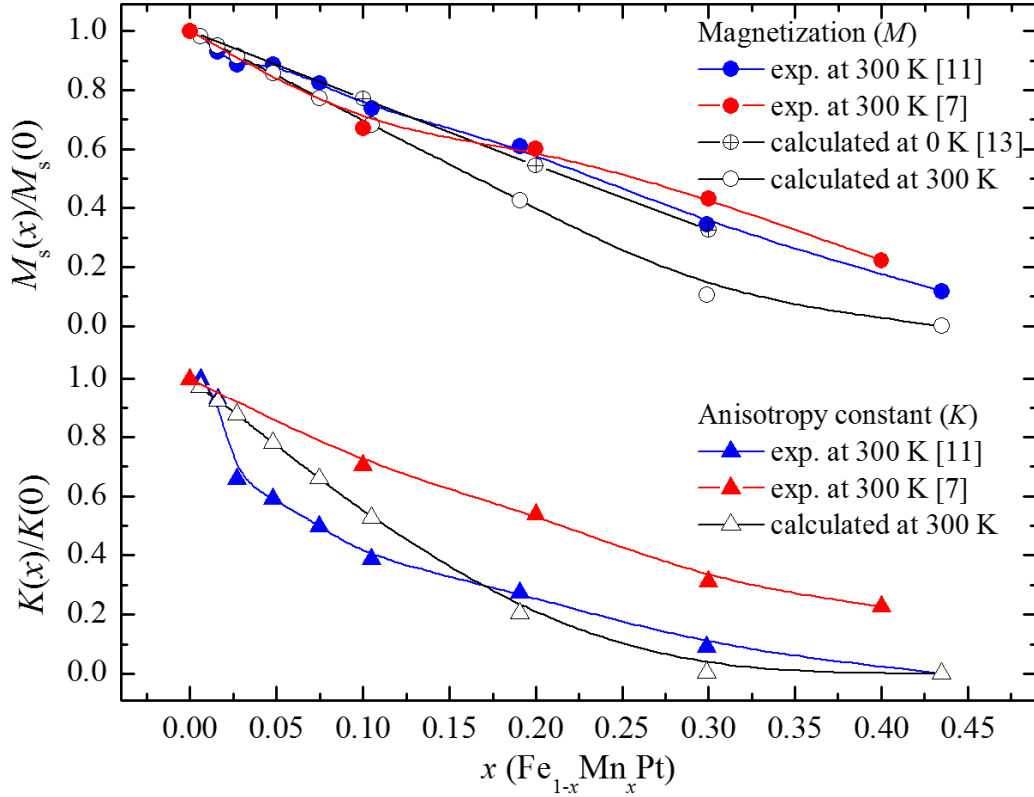


FIG. 6.7. The normalized  $x$  dependence of magnetization  $M_s(x)$  and anisotropy constant  $K(x)$  for experimental and calculated  $\text{Fe}_{1-x}\text{Mn}_x\text{Pt}$ .

However, our calculated  $K(T)$  for  $\text{Fe}_{46.435}\text{Mn}_{3.565}\text{Pt}_{50}$  is in good agreement with the experimental  $K(T)$  for 50 nm thick  $\text{Fe}_{45}\text{Mn}_5\text{Pt}_{50}$  film [7] above 300 K.

As shown in Fig. 6.5 and 6.6, our calculated  $M_s$  and  $K$  at 300 K are 1022, 930, and 800  $\text{emu}/\text{cm}^3$  and 8.33, 7.18, and  $5.61 \times 10^6 \text{ J}/\text{m}^3$  at 0.0000, 0.0294, and 0.0713 of  $x$ , respectively. Therefore, it can be concluded that the optimum  $x$  in  $\text{Fe}_{1-x}\text{Mn}_x\text{Pt}$  is between 0.0294 and 0.0713 for HAMR media design, since both calculated  $M_s$  and  $K$  at 300 K meet 4  $\text{Tb}/\text{in}^2$  HAMR media requirements, which are  $M_s$  of 800  $\text{emu}/\text{cm}^3$  and  $K$  of  $5.00 \times 10^6 \text{ J}/\text{m}^3$  at 300 K [1], while maintaining the  $T_c$  in the range of 650 and 600 K.

In order to validate our method to calculate  $M_s$  and  $K$  of  $\text{Fe}_{1-x}\text{Mn}_x\text{Pt}$  at 300 K, we have compared the calculated data with the experimental results. The calculated  $M_s$  and  $K$  at 300 K as a function of  $x$  are normalized and compared with the normalized experimental data at 300 K

[7,11] as shown in Fig. 6.7. The data points of the experimental  $x$  [11] were used to calculate  $M_s(x)/M_s(0)$  and  $K(x)/K(0)$ . For comparison with previously reported calculations, we had also added the large-scale first-principles calculation results at 0 K [13] to Fig. 6.7. Our calculated and experimental  $M_s(x)/M_s(0)$  [11] for  $x < 0.11$  at 300 K are in good agreement, but the difference between the calculated and experimental  $M_s(x)/M_s(0)$  increases for  $x > 0.11$ . Furthermore, overall trends of the calculated and experimental  $K(x)/K(0)$  are in good agreement with each other, but the experimental  $K(x)/K(0)$  dramatically drops from  $x = 0.03$ . This disagreement between calculated and experimental  $M_s(x)/M_s(0)$  and  $K(x)/K(0)$  might be attributed to the following possible reasons. The first is the limited accuracy of our calculation method that assumes a linear relation between the magnetic properties ( $T_c$ ,  $M_s$ , and  $K$ ) and  $x$ . The other is the difference between calculated and experimental compositions. According to *G. Meyer* and *J.-U. Thiele* [11], their experimental composition is based on  $(\text{Fe}_{1-x}\text{Mn}_x)_y\text{Pt}_{1-y}$ , where  $y$  varies from 0.47 to 0.53, but we used an L1<sub>0</sub>-ordered  $(\text{Fe}_{1-x}\text{Mn}_x)_{50}\text{Pt}_{50}$  composition in our calculations.

#### 6.4. Conclusions

We calculated the magnetization ( $M_s$ ), magnetocrystalline anisotropy constant ( $K$ ), and Curie temperature ( $T_c$ ) for L1<sub>0</sub>-ordered FePt and Fe<sub>0.5</sub>Mn<sub>0.5</sub>Pt. The calculated  $M_s$  and  $K$  for FePt were in good agreement with reported experimental results. The DOS study indicates that the  $d$ - $d$  hybridization stabilizes the crystal structure of Fe<sub>0.5</sub>Mn<sub>0.5</sub>Pt.

Our calculated composition Fe<sub>1-x</sub>Mn<sub>x</sub>Pt ( $0.0294 \leq x \leq 0.0713$ ) meets  $T_c = 650 - 600$  K,  $M_s = 930 - 800$  emu/cm<sup>3</sup> and  $K = 7.18 - 5.61 \times 10^6$  J/m<sup>3</sup> at 300 K. These magnetic properties are suitable for achieving 4 Tb/in<sup>2</sup> HAMR media [1].

## 6.5. References

1. D. Weller, G. Parker, O. Mosendz, E. Champion, B. Stipe, X. Wang, T. Klemmer, G. Ju, and A. Ajan, *IEEE Trans. Magn.* **50**, 3100108 (2014).
2. T. B. Massalski, *Binary Alloy Phase Diagrams*, 2nd ed. (ASM International, Materials Park, 1990).
3. J.-U. Thiele, K. R. Coffey, M. F. Toney, J. A. Hedstrom, and A. J. Kellock, *J. Appl. Phys.* **91**, 6595 (2002).
4. B. Wang and K. Barmak, *J. Appl. Phys.* **109**, 123916 (2011).
5. Dustin A. Gilbert, Liang-Wei Wang, Timothy J. Klemmer, Jan-Ulrich Thiele, Chih-Huang Lai, and Kai Liu, *Appl. Phys. Lett.* **102**, 132406 (2013).
6. A. Z. Menshikov, V. P. Antropov, G. P. Gasnkova, Yu. A. Dorofeyev, and V. A. Kazantsev, *J. Magn. Magn. Mat.* **65**, 159 (1987).
7. D. B. Xu, J. S. Chen, T. J. Zhou, and G. M. Chow, *J. Appl. Phys.* **109**, 07B747 (2011).
8. V. Tzitzios, G. Basina, M. Gjoka, N. Boukos, D. Niarchos, E. Devlin and D. Petridis, *Nanotechnology* **17**, 4270 (2006).
9. J. C. A. Huang, Y. C. Chang, C. C. Yu, Y. D. Yao, Y. M. Hu, and C. M. Fu, *J. Appl. Phys.* **93**, 8173 (2003).
10. C. J. Sun, D. Xu, S. M. Heald, J. Chen, and G. M. Chow, *Phys. Rev. B* **84**, 140408 (2011).
11. G. Meyer and J.-U. Thiele, *Phys. Rev. B* **73**, 214438 (2006).
12. T. Burkert, O. Eriksson, S. I. Simak, A. V. Ruban, B. Sanyal, L. Nordström, and J. M. Wills, *Phys. Rev. B* **71** 134411 (2005).
13. M. E. Gruner and P. Entel, Beilstein *J. Nanotechnol.* **2**, 162 (2011).
14. P. Blaha, K. Schwarz, G. K. H. Madsen, D. Kvasnicka and J. Luitz, WIEN2k, Inst. f. Materials Chemistry TU Vienna (2001).
15. J. Lyubina, I. Opahle, M. Richter, O. Gutfleisch, K.-H Müller, and L. Schultz, *Appl. Phys. Lett.* **89**, 032506 (2006).
16. Z. Lu, R. V. Chepulskaa, and W. H. Butler, *Phys. Rev. B* **81**, 094437 (2010).
17. A. Dannenberg, M. Ernst Gruner and P. Entel, *Journal of Physics: Conference Series* **200**, 072021 (2010).
18. A. Sakuma, *J. Phys. Soc. Jpn.* **63**, 3053 (1994).

19. C. Antoniak, J. Lindner, M. Spasova, D. Sudfeld, M. Acet, and M. Farle, K. Fauth, U. Wiedwald, H.-G. Boyen, P. Ziemann, F. Wilhelm, A. Rogalev, and S. Sun, *Phys. Rev. Lett.* **97**, 117201 (2006).
20. J. M. MacLaren, T. C. Schulthess, W. H. Butler, R. Sutton, and M. McHenry, *J. Appl. Phys.* **85**, 4833 (1999).
21. P. Novák and J. Pusz, *Phys. Rev. B* **71**, 184433 (2005).
22. M. Nakanishi, G.-i. Furusawa, K. Waki, Y. Hattori, K. Sasaki, K. Fukunaga, T. Hirayama, H. Saka and K. Kuroda, *Mater. Trans.* **48**, 2599 (2007).
23. O. A. Ivanov, L. V. Solina, V. A. Demshina, and L. M. Magat, *Phys. Met. Metallogr.* **35**, 81 (1973).
24. S. Sun, C. B. Murray, D. Weller, L. Folks, and A. Moser, *Science* **287**, 1989 (2000).
25. O. N. Mryasov, U. Nowak, K. Y. Guslienko, and R. W. Chantrell, *Europhys. Lett.* **69**, 805 (2005).
26. J. B. Staunton, L. Szunyogh, A. Buruzs, B. L. Gyorffy, S. Ostanin, and L. Udvardi, *Phys. Rev. B* **74**, 144411 (2006).
27. B. D. Cullity and C. D. Graham, *Introduction to Magnetic Materials*, Second Edition (Wiley, New Jersey, 2009), p. 121.
28. H. B. Callen and E. Callen, *J. Phys. Chem. Solids.* **27**, 1271 (1966).

## CHAPTER 7

### ELECTRONIC STRUCTURE AND MAGNETIC PROPERTIES OF NANOCRYSTALLINE SOFT MAGNETS<sup>8</sup>

#### 7.1. Introduction

Soft magnetic materials with high saturation magnetic flux density ( $B_s$ ), low coercivity ( $H_c$ ), high permeability ( $\mu$ ), and low core loss ( $P$ ) are necessary for the electronics and power industry, especially for energy saving. Among the important magnetic properties for the application, the  $B_s$  is especially significant for miniaturization of the devices in the electric and power systems because high  $B_s$  materials produce large magnetic flux per unit volume. Therefore, silicon steel [1] is widely used due to its high  $B_s$  ( $\geq 1.90$  T), low cost, and good productivity [2]. However, its low  $\mu$  of 720 at 1 kHz and high  $H_c$  of 26 A/m lead to a magnetic flux density ( $B$ ) of only 1.51 T at an applied magnetic field of 800 A/m [3]. In recent decades, soft magnetic materials with excellent magnetic softness and high  $\mu$ , such as FINEMET (Fe-Si-B-Nb-Cu) [4], NANOPERM (Fe- $M$ -Cu,  $M = \text{Zr, Hf, Nb, etc.}$ ) [5], HITPERM [(Fe, Co)- $M$ -B-Cu,  $M = \text{Zr, Hf, Nb, etc.}$ ] [6], and NANOMET (Fe-Si-B-P-Cu) [7,8] have been developed. These magnetic materials consist of Fe-based magnetic crystalline and amorphous phases, as well as a Cu based paramagnetic phase. The paramagnetic Cu is used as a nucleation agent of the Fe based crystalline phase [9], and its addition in the proper amount causes a decrease in the average grain size, as well as an increase in the density of nanograins, therefore, resulting in a decreased  $H_c$  [8]. Also, the B stabilizes the glassy amorphous phase [10]. The  $H_c$  and  $\mu$  of the FINEMET (Fe-Si-B-Nb-Cu) are noticeably improved to 0.5 A/m and 150,000 at 1 kHz, respectively. However, its

---

<sup>8</sup> This work was published as “Electronic Structures of Nanocrystalline  $\text{Fe}_{90-x}\text{Cu}_x\text{Si}_{10-y}\text{B}_y$  Soft Magnets,” in *AIP Advances* **6**, 055915 (2016) by Jihoon Park, Yang-Ki Hong, et al.

low  $B$  of 1.23 T at 800 A/m restricts the full usage of the material. The most recently developed nanocrystalline soft magnetic material, NANOMET, with high Fe concentration exhibits a high  $B$  of 1.82 T at 800 A/m, low  $H_c$  of 5.8 A/m, and high  $\mu$  of 27,000 at 1 kHz [3]. However, the theoretical study on the composition dependence of  $B_s$  for Fe-Si-B-Cu has not yet been reported.

Therefore, in this paper, we study the  $B_s$  dependence on the composition of  $\text{Fe}_{90-x}\text{Cu}_x\text{Si}_{10-y}\text{B}_y$  ( $0 \leq x \leq 2$  and  $0 \leq y \leq 10$ ). The density of states (DOS) of crystalline (Fe<sub>3</sub>Si) and amorphous (Fe-B) phases were separately obtained, and the corresponding magnetic moments and  $B_s$  were calculated. The calculated  $B_s$  of crystalline and amorphous phases were subsequently used to obtain the total  $B_s$  of  $\text{Fe}_{90-x}\text{Cu}_x\text{Si}_{10-y}\text{B}_y$  by  $B_s = B_{sc} \cdot V_c/V + B_{sa} \cdot V_a/V$ , where  $V$  is the total volume, and the subscripts  $c$  and  $a$  represent the crystalline and amorphous phase, respectively.

## 7.2. Method of calculations

In order to calculate the two different magnetic phases, we have used two separate tools to perform the first-principles calculations. The electronic structure of crystalline phase (Fe-Si) was calculated by the WIEN2k package [11] and the electronic structure of the amorphous phase (Fe-B) was calculated by the Vienna *ab initio* simulation package (VASP) [12,13]. The WIEN2k package is based on the density functional theory (DFT) and uses the full-potential linearized augmented plane wave (FP-LAPW) method with the dual basis set. The number of k-points in the full Brillouin zone was set to be 9,261 ( $21 \times 21 \times 21$ ). Experimental lattice constants of  $a = b = c = 5.65 \text{ \AA}$  [14] were used for the crystalline phase (Fe<sub>3</sub>Si) calculation. Fig. 7.1 illustrates the crystal structure of the Fe<sub>3</sub>Si used in the present calculations. In the Fe<sub>3</sub>Si structure, there are two

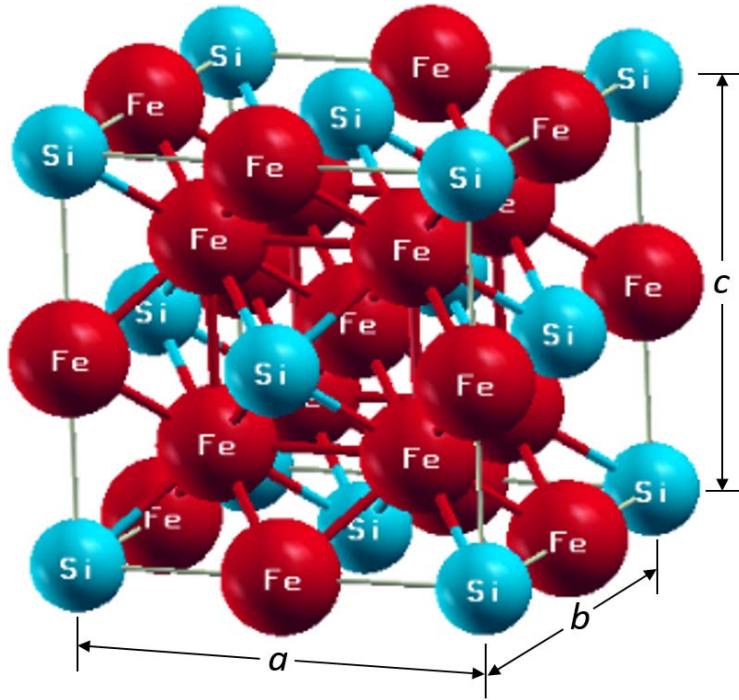


FIG. 7.1. Crystal structure of  $\text{Fe}_3\text{Si}$  with atoms colored as Fe-red and Si-light blue.

different sublattices for Fe. The Wyckoff symbols for the two sublattices are  $8c$  and  $4b$ , consisting of 8 and 4 Fe atoms, respectively, in a unit cell as shown in Fig. 7.1. All spin-polarized and spin-orbit coupling calculations were performed within the local-spin-density approximation (LSDA).

The electronic structure of amorphous phase (Fe-B) was calculated by the *ab initio* molecular dynamics (AIMD) [15] using VASP. Cubic supercells containing 250 atoms with a periodic boundary condition are used to model the alloys. All the alloys are initially equilibrated at 3000 K for 8 ps ( $1 \text{ ps} = 10^{-12} \text{ s}$ ), followed by quenching to 0 K to produce amorphous structures. The cubic cell is further relaxed to reach its local stable structure within the minimum energy landscape. In the amorphous Fe-B structures, Fe and B are randomly positioned. Therefore, atomic distances are also random, but the distance between each Fe is regularly much

larger than that between Fe and B. Accordingly, the volume of the Fe-B decreases with increasing B concentration. The structures are not shown in this paper.

### 7.3. Results and discussion

The DOS of Fe<sub>3</sub>Si is shown in Fig. 7.2. It is seen that the energy region near the Fermi energy ( $E_F$ ) is mostly attributed to the  $d$  bands of Fe. The  $d$  bands from  $8c$  and  $4b$  sublattices near the  $E_F$  show different behaviors, therefore, the magnetic moments from the  $8c$  and  $4b$  sublattices are different. The spin and orbital magnetic moments from Fe ( $8c$ ), Fe ( $4b$ ), and Si are summarized and compared with calculated [16] and experimental [17] results in Table 7.1. It is seen that the calculated spin moments are in good agreement with the calculated and

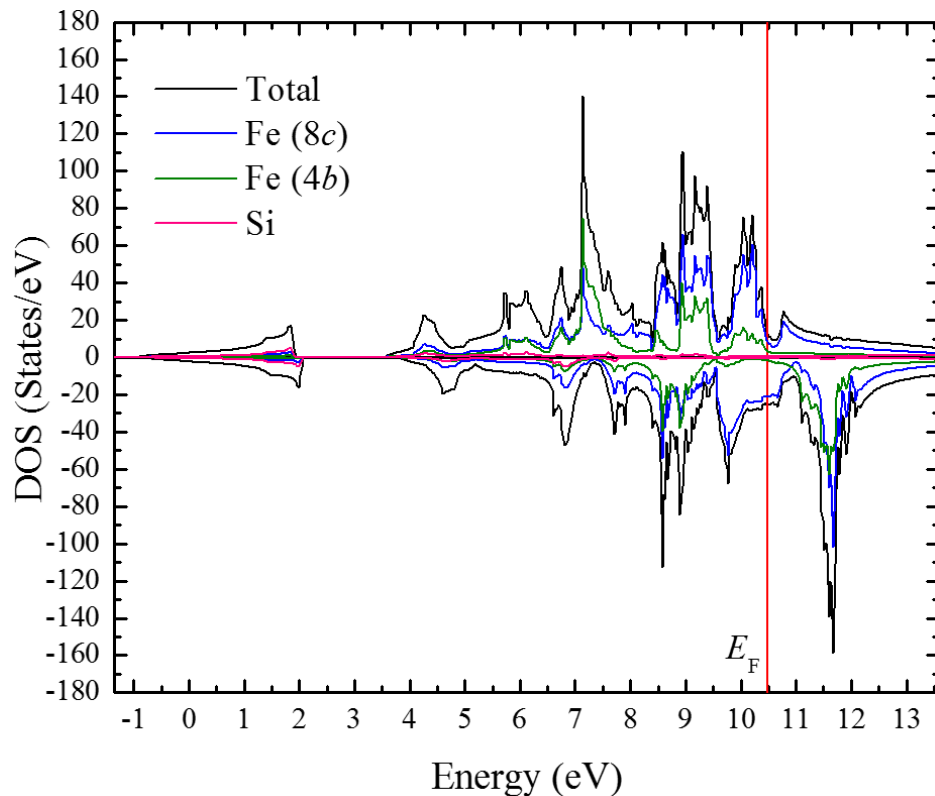


FIG. 7.2. Density of states (DOS) for Fe<sub>3</sub>Si. The black line represents the total DOS, and blue, green, and pink lines represent the partial DOS of Fe ( $8c$ ), Fe ( $4b$ ), and Si, respectively. The red vertical line corresponds to the Fermi energy ( $E_F$ ).

Table. 7.1. Calculated and experimental total and element specific spin and orbital magnetic moments ( $\mu_B$ ) and corresponding magnetic flux density (T) for crystalline Fe<sub>3</sub>Si.

	Spin Moment ( $\mu_B$ )			Orbital Moment ( $\mu_B$ )			Total Moment ( $\mu_B$ )	Magnetic Flux density (T)
	Fe (8c)	Fe (4b)	Si	Fe (8c)	Fe (4b)	Si		
Cal. <sup>a</sup>	1.31	2.54	-0.04	0.02245	0.04727	-0.00008	5.21	1.35
Cal. <sup>b</sup>	1.35	2.56	-0.06	-	-	-	5.20	1.35
Exp. <sup>c</sup>	1.35	2.4	-0.07	-	-	-	5.03	1.30

<sup>a</sup>This work, WIEN2K calculations within the DFT-LSDA.

<sup>b</sup>Ref. 16. WIEN2K calculations within the DFT-GGA.

<sup>c</sup>Ref. 17. particle size  $\leq 44 \mu\text{m}$ .

experimental results in the references. The total magnetic moment of Fe<sub>3</sub>Si is calculated to be 5.21  $\mu_B$ /f.u., which is converted to 1.35 T.

If only one Cu atom ( $x = 1$ ) exists in Fe<sub>90-x</sub>Cu<sub>x</sub>Si<sub>10-y</sub>B<sub>y</sub> and the number of B atoms vary from 1 to 9 ( $1 \leq y \leq 10$ ), the number of Fe<sub>3</sub>Si crystallites can vary from 9 to 0 and the consequent Fe-B compositions become Fe<sub>62</sub>B<sub>1</sub>, Fe<sub>65</sub>B<sub>2</sub>, Fe<sub>68</sub>B<sub>3</sub>, Fe<sub>71</sub>B<sub>4</sub>, Fe<sub>74</sub>B<sub>5</sub>, Fe<sub>77</sub>B<sub>6</sub>, Fe<sub>80</sub>B<sub>7</sub>, Fe<sub>83</sub>B<sub>8</sub>, Fe<sub>86</sub>B<sub>9</sub> and Fe<sub>89</sub>B<sub>10</sub>, respectively. These Fe to B ratio is fixed in the 250 atom cubic supercell to perform the AIMD calculation. The calculated DOS of Fe<sub>62</sub>B<sub>1</sub> and Fe<sub>86</sub>B<sub>9</sub> are shown in Fig. 7.3. The increasing B concentration results in the destroyed degeneracy of the DOS near the  $E_F$ , therefore, decreasing magnetic moments. The calculated magnetic moments of the Fe<sub>62</sub>B<sub>1</sub> (Fe<sub>0.984</sub>B<sub>0.016</sub>), Fe<sub>68</sub>B<sub>3</sub> (Fe<sub>0.958</sub>B<sub>0.042</sub>), Fe<sub>74</sub>B<sub>5</sub> (Fe<sub>0.937</sub>B<sub>0.063</sub>), Fe<sub>80</sub>B<sub>7</sub> (Fe<sub>0.920</sub>B<sub>0.080</sub>), and Fe<sub>86</sub>B<sub>9</sub>

Table. 7.2. Calculated magnetic moments ( $\mu_B$ ) and corresponding magnetic flux density (T) for the amorphous Fe-B in Fe<sub>89</sub>Cu<sub>1</sub>Si<sub>10-y</sub>B<sub>y</sub>.

	Fe <sub>62</sub> B <sub>1</sub> (Fe <sub>0.984</sub> B <sub>0.016</sub> )	Fe <sub>68</sub> B <sub>3</sub> (Fe <sub>0.958</sub> B <sub>0.042</sub> )	Fe <sub>74</sub> B <sub>5</sub> (Fe <sub>0.937</sub> B <sub>0.063</sub> )	Fe <sub>80</sub> B <sub>7</sub> (Fe <sub>0.920</sub> B <sub>0.080</sub> )	Fe <sub>86</sub> B <sub>9</sub> (Fe <sub>0.905</sub> B <sub>0.095</sub> )
Total Moment ( $\mu_B$ )	567.18	533.91	523.09	519.16	510.33
Magnetic Flux Density (T)	2.22	2.14	2.12	2.10	2.08

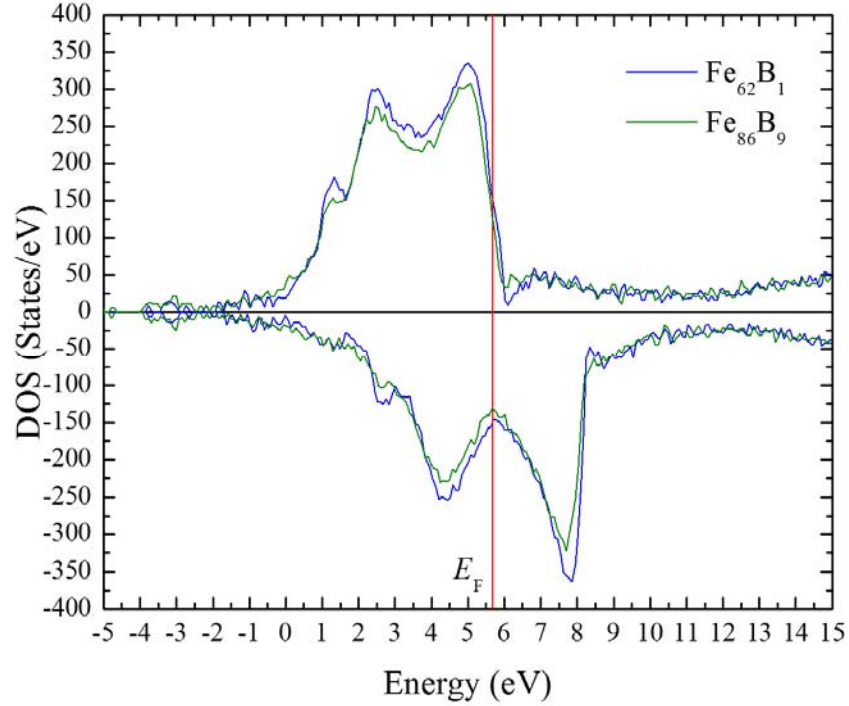


FIG. 7.3. Density of states (DOS) for (a)  $\text{Fe}_{62}\text{B}_1$  and (b)  $\text{Fe}_{86}\text{B}_9$ . The blue and green lines represent the total DOS of  $\text{Fe}_{62}\text{B}_1$  and  $\text{Fe}_{86}\text{B}_9$ , respectively. The red vertical line corresponds to the Fermi energy ( $E_F$ ).

( $\text{Fe}_{0.905}\text{B}_{0.095}$ ) are listed in Table 7.2. It is noted that the magnetic moment decreases with the increasing B concentration due to the decreasing Fe concentration, therefore, decreasing  $\alpha$ -Fe like crystal structure in the amorphous Fe-B.

Similarly, in the case where two Cu atoms ( $x = 2$ ) exit in  $\text{Fe}_{90-x}\text{Cu}_x\text{Si}_{10-y}\text{B}_y$  and the number of B atoms vary from 1 to 9 ( $1 \leq y \leq 10$ ), the number of  $\text{Fe}_3\text{Si}$  crystallites can vary from 9 to 0 and the consequent Fe-B compositions become  $\text{Fe}_{61}\text{B}_1$ ,  $\text{Fe}_{64}\text{B}_2$ ,  $\text{Fe}_{67}\text{B}_3$ ,  $\text{Fe}_{70}\text{B}_4$ ,  $\text{Fe}_{73}\text{B}_5$ ,  $\text{Fe}_{76}\text{B}_6$ ,  $\text{Fe}_{79}\text{B}_7$ ,  $\text{Fe}_{82}\text{B}_8$ ,  $\text{Fe}_{85}\text{B}_9$ , and  $\text{Fe}_{88}\text{B}_{10}$ , respectively. The trends of the calculated DOS of  $\text{Fe}_{61}\text{B}_1$  and  $\text{Fe}_{85}\text{B}_9$  in Fig. 7.4 and magnetic moments of  $\text{Fe}_{61}\text{B}_1$  ( $\text{Fe}_{0.984}\text{B}_{0.016}$ ),  $\text{Fe}_{73}\text{B}_5$  ( $\text{Fe}_{0.936}\text{B}_{0.064}$ ), and  $\text{Fe}_{85}\text{B}_9$  ( $\text{Fe}_{0.904}\text{B}_{0.096}$ ) in table 7.3 are similar to the case of  $x = 1$ , i.e., the decreasing magnetic moment with increasing B concentration.

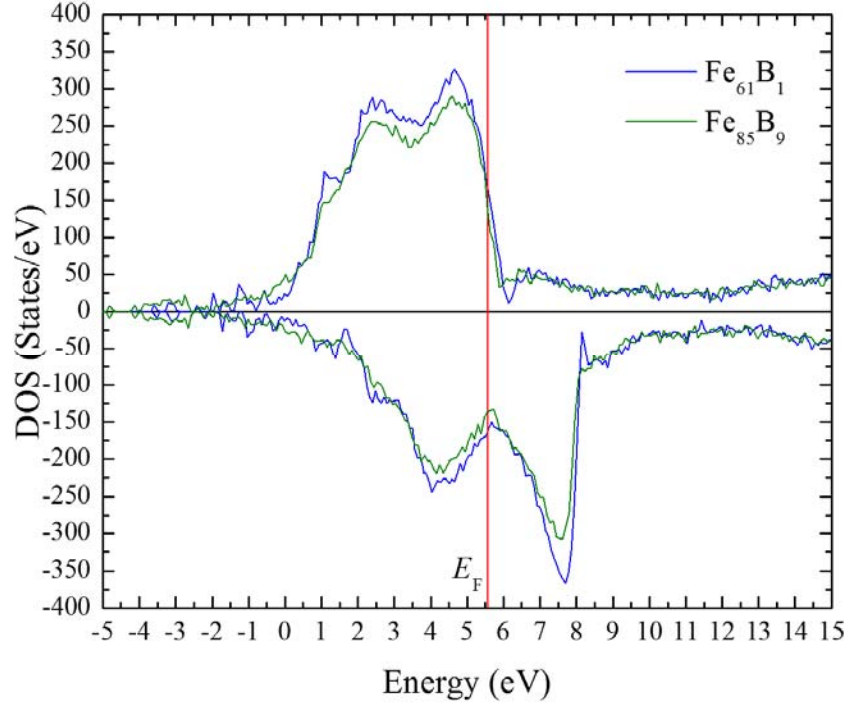


FIG. 7.4. Density of states (DOS) for (a)  $\text{Fe}_{61}\text{B}_1$  and (b)  $\text{Fe}_{85}\text{B}_9$ . The blue and green lines represent the total DOS of  $\text{Fe}_{61}\text{B}_1$  and  $\text{Fe}_{85}\text{B}_9$ , respectively. The red vertical line corresponds to the Fermi energy ( $E_F$ ).

Table. 7.3. Calculated magnetic moments ( $\mu_B$ ) and corresponding magnetic flux density (T) for the amorphous Fe-B in  $\text{Fe}_{88}\text{Cu}_2\text{Si}_{10-y}\text{B}_y$ .

	$\text{Fe}_{61}\text{B}_1$ ( $\text{Fe}_{0.984}\text{B}_{0.016}$ )	$\text{Fe}_{73}\text{B}_5$ ( $\text{Fe}_{0.936}\text{B}_{0.064}$ )	$\text{Fe}_{85}\text{B}_9$ ( $\text{Fe}_{0.904}\text{B}_{0.096}$ )
Total Moment ( $\mu_B$ )	561.60	528.18	502.64
Magnetic Flux Density (T)	2.15	2.10	2.04

Next, the  $B_s$  dependence on the compositions of  $\text{Fe}_{90-x}\text{Cu}_x\text{Si}_{10-y}\text{B}_y$  ( $0 \leq x \leq 2$  and  $0 \leq y \leq 10$ ) was calculated by  $B_s = B_{sc} \cdot V_c/V + B_{sa} \cdot V_a/V$ , where  $V$  is the total volume, and the subscripts  $c$  and  $a$  represent the crystalline ( $\text{Fe}_3\text{Si}$ ) and amorphous (Fe-B) phases, respectively. Here, the  $B_{sc}$  and  $B_{sa}$  are the  $B_s$  of  $\text{Fe}_3\text{Si}$  and Fe-B, respectively, and the  $V_c$  and  $V_a$  are the volumes of  $\text{Fe}_3\text{Si}$  and Fe-B. It is noted that the volume of Cu was also considered in the  $B_s$  calculations for the  $\text{Fe}_{90-x}\text{Cu}_x\text{Si}_{10-y}\text{B}_y$ . The calculated  $B_s$  and volumes are summarized in Table 7.4 for  $\text{Fe}_{89}\text{Cu}_1\text{Si}_{10-y}\text{B}_y$

Table. 7.4. Calculated magnetic flux density (T) and volumes ( $\text{\AA}^3$ ) for  $(10 - y) \cdot \text{Fe}_3\text{Si}$ , Fe-B, and  $1 \cdot \text{Cu}$ , and corresponding magnetic flux density (T) for  $\text{Fe}_{89}\text{Cu}_1\text{Si}_{10-y}\text{B}_y$ .

$y$	$\text{Fe}_{89}\text{Cu}_1\text{Si}_{10-y}\text{B}_y$						Composition
1	$9 \cdot \text{Fe}_3\text{Si}$		$\text{Fe}_{62}\text{B}_1$		$1 \cdot \text{Cu}$		$\text{Fe}_{89}\text{Cu}_1\text{Si}_9\text{B}_1$
	1.35 T	$203 \text{\AA}^3$	2.22 T	$740 \text{\AA}^3$	0 T	$12 \text{\AA}^3$	1.73 T
3	$7 \cdot \text{Fe}_3\text{Si}$		$\text{Fe}_{68}\text{B}_3$		$1 \cdot \text{Cu}$		$\text{Fe}_{89}\text{Cu}_1\text{Si}_7\text{B}_3$
	1.35 T	$158 \text{\AA}^3$	2.14 T	$826 \text{\AA}^3$	0 T	$12 \text{\AA}^3$	1.78 T
5	$5 \cdot \text{Fe}_3\text{Si}$		$\text{Fe}_{74}\text{B}_5$		$1 \cdot \text{Cu}$		$\text{Fe}_{89}\text{Cu}_1\text{Si}_5\text{B}_5$
	1.35 T	$113 \text{\AA}^3$	2.12 T	$911 \text{\AA}^3$	0 T	$12 \text{\AA}^3$	1.87 T
7	$3 \cdot \text{Fe}_3\text{Si}$		$\text{Fe}_{80}\text{B}_7$		$1 \cdot \text{Cu}$		$\text{Fe}_{89}\text{Cu}_1\text{Si}_3\text{B}_7$
	1.35 T	$68 \text{\AA}^3$	2.10 T	$999 \text{\AA}^3$	0 T	$12 \text{\AA}^3$	1.96 T
9	$1 \cdot \text{Fe}_3\text{Si}$		$\text{Fe}_{86}\text{B}_9$		$1 \cdot \text{Cu}$		$\text{Fe}_{89}\text{Cu}_1\text{Si}_1\text{B}_9$
	1.35 T	$23 \text{\AA}^3$	2.08 T	$1084 \text{\AA}^3$	0 T	$12 \text{\AA}^3$	2.03 T

Table. 7.5. Calculated magnetic flux density (T) and volumes ( $\text{\AA}^3$ ) for  $(10 - y) \cdot \text{Fe}_3\text{Si}$ , Fe-B, and  $2 \cdot \text{Cu}$ , and corresponding magnetic flux density(T) for  $\text{Fe}_{88}\text{Cu}_2\text{Si}_{10-y}\text{B}_y$ .

$y$	$\text{Fe}_{88}\text{Cu}_2\text{Si}_{10-y}\text{B}_y$						Composition
1	$9 \cdot \text{Fe}_3\text{Si}$		$\text{Fe}_{61}\text{B}_1$		$2 \cdot \text{Cu}$		$\text{Fe}_{88}\text{Cu}_2\text{Si}_9\text{B}_1$
	1.35 T	$203 \text{\AA}^3$	2.22 T	$753 \text{\AA}^3$	0 T	$24 \text{\AA}^3$	1.69 T
5	$5 \cdot \text{Fe}_3\text{Si}$		$\text{Fe}_{73}\text{B}_5$		$2 \cdot \text{Cu}$		$\text{Fe}_{88}\text{Cu}_2\text{Si}_5\text{B}_5$
	1.35 T	$113 \text{\AA}^3$	2.16 T	$916 \text{\AA}^3$	0 T	$24 \text{\AA}^3$	1.85 T
9	$1 \cdot \text{Fe}_3\text{Si}$		$\text{Fe}_{85}\text{B}_9$		$2 \cdot \text{Cu}$		$\text{Fe}_{88}\text{Cu}_2\text{Si}_1\text{B}_9$
	1.35 T	$23 \text{\AA}^3$	2.10 T	$1078 \text{\AA}^3$	0 T	$24 \text{\AA}^3$	1.99 T

and in Table 7.5 for  $\text{Fe}_{88}\text{Cu}_2\text{Si}_{10-y}\text{B}_y$ . According to Table 7.4 and Table 7.5, the  $B_s$  of  $\text{Fe}_{90-x}\text{Cu}_x\text{Si}_{10-y}\text{B}_y$  increases with increasing B concentrations ( $y$ ). The relation between B concentration and  $B_s$  for the  $\text{Fe}_{89}\text{Cu}_1\text{Si}_{10-y}\text{B}_y$  and  $\text{Fe}_{88}\text{Cu}_2\text{Si}_{10-y}\text{B}_y$  are presented in Fig. 7.5, and compared with  $B_s$  of  $\alpha\text{-Fe}$  and  $\text{Fe}_3\text{Si}$ . Fig. 7.5 shows that a  $B_s$  higher than 1.8 T can be achieved with a  $y$  similar to or higher than 4 for both  $\text{Fe}_{89}\text{Cu}_1\text{Si}_{10-y}\text{B}_y$  and  $\text{Fe}_{88}\text{Cu}_2\text{Si}_{10-y}\text{B}_y$ .

#### 7.4. Conclusions

In summary, in an effort to investigate the composition dependence of saturation magnetic flux density ( $B_s$ ) for the nanocrystalline  $\text{Fe}_{90-x}\text{Cu}_x\text{Si}_{10-y}\text{B}_y$ , FPLAPW and AIMD

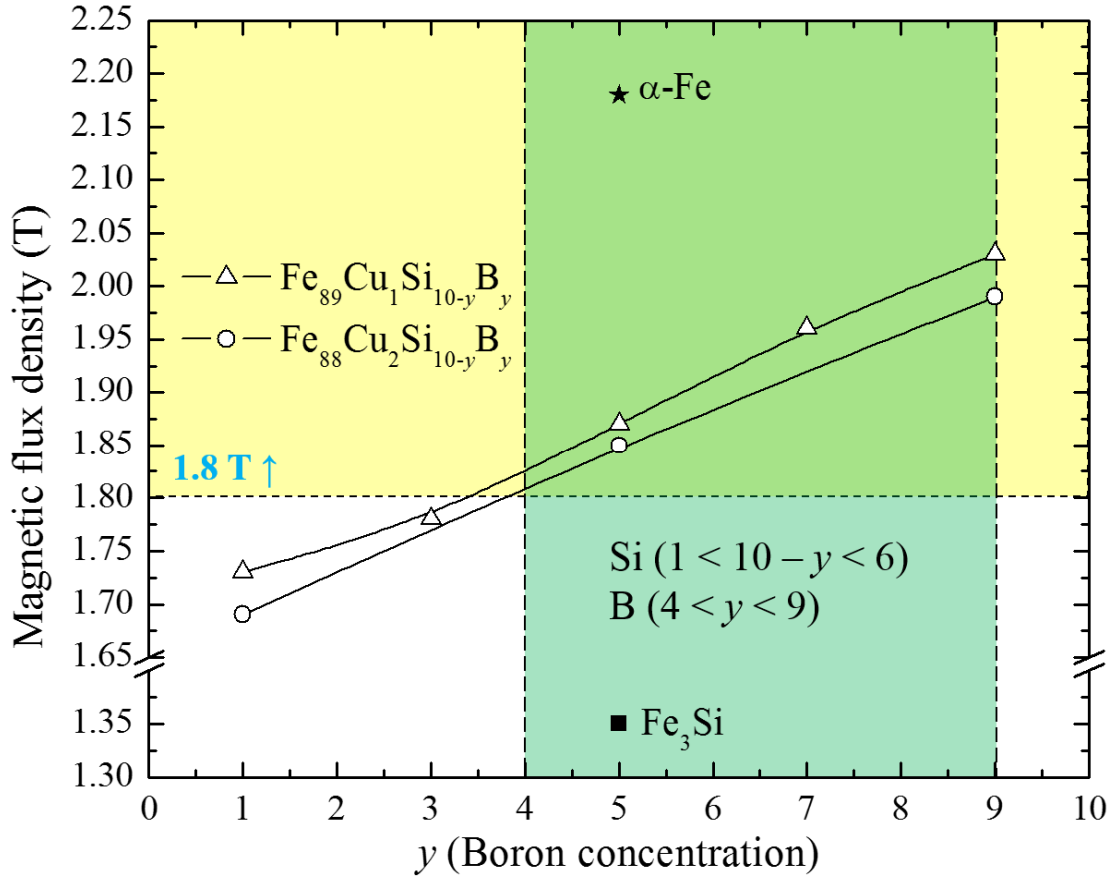


FIG. 7.5. Magnetic flux density for the  $\text{Fe}_{90-x}\text{Cu}_x\text{Si}_{10-y}\text{B}_y$  ( $1 \leq x \leq 2$  and  $1 < y < 9$ ). The yellow region indicates the magnetic flux density higher than 1.8 T, and the green region corresponds to the B concentration of  $4 < y < 9$ .

calculations for the crystalline ( $\text{Fe}_3\text{Si}$ ) and amorphous (Fe-B) phases were performed, respectively. The calculated  $B_s$  for the  $\text{Fe}_3\text{Si}$  and Fe-B were used to derive the total  $B_s$  of  $\text{Fe}_{90-x}\text{Cu}_x\text{Si}_{10-y}\text{B}_y$  ( $1 \leq x \leq 2$  and  $1 < y < 9$ ). It was found that increasing the B concentration results in an increased  $B_s$  for both  $x = 1$  and 2, and consequently, reaching higher than 1.8 T for  $y \geq 4$ .

## 7.5. References

1. N. P. Goss, *Trans. Am. Soc. Met.* **23**, 511531 (1935).
2. K. Takenaka, A. D. Setyawan, Y. Zhang, P. Sharma, N. Nishiyama, and A. Makino, *Materials Transactions* **56**, 372 (2015).

3. A. Makino, *IEEE Trans. Magn.* **48**, 1331 (2012).
4. P. Allia, C. Beatrice, F. Vinai, M. Knobel, R. Turtelli, *Applied Physics Lett.* **59**, 2454 (1991).
5. A. Makino, T. Hatanai, Y. Naitoh, T. Bitoh, *IEEE Trans. Magn.* **33**, 3793 (1997).
6. M. A. Willard, M.-Q. Huang, D. E. Laughlin, M. E. McHenry, J. O. Cross, V. G. Harris, C. Franchetti, *J. Appl. Phys.* **85**, 4421 (1999).
7. A. Makino, H. Men, T. Kubota, K. Yubuta, A. Inoue, *IEEE Trans. Magn.* **45**, 4302 (2009).
8. F. Kong, A. Wang, X. Fan, H. Men, B. Shen, G. Xie, A. Makino, A. Inoue, *J. Appl. Phys.* **109**, 07A303 (2011).
9. K. Hono, D. H. Ping, M. Ohnuma, and H. Onodera, *Acta Materialia.* **47**, 997 (1999).
10. K. Hono, K. Hiraga, Q. Wang, A. Inoue, and T. Sakurai, *Acta Metall. Mater.* **40**, 2137 (1992).
11. P. Blaha, K. Schwarz, G. K. H. Madsen, D. Kvasnicka and J. Luitz, WIEN2k, Inst. f. Materials Chemistry TU Vienna (2001).
12. G. Kresse, J. Hafner, *Phys. Rev. B* **47**, 558 (1993).
13. G. Kresse, J. Furthmüller, *Phys. Rev. B* **54**, 11169 (1996).
14. A. Niculescu, T. J. Burch, and J. I. Budnik, *J. Magn. Magn. Mater.* **39**, 223 (1983).
15. A. Tilocca, *Phys. Rev. B* **76**, 224202 (2007).
16. D. Odkhuu and S. C. Hong, *IEEE Trans. Magn.* **47**, 2920 (2011).
17. V. Niculescu, K. Raj, J. I. Budnick, T. J. Burch, W. A. Hines, and A. H. Menotti, *Phys. Rev. B* **14**, 4160 (1976).

## CHAPTER 8

### ELECTRONIC STRUCTURE AND MAGNETIC PROPERTIES OF MnB SOFT MAGNETS<sup>9</sup>

#### 8.1. Introduction

The  $3d$  transition metal borides have received much attention because of their hardness, high melting point, wear resistance, corrosion resistance, and catalytic properties, as well as good electric and thermal conduction and magnetic properties [1-5]. We are interested in MnB due to its high saturation magnetization ( $M_s$ ) and low coercivity ( $H_{ci}$ ). Although Hund's rule predicts the highest magnetic moment for Mn among all the  $3d$  transition metals, Mn metal shows antiferromagnetic behavior due to its close atomic distance, filling the outer electron shell with electrons of both up and down spins. Therefore, in order to increase the distance between Mn atoms, second and third elements have been doped into the Mn metals [6]. Likewise, B doping into Mn metal increases the distance between Mn atoms, therefore, transition from antiferromagnetic to ferromagnetic order occurs, and its magnetic moment increases.

In this paper, in order to gain more insight into magnetic properties of the  $3d$  transition metal boride MnB alloy, we have performed first-principles calculations to calculate electronic structures. We report theoretical  $M_s$ , anisotropy constant ( $K$ ) and temperature dependence of saturation magnetization [ $M_s(T)$ ].

#### 8.2. Method of calculations

---

<sup>9</sup> This work was published as "Electronic Structures of MnB Soft Magnets," in *AIP Advances* **6**, 055911 (2016) by Jihoon Park, Yang-Ki Hong, et al.

The WIEN2k package [7] was used to perform first-principles calculations. The package is based on the density functional theory (DFT) and uses the full-potential linearized augmented plane wave (FPLAPW) method with the dual basis set. For the MnB calculations, the  $3p$ ,  $3d$ , and  $4s$  states of Mn and the  $2s$  and  $2p$  states of B were treated as valence states. All calculations used a  $12 \times 12 \times 17$  mesh generating 2,448 k-points in the irreducible part of the Brillouin zone. The muffin tin radii (RMT) were 2.09 a.u. for Mn and 1.63 a.u. for B. Fig. 8.1 illustrates the crystal structure of MnB with experimental lattice constants  $a = 5.58 \text{ \AA}$ ,  $b = 2.98 \text{ \AA}$  and  $c = 4.15 \text{ \AA}$  [8] used in the present calculations. All spin-polarized and spin-orbit coupling calculations are based on the density functional theory within the local-spin-density approximation (LSDA).

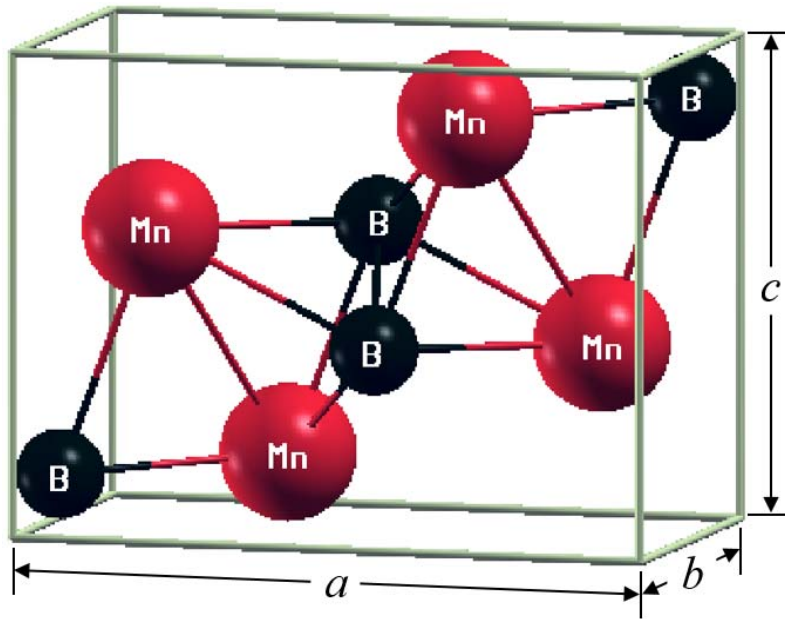


FIG. 8.1. Crystal structures of MnB with atoms colored as Mn-red and B-black.

### 8.3. Results and discussion

The spin-polarized and spin-orbit coupling calculations were performed for different magnetization directions and their relative total energies ( $\Delta E$ ) are summarized in Table 8.1. The

Table 8.1. Magnetization directions and corresponding relative energies ( $\Delta E$ ) in the unit of mRy.

Magnetization direction	$\Delta E$ (mRy)
001	0.00000
010	-0.02905
100	-0.01597
011	-0.00222
101	-0.01267
110	-0.01507
111	-0.05951

lowest total energy is found for the magnetization direction of  $\langle 111 \rangle$  in the MnB crystal structure, therefore, the spins tend to align in  $\langle 111 \rangle$  direction at zero applied magnetic field. The second lowest energy is found when magnetization is in  $\langle 010 \rangle$  direction. Therefore, if the spins rotate through  $\langle 010 \rangle$  direction from  $\langle 111 \rangle$  direction, the anisotropy constant ( $K$ ) of MnB can be calculated by the total energy difference between  $\langle 010 \rangle$  and  $\langle 111 \rangle$  spin configurations,  $\Delta E =$

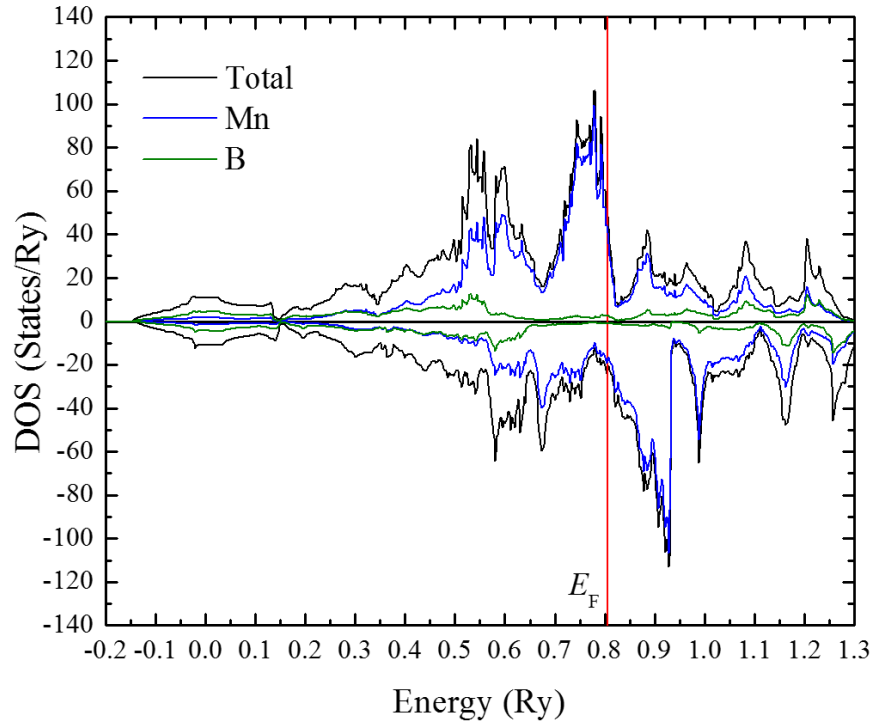


FIG. 8.2. Density of states (DOS) for MnB. The black line represents the total DOS, and blue and green lines represent the partial DOS of Mn and B, respectively. The red vertical line corresponds to the Fermi energy ( $E_F$ ).

$E_{\langle 010 \rangle} - E_{\langle 111 \rangle} = 0.03046$  meV/u.c., corresponding to  $K$  of  $9.6 \times 10^6$  erg/cm<sup>3</sup> which is higher than the calculated  $K$  of  $3.3 \times 10^6$  erg/cm<sup>3</sup> at 300 K by the Law of Approach to Saturation [9].

Fig. 8.2 shows the density of states (DOS) of MnB. It is seen that the energy region near the Fermi energy ( $E_F$ ) is mostly attributed to  $d$  bands of Mn, therefore, the magnetic moment of MnB is mostly contributed by the  $d$  bands of Mn. The spin and orbital magnetic moments from the spin-polarized and spin-orbit coupling calculations for Mn and B are listed in Table 8.2.

The total magnetic moment of MnB, i.e.,  $1.795 \mu_B/\text{f.u.}$ , is converted to  $964.5$  emu/cm<sup>3</sup> (1.21 T), and compared with calculated [9] and experimental [10] results in Table 8.3. It is seen that the calculated spin moments are in good agreement with the calculated and experimental results in the references.

Table 8.2. The calculated spin and orbital magnetic moments per formula unit (f.u.) and Mn and B atoms for MnB in the unit of  $\mu_B$ .

Direction of magnetization	Spin Moment		Orbital Moment		Total Moment	
	f.u.	Mn B	f.u.	Mn B	f.u.	Mn B
Spin-polarized	1.802	1.862 -0.060			1.802	1.862 -0.060
$\langle 111 \rangle$	1.779	1.837 -0.058	0.01563	0.01587 -0.00024	1.795	1.853 -0.058

Table 8.3. The calculated magnetic moments per formula unit ( $\mu_B/\text{f.u.}$ ) and corresponding magnetizations (emu/cm<sup>3</sup>) and magnetic flux densities (T) of MnB.

	Magnetic Moment ( $\mu_B/\text{f.u.}$ )	Magnetization (emu/cm <sup>3</sup> )	Magnetic Flux Density (T)
Cal. <sup>a</sup>	1.795	964.5	1.21
Cal. <sup>b</sup>	1.914	1034.4	1.30
Exp. <sup>c</sup>	-	799.8	1.00

<sup>a</sup>This work, WIEN2k calculations within the DFT-LSDA.

<sup>b</sup>Ref. 9. WIEN2k calculations within the DFT-GGA.

<sup>c</sup>Ref. 10. bulk.

We used the mean field approximation (MFA) [11] to calculate  $M_s(T)$ , given by:

$$M_s(T) = M_s(0)B_J(\tau) \quad (8.1)$$

where  $M_s(0)$  is the saturation magnetization at 0 K,  $B_J$  is the Brillouin function with angular quantum number ( $J$ ) and normalized temperature ( $\tau = T/T_c$ ). The calculated  $M_s(0)$  of 964.5 emu/cm<sup>3</sup> and  $J$  of two and experimental  $T_c$  of 578 K [10] were used to calculate the  $M_s(T)$ . The calculated  $M_s(T)$  is shown in Fig. 8.3 and compared with calculated and experimental  $M_s$  [9,10]. It is seen that the calculated  $M_s(T)$  is in good agreement with the previously reported results. The calculated  $M_s$  at 300 K is 859.3 emu/cm<sup>3</sup> (1.08 T) which is close to the experimental  $M_s$  of 851.5 emu/cm<sup>3</sup> [9]. According to the calculated  $M_s(T)$  and experimental  $M_s$  at 300 K, the  $M_s$  of MnB (859.3 emu/cm<sup>3</sup>) is higher than that of permalloy (721.5 emu/cm<sup>3</sup>) [12], but the  $K$  of MnB ( $9.6 \times 10^6$  erg/cm<sup>3</sup>) at 0 K.

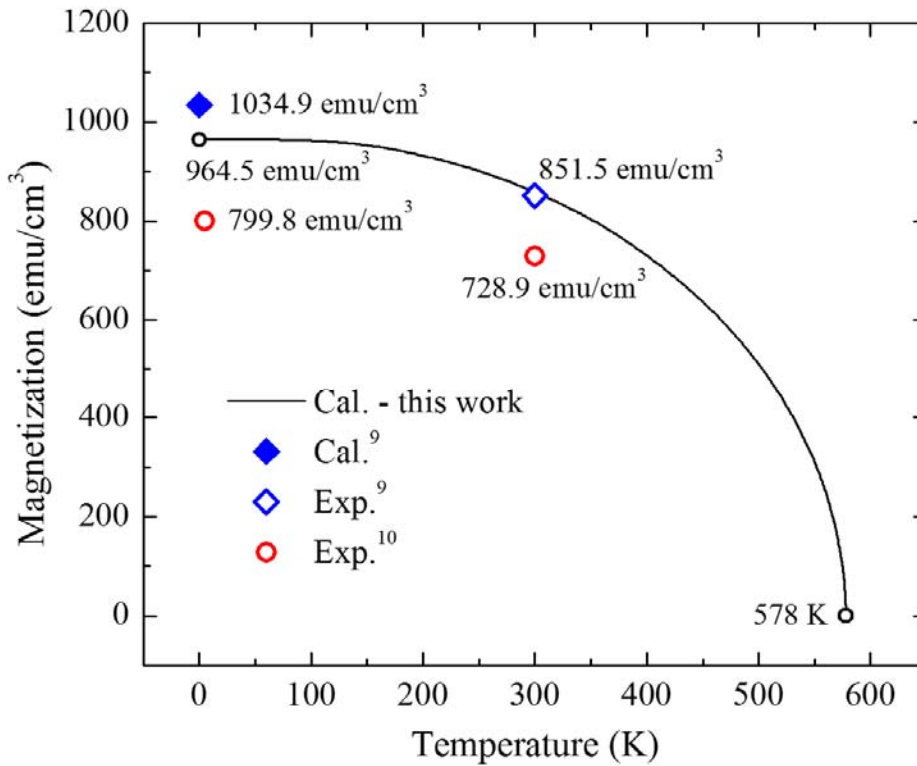


FIG. 8.3. The calculated temperature dependence of magnetization  $M_s(T)$  for MnB. The  $M_s(T)$  is compared with calculated and experimental magnetizations.

## 8.4. Conclusions

In summary, first-principles calculations were performed on MnB alloy to investigate its electronic structure. The density of states (DOS) and corresponding saturation magnetization ( $M_s$ ) at 0 K were calculated. The calculated  $M_s$  and experimental  $T_c$  were used to obtain temperature dependence of magnetization [ $M_s(T)$ ], and compared with previously reported calculated and experimental results.  $M_s$  and anisotropy constant ( $K$ ) were calculated to be 859.3 emu/cm<sup>3</sup> at 300 K and  $9.6 \times 10^6$  erg/cm<sup>3</sup> at 0 K, respectively.

## 8.5. References

1. P. Mohn, D. G. Pettifor, J. Phys. C. Solid State Phys. **21**, 2829 (1988).
2. G. Li, D. Wang, J. Phys. Condens. Matter **1**, 1799 (1989).
3. W. Y. Ching, Y.-N. Xu, B. N. Harmon, J. Ye, T. C. Leung, Phys. Rev. B **42**, 4460 (1990).
4. B. Xiao, J. D. Xing, S. F. Ding, W. Su, Physica B **403**, 1723 (2008).
5. P. H. Lee, Z. R. Xiao, K. L. Chen, Y. Chen, S. W. Kao, T. S. Chin, Physica B **404**, 2009 (1989).
6. J. H. Park, Y. K. Hong, J. J. Lee, W. C. Lee, S. G. Kim, and C. J. Choi, Metal **4**, 455 (2014).
7. P. Blaha, K. Schwarz, G. K. H. Madsen, D. Kvasnicka and J. Luitz, WIEN2k, Inst. f. Materials Chemistry TU Vienna (2001).
8. G. Pradelli, C. Gianoglio, E. Quadrini, *Ricerca sui boruri di cobalto e manganese*. Metallurgia Italiana **70**, 122 (1978).
9. T. Simsek and S. Ozcan, *IEEE Trans. Magn.* **51**, p. 2001903 (2015).
10. H. Zhu, C. Ni, F. Zhang, Y. Du, and J. Q. Xiao, J Appl. Phys. **97**, 10M512 (2005).
11. B. D. Cullity, C. D. Graham, *Introduction to Magnetic Materials*, 2nd ed. (Wiley: Hoboken, NJ, USA, 2009) p. 121.
12. C. Luo, Y. Fu, D. Zhang, S. Yuan, Y. Zhai, S. Dong, H. Zhai, J. Magn. Mater. **374**, 711 (2015).

## CHAPTER 9

### MAGNETIC PROPERTIES OF EXCHANGE COUPLED MnAl/FeCo<sup>10</sup>

#### 9.1. Introduction

A figure of merit for permanent magnets is the maximum energy product  $(BH)_{\max}$ . The  $(BH)_{\max}$  for Nd<sub>2</sub>Fe<sub>14</sub>B are theoretically 64 MGOe [1] and experimentally 56 MGOe [2]. However, a low operation temperature and limited availability of rare-earth (RE) elements are potential barriers against the use of these RE element-based permanent magnets. Therefore, discovery of RE-free permanent magnets with high  $(BH)_{\max}$  is an emerging issue to address. Accordingly, ferromagnetic  $\tau$ -phase Mn-Al [3,4] receives much attention, because of its high magnetic moment ( $2.4 \mu_B/\text{f.u.}$ ) [5,6] and magnetocrystalline anisotropy constant ( $1.5 \times 10^6 \text{ J/m}^3$ ) [5,6], and low cost. It has been reported [7] that experimental remanent magnetic flux density ( $B_r$ ), intrinsic coercivity ( $H_{ci}$ ), and  $(BH)_{\max}$  of  $\tau$ -phase Mn-Al magnet are 7 kG, 2.35 kOe, and 9.2 MGOe, respectively. However, it is noted that those  $B_r$ ,  $H_{ci}$ , and  $(BH)_{\max}$  are still much lower compared to RE-based permanent magnets.

Therefore, magnetic exchange coupling between hard and soft magnetic phases has been proposed and experimentally studied to further increase  $(BH)_{\max}$  of RE-free permanent magnets. Soft magnetic phase can be exchange coupled with hard magnetic phase within two times of domain wall thickness ( $2\delta_w$ ) of hard magnetic phase [8]. The exchange coupling makes full use of high coercivity from hard phase and magnetization from soft phase. Therefore, it is possible to achieve large  $(BH)_{\max}$  of the RE-free permanent magnet by the exchange coupling. Exchange

---

<sup>10</sup> This work was published as “Magnetization and Intrinsic Coercivity for  $\tau$ -phase Mn<sub>54</sub>Al<sub>46</sub>/ $\alpha$ -phase Fe<sub>65</sub>Co<sub>35</sub> Composite,” in *Journal of Magnetism* **91**, 55 (2014) by Jihoon Park, Yang-Ki Hong, et al.

coupled magnets based on hard magnetic phases of Fe-Pt [9,10,11], Sm-Co [12], and Nd<sub>2</sub>Fe<sub>14</sub>B [13], have been extensively studied. However, these exchange coupled magnets still contain RE or precious elements, and the exchange coupling effect is not noticeable in Nd<sub>2</sub>Fe<sub>14</sub>B because there is already a high magnetic moment.

In this paper, we report a unique annealing process to synthesize two-phase hard  $\tau$ -phase Mn<sub>54</sub>Al<sub>46</sub>/soft  $\alpha$ -phase Fe<sub>65</sub>Co<sub>35</sub> composite magnets, and propose a simple composition dependent coercivity equation to explain experimental coercivity.

## 9.2. Experiments

Paramagnetic  $\varepsilon$ -phase Mn<sub>54</sub>Al<sub>46</sub> particles were synthesized by gas-atomization. After having dissolved Fe- and Co-salts and dispersed the  $\varepsilon$ -phase Mn<sub>54</sub>Al<sub>46</sub> particles in de-ionized water, a NaBH<sub>4</sub> solution was added to the solution. Thereby, Fe- and Co-salts were reduced to  $\alpha$ -phase Fe<sub>65</sub>Co<sub>35</sub> metal alloy particles. Then,  $\varepsilon$ -phase Mn<sub>54</sub>Al<sub>46</sub>/ $\alpha$ -phase Fe<sub>65</sub>Co<sub>35</sub> cakes ( $0 < f_h < 1$ ) were dried at 100 °C, and consequently, annealed at 650 °C for 1 hour under Ar environment. The  $f_h$  is the volume fraction of magnetically hard phase. Both  $\alpha$ -phase Fe<sub>65</sub>Co<sub>35</sub> ( $f_h = 0$ ) and  $\tau$ -phase Mn<sub>54</sub>Al<sub>46</sub> ( $f_h = 1$ ) particles were also prepared as reference materials.

The crystalline phases of Fe<sub>65</sub>Co<sub>35</sub> and Mn<sub>54</sub>Al<sub>46</sub> particles and their composites were identified with X-ray diffraction (XRD). A vibrating sample magnetometer (VSM) was used to characterize their magnetic properties. The particle size and size distribution were determined using transmission electron microscopy (TEM) and scanning electron microscope (SEM). Also, we have performed elemental mappings on the composites with scanning electron microscopy-energy dispersive X-ray spectrometry (SEM-EDS) to observe elemental distribution.

### 9.3. Results and discussion

The gas-atomized  $\text{Mn}_{54}\text{Al}_{46}$  is paramagnetic  $\varepsilon$ -phase, and its shape is spherical (7 - 70  $\mu\text{m}$  in diameter), while the as-synthesized  $\text{Fe}_{65}\text{Co}_{35}$  is ferromagnetic  $\alpha$ -phase spherical chain (40 nm in average diameter). These were confirmed by XRD, SEM, and TEM, which are not shown in this paper. We have synthesized  $\varepsilon$ -phase  $\text{Mn}_{54}\text{Al}_{46}/\alpha$ -phase  $\text{Fe}_{65}\text{Co}_{35}$  composites with various volume fractions of hard phase, i.e.  $f_h = 0.327, 0.500, 0.694, 0.773, \text{ and } 0.819$ . As described in the experimental section, the synthesized composite was annealed at 650  $^{\circ}\text{C}$  to convert the paramagnetic  $\varepsilon$ -phase  $\text{Mn}_{54}\text{Al}_{46}$  to ferromagnetic  $\tau$ -phase  $\text{Mn}_{54}\text{Al}_{46}$ . The prolonged annealing causes paramagnetic  $\beta$ - or  $\gamma$ -phase  $\text{Mn}_{54}\text{Al}_{46}$  to nucleate. Therefore, we have optimized annealing time of one hour. Ferromagnetic  $\alpha$ -phase  $\text{Fe}_{65}\text{Co}_{35}$  ( $f_h = 0.000$ ) and paramagnetic  $\varepsilon$ -phase  $\text{Mn}_{54}\text{Al}_{46}$  ( $f_h = 1.000$ ) particles were annealed, separately, under the same annealing conditions as those used for annealing of  $\varepsilon$ -phase  $\text{Mn}_{54}\text{Al}_{46}/\alpha$ -phase  $\text{Fe}_{65}\text{Co}_{35}$  composites. This is because we wanted to compare magnetic properties of annealed single phase  $\tau$ -phase  $\text{Mn}_{54}\text{Al}_{46}$  and  $\alpha$ -phase  $\text{Fe}_{65}\text{Co}_{35}$  to those of  $\tau$ -phase  $\text{Mn}_{54}\text{Al}_{46}/\alpha$ -phase  $\text{Fe}_{65}\text{Co}_{35}$  composite.

Figure 9.1 shows elemental mapping image of ferromagnetic  $\tau$ -phase  $\text{Mn}_{54}\text{Al}_{46}/\alpha$ -phase  $\text{Fe}_{65}\text{Co}_{35}$  composite ( $f_h = 0.819$ ). It can be seen that Mn, Al, Fe, and Co elements are well distributed, and Fe and Co elements are more concentrated on the MnAl particles' surface than Mn and Al elements. This indicates that  $\text{Mn}_{54}\text{Al}_{46}$  particles are well covered with  $\text{Fe}_{65}\text{Co}_{35}$  particles during the reducing and annealing processes.

Figure 9.2 shows XRD patterns and magnetic hysteresis loops of the  $\tau$ -phase  $\text{Mn}_{54}\text{Al}_{46}$ ,  $\alpha$ -phase  $\text{Fe}_{65}\text{Co}_{35}$ , and composite with  $f_h = 0.819$ . All the  $\tau$ -phase  $\text{Mn}_{54}\text{Al}_{46}$ ,  $\alpha$ -phase  $\text{Fe}_{65}\text{Co}_{35}$ , and composite ( $f_h = 0.819$ ) are well crystallized. The  $\tau$ -phase  $\text{Mn}_{54}\text{Al}_{46}$  shows the saturation magnetization of 53 emu/g and intrinsic coercivity ( $H_{ci}$ ) of 3093 Oe, and  $\alpha$ -phase  $\text{Fe}_{65}\text{Co}_3$  shows

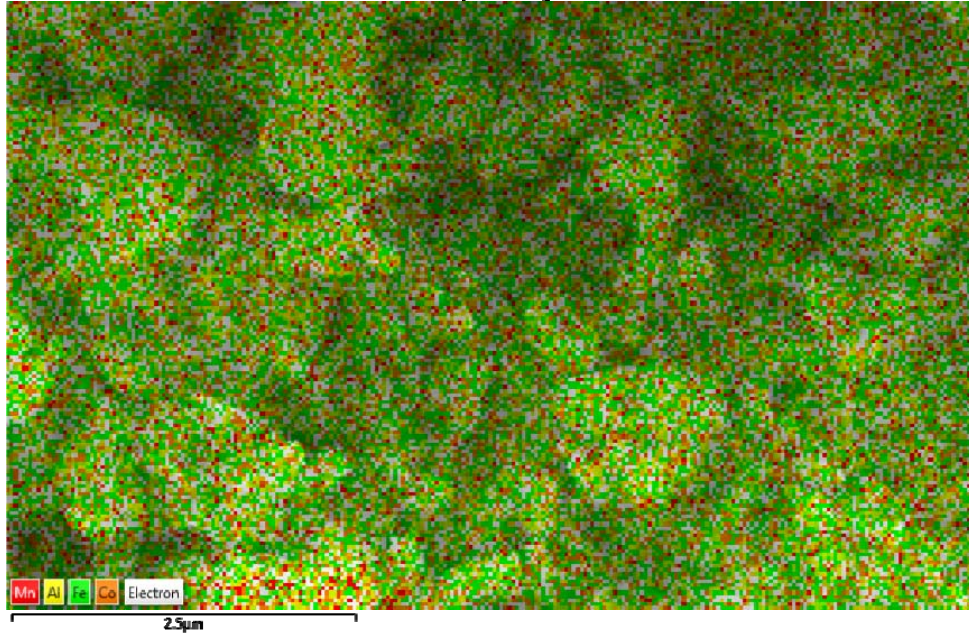


FIG. 9.1. Elemental mapping image of ferromagnetic  $\tau$ -phase  $\text{Mn}_{54}\text{Al}_{46}/\alpha$ -phase  $\text{Fe}_{65}\text{Co}_{35}$  composite ( $f_h = 0.819$ ).

131 emu/g and 75 Oe as shown in Fig. 9.2 (b). It is noted that the magnetization of  $\alpha$ -phase  $\text{Fe}_{65}\text{Co}_{35}$  powder is lower than 240 emu/g of its bulk value [14]. This is due to the thermal agitation of magnetization, slight oxidation of  $\text{Fe}_{65}\text{Co}_{35}$  particle or incomplete reduction of Fe- and Co-salts. After converting a mixture of paramagnetic  $\varepsilon$ -phase  $\text{Mn}_{54}\text{Al}_{46}$  and ferromagnetic  $\alpha$ -phase  $\text{Fe}_{65}\text{Co}_{35}$  particles to ferromagnetic  $\tau$ -phase  $\text{Mn}_{54}\text{Al}_{46}/\text{soft } \alpha$ -phase  $\text{Fe}_{65}\text{Co}_{35}$  composite ( $f_h = 0.819$ ), the saturation magnetization increased to 69 emu/g from 53 emu/g in Fig. 9.2 (b). On the other hand, the  $H_{ci}$  decreased to 1926 Oe from 3093 Oe. No kink was observed from hysteresis loops of  $\tau$ -phase  $\text{Mn}_{54}\text{Al}_{46}/\alpha$ -phase  $\text{Fe}_{65}\text{Co}_{35}$  composites with  $0 \leq f_h \leq 1$ . However, the remanent magnetization of the composite was lower than that of the hard phase. The exchange coupling between hard and soft phases occurs only if the thickness of soft phase is thinner than two times of the hard phase's domain wall thickness ( $2\delta_w$ ) [8]. The experimental  $\delta_w$  of Mn-Al is 15 nm [15]. The diameter of the synthesized  $\alpha$ -phase  $\text{Fe}_{65}\text{Co}_{35}$  particle is 40 nm in average, which is

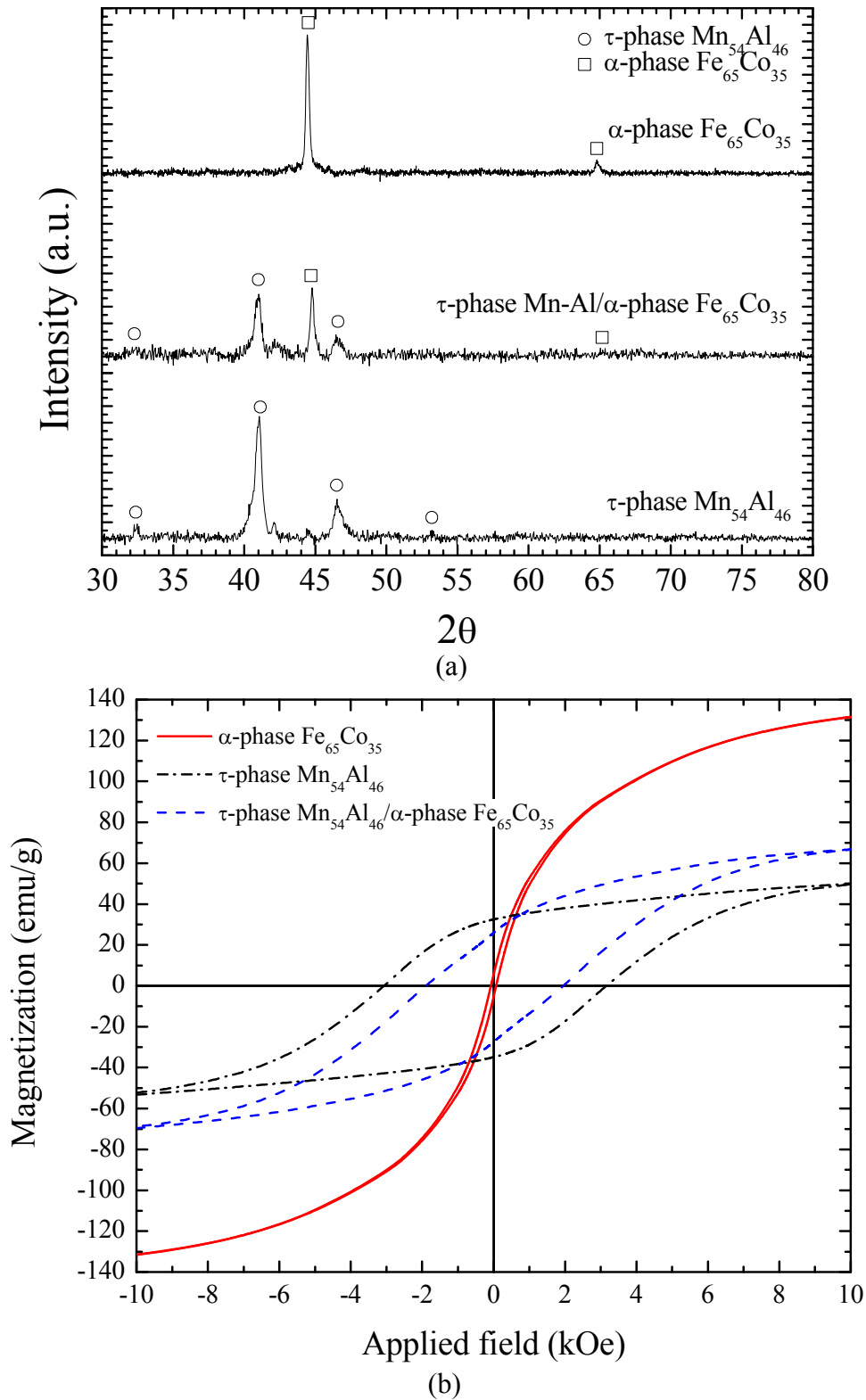


FIG. 9.2. (a) the XRD patterns and (b) hysteresis loops for synthesized single phase  $\tau$ -phase  $\text{Mn}_{54}\text{Al}_{46}$ ,  $\alpha$ -phase  $\text{Fe}_{65}\text{Co}_{35}$ , and composite ( $f_h = 0.819$ ).

greater than  $2\delta_w$  (30 nm) of  $\tau$ -phase  $\text{Mn}_{54}\text{Al}_{46}$ . Therefore, it can be assumed that the soft  $\alpha$ -phase  $\text{Fe}_{65}\text{Co}_{35}$  particles are partially involved in exchange coupling.

Figure 9.3 (a) and (b) show  $f_h$  dependence of magnetization  $\sigma(f_h)$  and intrinsic coercivity  $H_{ci}(f_h)$  for ferromagnetic  $\tau$ -phase  $\text{Mn}_{54}\text{Al}_{46}/\alpha$ -phase  $\text{Fe}_{65}\text{Co}_{35}$  composites. The magnetization monotonically decreases as the  $f_h$  increases, while the intrinsic coercivity increases. We now analyze  $\sigma(f_h)$  and  $H_{ci}(f_h)$  for ferromagnetic  $\tau$ -phase  $\text{Mn}_{54}\text{Al}_{46}/\alpha$ -phase  $\text{Fe}_{65}\text{Co}_{35}$  composites. According to theoretical studies on two-phase composite magnet, the saturation magnetization [8] and anisotropy constant [16] of composite can be expressed as:

$$\sigma = \frac{\sigma_h \rho_h f_h + \sigma_s \rho_s f_s}{\rho_h f_h + \rho_s f_s} \quad (9.1)$$

$$K = (1 - f_h)K_s + f_h K_h, \quad (9.2)$$

where  $\sigma$  is the saturation magnetization,  $K$  is the magnetocrystalline anisotropy constant, and  $\rho$  is the density.  $h$  and  $s$  in the subscript denote hard and soft phase, respectively. Because of the experimental difficulty of obtaining  $K$ , we developed an expression for  $H_{ci}$  of two-phase magnetic composite using experimentally accessible  $H_{ci}$  for both hard and soft phases.  $H_{ci}$  due to magnetocrystalline anisotropy [17] is

$$H_{ci} = \frac{\alpha K}{\sigma \rho}, \quad (9.3)$$

where  $\alpha$  is a constant depending on the crystal structure and degree of alignment. For aligned particles,  $\alpha$  is 2; for unaligned (random) particles,  $\alpha$  is 0.64 for cubic crystals and 0.96 for uniaxial crystals. Then,  $H_{ci}$  of the two-phase magnetic composite can be modified to equation (9.4) by combining Eq. (9.2) and (9.3):

$$H_{ci} = \alpha \frac{(1 - f_h)K_s + f_h K_h}{(1 - f_h)\sigma_s \rho_s + f_h \sigma_h \rho_h}. \quad (9.4)$$

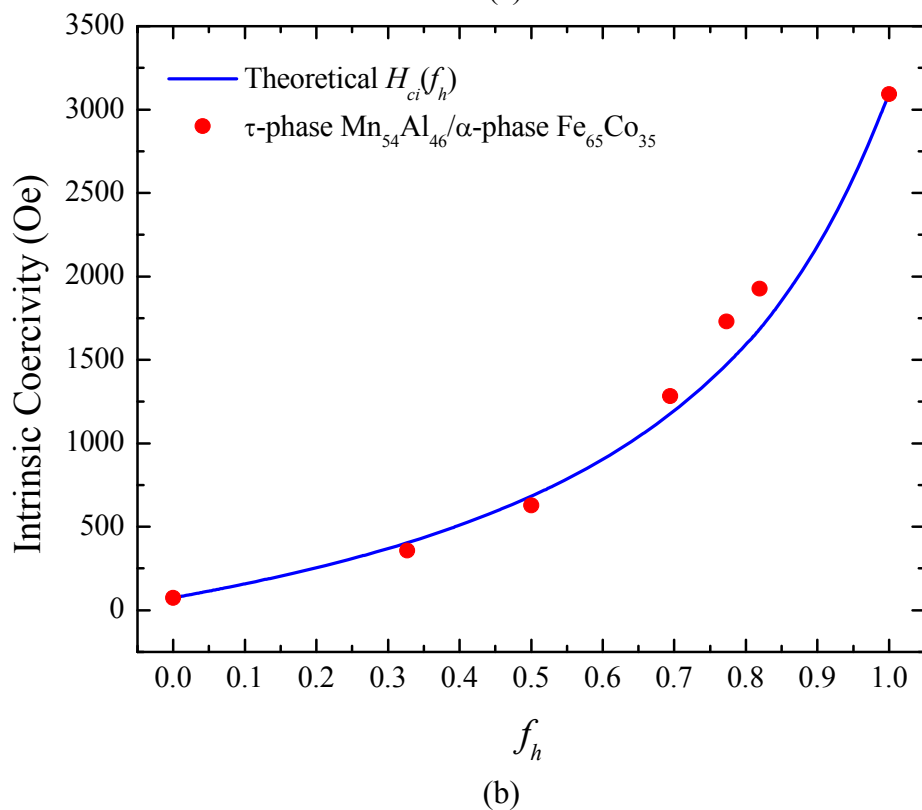
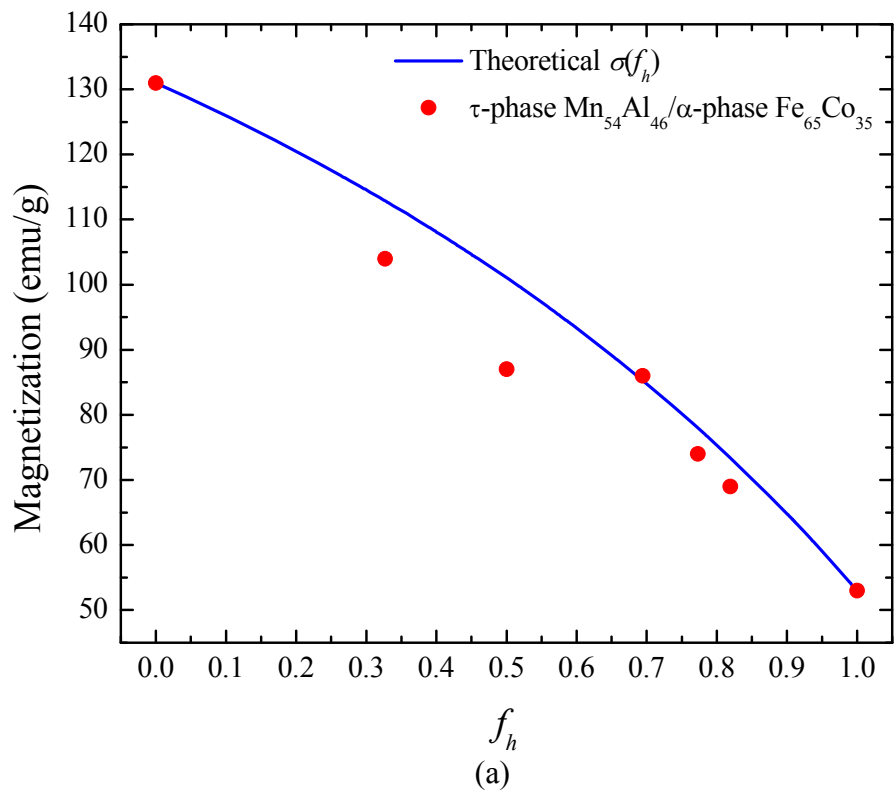


FIG. 9.3. The calculated and experimental  $f_h$  dependence of (a) magnetization  $\sigma(f_h)$  and (b) intrinsic coercivity  $H_{ci}(f_h)$  for  $\tau$ -phase  $\text{Mn}_{54}\text{Al}_{46}/\alpha$ -phase  $\text{Fe}_{65}\text{Co}_{35}$  composites.

By replacing  $K$  in Eq. (9.4) with  $H_{ci}$  in Eq. (9.3), Eq. (9.4) becomes Eq. (9.5).

$$H_{ci} = \frac{\sigma_s \rho_s H_s (1 - f_h) + \sigma_h \rho_h H_h f_h}{\sigma_s \rho_s (1 - f_h) + \sigma_h \rho_h f_h} . \quad (9.5)$$

Equation (9.5) suggests that the coercivity of a composite can be estimated by experimental  $H_{ci}$  of hard and soft phase materials instead of  $K$  of each phase.

The  $\sigma$  and  $H_{ci}$  of single phase  $\tau$ -phase  $Mn_{54}Al_{46}$  ( $\sigma_h = 53$  emu/g and  $H_h = 3093$  Oe) and  $\alpha$ -phase  $Fe_{65}Co_{35}$  ( $\sigma_s = 131$  emu/g and  $H_s = 75$  Oe) were used as input parameters in Eq. (9.1) and (9.5) to calculate  $\sigma(f_h)$  and  $H_{ci}(f_h)$ . The calculated  $\sigma(f_h)$  and  $H_{ci}(f_h)$  are shown in Fig. 9.3, and are in good agreement with the experimental results. Therefore, our developed coercivity equation, i.e. Eq. (9.5), serves as guidance to predict  $H_{ci}$  for two-phase magnetic composite.

#### 9.4. Conclusions

Ferromagnetic  $\tau$ -phase  $Mn_{54}Al_{46}$  ( $f_h = 1.000$ ),  $\alpha$ -phase  $Fe_{65}Co_{35}$  ( $f_h = 0.000$ ), and  $\tau$ -phase  $Mn_{54}Al_{46}/\alpha$ -phase  $Fe_{65}Co_{35}$  composites ( $0 < f_h < 1$ ) were synthesized. The magnetization and intrinsic coercivity of single phase  $\tau$ -phase  $Mn_{54}Al_{46}$  were 53 emu/g and 3090 Oe, and those of single phase  $\alpha$ -phase  $Fe_{65}Co_{35}$  were 131 emu/g and 75 Oe, respectively. The magnetization and intrinsic coercivity of two-phase magnetic composite monotonically decreased and increased, respectively, as the  $f_h$  increased.

The experimental intrinsic coercivity and magnetization of the composite with various  $f_h$  are in good agreement with the proposed coercivity and modified magnetization equations, respectively.

## 9.5. References

1. M. Sagawa, S. Fujimara, H. Yamamoto, Y. Matsuura, and S. Hirose, *J. Appl. Phys.* **57**, 4094 (1985).
2. S. Sugimoto, *J. Phys. D: Appl. Phys.* **44**, 064001 (2011).
3. H. Kono, *J. Phys. Soc. Jpn.* **13**, 1444 (1958).
4. A. J. J. Koch, P. Hokkelling, M. G. V. D. Steeg, and K. J. DeVos, *J. Appl. Phys.* **31**, S75 (1960).
5. A. Sakuma, *J. Phys. Soc. Jpn.* **63**, 1422 (1993).
6. J. H. Park, Y. K. Hong, S. Bae, J. J. Lee, J. Jalli, G. S. Abo, N. Neveu, S. G. Kim, C. J. Choi, and J. G. Lee, *J. Appl. Phys.* **107**, 09A731 (2010).
7. T. Kubo, US Patent 3,976,519 (1976).
8. E. F. Kneller and R. Hawig, *IEEE Trans. Mag.* **27**, 3588 (1991).
9. Y. Liu, A. George, R. Skomski, and D. J. Sellmyer, *Appl. Phys. Lett.* **99**, 172504 (2011).
10. H. Zeng, S. Sun, J. Li, Z. L. Wang, and J. P. Liu, *Appl. Phys. Lett.* **85**, 792 (2004).
11. B. Ma, H. Wang, H. Zhao, C. Sun, R. Acharya, and J. P. Wang, *J. Appl. Phys.* **109**, 083907 (2011).
12. M. Marinescu, J. F. Liu, M. J. Bonder, and G. C. Hadjipanayis, *J. Appl. Phys.* **103**, 07E120 (2008).
13. C. W. Kim, Y. H. Kim, H. G. Cha, J. C. Kim, and Y. S. Kang, *Mol. Cryst. Liq. Cryst.* **472**, 155 (2007).
14. C. W. Chen, *J. Appl. Phys.* **32**, S348 (1961).
15. G. F. Korznikova, *J. Microsc.* **239**, 239 (2010).
16. R. Skomski and J. M. D. Coey, *Phys. Rev. B* **48**, 15812 (1993).
17. C. Kittel, *Rev. Mod. Phys.* **21**, 541, (1949).

## CHAPTER 10

### ELECTRIC MACHINE: PERMANENT MAGNET SYNCHRONOUS MOTOR

#### 10.1. Introduction

Recently, the automotive industry has tried to reduce dependency on fossil fuels in order to reduce greenhouse gas emissions. For this effort, the automotive industry are shifting towards electric vehicles (EV) and hybrid electric vehicles (HEV), which are powered by motors. The technologies for EVs and HEVs have been increasingly advanced, but some of the current major issues are low power density, poor efficiency, large size, significant motor weight, and limited supply of rare-earth metals for motor.

Permanent magnet synchronous machines (PMSM) are among the most promising motor type for EV and HEV applications due to its excellent power density, efficiency, size, and motor weight. PMSMs are of two different types; the first one is interior permanent magnet synchronous motor (IPMSM) and the other is surface permanent magnet synchronous motor (SPMSM). The IPMSM is more advantageous than the SPMSM for EV and HEV application due to its high speed operation and no power dropoff at high speed.

The permanent magnets in the PMSM play important roles in the overall motor operation. The magnetic flux density ( $B$ ) from the permanent magnet is limited to the intrinsic material properties, therefore, developing an advanced motor design (rotor, stator, etc) is needed to improve the motor power, torque, and efficiency. In response to this, there have been many attempts to find a better design for the given magnetic properties of permanent magnets. The rare-earth (RE) Nd-Fe-B magnet possesses a high magnetic  $B$  of about 1.5 T, while RE-free

ferrite magnets (Sr-Fe-O) have only about 0.5 T. Therefore, in this dissertation, we have compared the torque of a PMSM at room and elevated temperature with both RE and RE-free magnets, such as Nd-Fe-B, MnAl, MnBi, SrFe<sub>12</sub>O<sub>19</sub>, and Alnico.

## 10.2. Background: principles of motor

When current flows in a wire, magnetic field  $B$  is induced around the wire by the right-hand rule. An external magnetic field  $B$  exerts a force on a current-carrying wire. In a rectangular loop of dimensions  $a$  and  $b$  carrying a current  $I$  as shown in Fig. 10.1 (a), the magnetic field produces a torque about an axis. The force on  $a$  side is defined as  $F = IaB$ , the force on  $b$  side is  $F' = IbB \sin(90^\circ - \varphi)$ , and the magnitude of torque on a current loop is  $\tau = IBA \sin\varphi$ , where  $A$  is the area of the loop, and  $\varphi$  is the angle between the plane of the loop and the direction of the magnetic field  $B$ . Maximum torque occurs when  $\varphi$  is 90 degrees, and minimum torque is 0 at  $\varphi$  of 0 degree. When the loop rotates past  $\varphi = 0$ , the torque reverses. Fig. 10.1 (b) depicts the magnetic force directions of two wires that carry current in opposite directions in a magnetic field.  $N$  and  $S$  are the abbreviations of north and south poles, respectively. The interaction

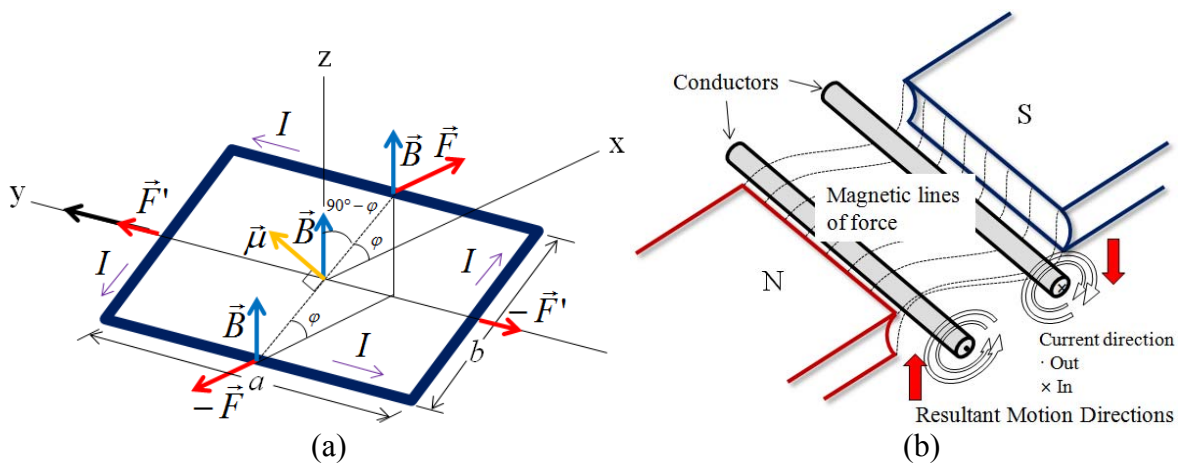


FIG. 10.1. (a) The right-hand rule between current  $I$  in a uniform magnetic field  $B$  and force  $F$  in a rectangular loop, and (b) schematic drawing of magnetic fields in the loop.

between the generated magnetic field by the flowing current and the external magnetic field results in the force  $F$  and torque  $\tau$  on the wires as drawn in Fig. 10.1 (b) by dotted lines. Therefore, the electrical energy from the current is converted to mechanical energy as the rectangular loop rotate, and this mechanical energy is then used to power another machine.

This principle of generation of force  $F$  and torque  $\tau$  by magnetic fields is commonly used in motors, in which the loop is connected to a shaft that rotates as a result of the torque. One of the simplest motor is a direct current (DC) motor in which magnet poles repel and attract a current loop. Fig. 10.2 shows a simple DC motor. When brushes are aligned with commutator segments, i.e., the current loop plane and magnets are on the same plane as shown in Fig. 10.2 (a), the maximum torque is generated. This is in consistent with the above explanation that when  $\varphi$  is 90 degrees, the maximum torque occurs. On the other hand, when the rotor turn 90 degrees and each brush is in contact with both commutator segments as shown in Fig. 10.2 (b), the minimum torque is generated. This is because the current bypasses the rotor altogether, which results in no magnetic torque generated on the rotor.

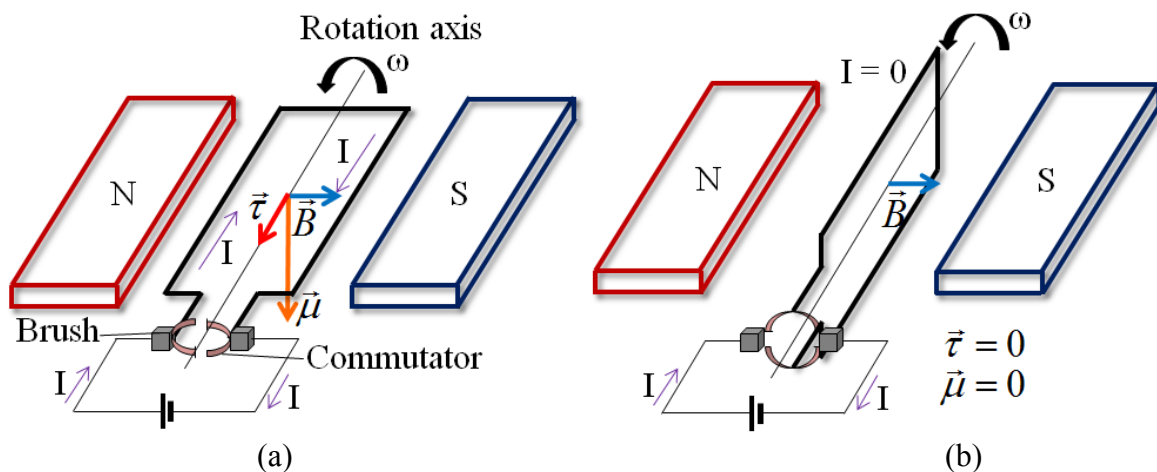


FIG. 10.2. A simple direct current motor. (a) Brushes are aligned with commutator segments and (b) each brush is in contact with both commutator segments.

Fig. 10.3 (a) and (b) show the two pole and three pole DC motors, respectively. The geometry of the brushes, commutator, and rotor make the rotor rotate until it is aligned with the magnetic field by stators when power is applied. When the rotor rotates past the alignment, the brushes move to the next commutator contacts, and then the current direction changes to the opposite direction, which makes the north and south poles of the electromagnet transform to south and north poles, respectively. In this way, the DC motor continues rotating.

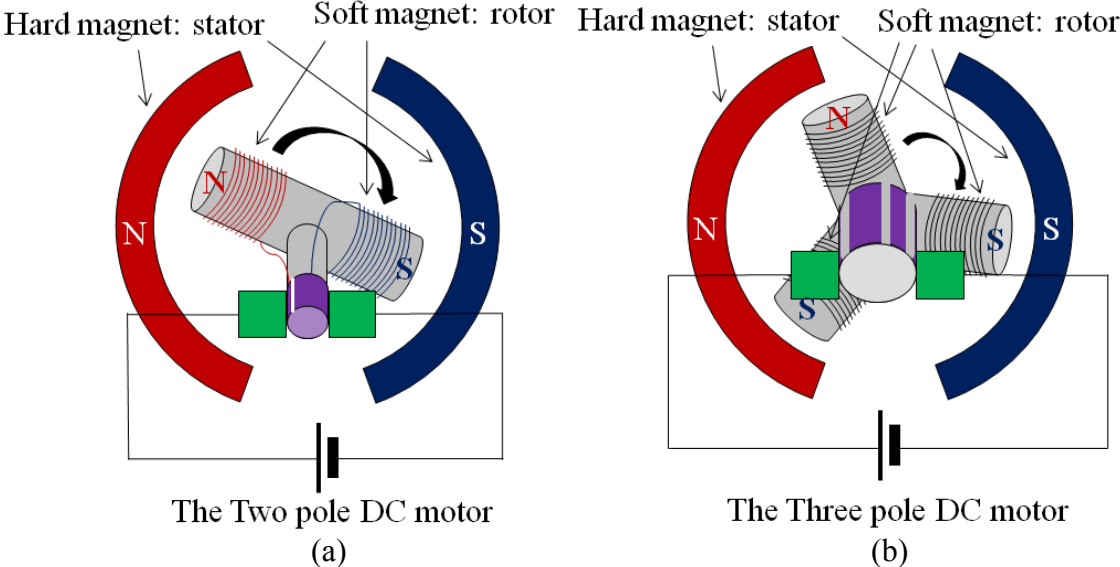


FIG. 10.3. (a) Two-pole and (b) three-pole DC motors.

One drawback of the two-pole motor is that if the rotor is exactly at the middle of its rotation (perfectly aligned with the field magnets), it will become stuck at this point. In addition, the commutator shorts out the power supply (i.e., both brushes touch both commutator contacts simultaneously), which is bad for the power supply, wastes energy, and damages motor components.

However, the three-pole motor does not suffer from this issue. Therefore, the motor can start from any position and is able to be operated smoothly without power shorts or becoming

stuck. Although the three-pole motor can solve these problem, it still has disadvantages compared to recently-developed motors with respect to design. Thos disadvantages include wearing out the brushes, a limited maximum speed of the motor due to the brushes, difficulty in cooling the electromagnet in the center of the motor, and a limited number of poles due to the use of brushes.

The brushless DC (BLDC) motor is a better choice for many applications due to high reliability, high efficiency, and high power-to-volume ratio. The structure of the BLDC motor is simpler without brushes and a commutator, but more powerful. Fig. 10.4 shows the typical design and an actual example of a BLDC motor. Therefore, it is considered to be a high performance motor that is capable of providing large amounts of torque over a vast speed range.

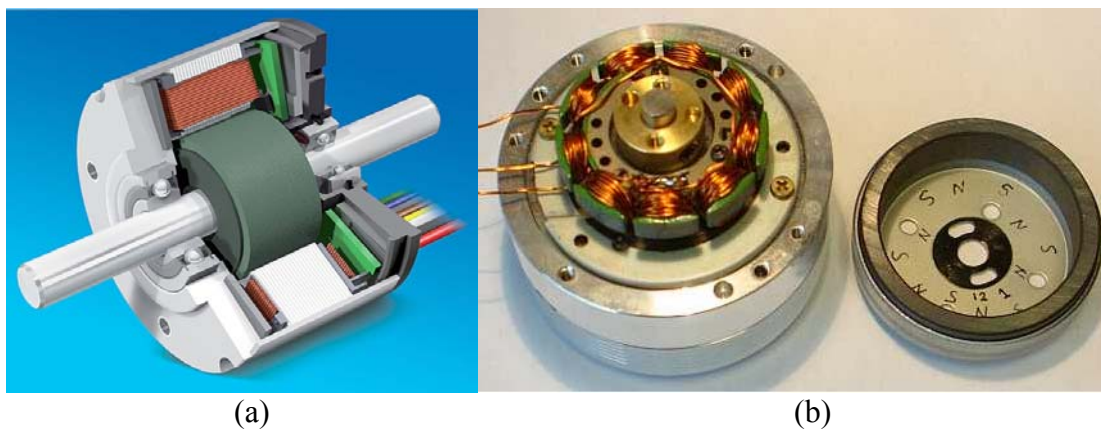


FIG. 10.4. (a) Typical design [1] and (b) an actual example of a BLDC motor [2].

The BLDC motor has two primary parts: the rotor and the stator as shown in Fig. 10.5. There are two different BLDC motor designs according to where the windings are located: an inner rotor and an outer rotor design. In an outer rotor design, the windings are located in the core of the motor; the rotor magnets surround the stator windings. The rotor magnets act as an insulator, therefore, reducing the rate of heat dissipation from the motor. Due to the location of

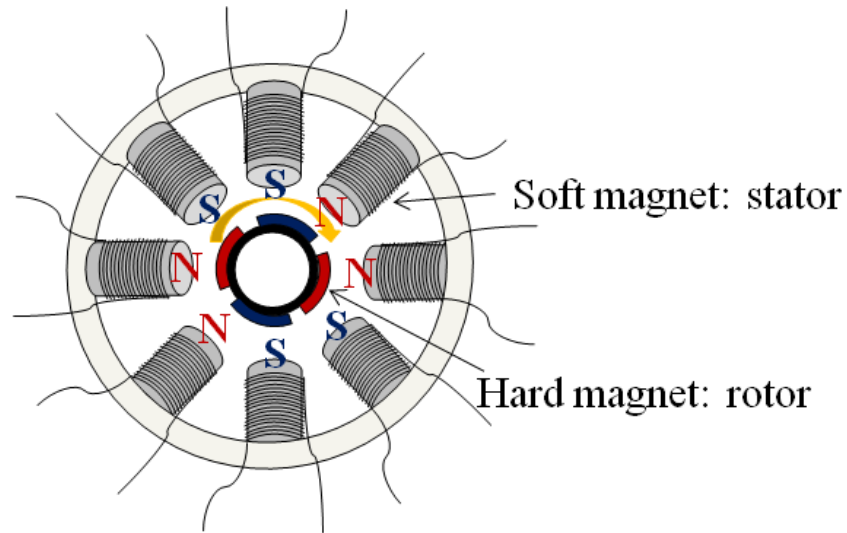


FIG. 10.5. Schematic drawing of a BLDC motor.

the stator windings, outer rotor designs typically operate at lower duty cycles or at a lower rated current. The primary advantage of an outer rotor BLDC motor is relatively low cogging torque.

In an inner rotor design, the stator windings surround the rotor. The advantage of the inner rotor is good heat dissipation. The heat dissipation rate directly affects the torque produced. For this reason, the majority of BLDC motors use the inner rotor design. In addition, there are many other advantages of the BLDC motor, such as high operation speed (BLDC motor can operate at speeds above 10,000 rpm under loaded and unloaded conditions), responsiveness & quick acceleration (inner rotor Brushless DC motors have low rotor inertia, allowing them to accelerate, decelerate, and reverse direction quickly), high power density (BLDC motors have the highest running torque per cubic inch of any DC motor), and high reliability (BLDC motors do not have brushes, meaning they are more reliable and have life expectancies of over 10,000 hours. This results in fewer instances of replacement or repair and less overall down time for your project). [3]

### 10.3. Permanent magnet synchronous motors (PMSM)

Permanent Magnet Synchronous Motors (PMSM) is similar to the BLDC motor. PMSMs are constructed with the electric winding on the stator and permanent magnets on the rotor. The difference between the PMSM and BLDC is the shape of the current flux. The shape of the current flux for a PMSM is synchronous, while the shape in a BLDC is rectangular as shown in Fig. 10.6. The advantages of the PMSM are the ability to control the power factor, the constant speed of the loads, wider air gaps allowed than in induction motors, linear variability of electromagnetic power with the voltage, higher efficiencies especially at low speed, and unity of power factor applications compared to induction motors. The advantages and disadvantages of the DC motor, induction motor (IM), switched reluctance motor (SRM), and PMSM are listed in Table 10.1 [4-6].

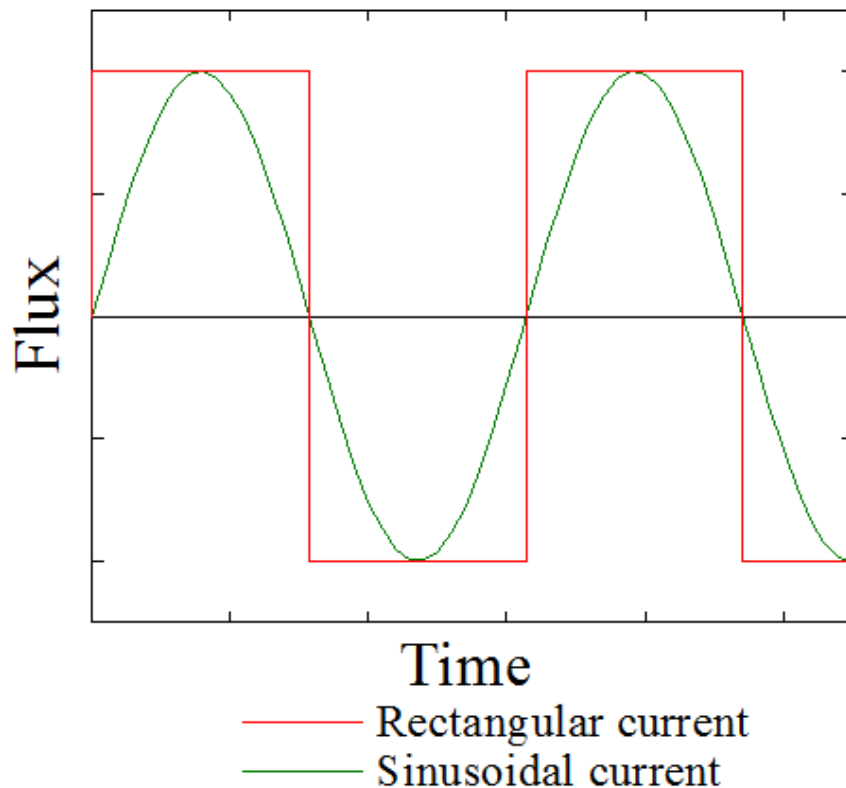


FIG. 10.6. The comparison between rectangular and sinusoidal currents in a BLDC motor and PMSM, respectively.

Table 10.1. Comparison of the electric motors for hybrid electric vehicle (HEV) application.

Machine Type	Advantages	Disadvantages
DC Motor	Easy control Desirable torque-speed characteristics	Frequent need of maintenance Low efficiency and reliability Low speed range
Induction Motor (IM)	High speed range High reliability Low cost Rigidity in hostile environments	Low power density and large size Low efficiency Thermal problem at high speed
Switched Reluctance Motor (SRM)	Desirable torque-speed characteristics High reliability Low cost Rigidity in hostile environments	High torque ripple and noise Low power density Low efficiency
PM Synchronous Motor (PMSM)	High power density and small size High efficiency Lighter	Limited speed range High cost High stator core loss at high speed Significant back electromotive force (emf)

There are two types of PMSMs. The first one is the interior permanent magnet synchronous motor (IPMSM) and the other is the surface permanent magnet synchronous motor (SPMSM). In contrast to the SPMSM, the IPMSM has certain advantages, such as better suitability at high-speed operation. The fundamental difference between the IPMSM and SPMSM is that in a SPMSM, the flux cannot be moved tangentially within the magnet to provide a rotor-to-stator phase advance, while in an IPMSM, the flux can flow tangentially above the magnets in the rotor so that a quite significant rotor-to-stator phase advance results. In favor of surface mounting, the presence of ferromagnetic material at the rotor surface increases the air gap inductance [7].

As a result of the rotor-to-stator phase shift, IPMSMs add a reluctance component to the torque produced by the motor, which tends to improve the constant-power speed range. This

avoids the power drop-off that is common in SPMSMs operating at high speeds. IPM machines can provide torque under certain conditions with less  $I^2R$  losses than other permanent magnet machines. IPMSMs facilitate the use of easily manufactured rectangular magnets or other convenient geometries. Because of their high torque/inertia ratio, IPMSMs with high-energy magnets can be designed to provide rapid acceleration.

Table 10.2. Comparison of the interior permanent magnet synchronous motor (IPMSM) and surface permanent magnet synchronous motor (SPMSM).

Machine Type	Advantages	Disadvantages
Interior Permanent Magnet Synchronous Motor (IPMSM)	High speed operation Flux move tangentially (rotor to stator phase advance) Reluctance component to torque (improve constant power speed range → No power dropoff) Less $I^2R$ losses Rectangular magnets (easy to make)	High cost Complicated manufacturing
Surface Permanent Magnet Synchronous Motor (SPMSM)	high torque/inertia ratio Simple manufacturing	Flux move not tangentially Power dropoff at high speed Limited rotational speed

Due to the advantages of the IPMSM in contrast to the SPMSM, a majority of motor manufacturers focus on the IPMSM. Fig. 10.7 shows four types of IPMSM according to the rotor configurations. d-axis means the north pole of magnetized direction. The magnetic flux of the IPMSM is proportional to the amount of permanent magnet, which increases the torque and efficiency, but decreases the constant power region [9-10]. For this reason, the double layer configuration in Fig. 10.7 (b) has a higher torque and wider efficient operating range than the single layer as shown in Fig. 10.7 (a) [9], but decreases the constant power region. The

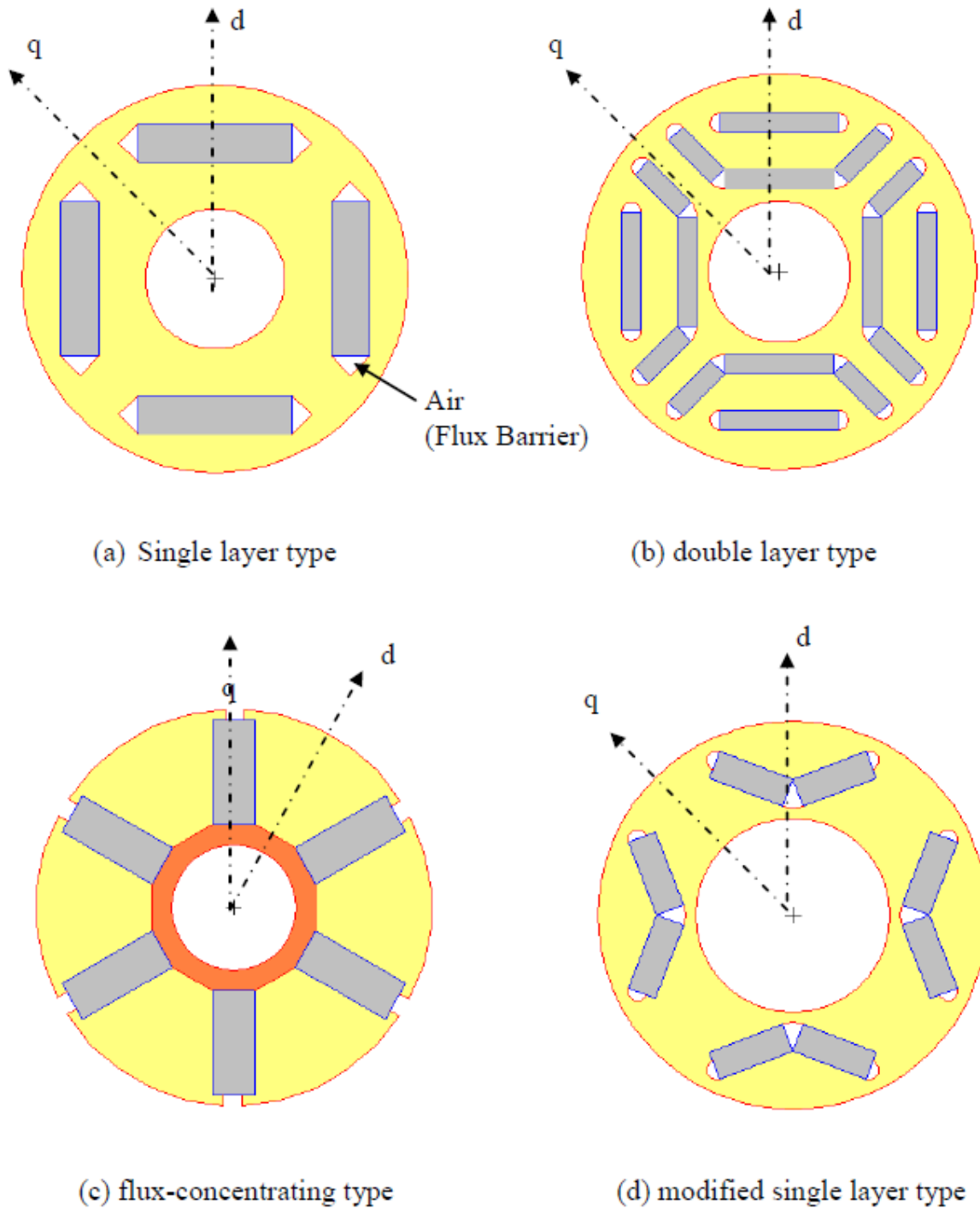


FIG. 10.7. Various rotor configurations of IPMSM [8].

arrangement of Fig. 10.7 (c) is known as a flux-concentrating design due to the fact that the magnet pole area at the air-gap produces an air-gap flux density higher than that in the magnet

[11]. Some drawbacks are that the high electro motive force (back-emf) voltage from a motor caused by the permanent magnets limits its maximum constant speed operation, and high flux from the permanent magnets is a major factor of the core loss when the machine rotates at high speed.

#### 10.4. Design of IPMSM

In order to observe the performance of IPMSMs with different permanent magnets, an 8-pole V-shape IPMSM, which is used in the 2010 Toyota Prius, was designed using ANSYS Maxwell. Fig. 10.8 (a) and (b) show a 2-D view and 3-D view of the designed IPMSM, respectively, while the designs and corresponding design parameters of the stator and rotor of the 8-pole V-shape IPMSM are shown and summarized in Fig. 10.9.

As the figures exhibit, the stator of this motor features 48 slots and distributed winding while the rotor has a total of 8 poles. The material of the stator and rotor is a soft magnetic material with high magnetization and permeability, therefore, decreasing magnetic core loss. Furthermore, it is noted that the air void in the rotor helps focus the magnetic field from the

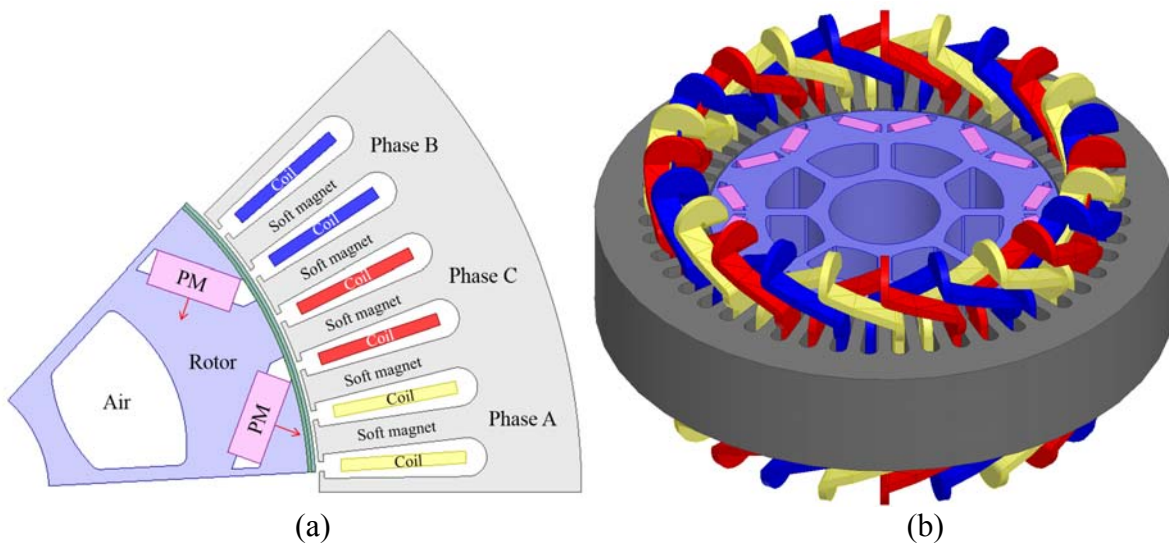
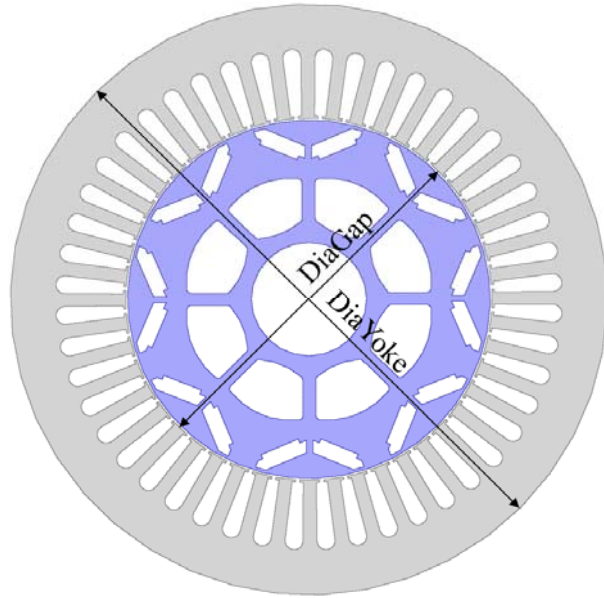


FIG. 10.8. Design of 8-pole V-shape IPMSM in (a) 2-D and (b) 3-D view.

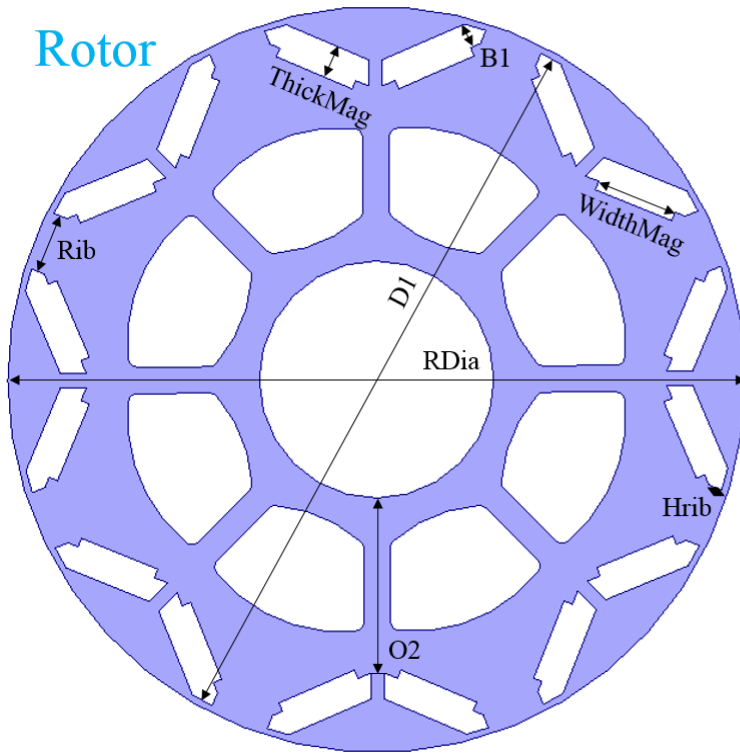


### Stator + Rotor

	Size (mm)
DiaYoke	269.24
DiaGap	161.9
No. Slot	48

(a)

### Rotor



	Size (mm)
Rdia	160.4
D1	157.44
O2	37.6
B1	5.2
Rib	12.925
Hrib	3
ThickMag	7.16
WidthMag	35.76

(b)

FIG. 10.9. Detailed design parameters of (a) outer diameters of stator and rotor and (b) inside of rotor of the 8-pole V-shape IPMSM.

permanent magnets to the pole directions, therefore, increasing magnetic flux density at the poles. Because of the symmetry, only 1/8<sup>th</sup> of the motor is used in the simulation to reduce the

computation time. The motor operation temperature was varied from room temperature (23 °C) to 200 °C to calculate torque at different temperatures. The following magnetizations were used for torque calculation: 1.31 T for Nd-Fe-B [12], 0.56 T for MnAl [13], 0.82 T for MnBi [14], 0.41 T for SrFe<sub>12</sub>O<sub>19</sub> [15], and 1.05 T for Alnico [16] at 23 °C and 0.51 T for Nd-Fe-B, 0.35 T for MnAl, 0.64 T for MnBi, 0.27 T SrFe<sub>12</sub>O<sub>19</sub>, and 1.01 T for Alnico at 200 °C.

### 10.5. Finite element analysis – Maxwell 3D

FEA is a numerical technique based on the determination of the electric or magnetic field distributions inside the machine structure. The FEA solver computes  $H$  under a constant input current condition, thus, it uses coenergy differentiation for a given angle instead of energy differentiation for torque calculation with nonlinear material data. The total magnetic energy  $W$  stored in a FEA model is calculated by

$$W = \int_v (\vec{d}\vec{B}) \cdot \vec{H} dv, \quad (10.1)$$

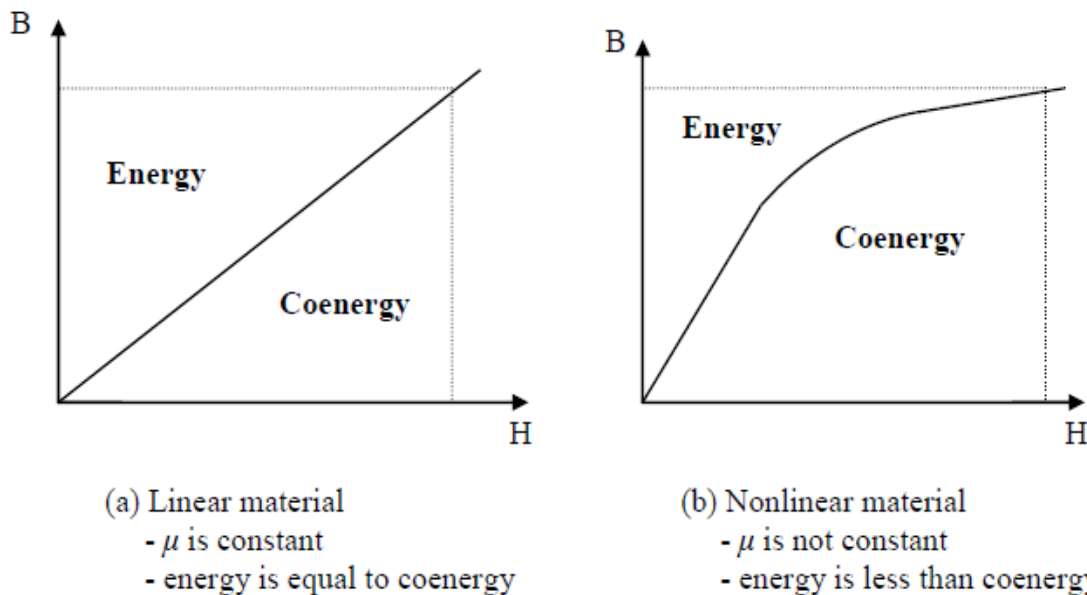


FIG. 10.10. The energy and coenergy relations for (a) linear material and (b) nonlinear material under constant current conditions (steady state) [8].

where  $B$  is the magnetic flux density and  $H$  is the magnetic field strength amplitude. The total magnetic coenergy  $W_c$  stored in a FEA model is calculated by

$$W = \int_v \vec{B} \cdot (d\vec{H}) \quad (10.2)$$

Eq. (10.1) and (10.2) are equal for a linear material, while they are not equal for a nonlinear material as shown in Fig. 10.10. The difference in the areas for the energy and coenergy of the  $B$ - $H$  curves under a constant current condition (steady-state) indicates that the motion of a material has occurred. Therefore, in order to increase the mechanical work of a motor system, one should increase its coenergy [17].

## 10.6. Results and discussion

The torque of the 8-pole V-shape IPMSM is obtained by feeding it with a three-phase balanced sinusoidal current source. The three-phase currents are expressed below.

$$I_a = A \cdot \sin(2\pi \cdot f \cdot t + \theta \cdot \pi/180), \quad (10.1)$$

$$I_b = A \cdot \sin(2\pi \cdot f \cdot t + (\theta - 120) \cdot \pi/180), \quad (10.2)$$

$$I_c = A \cdot \sin(2\pi \cdot f \cdot t + (\theta + 120) \cdot \pi/180), \quad (10.3)$$

where  $I$  is the current,  $A$  is the peak value of current,  $f$  is the frequency,  $t$  is the time, and  $\theta$  is the initial phase angle. We used  $A = 250$  A,  $f = 200$  Hz, and  $\theta = 20$  degree for 3000 rpm, while setting  $t$  as a variable. Constant input sinusoidal three-phase currents were used for all the IPMSMs, but  $B$  varied between magnets. The effect of  $B$  on torque can be written as

$$T = r \cdot B \cdot Z \cdot i, \quad (10.4)$$

where  $T$  is the rotor torque,  $r$  is the average winding radius,  $Z$  is the number of conductors, and  $i$  is the current. Therefore,  $T$  is proportional to  $B$ . The  $B$  of Nd-Fe-B and MnBi magnets in the

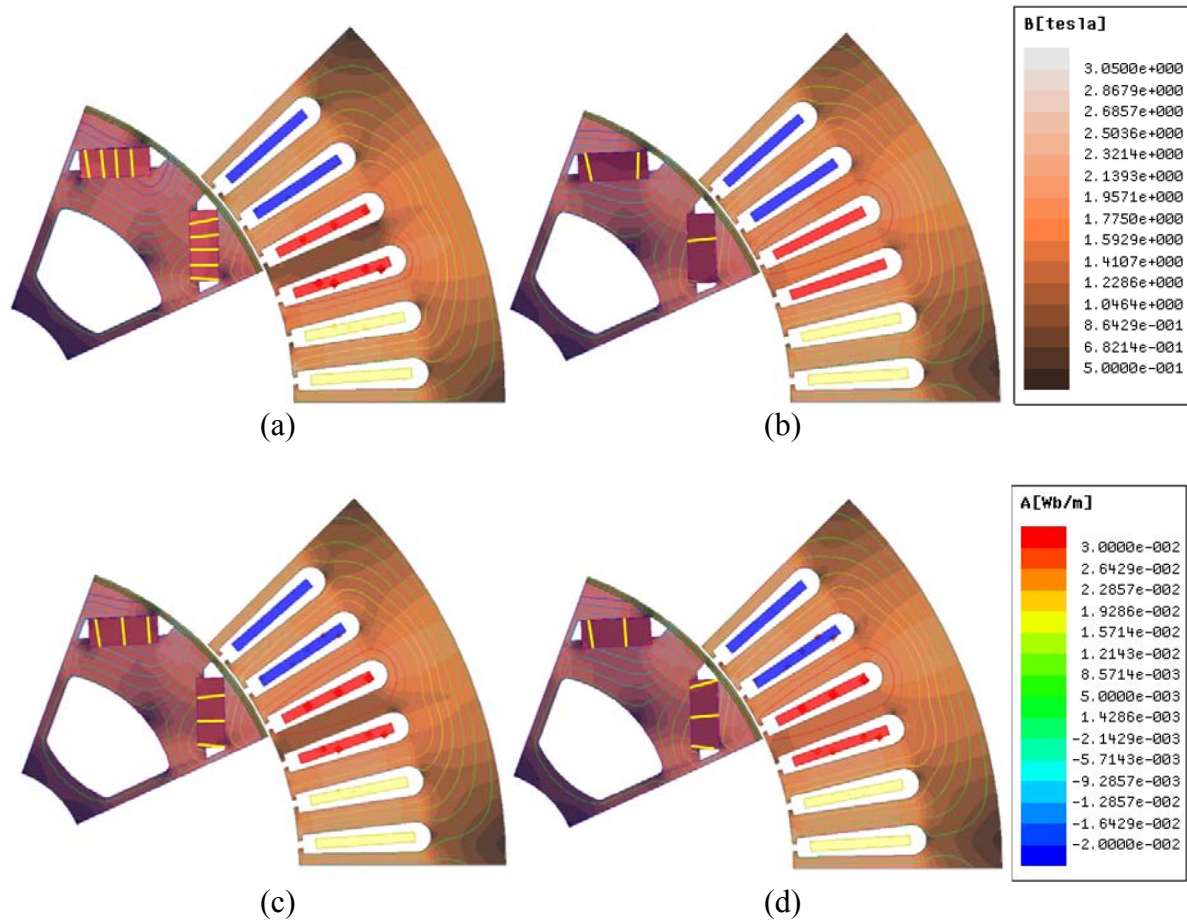
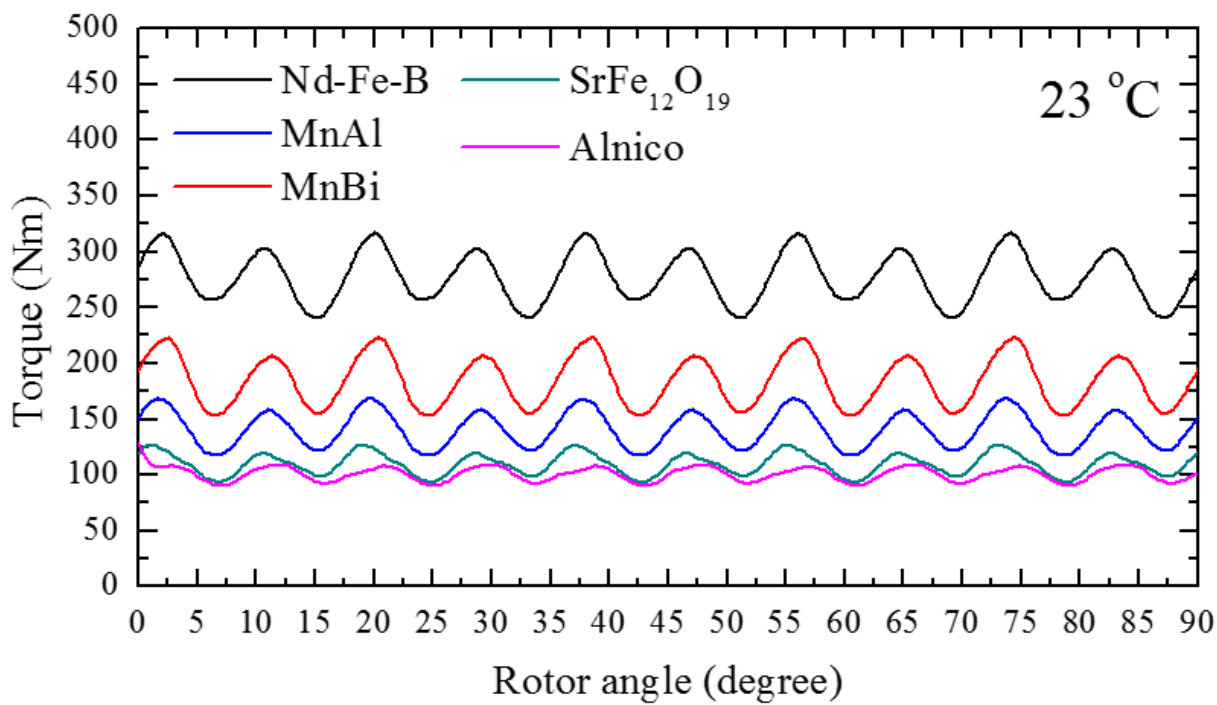
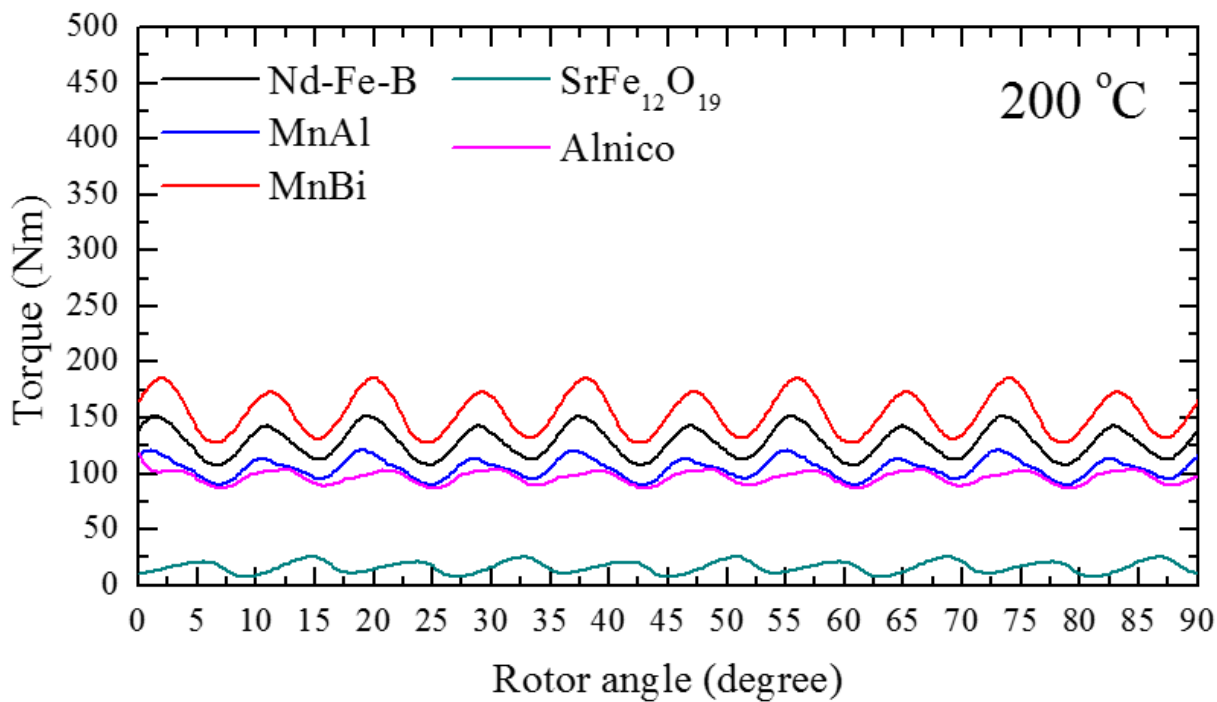


FIG. 10.11. IPMSM operation views with magnetic flux density and current flux line. IPMSM with Nd-Fe-B magnet at (a) 23 °C and (b) 200 °C, and MnBi at (c) 23 °C and (d) 200 °C are shown.

operating IPMSMs are visualized in Fig. 10.11. The lighter color of the Nd-Fe-B IPMSM in Fig. 10.11 (a) over that of the MnBi IPMSM in Fig. 10.11 (c) shows that the torque with the Nd-Fe-B magnet is stronger than with the MnBi magnet at 23 °C. However, the color comparison between the Nd-Fe-B IPMSM (Fig. 10.11 (b)) and MnBi IPMSM (Fig. 10.11 (d)) at 200 °C proves that the torque with the MnBi magnet is stronger than with the Nd-Fe-B magnet. The rotor angle dependence of torque (N·m) for the IPMSMs with Nd-Fe-B, MnAl, MnBi, SrFe<sub>12</sub>O<sub>19</sub>, and Alnico magnets at 23 and 200 °C are compared in Fig. 10.12. Fig. 10.12 clearly shows that the torque for the IPMSM with a Nd-Fe-B magnet is higher than with RE-free magnets such as



(a)



(b)

FIG. 10.12. Rotor rotation angle dependence of torque at (a) 23 °C and (b) 200 °C.

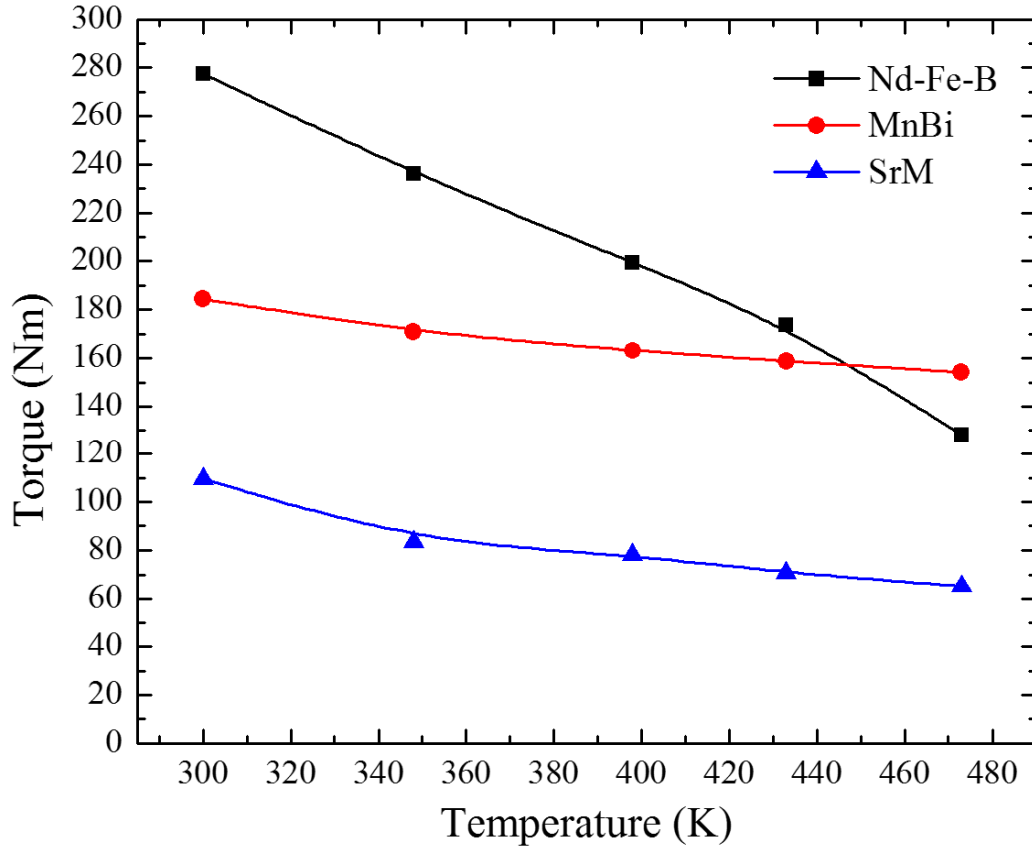


FIG. 10.13. Temperature dependence of average torque from IPMSM with Nd-Fe-B, MnBi, and SrFe<sub>12</sub>O<sub>19</sub>.

MnAl, MnBi, SrFe<sub>12</sub>O<sub>19</sub>, and Alnico at 23 °C (Fig. 10.12 (a)), but is lower than with a MnBi magnet at 200 °C (Fig. 10.12 (b)). To further investigate the temperature dependence of torque for the IPMSMs with Nd-Fe-B, MnBi, and SrFe<sub>12</sub>O<sub>19</sub> magnets, the motor simulations were performed at temperatures between 23 to 200 °C. The resultant average torque from the IPMSMs with Nd-Fe-B, MnBi, and SrFe<sub>12</sub>O<sub>19</sub> magnets are compared in Fig. 10.13. It is observed that the torque of the IPMSM with a Nd-Fe-B magnet is higher than with MnBi and SrFe<sub>12</sub>O<sub>19</sub> magnets from 23 to 174 °C, while it becomes lower above 174 °C. This is because the temperature coefficient of  $B$  of the Nd-Fe-B magnet is a larger negative value than that of the MnBi magnet throughout the temperature range. It is noted that the torque of the IPMSM with a SrFe<sub>12</sub>O<sub>19</sub>

magnet is always lower than the IPMSMs with Nd-Fe-B and MnBi magnets over the aforementioned temperature range. This indicates that MnBi is a better permanent magnet than Nd-Fe-B for high temperature IPMSM applications.

In order to further improve torque, power density, efficiency, and power speed range with decreased size and weight, it is necessary to design advanced IPMSMs. Advanced types of IPMSMs include a Dual Stator Axial Flux Permanent Magnet Motor (DSAFPMM) and Permanent Magnet assisted Synchronous Reluctance Motor (PMA-SynRM).

## 10.7. Conclusions

The overall motor principles from a simple DC motor to a complex IPMSM were introduced. A DC motor, induction motor, switched reluctance motor, and PM motor were compared, and it was noted that the PM motor is suitable as an electric vehicle's motor due to its high power density, small size, high efficiency, and light weight.

The torque performance of IPMSMs with Nd-Fe-B, MnAl, MnBi, SrFe<sub>12</sub>O<sub>19</sub>, and Alnico magnets at 23 and 200 °C were compared, and the temperature dependence of torque in an IPMSM with Nd-Fe-B, MnBi, and SrFe<sub>12</sub>O<sub>19</sub> magnets in the range between 23 and 200 °C was analyzed. Consistent input parameters such as three-phase currents and rotational speed were constant. However, the magnetic flux density ( $B$ ) varied according to the permanent magnet properties. The resultant torque for the IPMSMs with Nd-Fe-B, MnAl, MnBi, SrFe<sub>12</sub>O<sub>19</sub>, and Alnico magnets at 23 and 200 °C reveal that the torque with a Nd-Fe-B magnet is higher than with the others at 23 °C, but the IPMSM with a MnBi magnet shows better torque performance at the electric vehicle's motor operation temperature of above 174 °C.

## 10.8. References

1. <http://www.directindustry.com>
2. <http://home.solcon.nl>
3. <http://www.nmbtc.com>
4. M. Zeraoulia, M. E. H. Benbouzid, and D. Diallo, "Electric Motor Drive Selection Issues for HEV Propulsion Systems: A Comparative Study," *IEEE Transactions on Vehicular Technology*, vol. 55, Issue 6, Apr. 2006, pp. 1576 – 1764.
5. R. H. Staunton, S. C. Nelson, P. J. Otaduy, J. W. McKeever, J. M. Bailey, S. Das, and R. L. Smith, "PM Motor Parametric Design Analyses for a Hybrid Vehicle Traction Drive Application," *Oak Ridge National Laboratory*, ORNL/TM-2004/217.
6. M. Ehsani, G. Yimin, and S. Gay, "Characterization of electric motor drives for traction applications," *Industrial Electronics Society, 2003. IECON '03. The 29th Annual Conference of the IEEE*, vol. 1, Nov. 2003, pp. 891 – 896.
7. R. H. Staunton, et. al., "PM Motor Parametric Design Analyses for a Hybrid Electric Vehicle Traction Drive Application." *DOE final report, Oak Ridge National Laboratory*, 2004.
8. Lee, Seong Taek, "Development and Analysis of Interior Permanent Magnet Synchronous Motor with Field Excitation Structure." *PhD diss., University of Tennessee*, 2009.
9. S. Morimoto, M. Sanada, and Y. Takeda, "Performance of PM-assisted synchronous reluctance motor for high-efficiency and wide constant-power operation," *IEEE Transactions on Industry Applications*, vol. 37, no. 5, Sept./Oct. 2001, pp. 1234 – 1240.
10. S. Morimoto, M. Sanada, and Y. Takeda, "Performance of PM/reluctance hybrid motor with multiple flux-barrier," *Proceedings of the Power Conversion Conference - Nagaoka*, vol. 2, 3-6 Aug. 1997, pp. 649 – 654.
11. S. Kawano, H. Murakami, N. Nishiyama, Y. Ikkai, Y. Honda, and T. Higaki, "High performance design of an interior permanent magnet synchronous reluctance motor for electric vehicles," *Proceedings of the Power Conversion Conference - Nagaoka*, vol. 2, 3-6 Aug. 1997, pp. 33-36.
12. T. Akiya, H. Kato, M. Sagawa, and K. Koyama, *Mater. Sci. and Eng.*, **1**, 012034 (2009).
13. Q. Zeng, I. Baker, J. B. Cui, and Z. C. Yan, *J. Magn. Magn. Mater.* **308**, 214 (2007).
14. J. H. Park, Y. K. Hong, J. J. Lee, W. C. Lee, S. G. Kim, and C. J. Choi, *Metals* **4**, 455 (2014).
15. J. H. Park, Y. K. Hong, S. G. Kim, S. H. Kim, L. Liyanage, J. J. Lee, W. C. Lee, G. Abo, K. H. Hur, and S. Y. An, *J. Magn. Magn. Mater.* **355**, 1 (2014).
16. Arnold Magnetic Technologies Catalog (2003).

17. P. C. Sen, *Principles of Electric Machines and Power Electronics*, 2nd, NewYork, U.S., John Wiley & Sons, 1997.

## CHAPTER 11

### CONCLUSIONS

Low operating temperature and limited supply of RE magnetic materials are the two important issues that must be addressed for continued full utilization of PMs in high-efficiency sustainable energy applications. Therefore, RE-free permanent magnetic materials with a high  $T_c$  were investigated. Theoretical and experimental studies were conducted in parallel to design RE-free permanent magnetic materials and to realize their applications to IPMSM and HAMR media.

The calculated  $M_s$  of single phase magnetic materials are 0.84 T for MnBi and 0.49 T for SrFe<sub>12</sub>O<sub>19</sub> at 23 °C, and 0.73 T for MnBi and 0.31 T for SrFe<sub>12</sub>O<sub>19</sub> at 200 °C. This temperature dependent  $M_s$  leads to  $(BH)_{\max}$  of 17.7 MGOe for MnBi and 5.9 MGOe for SrFe<sub>12</sub>O<sub>19</sub> at 23 °C and 11.9 MGOe for MnBi and 2.6 MGOe for SrFe<sub>12</sub>O<sub>19</sub> at 200 °C. The  $(BH)_{\max}$  of Nd-Fe-B is 42 MGOe at 23 °C and 6.1 MGOe at 200 °C, therefore, exhibiting a higher negative temperature coefficient of  $H_{ci}$  than RE-free permanent magnetic materials.

The  $M_s$  and  $H_{ci}$  models for the exchange coupled two-phase magnetic materials were developed and experimentally proved. The exchange coupled  $\tau$ -phase MnAl and  $\alpha$ -phase FeCo composites were synthesized and compared with the theoretical  $M_s$  and  $H_{ci}$  models. The experimental  $M_s$  and  $H_{ci}$  in terms of the  $f_h$  are in good agreement with the theoretically developed models.

Lastly, RE-free IPMSMs were designed and characterized with the FEM. The torque of RE and RE-free IPMSMs are calculated at temperatures between 23 and 200 °C for comparison. The torques for Nd-Fe-B, MnAl, MnBi, SrFe<sub>12</sub>O<sub>19</sub>, and Alnico at 23 and 200 °C clearly show

that the torque with the Nd-Fe-B magnet is higher than with the others at low temperatures, but the IPMSM with the MnBi magnet shows a higher torque above 174 °C. The MnBi IPMSM outperforms the Nd-Fe-B IPMSM above 174 °C due to the positive temperature coefficient of intrinsic coercivity of MnBi.

## CHAPTER 12

### FUTURE WORK

Future works include the development of (i) new RE-free permanent magnetic materials with increased saturation magnetization ( $M_s$ ), anisotropy constant ( $K$ ), and Curie temperature ( $T_c$ ) using both theoretical calculation and experimental fabrication and (ii) an advanced PMSM with improved torque, efficiency, speed range, etc. with RE-free permanent magnets. The new RE-free permanent magnetic materials will be based on ferromagnetic Mn or Fe transition metals. High magnetocrystalline anisotropy will be achieved by alloying Mn/Fe with V, Cr, Ni, Cu, etc.,

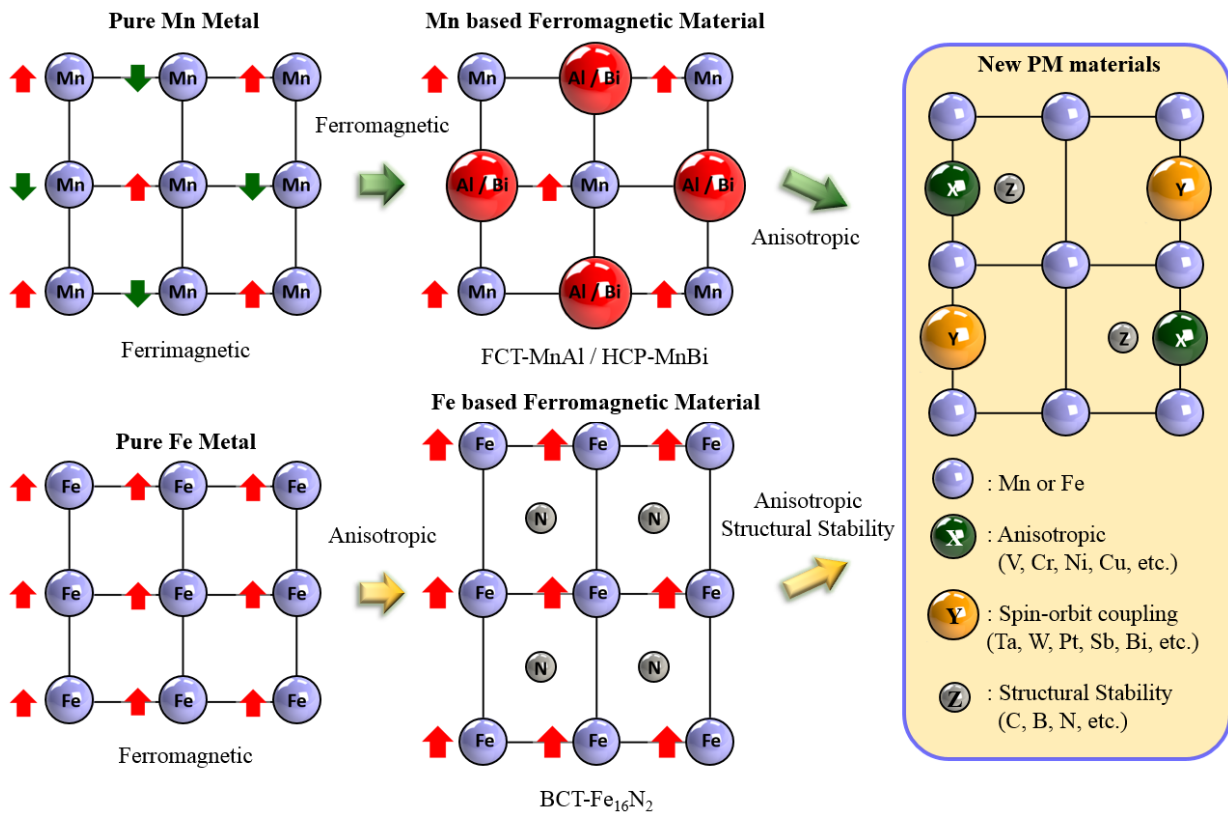


FIG. 12.1. Design methodology of new permanent magnetic materials based on ferromagnetic Mn or Fe.

and strong spin-orbit coupling will be realized by adding Ta, W, Pt, Sb, Bi, etc. In addition, high structural stability will be attempted by alloying with C, B, N, etc. Design methodology of new permanent magnetic materials based on metallic Mn/Fe element is shown in Fig. 12.1.

Design of advanced RE-free PMSM will be performed to achieve a similar performance to RE-PMSMs. Finite element method (FEM) will be used to design the PMSM with RE free permanent magnet. Advanced types of PMSMs include segmented rotor structure, spoke-type motor with segmented wing-shaped PMs, and spoke-type motor with two layers of PMs per pole due to their small air gap between PMs and electromagnets, therefore, providing strong torque with high  $B$ . Examples of a Dual Stator Axial Flux Permanent Magnet Motor (DSAFPMM) and Permanent Magnet assisted Synchronous Reluctance Motor (PMA-SynRM) are shown in Fig. 12.2. The DSAFPMM incorporating the unaligned arrangement of two stators together with the use of a spoke-type permanent magnet array and phase-group concentrated-coil windings will be explored for the purpose of increasing torque density and reducing torque ripple. The PMA-SynRM will also be investigated due to its high reluctance torque, which enhances Flux

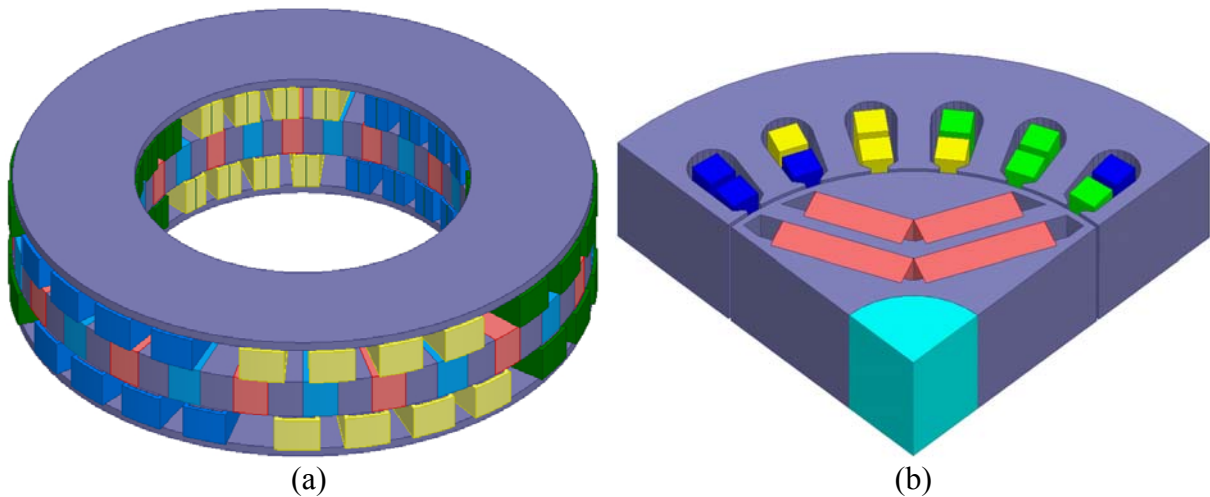


FIG. 12.2. (a) Dual Stator Axial Flux Permanent Magnet Motor (DSAFPMM) and (b) Permanent Magnet assisted Synchronous Reluctance Motor (PMA-SynRM) design. The blue, yellow, and green colors indicate three-phases.

Weakening Controllability usually applied for high speed running, and higher power density at high speed. The back electromotive force (EMF), cogging torque, electromagnetic torque, torque ripple, iron loss, and efficiency will be calculated by the FEM.

## APPENDIX

### LIST OF PUBLICATIONS

PEER-REVIEWED JOURNAL PUBLICATIONS: TOTAL 49

1. **Jihoon Park**, Yang-Ki Hong, Chang-Dong Yeo, Seong-Gon Kim, Li Gao, and Jan-Ulrich Thiele, “Electronic Structure and Magnetic Properties of Mn Substituted Fe-Pt (in press),” *IEEE Transactions on Magnetics* (2016).
2. Woncheol Lee, Yang-Ki Hong, **Jihoon Park**, Jaejin Lee, In-Seung Baek, Nam-Pal Hur, and Won-Mo Seong, “Low-Profile Multiband Ferrite Antenna for Telematics Application (in press),” *IEEE Transactions on Magnetics* (2016).
3. Xia Xu, Yang-Ki Hong, **Jihoon Park**, Woncheol Lee, and Alan Lane, “Ex-situ Synthesis of Magnetically Exchange Coupled SrFe<sub>12</sub>O<sub>19</sub>/Fe-Co Composites,” *AIP Advances* **6**, 056026 (2016).
4. **Jihoon Park**, Yang-Ki Hong, Woncheol Lee, Seok Bae, Seong-Gon Kim, and Chul-Jin Choi, “Electronic Structures of Nanocrystalline Fe<sub>90-x</sub>Cu<sub>x</sub>Si<sub>10-y</sub>B<sub>y</sub> Soft Magnets,” *AIP Advances* **6**, 055915 (2016).
5. **Jihoon Park**, Yang-Ki Hong, Hyun-Kyu Kim, Woncheol Lee, Chang-Dong Yeo, Seong-Gon Kim, Myung-Hwa Jung, Chul-Jin Choi, and Oleg N. Mryasov, “Electronic Structures of MnB Soft Magnet,” *AIP Advances* **6**, 055911 (2016).
6. **Jihoon Park**, Yang-Ki Hong, Woncheol Lee, Byong-Chul Choi, and Chul-Jin Choi, “Electronic Structure of La-Co Substituted Strontium Hexaferrite (Sr<sub>1-x</sub>La<sub>x</sub>Fe<sub>12-x</sub>Co<sub>x</sub>O<sub>19</sub>) Permanent Magnet,” *IEEE Magnetics Letters* **7**, 5500403 (2016).
7. **Jihoon Park**, Yang-Ki Hong, Woncheol Lee, Chin-Mo Kim, Kang-Ryong Choi, Sung-Yong An, Jung-Wook Seo, and Kang-Heon Hur, “Thermomagnetic Stability of M-Type Strontium Ferrite (SrFe<sub>12</sub>O<sub>19</sub>) Particles with Different Shapes,” *Electronic Materials letters* **12**, 100 (2016).
8. **Jihoon Park**, Yang-Ki Hong, Woncheol Lee, Sung-Yong An, Jung-Wook Seo, and Kang-Heon Hur, “Coercivity of SrFe<sub>12</sub>O<sub>19</sub> Hexaferrite Platelets Near Single Domain Size,” *IEEE Magnetics Letters* **6**, 5500203 (2015).
9. **Jihoon Park**, Yang-Ki Hong, Seong-Gon Kim, Li Gao, and Jan-Ulrich Thiele, “Magnetic properties of Fe-Mn-Pt for HAMR applications,” *Journal of Applied Physics* **117**, 053911 (2015).

10. Xia Xu, Yang-Ki Hong, **Jihoon Park**, Woncheol Lee, Alan M. Lane, "Exchange Coupled SrFe<sub>12</sub>O<sub>19</sub>/FeCo Core/shell Particles with Different Shell Thickness," *Electronic Materials Letters* **11**, 1021 (2015).
11. Vivek Dixit, Chandani N. Nandadasa, Seong-Gon Kim, Sungho Kim, **Jihoon Park**, Yang-Ki Hong, "Site preference and magnetic properties of Ga/In-substituted Strontium hexaferrite: an ab initio study," *Journal of Applied Physics* **118**, 203908 (2015).
12. Xia Xu, Yang-Ki Hong, **Jihoon Park**, Woncheol Lee, Alan M. Lane, and Jun Cui, "Magnetic Self-Assembly for the Synthesis of Magnetically Exchange Coupled MnBi/Fe-Co Composites," *Journal of Solid State Chemistry* **231**, 108 (2015).
13. Vivek Dixit, Chandani N. Nandadasa, Seong-Gon Kim, Sungho Kim, **Jihoon Park**, Yang-Ki Hong, Laalitha S. I. Liyanage, and Amitava Moitra, "Site occupancy and magnetic properties of Al-substituted M-type strontium hexaferrite," *Journal of Applied Physics* **117**, 243904 (2015).
14. Xia Xu, **Jihoon Park**, Yang-Ki Hong, Alan M. Lane, "Ethylene glycol assisted spray pyrolysis for the synthesis of hollow BaFe<sub>12</sub>O<sub>19</sub> spheres," *Materials Letters* **144**, 119 (2015).
15. Xia Xu, **Jihoon Park**, Yang-Ki Hong, Alan M. Lane, "Magnetically self-assembled SrFe<sub>12</sub>O<sub>19</sub>/Fe-Co core/shell particles," *Materials Chemistry and Physics* **152**, 9 (2015).
16. Xia Xu, **Jihoon Park**, Yang-Ki Hong, Alan M. Lane, "Synthesis and characterization of hollow mesoporous BaFe<sub>12</sub>O<sub>19</sub> spheres," *Journal of Solid State Chemistry* **222**, 84 (2015).
17. Woncheol Lee, Yang-Ki Hong, Jaejin Lee, **Jihoon Park**, and Won-Mo Seong, "Omnidirectional Low-Profile Multiband Antenna for Vehicular Telecommunication," *Progress In Electromagnetics Research Letters* **51**, 53 (2015).
18. **Jihoon Park**, Yang-Ki Hong, Jaejin Lee, Woncheol Lee, Seong-Gon Kim, and Chul-Jin Choi, "Electronic structure and maximum energy product of MnBi (invited)," *Metals* **4**, 455 (2014).
19. **Jihoon Park**, Yang-Ki Hong, Jaejin Lee, Woncheol Lee, Chul-Jin Choi, Xia Xu, and Alan M. Lane, "Magnetization and Intrinsic Coercivity for  $\tau$ -phase Mn<sub>54</sub>Al<sub>46</sub>/ $\alpha$ -phase Fe<sub>65</sub>Co<sub>35</sub> Composite," *Journal of Magnetism* **19**, 55 (2014).
20. **Jihoon Park**, Yang-Ki Hong, Seong-Gon Kim, Sungho Kim, Laalitha S.I. Liyanage, Jaejin Lee, Woncheol Lee, Gavin S. Abo, Kang-Heon Hur, Sung-Yong An, "Maximum energy product at elevated temperature for hexagonal strontium ferrite (SrFe<sub>12</sub>O<sub>19</sub>) magnet," *Journal of Magnetism and Magnetic Materials* **355**, 1 (2014).
21. Amitava Moitra, Sungho Kim, Seong-Gon Kim, S.C. Erwin, Yang-Ki Hong, **Jihoon Park**, "Defect formation energy and magnetic properties of aluminum-substituted M-type barium hexaferrite," *Computational Condensed Matter* **1**, 45 (2014).

22. Jaejin Lee, Yang-Ki Hong, Changhan Yun, Woncheol Lee, **Jihoon Park**, and Byoung-Chul Choi, "Magnetic parameters for ultra-high frequency (UHF) ferrite circulator design," *Journal of Magnetism* **19**, 399 (2014).
23. Jaejin Lee, Yang-Ki Hong, Woncheol Lee, **Jihoon Park**, Terumitsu Tanaka, and Changhan Yun, "Electrically small ferrite antenna gain with dc magnetic field for mobile device application," *Microwave and Optical Technology Letters* **56**, 1531 (2014).
24. Yang-Ki Hong, **Jihoon Park**, Oleg N. Mryasov, Seong-Gon Kim, Sungho Kim, Jaejin Lee, Gavin S. Abo, Chul-Jin Choi, "Magnetic properties of MnBi based alloys: First-principles calculations for MnBi-Co and MnBi-Co-Fe cases," *AIP Advances* **3**, 052137 (2013).
25. Laalitha S.I. Liyanage, Sungho Kim, Yang-Ki Hong, **Jihoon Park**, Steven C. Erwin, Seong-Gon Kim, "Theory of magnetic enhancement in strontium hexaferrite through Zn-Sn pair substitution," *Journal of Magnetism and Magnetic Materials* **348**, 75 (2013).
26. Gavin S. Abo, Yang-Ki Hong, **Jihoon Park**, Jaejin Lee, Woncheol Lee and Byoung-Chul Choi, "Definition of magnetic exchange length," *IEEE Transactions on Magnetism* **49** (8), 4937 (2013).
27. Jaejin Lee, Yang-Ki Hong, Woncheol Lee, and **Jihoon Park**, "Impedance matching of electrically small antenna with Ni-Zn ferrite film," *Journal of Magnetism* **18** (4), 428 (2013).
28. Jaejin Lee, Yang-Ki Hong, Woncheol Lee, Gavin S. Abo, **Jihoon Park**, Won-Mo Seong, and Won-Ki Ahn, "Control of magnetic loss tangent of hexaferrite for advanced RF antenna applications," *Journal of Applied Physics* **113**, 073909 (2013).
29. Nicholas Neveu, Yang-Ki Hong, Jaejin Lee, **Jihoon Park**, Gavin Abo, Woncheol Lee, and David Gillespie, "Miniature hexaferrite axial-mode helical antenna for unmanned aerial vehicle applications," *IEEE Transactions on Magnetism* **49** (7), 4265 (2013).
30. Jaejin Lee, Yang-Ki Hong, Woncheol Lee, Gavin S. Abo, **Jihoon Park**, Won-Mo Seong, and Seok Bae, "Role of small permeability in gigahertz ferrite antenna performance," *IEEE Magnetism Letters* **4**, 5000104 (2013).
31. Seok Bae, Yang-Ki Hong, Jaejin Lee, **Jihoon Park**, Jeevan Jalli, Gavin S. Abo, Hyuck M. Kwon, and Chandana K. K. Jayasooriya, "Pulsed Ferrite Magnetic Field Generator for Through-the-earth (TTE) Communication Systems for Disaster Situation in Mines," *Journal of Magnetism* **18**, 43 (2013).
32. Gavin S. Abo, Yang-Ki Hong, Jeevan Jalli, Jaejin Lee, **Jihoon Park**, Seok Bae, Seong-Gon Kim, Byoung-Chul Choi, and Terumitsu Tanaka, "Shape dependent coercivity simulation of a spherical barium ferrite (S-BaFe) particle with uniaxial anisotropy," *Journal of Magnetism* **17**, 1 (2012).
33. Jaejin Lee, Yang-Ki Hong, Woncheol Lee, Gavin S. Abo, **Jihoon Park**, Nicholas Neveu, Won-Mo Seong, Sang-Hoon Park and Won-Ki Ahn, "Soft M-type hexaferrite for very high

- frequency (VHF) miniature antenna applications,” *Journal of Applied Physics* **111**, 07A520 (2012).
34. Jaejin Lee, Yang-Ki Hong, Woncheol Lee, Gavin S. Abo, **Jihoon Park**, Ryan Syslo, Won-Mo Seong, Sang-Hoon Park and Won-Ki Ahn, “High ferromagnetic resonance and thermal stability spinel  $\text{Ni}_{0.7}\text{Mn}_{0.3-x}\text{Co}_x\text{Fe}_2\text{O}_4$  ferrite for ultra high frequency devices,” *Journal of Applied Physics* **111**, 07A516 (2012).
  35. Gavin S. Abo, Yang-Ki Hong, Byoung-Chul Choi, Michael J. Donahue, Seok Bae, Jeevan Jalli, **Jihoon Park**, Jaejin Lee, Mun-Hyun Park, and Sung-Hoon Gee, “Micromagnetic computer simulated scaling effect of S-shaped permalloy nano-element on operating fields for AND or OR logic,” *IEEE Transactions on Magnetics* **48** (5), 1851 (2012).
  36. Jaejin Lee, Yang-Ki Hong, **Jihoon Park**, Won-Mo Seong, Gi-Ho Kim, and Akimitsu Morisako, “M-type hexaferrite for gigahertz chip antenna applications,” *IEEE Magnetics Letters* **2**, 5000204 (2011).
  37. Jeevan Jalli, Yang-Ki Hong, Gavin S. Abo, Seok Bae, Jaejin Lee, **Jihoon Park**, Byoung C. Choi, and Seong-Gon Kim, “MFM studies of magnetic domain patterns in bulk barium ferrite ( $\text{BaFe}_{12}\text{O}_{19}$ ) single crystals,” *Journal of Magnetism and Magnetic Materials* **323**, 2627 (2011).
  38. Jeevan Jalli, Yang-Ki Hong, Seok Bae, Jaejin Lee, Gavin S. Abo, **Jihoon Park**, Byoung-Chul Choi, Tim Mewes, Seong-Gon Kim, Sung-Hoon Gee, In-Tak Nam, and Terumitsu Tanaka, “Magnetic and microwave properties of ferrimagnetic Zr-substituted  $\text{Ba}_2\text{Zn}_2\text{Fe}_{12}\text{O}_{22}$  (ZnY) single crystals,” *Journal of Applied Physics* **109**, 07A509 (2011).
  39. Jaejin Lee, Yang-Ki Hong, Seok Bae, Jeevan Jalli, Gavin S. Abo, **Jihoon Park**, Won-Mo Seong, Sang-Hoon Park, Won-Ki. Ahn, Ryan Syslo, and Nicholas Neveu, "Low loss  $\text{Co}_2\text{Z}$  ( $\text{Ba}_3\text{Co}_2\text{Fe}_{24}\text{O}_{41}$ )-glass composite for gigahertz antenna application," *Journal of Applied Physics* **109**, 07E530 (2011).
  40. Jeevan P. Jalli, Yang-Ki Hong, Seok Bae, Jae-Jin Lee, Gavin Abo, **Jihoon Park**, Tim Mewes, Byoung-Chul Choi, and Seong-Gon Kim, “Magnetic and microwave properties of ferrimagnetic Zr-substituted  $\text{Ba}_2\text{Zn}_2\text{Fe}_{12}\text{O}_{22}$  (ZnY) single crystal,” *Journal of Applied Physics* **109**, 07A509 (2011).
  41. Jaejin Lee, Yang-Ki Hong, Seok Bae, Gavin S. Abo, Jeevan Jalli, **Jihoon Park**, Won-Mo Seong, Sang-Hoon Park, Won-Gi An, and Gi-Ho Kim, “Broadband Bluetooth Antenna based on  $\text{Co}_2\text{Z}$  Hexaferrite-Glass Composite,” *Microwave and Optical Technology Letters* **53**, No.6, 1222 (2011).
  42. Jaejin Lee, Yang-Ki Hong, Seok Bae, Jeevan Jalli, **Jihoon Park**, Gavin S. Abo, Gregory W. Donohoe, and Byoung-Chul Choi, “Integrated ferrite film inductor for power system-on-chip (PowerSoC) smart phone applications,” *IEEE Transactions on Magnetics* **47**, 304 (2011).

43. Seok Bae, Yang-Ki Hong, Jaejin Lee, **Jihoon Park**, Jeevan Jalli, Gavin S. Abo, Won-Mo Seong, Sang-Hoon Park, Jun-Sik Kum, Won-Ki Ahn, and Gi-Ho Kim, "Dual-band ferrite chip antenna for global positioning system and Bluetooth applications," *Microwave and Optical Technology Letters* **53**, 14 (2011).
44. **Jihoon Park**, Yang-Ki Hong, Seok Bae, Jaejin Lee, Jeevan Jalli, Gavin S. Abo, Nick Neveu, Seong-Gon Kim, Chul-Jin Choi, and Jung-Gu Lee, "Saturation magnetization and crystalline anisotropy calculations for MnAl permanent magnet," *Journal of Applied Physics* **107**, 09A731 (2010).
45. Seok Bae, Yang-Ki Hong, Jaejin Lee, **Jihoon Park**, Jeevan Jalli, Gavin S. Abo, Hyuck M. Kwon, and C. Chandana K. K. Jayasooriya, "Miniature and higher-order mode ferrite MIMO ring patch antenna for mobile communication system," *Progress in Electromagnetics Research B* **25**, 53 (2010).
46. Jeevan Jalli, Yang-Ki Hong, Jaejin Lee, Gavin S. Abo, **Jihoon Park**, Alan M. Lane, Seong-Gon Kim, and Steven C. Erwin, "Conversion of worm-shaped antiferromagnetic hematite to ferrimagnetic spherical barium-ferrite nanoparticles for particulate recording media," *IEEE Magnetics Letters* **1**, 4500204 (2010).
47. Seok Bae, Yang-Ki Hong, Jaejin Lee, Won-Mo Seong, Jun-Sik Kum, Won-Ki Ahn, Sang-Hoon Park, Gavin S. Abo, Jeevan Jalli, and **Jihoon Park**, "Miniaturized broadband ferrite T-DMB antennas for mobile phone applications," *IEEE Transactions on Magnetics* **46** (6), 2361 (2010).
48. Jaejin Lee, Yang-Ki Hong, Seok Bae, **Jihoon Park**, Jeevan Jalli, Gavin S. Abo, Byoung-Chul Choi, and Gregory W. Donohoe, "High quality factor Ni-Zn ferrite planar inductor," *IEEE Transactions on Magnetics* **46** (6), 2417 (2010).

#### BOOK CHAPTER

Fei Hu, Xiaojun Cao, David Brown, **Jihoon Park**, Mengcheng Guo, Qingquan Sun, Yeqing Wu, "Tele-Healthcare Computing and Engineering: Principles and Design." Chapter 4: Virtual Reality-based Tele-Rehabilitation Computing.

#### US PATENT

Yang-Ki Hong and **Jihoon Park**, "Non-rare Earth Magnets having Manganese (Mn) and Bismuth (Bi) Alloyed with Cobalt (Co)," US 20150125341 (WO 2013158635 A1), May. 7, 2015.

## US PROVISIONAL PATENTS

1. US Provisional Patent Application: Yang-Ki Hong, Xia Xu, **Jihoon Park**, and Alan Lane, “Manufacturing Method for Hard Magnetic Metal Soft Magnetic Metal Alloy Composite (Exchange Coupled) Magnets,” filed on March 3, 2014. Assigned Serial No.: Patent draft in process (UAIPD14-0041).
2. US Provisional Patent Application: Yang-Ki Hong, Xia Xu, **Jihoon Park**, and Alan Lane, “Remanent Magnetization Assisted Self-Assembled Core-Shell Magnets for Magnetic Exchange Coupling,” filed on July 7, 2014. U.S. Provisional Application No. 62/021,553.